

HIERARCHICAL MATERIALS INFORMATICS

HIERARCHICAL MATERIALS INFORMATICS

Novel Analytics for Materials Data

SURYA R. KALIDINDI

Professor, George W. Woodruff School of Mechanical Engineering
School of Computational Science and Engineering
School of Materials Science and Engineering
Atlanta, GA, USA



AMSTERDAM • BOSTON • HEIDELBERG • LONDON
NEW YORK • OXFORD • PARIS • SAN DIEGO
SAN FRANCISCO • SINGAPORE • SYDNEY • TOKYO

Butterworth-Heinemann is an imprint of Elsevier



Butterworth-Heinemann is an imprint of Elsevier
The Boulevard, Langford Lane, Kidlington, Oxford OX5 1GB, UK
225 Wyman Street, Waltham, MA 02451, USA

Copyright © 2015 Elsevier Inc. All rights reserved.

No part of this publication may be reproduced or transmitted in any form or by any means, electronic or mechanical, including photocopying, recording, or any information storage and retrieval system, without permission in writing from the publisher. Details on how to seek permission, further information about the Publisher's permissions policies and our arrangements with organizations such as the Copyright Clearance Center and the Copyright Licensing Agency, can be found at our website: www.elsevier.com/permissions.

This book and the individual contributions contained in it are protected under copyright by the Publisher (other than as may be noted herein).

Notices

Knowledge and best practice in this field are constantly changing. As new research and experience broaden our understanding, changes in research methods, professional practices, or medical treatment may become necessary.

Practitioners and researchers must always rely on their own experience and knowledge in evaluating and using any information, methods, compounds, or experiments described herein. In using such information or methods they should be mindful of their own safety and the safety of others, including parties for whom they have a professional responsibility.

To the fullest extent of the law, neither the Publisher nor the authors, contributors, or editors, assume any liability for any injury and/or damage to persons or property as a matter of products liability, negligence or otherwise, or from any use or operation of any methods, products, instructions, or ideas contained in the material herein.

ISBN: 978-0-12-410394-8

Library of Congress Cataloging-in-Publication Data

A catalog record for this book is available from the Library of Congress.

British Library Cataloguing-in-Publication Data

A catalogue record for this book is available from the British Library.

For Information on all Butterworth-Heinemann publications
visit our website at <http://store.elsevier.com/>



Working together
to grow libraries in
developing countries

www.elsevier.com • www.bookaid.org

ACKNOWLEDGMENTS

I acknowledge the tremendous support and inspiration I have been lucky to receive from numerous colleagues, students, and my family over the many years it took to develop the concepts and ideas presented in this book. Most of the concepts presented here were formulated in deep discussions with my colleagues Brent L. Adams (Brigham Young University), David Fullwood (Brigham Young University), Hamid Garmestani (Georgia Tech), Marc DeGraef (Carnegie Mellon University), and David L. McDowell (Georgia Tech) over much of my academic career. These ideas were sharply refined, extended, and demonstrated through the PhD theses of numerous brilliant young individuals that I am very lucky to claim as my students, though in reality, they have been my teachers. In particular, all of the material presented here come from the PhD theses of Stephen Niezgoda, Giacomo Landi, Tony Fast, Marko Knezevic, Hamad Al-Harbi, Yuksel Yabansu, Ahmet Cecen, David Brough, and Joshua Gomberg. My special thanks to Ali Khosravani and Ahmet Cecen for the beautiful figures they contributed to this book (including those used for the cover).

I acknowledge the tremendous support I received from numerous funding agencies for conducting the research that lead to this book. In particular, I acknowledge that ONR funding from the D 3-D program managed by Julie Christodoulou is where many of the foundational concepts presented in this book took birth. These new research directions came out of an earlier, more foundational, work supported by ARO (David Stepp). Subsequent to the D 3-D program, different aspects of the work were supported by ONR (William Mullins), NIST (James Warren), AFOSR (Ali Sayir and Fariba Fahroo), and NSF-IGERT (FLAMEL). All of this support were essential to undertake the necessary and continuing iterations conducted in refining my understanding of the subject matter presented in this book. I feel uniquely lucky to have had so much sustained support over the past two decades, without which this book would not have come to fruition.

I want to dedicate this book to my loving family members, my wife Manjula, my sons Arvind and Bharath, and my inspiring parents Aravinda and Venkata Rama Raju.

MATERIALS, DATA, AND INFORMATICS

A defining core tenet in the field of materials science and engineering is that the hierarchical internal structure of a material controls completely the macroscale properties or performance characteristics exhibited by the material. Clearly, the overall chemical composition is one of the salient averaged measures of the material structure. However, one can also imagine that even for a fixed overall chemical composition, the internal structures in the material can be dramatically altered through a broad range of manufacturing (also called processing) options (typically involving the application of specific thermomechanical histories). Therefore, since the dawn of human civilization, tremendous effort has been expended in developing or discovering novel processing routes that produced materials with enhanced performance characteristics. Such materials have always served as critical enablers for the successful development of advanced technologies throughout human history [1].

A majority of the materials employed in advanced technologies exhibit hierarchical internal structures with rich details at multiple length and/or structure scales (spanning from atomic to macroscale). Collectively, these features of the multiscale material internal structure are referred to as the *microstructure* or simply the *structure*, and constitute the central consideration in the development of advanced hierarchical materials discussed in this book. In this book, these terms (i.e., microstructure or simply the structure) are used very broadly to represent all details of the material internal structure (spanning all relevant length or structure scales involved). Indeed, the representation of the material internal structure in its entirety, even in a single material system, is unimaginably complex and demands very high-dimensional representations. For example, most materials being explored for structural applications (e.g., Ti alloys in jet engines, Advanced High Strength Steels and Mg

alloys in lightweight automobiles, Al alloys in aerospace frames, Zr alloys in the nuclear industry) exhibit polycrystalline microstructures at the mesoscale [2–5]. A rigorous description of such material structures should include precise quantification of the spatial distributions of the crystal lattice orientations and various hierarchical defect populations (e.g., point defects, dislocations, grain boundaries, phase boundaries, pores, and microcracks). Given the vast number of tiered spatial distributions that must be quantified to faithfully represent the complex hierarchical microstructure in these material systems, the need for an extremely large-dimensional representation becomes obvious.

Fortunately, the field of materials science and engineering has already taught us that only certain salient features of the material structure dominate the macroscale performance characteristics of interest for any selected application. Therefore, the main challenge in the development of materials with improved/enhanced properties reduces to identifying and tracking the salient microstructure features that are important to a specific engineering or technology application. In other words, the core knowledge needed to guide the materials development efforts can be sought and expressed as reduced-order *process—structure—property (PSP) linkages* that capture the roles of different unit manufacturing (or processing) steps on the salient microstructure features controlling the properties of interest. It is important to recognize that these linkages represent reduced-order models as they utilize reduced-order representations of the material structure. Historically, such efforts have been largely guided by the scientific approach which entails formulating a fundamental hypothesis and then validating it with carefully designed experiments conducted in highly controlled environments. Such science-driven approaches for establishing PSP linkages have been expensive and slow [6–8], because their focus has been to isolate and study each physical mechanism (i.e., cause) and its associated effect in a highly systematic manner.

In this chapter, we first familiarize ourselves with the main concepts and protocols employed by materials experts in establishing the PSP linkages, along with an understanding of the central challenges involved in these important endeavors. We simultaneously identify specific areas where the emerging concepts in data science and analytics can have a transformative effect in dramatically accelerating these protocols, while reducing the overall cost. We expound these opportunities systematically in the later chapters of this book.

1.1 PSP Linkages

As mentioned earlier, the core knowledge needed to guide the materials development efforts is often expressed as PSP linkages, shown schematically in [Figure 1.1](#) in the direction they are conventionally formulated, that is, from process to material internal structure to properties. It is important to define these terms precisely as they are central to the concepts discussed in this book. In this book, we shall reserve the word *space* to indicate a complete set, which may typically be exceedingly large. For example, structure space in [Figure 1.1](#) refers to the complete set of all theoretically feasible material internal structures. In other words, any conceivable material internal structure would be an element of this set. Therefore, the structure space shown in [Figure 1.1](#) is unimaginably large. Similarly, a point (or element) in the process space depicts one hybrid process route. A hybrid process route is made up of an ordered sequence of multiple unit manufacturing processes (potentially involving some ordered sequence of refinement, casting, shaping, machining, joining, and finishing steps). Consequently, it is easy to see that one can build an extremely large number of distinct hybrid process routes even when only a few unit processes are considered. In this book, the word *property* will be used exclusively to refer to physical properties of interest that directly control the performance of a manufactured part. Physical properties are often conceptually defined as characteristics of the material's physical response to a specified set of idealized driving forces (e.g., thermomechanical loading conditions) imposed

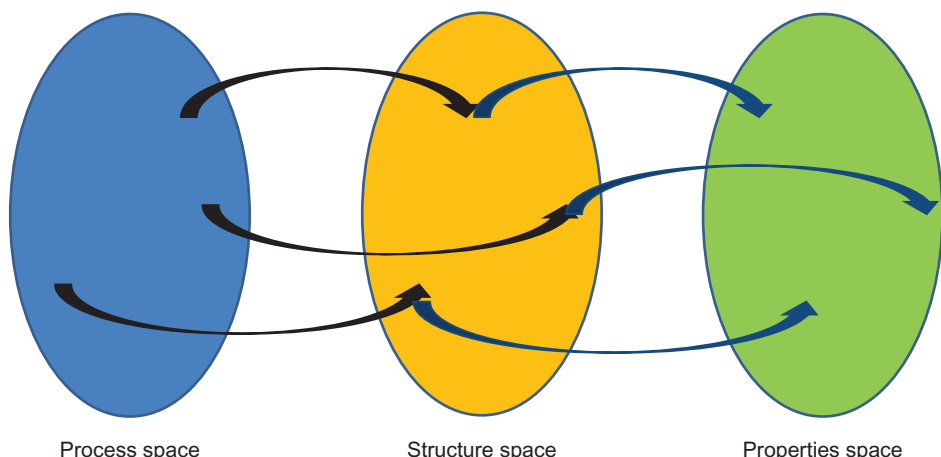


Figure 1.1 Central considerations in the materials development efforts.

on a material. For example, in structural applications, the properties of typical interest include elastic stiffness, yield strength, fracture toughness, and fatigue strength. On a relative scale, the property space is likely to be the smallest of the three spaces depicted in [Figure 1.1](#) but can be high-dimensional when the application demands multifunctional performance requirements.

Historically, the conventional approaches used in the field of materials science and engineering have only explored very limited subspaces in the directions depicted in [Figure 1.1](#). In fact, most of the effort to date has focused on establishing direct linkages between the process and the properties, with token attention paid to the material structure. However, the main difficulty of the conventional approach stems from the fact that the hybrid process space as defined earlier is not a continuous space where we can interpolate with confidence. Since the hybrid process space is made up of a multitude of unit manufacturing steps, any change in the process parameters of any of the steps involved or any change in the sequence of steps would constitute a new hybrid process. If one represents two hybrid processes as two different points in the process space shown in [Figure 1.1](#), the points lying on a straight line connecting these two points cannot be necessarily assigned or associated with meaningful new hybrid processes. As a simple example, consider hybrid process HP1 as a point in the process space denoting an ordered sequence of unit processes as $HP1 = (P1, P2, P5, P2)$, where P1, P2, and P5 denote specific unit manufacturing processes. It is emphasized that HP1 is an ordered sequence, starting with P1, followed by P2, and so on. Likewise, one can imagine another point in the process space denoted as $HP2 = (P6, P5, P9, P1)$. Now, it should be easy to see that is not easy to assign a new hybrid process to a point halfway between HP1 and HP2. Because interpolation in the hybrid process space is essentially meaningless, the conventional approaches of establishing direct linkages between process and properties have fundamentally employed a discrete approach. Moreover, the traditional approaches have relied heavily on experiments while exploring such highly discretized process histories. Because of these reasons, the rate of discovery of new materials with improved properties has been dreadfully slow. The introduction of the structure space (and the formulation of PSP linkages) has the potential to dramatically alter traditional approaches. Unlike the process space, the structure space allows interpolation because a point in the structure space corresponds to a set of statistical measures of the material internal structure. In other words, interpolated points correspond to

structures with interpolated values of the selected structure measures. Also, as the structure space is expected to be a high-dimensional (and unimaginably large) space, it allows for efficient capture and easy visualization of many-to-one connections between the process and the properties of interest. The many-to-one connections imply that it is possible to arrive at distinct structures (exhibiting different statistical measures) through the use of different process routes, while exhibiting the same values for selected macroscale property combinations of interest in an application. It would be very difficult, if not impossible, to capture such subtleties in going directly from the process to the properties.

As mentioned earlier, a core tenet in the field of materials science and engineering is that the key to the realization of various material properties needed for advanced technology applications lies in the control of the material internal structure. In practice, this is made very difficult by the fact that the material internal structure is very complex (this will be elaborated later), and its rigorous quantification is likely to benefit immensely from the adoption of modern data science and analytics tools. The main impediment for bringing about the desired digital revolution in the materials development arena lies in the lack of a broadly adopted and broadly applicable framework for the digital representation of the material itself. Historically, it has been a common practice to label a material based on its dominant chemical components. For example, a very large set of materials exhibiting widely different property combinations are simply referred to as steels (more than 3500 grades according to the World Steel Association; <http://www.worldsteel.org/>) because their chemical composition is dominated by the chemical element Iron. [Figure 1.2](#) summarizes the measured values in steels for a specific property combination of interest in typical structural applications. The reader should take note of the vast range of property values realizable in a single class of metal alloys, namely steels. From the perspective of product design and manufacturing, [Figure 1.2](#) showcases the potential availability of a very large number of material choices in aiding the designer in meeting the customized performance demands in any specific targeted application. The spaces identified in [Figure 1.2](#) would then constitute the *design space*, as the designer would consider these choices along with a very large number of other available material systems, while also addressing several other performance requirements (could be based on other material properties and/or other design constraints such as cost, environmental impact, etc.). It should be noted

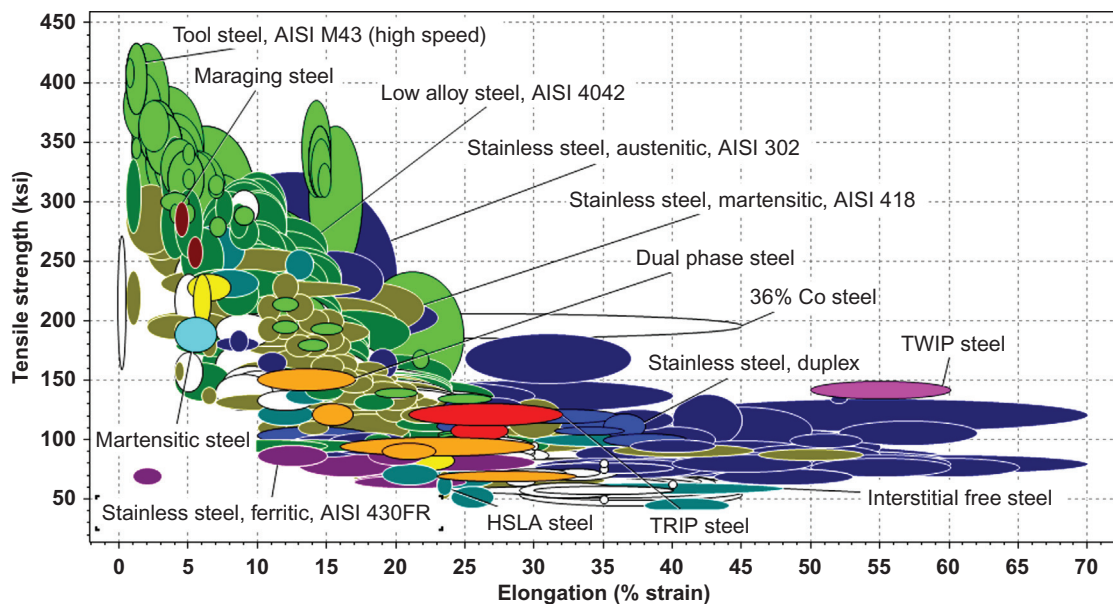


Figure 1.2 Values of tensile strength and ductility exhibited by different steels. The plot was generated using data from CES Selector Database [9].

that the spaces identified in Figure 1.2 represent only those steels that have been produced and mechanically evaluated to date. The theoretically available design space is expected to be significantly larger, as a very large number of new steels are yet to be produced and tested.

1.2 Material Internal Structure

The main consideration in this book is a systematic framework that can be employed to expand the design space described earlier. Understandably, we must start our discussion with the implicit challenges in uniquely identifying and cataloguing a single material and its associated properties. In this regard, it should be noted that the currently employed material naming conventions are based largely on the overall chemical composition and some details of final processing steps. As an example, 7075-T6 Al generally implies that this Al metal alloy has 5.6–6.1% Zn, 2.1–2.5% Mg, and 1.2–1.6% Cu, while the label “T6” implies the use of an aging treatment that results in an ultimate tensile strength of 510–572 MPa, a yield strength of 434–503 MPa, and a failure elongation of 5–11%. Although the

T6 temper is usually achieved by homogenizing the cast 7075 Al alloy at 450°C for several hours, and then aging at 120°C for 24 h, it does not automatically imply that this was the exact temper treatment employed. This is because it is entirely possible to obtain the set of properties described earlier using another thermomechanical processing history on the same alloy. This is the main limitation of the current approach in naming the materials. They do not capture or reflect the salient hierarchical structure measures of the material that would uniquely catalogue the material. They are currently only used to imply certain combinations of properties of general (not customized) interest to applications.

It is emphasized here that the digital representation of a material along with its associated properties is the core materials knowledge that needs to be communicated accurately among the materials specialist, the product designer, and the various stakeholders in the manufacturing value chain. New tools for the digital capture and seamless communication of the essential materials knowledge are critically needed to instigate a major transformation in the current practices employed by the materials development community. This in turn will dramatically reduce the cost and time expended in these endeavors [6,7].

Going back to [Figure 1.2](#), it is important to recognize that any one given sample of a material is expected to exhibit only one combination of properties. When one takes a deeper look at the property data shown in [Figure 1.2](#), it becomes apparent that the property values are significantly affected by relatively small changes in the overall (averaged) chemical composition of the steels. From this observation, one might be tempted to attribute all of the variation in the properties to the variation in the overall chemical composition of the metal alloys. However, the data also shows large variations in the properties even when the overall composition is nominally the same. This can be easily seen from the large intragrade variation of the properties depicted in [Figure 1.2](#). This variation of properties has been the central focus of investigations in the field of materials science and engineering over the past century, and has largely been attributed to the differences in the hierarchical internal structures of the materials. In other words, even when the overall chemical composition in a material is fixed, the internal structures of the materials can be altered in dramatic ways through various thermomechanical processes. Consequently, the large variation of properties seen in [Figure 1.2](#) is generally attributed to the differences in the internal structure of the different steels.

The above discussion now leads us to the next logical question—exactly what is in the internal structure of the material and which specific aspects of the internal structure play an important role in controlling the macroscale properties of interest? The answer to this relatively simple question is complicated by the fact that the material internal structure spans several length scales from the atomistic ($\sim 10^{-10}$ m) to the macroscale ($>10^{-3}$ m). Over this large span of length scales covering about seven orders of magnitude, the material internal structure exhibits a very large set of salient features that can potentially influence the macroscale mechanical properties of interest. It is very important that the reader appreciates the high degree of complexity the material internal structure presents in establishing the core materials knowledge (e.g., structure–property linkages that describe how certain salient attributes and measures of the material internal structure control the macroscale properties of interest). As a continuation of the earlier discussion on steels, let us probe a little more into their internal structure. If one looks into the mesoscale internal structures (at length scales in the range of 1–100 μm ; see [Figure 1.3](#)), one finds that different grades of steels are actually made of varying quantities (i.e., volume fractions) and types of constituents that can be identified as distinct thermodynamic phases (e.g., ferrite, austenite, cementite, and martensite). Each of the different phases encountered in the steels occurs with a range of chemical compositions (i.e., each phase does not have the same chemical composition in the different grades of steel) and exhibits dramatically different individual physical and mechanical properties. In fact, some of the phases (e.g., martensite) are metastable and can only be retained in the hierarchical structure of the material at room temperature through cleverly designed heat treatments that involve fast-quenching of the alloys from high temperatures (where these phases are produced). Furthermore, the different phases generally exhibit varying morphologies (e.g., equiaxed, lamellar, and needle-shaped; see [Figure 1.3](#)) and are likely to be spatially distributed in very different ways. Given all these variations at the mesoscale alone, it is easy to see why a certain grade of steel with a fixed overall chemical composition can exhibit dramatically different internal structures, which in turn can lead to large variations in the macroscale properties of interest (these variations can be as large as an order of magnitude). [Figure 1.3](#) shows several example mesoscale microstructures found in different grades of steels [10–16].

In addition to the rich diversity of structures found at the mesoscale shown in [Figure 1.3](#), the mechanical properties of

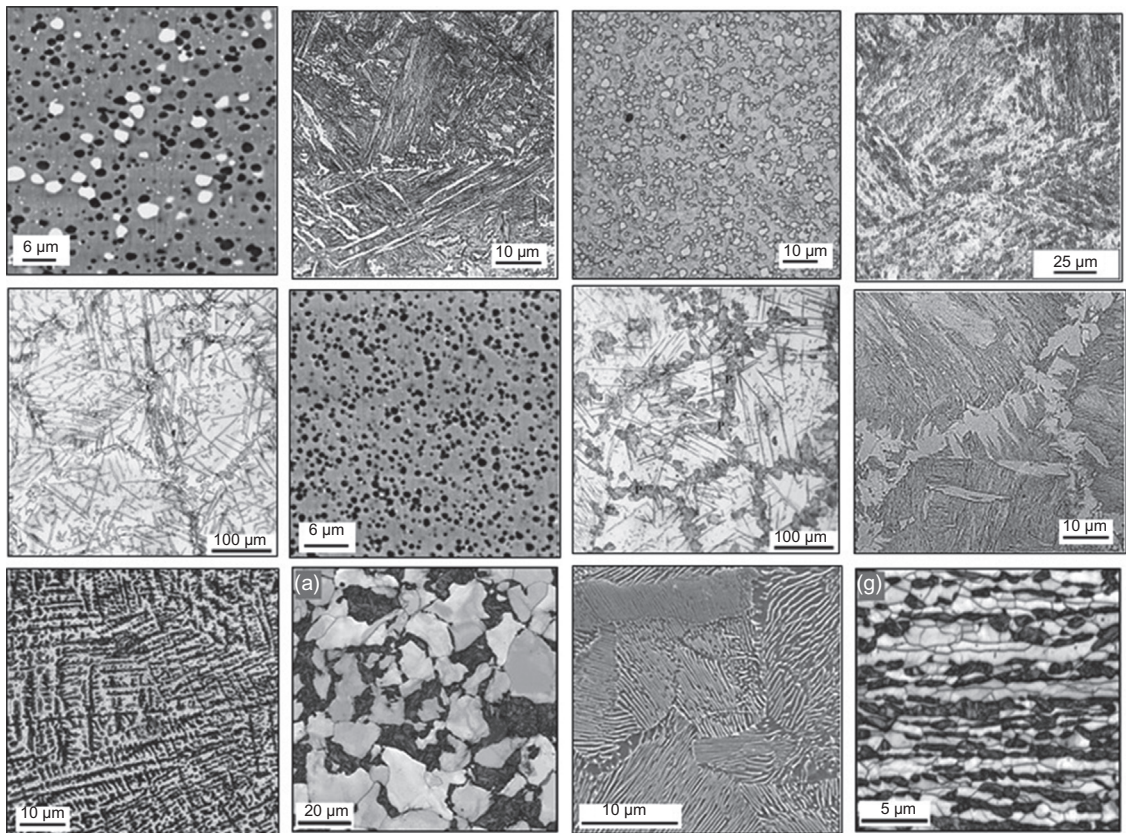


Figure 1.3 Example mesoscale internal structures seen in different steel grades [10–16].

most materials are strongly influenced by a large set of additional details at lower length scales [17]. Most metals of interest in structural applications exhibit crystalline structures at the atomic length scales. In other words, in these material systems, the atoms are placed in a well-defined spatial lattice that can be conveniently described using a repeating unit cell. For example, most of the individual phases found in steels exhibit a body-centered cubic (bcc) structure. However, there are well-known exceptions to this rule, as austenite exhibits a face-centered cubic (fcc) structure and martensite exhibits a body-centered tetragonal crystal structure. The crystal structure has been known to have a profound effect on the plastic properties of materials and their anisotropy. For example, the martensite phase is typically four to five times stronger compared to the ferrite phase. Even more importantly, the defects in the crystal

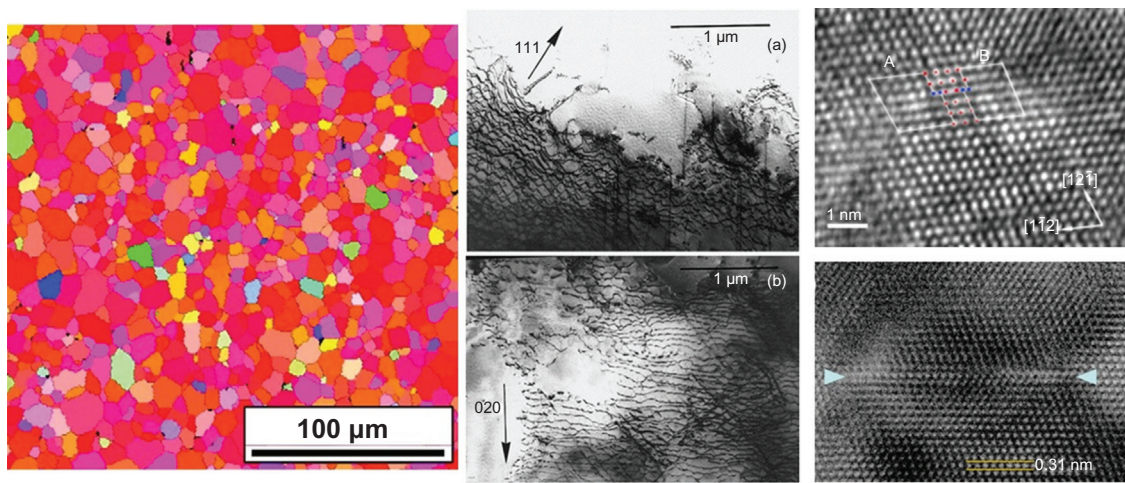


Figure 1.4 Some of the salient attributes of the material structure at the lower length scales that are known to play an important role in controlling the macroscale plastic properties of the metal [18–21].

structure influence strongly the plastic properties of the material. Such defects occur very naturally in the internal structure of metals at various length scales (Figure 1.4), and their distributions can be dramatically altered by subjecting the metal to various thermomechanical processes (empirical knowledge of this goes all the way back to blacksmiths in ancient cultures who figured out how to make superior swords through a combination of heating, beating, and quenching).

At the lowest (atomic) length scales, the most important defects in the crystal structure controlling the macroscale plastic properties of the material are the line defects called dislocations [22–24] (Figure 1.4). They play a dominant role in most plastic (inelastic) properties of all metals and alloys. This is because the easy glide of these line defects (called slip) on specific crystallographic planes and in specific crystallographic directions constitutes the main physical mechanism of plastic deformation in these materials. The complex interactions among the dislocations from the different slip systems in a given crystalline material lead to highly complex spatial arrangements called as dislocation cells and walls at the next higher length scale ($\sim 1 \mu\text{m}$; see Figure 1.4). At the scale of individual crystals ($\sim 10 \mu\text{m}$; each crystal or grain is shaded differently in Figure 1.4), the nature and distribution of the three-dimensional crystal lattice orientations, and the boundaries between the individual crystals and the multiple phases play a dominant role in controlling many of the plastic properties of the metal.

It is hoped that the brief description earlier provides the reader with the necessary appreciation and recognition of the hierarchical, multiphase, polycrystalline, and defective internal structures of most metals. Second, it should become clear that it is theoretically possible to produce a very large set of materials that have the same overall chemical composition but dramatically different hierarchical internal structures and attendant mechanical properties. Indeed, the theoretically possible materials space is unimaginably large.

The hierarchical internal structures of the materials are simply referred to as *microstructures* in this book (irrespective of the actual length or structure scales involved). It should also be noted that the overall chemical composition is included in the definition of the material microstructure used in this book. In fact, it is one of the primitive measures of the material microstructure that we shall later call as the 1-point statistics of the composition.

Based on the preceding discussion, it should become clear that a digital representation of the material essentially constitutes a digital representation of the material structure. It is easy to acknowledge the immense difficulty of this task given the vast number of tiered descriptions needed to represent the internal structure in the material systems of interest. Furthermore, it should be noted that the actual task of experimentally quantifying all details of the material microstructure in a given sample is effort intensive and arduous to say the least. This is because one has to employ different characterization tools (e.g., X-ray diffraction, optical microscopy, scanning electron microscopy, transmission electron microscopy, back-scattered diffraction, energy dispersive spectroscopy, and X-ray tomography) for revealing different aspects of the material internal structure at different length scales. In addition, it is often exponentially more expensive to quantify the desired microstructure details in a given sample in three dimensions (four dimensions when including time) compared to quantifying the microstructure details in only two dimensions.

The conventional approaches used in the materials development field have largely treated the material microstructure as images and have resorted to an *ad hoc* or intuitive selection of certain salient features from these images as the measures of the material microstructure. For example, microstructures in steels are typically quantified by the overall chemical composition, the volume fractions of the different phases, and the average grain (crystal) size. Furthermore, the conventional protocols utilized in this field have largely required substantial amount of

manual input (e.g., placing lines on a micrograph to estimate the average grain size [25,26]). Only in recent years, these protocols have been modified to include the conversion of microstructure images to digital signals (mostly for grayscale images from optical scanning electron microscopes) that allow application of modern image analyses tools.

One of the main consequences of the *ad hoc* approaches utilized thus far in the materials development field is that only very simple quantitative correlations among material structure, its associated properties, and their evolution during readily available manufacturing unit processes have been established and utilized successfully to date. For example, the most commonly used structure–property linkages are those established by the Hall–Petch rules [27,28], which suggest that the macro-scale yield strength of a metal is inversely proportional to the square root of the averaged grain (crystal) size. Likewise, at the lower length, it is now well established that the slip resistance (defined in a region smaller than the individual crystals in a polycrystal) is directly proportional to the square root of the local averaged dislocation density. There also exist a number of simple laws that capture the influence of the overall chemical composition on the yield strength of the alloy (e.g., solid-solution strengthening) [29] and the effect of precipitate type and size on the yield strength of the material (e.g., precipitation hardening) [30]. These correlations employ only the simplest of the microstructure measures that capture only the averaged values. In order to extract and utilize quantitative correlations between the material microstructure and defect-sensitive properties such as fatigue strength or toughness, it is imperative to develop new protocols that employ more advanced measures of the material microstructure. Similarly, it is also important to establish quantitative correlations between microstructure evolution and the process parameters in various unit operations involved in the manufacture of the final designed components. As noted earlier, such quantitative linkages formulated as PSP linkages constitute the core materials knowledge needed to accelerate materials development efforts, while reducing the overall cost. Consequently, they are the central focus of this book. It should be noted that in the absence of quantitative PSP linkages, the materials development efforts must rely on effort intensive and costly experiments, which require a large number of iterations to arrive at final products with the desired performance metrics.

1.3 Inverse Problems in Materials and Process Design

The digital representation of the microstructure is the central foundational building block of a new framework for microstructure quantification presented in this book. As noted earlier, it is the essential feature needed for the formulation of a data-driven approach to the design and development of hierarchical materials. It is emphasized here that the core knowledge needed for the development of advanced hierarchical materials is best archived, curated, and visualized in the higher dimensional space of variables used to represent the material microstructure [31–34]. This important concept is illustrated schematically in Figure 1.5. The elliptical region in Figure 1.5 schematically depicts the high-dimensional representation of the microstructure space (i.e., all microstructures relevant to a specific materials development effort can be represented in this space as distinct points). In other words, every point in this space corresponds to a distinct microstructure based on the selected microstructure measures. It is envisioned that this is a large-dimensional space as discussed earlier, if one were to successfully capture all of the salient microstructure features of interest

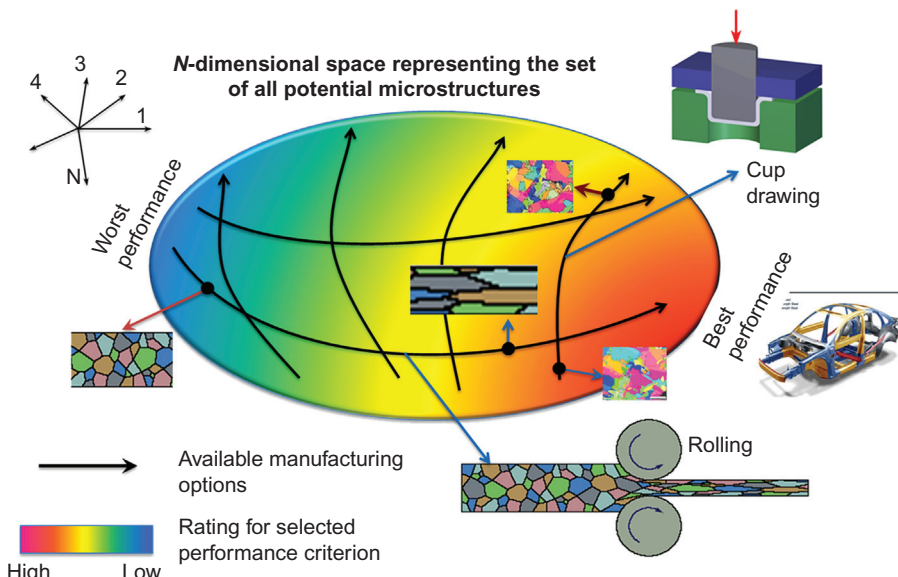


Figure 1.5 Schematic illustration of the benefits of visualizing PSP linkages in the microstructure space [35].

in a selected application. Indeed, as mentioned earlier, the primary focus of this book is to present a mathematically rigorous, data-driven framework for such microstructure description. However, for the present, one might think of the various axes in [Figure 1.5](#) as the traditional measures of microstructure (such as the average grain sizes and phase volume fractions) typically used in current practices in materials science and engineering.

Each microstructure (i.e., each point in the space depicted in [Figure 1.5](#)) can then be associated with a value of a selected performance metric (typically expressed as a function of selected macroscale properties of the material) obtained either from direct measurements or from model simulations or a combination of both. This claim is of course entirely based on the hypothesis that the microstructures' measures used to define the space are comprehensive enough to capture all of the salient structure features controlling the performance metric of interest. If this central requirement is met, the quantitative linkage between the structure and the performance metric of interest can be conveniently depicted as contours superposed on the microstructure space. In [Figure 1.5](#), this is illustrated schematically using colors ranging from red (high performance) to blue (low performance). Note that a hypersurface contour of a selected color in the high-dimensional elliptical volume identifies the complete set of microstructures expected to deliver an equivalent performance metric (cf. [2,33]).

When any selected unit manufacturing process is exercised on a given material, the microstructure is expected to evolve. Microstructure evolution can be visualized as a pathline (depicted schematically as the directional black lines in [Figure 1.5](#)) in the high-dimensional microstructure space. Once again, we are assuming that the microstructure space has been defined with sufficient detail and rigor that all of the salient microstructure features have been captured in defining the microstructure space. Indeed, different initial microstructures subjected to the same manufacturing unit process should not produce intersecting pathlines. This condition can actually be used to assess and guide the selection of the microstructure measures used to define the microstructure space. As another extension of the idea presented earlier, pathlines corresponding to different manufacturing unit processes are expected to intersect in the microstructure space. Identification (either from experiments or from model simulation) of all pathlines in the microstructure space corresponding to all available manufacturing

options that may be exercised results in a large database (called a process network; cf. [36]). Once such a database is established, it should be possible to identify hybrid process routes (i.e., process routes made up of an arbitrary sequence of unit manufacturing steps selected from a large list of available options) that will transform any selected initial microstructure into one that is expected to exhibit superior properties or performance characteristics. If multiple solutions are found, one might select a specific solution based on cost or some other criterion such as sustainability.

The vision expressed schematically in [Figure 1.5](#) essentially describes a strategy for finding high-value inverse solutions that are central to the materials development efforts. It is reiterated that the central foundational block of this approach is a sufficiently rigorous quantification of the hierarchical material internal structure. This concept, of course, is also the central theme of this book. If the strategy depicted in [Figure 1.5](#) is executed properly, it signifies a reversal of the paradigm by which new materials are developed from the present (deductive) “cause and effect” approach to a much more powerful and responsive (inductive) “goal-means” approach [37,38]. Implementation of this highly desired capability is critically dependent on the availability of *invertible*, high fidelity, PSP linkages. The inverse solution methodology is usually envisioned as a two-step process [2]. In the first step, the structure–property relationships are examined to identify the complete set of material microstructures that are expected to meet or exceed the specified (desired) combination of properties or performance characteristics. The solution space for this step is the space of all theoretically feasible material microstructures. In the second step, process–structure relationships are examined to identify manufacturing paths to achieve the desired material microstructure. The solution space for the second step is the set of all possible hybrid process routes. The goal of the second step is to identify one or more sequences of manufacturing processes that are theoretically predicted to transform a given initial material microstructure into an element of the desired set of optimal microstructures (identified in the first step). It should be noted that although the two steps (i.e., microstructure design and the process design) are described earlier as two separate tasks, they can be effectively combined into a single process using a suitable computational strategy (for example, as depicted schematically in [Figure 1.5](#)).

1.4 Data, Information, Knowledge, and Wisdom

In sections 1.1–1.3, we discussed numerous ways to extract high-value information from raw materials datasets acquired from either experiments and/or models. One can formalize these data transformations as shown in [Figure 1.6](#). As discussed earlier, raw materials data is generated by some combination of experiments, models, and simulations. The volume of this data can be very large (cf. [Figures 1.2–1.4](#)). Moreover, recent years have witnessed an explosion in the ability of materials experts in generating data from novel experiments [5,39–45] and simulations [38,46–59]. The volume of this data can be very large ushering the materials community into the *big data era*.

Experts in the field of materials science usually extract trends on the evolution of selected salient features of the material structure during a given manufacturing route and study how these details affect certain effective properties/performance characteristics of interest for the material. For example, considerable effort in the development of structural metals has been spent on correlating the average grain size in the final metal product to the various thermomechanical deformation histories applied during the manufacture of metal alloys. This is because the average grain size is generally observed to strongly influence the overall mechanical properties of the metal product in service [61–66]

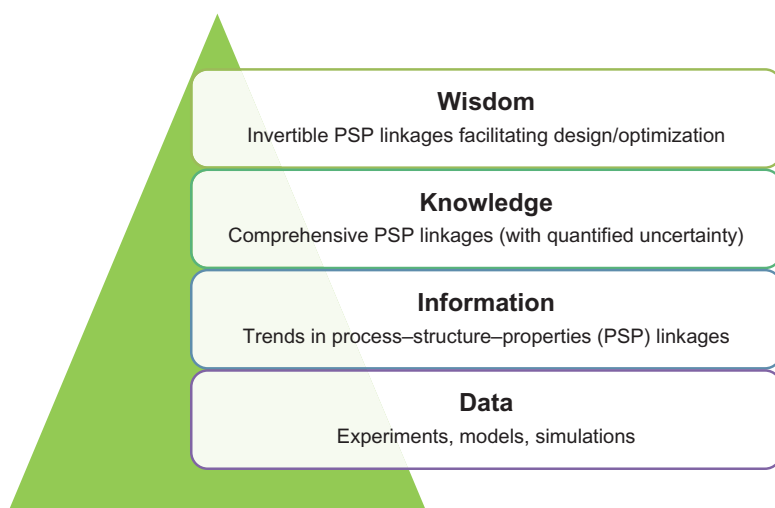


Figure 1.6 Schematic description of the envisioned transformations for materials data [60].

although it is not the only factor influencing the final performance. However, this approach of salient structure parameter identification and exploration has provided tremendous new insights (higher value information) to improve the performance of many material systems of interest. In the data science formalism, one might characterize these higher value descriptions (identifying specific trends between selected parameters as opposed to comprehensive multivariate linkages) of PSP linkages as Information. This is mainly because at this stage we have not yet identified all of the dominant PSP linkages of interest in a comprehensive manner with great certainty.

At the next higher level, one can aim to extract much more rigorous, reliable, and complete PSP linkages from all of the available data; this information could then be characterized as Materials Knowledge. One of the central goals of the emerging field of Materials Informatics is to introduce novel data-driven approaches for mining such materials knowledge from the large collections of experimental, modeling, and simulation datasets available (or being produced) today. Furthermore, as we have highly reliable and comprehensive PSP linkages at this level, we are now in a position to rigorously quantify the inherent uncertainty in the linkages. At this level of knowledge, we essentially have comprehensive and reliable PSP linkages that can be successfully employed in simulating manufacturing processes of interest and predicting performance of the final product. However, the main focus in the data transformations at the knowledge level continues to be in the forward direction (process→structure→properties).

At the final stage of data transformation, effort would be focused on establishing invertible PSP linkages that actually allow us to realize the promise of customized process and materials design for targeted applications (i.e., address inverse problems). This highest level of the understanding of PSP linkages can then be characterized as Wisdom. Our primary focus here will be on data analytics to extract materials knowledge, while eyeing toward attainment of wisdom.

1.5 Digital Representations

Digitization has completely transformed the way information is collected, analyzed, and curated in the modern computer age. There now exist plenty of examples in various application domains where the raw data or information is captured as images, sound, or video. Generally speaking, digitization involves

discretization (e.g., sampling at regular intervals) and *quantization* (e.g., rounding off to preset levels that could be established by the accuracy or the resolution limit of the measurement or the prediction). Although it is not explicitly acknowledged, most experimentally generated materials datasets are actually currently presented in a digital form. One can also make a weaker but similar argument for all datasets generated by numerical simulations with the caveats that the simulation datasets do not necessarily involve uniform sampling and are not typically quantized (although in principle they should be quantized to reflect the implicit errors included in the simulation).

The core competency necessary for all the data transformation described in Figure 1.6 is the ability to represent and quantify the material structure. As noted earlier, PSP linkages are most naturally formulated in the structure space. Since the high-dimensional representation of the material microstructure is the main impediment in all of the considerations described earlier, the central challenge therefore is to define a practically useful, robust, low-dimensional quantification of the material microstructure. Such low-dimensional quantifications may be called *microstructure measures* or *microstructure metrics*. Some authors have also referred to these as microstructure properties. In this book, we have reserved the word properties to refer exclusively to the engineering performance attributes of the material and will therefore avoid the use of the term “microstructure properties.”

If the microstructure metrics are defined using very primitive measures, we may not be able to distinguish between the microstructures that exhibit very distinct performance characteristics. On the other hand, if the microstructure metrics are defined to account for every minute detail of the microstructure, it would impede comprehensive exploration of materials knowledge in the development efforts (e.g., for the optimization of the performance characteristics of interest for a selected application). This is precisely where a data-driven approach offers many advantages. In a data-driven approach, the decision on exactly what constitutes the set of important salient features is not taken in a static manner—instead it is taken objectively based on the actual available data. It is continuously refined as more data become available.

Only an extensible framework would allow an automated, systematic, and efficient exploration of the unimaginably large spaces involved in the design and development of new materials. Moreover, only an extensible framework will allow automated documentation of standardized workflows, allowing

us to identify the best practices based on experience accumulated from the broader community. The desired requirements laid out above can be satisfied by seeking a digital representation of the material microstructure [67] as m_s^n , which denotes the probability that a specified spatial bin (or voxel) indexed by s is physically occupied by a potential local state indexed by n . Since the values of m are bounded between zero and one (in many cases it can be just binary [67]), it produces a generalized representation for a broad range of materials systems at different length/structure scales. The information on the different length scales is encoded into the attributes associated with the spatial bins (e.g., spatial bin size), while the information on the local state of the material (e.g., chemical composition, phase identifiers, and tensorial representations of different defect configurations of interest) is encoded into the attributes associated with the bins in the local state space. In addition to transforming the material structure into a versatile digital signal, this approach inherently treats the microstructure as a stochastic process because of the probabilistic interpretation assigned to the variable m . The digital signal representation of microstructure offers many advantages including fast computation of microstructure spatial correlations [2,68,69], automated identification of salient microstructure features in large datasets [70], extraction of representative volume elements from an ensemble of datasets [4,71,72], reconstructions of microstructures from measured statistics [68,73–75], building of real-time searchable microstructure databases [32,76], and mining of high-fidelity multiscale structure–performance–structure evolution correlations from physics-based models [77–80]. All of these different aspects will be expounded in the coming chapters of this book.

At this time, it is emphasized that although the word microstructure has been used with multiple meanings in prior literature, it has always been used as a *statistical measure* of the internal structure of the material. Given the range of scales involved and the large amount of structure data that needs to be considered to capture representative features at each length scale, it is important to recognize that any viable definition of microstructure has to be grounded in statistics. However, most materials scientists and engineers have thus far utilized only the lower order statistical measures of microstructure (e.g., average compositions, volume fractions, average grain size, and orientation distribution function) in extracting the core materials knowledge needed to tailor properties/performance characteristics of materials. Although, the higher order statistical measures of the microstructure are expected to play an influential role in

most engineering properties of practical interest exhibited by the material, they have not yet been employed systematically to improve the fidelity of the core materials knowledge (i.e., PSP linkages). The main impediments in this regard have been the high computational cost of extracting the higher order statistical measures, and the fact that they usually result in unmanageably large sets.

1.6 Hierarchical Materials Informatics

This book is mainly focused on introducing novel concepts and tools created in recent years to address the challenges described earlier. These new concepts build on advances in information sciences and data analytics, and their application to microstructure datasets have led to the emergence of *Hierarchical Materials Informatics* as a new interdisciplinary field of study. More specifically, the following “low-hanging” opportunities are readily identified:

- The abundance of data that could potentially be generated and curated from modern materials characterization equipment as well as numerous sophisticated physics-based multiscale models provides the incentive for the development and implementation of novel *data-driven* protocols for objective decision support at various stages of the materials development activities. Currently, many of these decisions are being made in an *ad hoc* manner based on empirical knowledge and instincts of the experts involved in these workflows. This is one of the main factors leading to the expensive late-stage iterations that dramatically increase the overall cost and time of the materials development efforts. Data-driven protocols will mitigate the inherent risk to a large extent not only by making the decisions more objective but also by recording the failures and successes in a manner that the knowledge is transferable to other endeavors.
- The availability of the data and the use of data-driven protocols allow us to objectively *quantify the uncertainty* associated with any piece of information or knowledge used in making decisions in the materials development workflows. It should be noted that all data or knowledge generated either by experiments or models are associated with some level of uncertainty and often are incomplete (e.g., in many materials development efforts, we often can afford only two-dimensional scans of material microstructure and are often required to make assumptions about the three-dimensional

microstructure of the material). Rigorous use of statistics and probability theories offer a practical approach for addressing these challenges. Data analytics and data-driven approaches are essential in order to take advantage of these advanced tools.

- Success in materials development efforts is often predicated on the availability and engagement of cross-disciplinary expertise that covers both multimodal measurements and multiphysics simulations in a broad range of materials phenomena occurring at multiple length and time scales. Since the expertise in these cutting-edge fields is often highly localized (in terms of specialization) and distributed (in terms of organizations and/or geography), there exist several hurdles to establishing highly productive collaborations. It is now being widely recognized that *Data Science and Cyberinfrastructure* provide the critically needed tools to mediate and accelerate such collaborations. In this regard, it is important to recognize that data is the fundamental currency of collaborations, and therefore *structured data* plays a central role in the realization of this ambitious vision.
- Standardization and automation of the workflows are highly desired for achieving scalability of any process. The current workflows used in most material development efforts are highly customized and not scalable, and this is a major contributing factor to the high cost of these efforts. *Digital recording* of the workflows is an important step toward standardization and automation of the materials development workflows. With digital capture of the workflows, it would become possible to identify the best practices and implement them in ways to achieve the desired acceleration at affordable cost in any materials development activity.

Two recent reports from the National Science and Technology Council [6,81] (a cabinet-level council within the Executive Office of the President of United States of America) have emphasized the critical importance of advanced materials to our nation's economy, prosperity, and security. These latest strategic initiatives (Materials Genome Initiative for Global Competitiveness [6]; A National Strategic Plan for Advanced Manufacturing [81]) call for the creation of a new materials innovation infrastructure to facilitate the design, manufacture, and deployment of advanced materials at a dramatically accelerated pace in emerging advanced technologies. In order to realize these goals, it is imperative to develop novel protocols that fully exploit the large data generation capabilities made possible through the recent advances in multiscale

measurements [39,40,42–45,72,82–91] and simulations of materials phenomena [38,52–59]. The central challenge is that in spite of the many advances there remain a large number of unknowns or gaps in capturing the underlying physics (at different length scales). These critical gaps hinder the development of fully predictive PSP linkages for most hierarchical materials of interest to advanced technologies. The only practical way forward for the foreseeable future is to formally treat the hierarchical material as a complex system [34], which by definition is not yet amenable to predictive models. If one embraces the premise that a certain degree of uncertainty is inevitable in the formulation of the desired PSP linkages for hierarchical material systems, the focus could then be shifted to managing the uncertainty (i.e., complexity). In other words, the effort could be focused on the design, development, and validation of decision support systems that will leverage the best available understanding (with its uncertainties) and provide objective guidance on future effort investment (e.g., what combination of experiments and simulations are needed to reduce the uncertainty).

Given the high cost of the multiscale measurements, it is also obvious that the desired protocols for establishing materials knowledge and wisdom (cf. Figure 1.6) will have to rely on a limited number of experimental investigations. However, these experiments have to be specifically designed to efficiently cross-feed multiscale structure-sensitive materials models. The central considerations for these new protocols should be (i) Model Maturity, (ii) Model Interoperability, and (iii) Model Inversion. Briefly, Model Maturity quantifies the reliability (or the uncertainty) of the predictions of any given model over a prescribed window on the input ranges. The focus here is largely in multiscale physics-based models (these are critical for achieving adequate accuracy over sufficiently large windows on the input ranges) for predicting either the structure–property relationships or the manufacturing process–structure evolution relationships. Consequently, protocols are critically needed for robust evaluation of the model maturity over any selected range of initial structures and boundary conditions (defining either the manufacturing process conditions or the in-service loading conditions). The main impediments for establishing these protocols are: (i) lack of a broadly adopted framework for rigorous quantification of the material structure and (ii) lack of validated experimental protocols for direct measurement of the various materials parameters introduced in the multiscale models and/or the “at-scale,” full-field, measurements of response variables

predicted by the multiscale models (needed for the critical validation of the models). Model Interoperability ensures that the distinct components of a hierarchical multiscale model chain that typically address specific materials phenomena at selected length/structure scales are able to exchange the high-value information with the other components of the model chain seamlessly with manageable (quantifiable) loss of accuracy [34]. For example, in modeling the plastic response of polycrystalline metals [17], it is not yet clear what information about the dislocation structure needs to be communicated from dislocation dynamics simulations to crystal plasticity simulations. As a simple approach, one might decide to just communicate only the average dislocation density. However, if one is interested in understanding and predicting strain hardening and damage initiation/evolution, it would be necessary to communicate information on the higher moments of the dislocation field (or equivalently higher order spatial correlations in the dislocation networks) to the crystal plasticity models operating at the next higher length/structure scale. The third key capability listed earlier, Model Inversion, is necessitated by the need to drive materials development efforts from considerations of performance requirements (i.e., invert the current “cause and effect” approach to a transformative “goal-means” approach articulated by Olson [37,38]). A major impediment in model inversion arises from the simple fact that most currently used approaches in computational materials modeling have not been designed with invertibility in mind. For example, numerical approaches such as the finite element methods or the finite volume methods have been designed to study effects of imposed loading or boundary conditions on a selected initial microstructure. They are completely ill-equipped for tackling inverse problems such as identifying the set of material structures that are expected to meet or exceed a specified set of property/performance requirements. Model invertibility in most cases needs formulation of simplified, but sufficiently accurate, metamodels (also referred to as surrogate models) that cover the desired space of material structures and loading/processing conditions. In general, these approaches demand compact, simple (e.g., algebraic), and sufficiently accurate representations of the PSP linkages [2,33,34,37,38,92] to be of practical utility in providing critical decision support in the materials development efforts.

The critical need for accelerated iterative loops between multiscale experiments and models, with each informing the other, in highly efficient cycles is self-evident. In most current materials development workflows, this integration is shown by

simple arrows between experiments and models. It is really not that simple. Since the experimental data often comes from different characterization equipment with different resolution limits and different levels of inherent uncertainty and/or incompleteness (each characterization technique used is often tuned to highlighting only selected aspects of the material structure), it is essential to extract and fuse the high-value information from these disparate (sometime conflicting) sets of experimental observations. On the other hand, as mentioned earlier, most multiscale models also have a fairly large number of parameters that need to be calibrated and a fairly large number of assumptions/idealizations that need to be refined. Hence, the central challenge reduces to data fusion at different scales from different sources. Reflection on this challenge reveals that the most practical way forward is to undertake this fusion of information in a statistical framework where all data (including both experimental and modeling results) are treated rigorously as stochastic quantities.

As a simple example, consider a set of microscopy images taken from a single sample or from similarly processed samples. These are likely to show some differences among them. Hence, exactly which image would one use to calibrate the relevant multiscale materials models? One cannot simply take an average image and call it an expected microstructure because averaging images is a completely meaningless mathematical operation. Therefore, we need to represent the microstructure in a stochastic framework and admit that different images taken from the same sample can have different microstructures (i.e., there is inherent variance in microstructures). Moreover, as mentioned earlier, when we have microstructure information from multiple characterization techniques, we can even have conflicting information. The different experimental data can be fused suitably in the statistical framework by treating all measurement variables as stochastic variables. In other words, there is not a single value, but a distribution of values with different levels of likelihood for each measurement. Of course, treating measurements as stochastic variables is relatively easy for properties and process variables. The framework of n -point spatial correlations described in this book will allow one to treat the microstructure as a stochastic variable. Then, one can essentially put the entire set of experimental observations data in a comprehensive and consistent stochastic framework. The same logic also applies to model results. Often one makes several guesses in either the initial conditions (e.g., initial microstructure) or the boundary conditions or the physics of the problem

or the values of the model parameters. Therefore, one can also represent the predictions from the models in a stochastic framework. Again, this is already easy to do for the predicted properties and/or process variables used in the simulation. The framework of n -point spatial correlations introduced in this book allows one to treat the material structure used in the models (as either input or output or both) as a stochastic variable.

Once we have the capability to represent both the experimental and modeling results in a stochastic framework, then it would become possible to objectively assess the reliability and maturity of the model. In other words, it is possible to quantitatively assess the probability that the model is wrong. The reader should note that formulated in this way, the answer is not deterministic (in other words, the answer is not just whether a model is correct or incorrect). Also, this approach allows one to conduct sensitivity studies to identify specific areas of high potential payoffs for future effort investment. In other words, we can objectively identify what new experiments or new refinements to models are needed to reduce the inherent uncertainties and further mature the models (and simultaneously our understanding of the physical phenomenon being studied).

The critical need and potential for the utilization of modern data sciences (including advanced statistics, dimensionality reduction, and formulation of metamodels) and cyberinfrastructure (including integration platforms, databases, and customized tools for enhancement of collaborations among cross-disciplinary team members) in overcoming the impediments has already been emphasized and reiterated several times already in this chapter. As noted earlier, data sciences and cyberinfrastructure are indeed the foundational pillars of Hierarchical Materials Informatics. This book lays the foundational framework for this emerging new discipline.

Figure 1.7 presents an overall schematic of the workflow (or equivalently data flow) cycles behind the strategy expounded in this book. The knowledge databases produced using this general workflow cycles will be called Materials Knowledge Systems and are designed to address the challenges described in this chapter. We start with the physical data gathered from experiments and models. These datasets (including structure information) will be analyzed using a set of Structure Quantification Modules that perform automated feature identification using smart filters [70], extract meaningful statistical measures such as n -point correlations [2,68,69,93], and microstructure metrics such as chord length distributions [70]. The physical data is then organized into the statistically meaningful Augmented

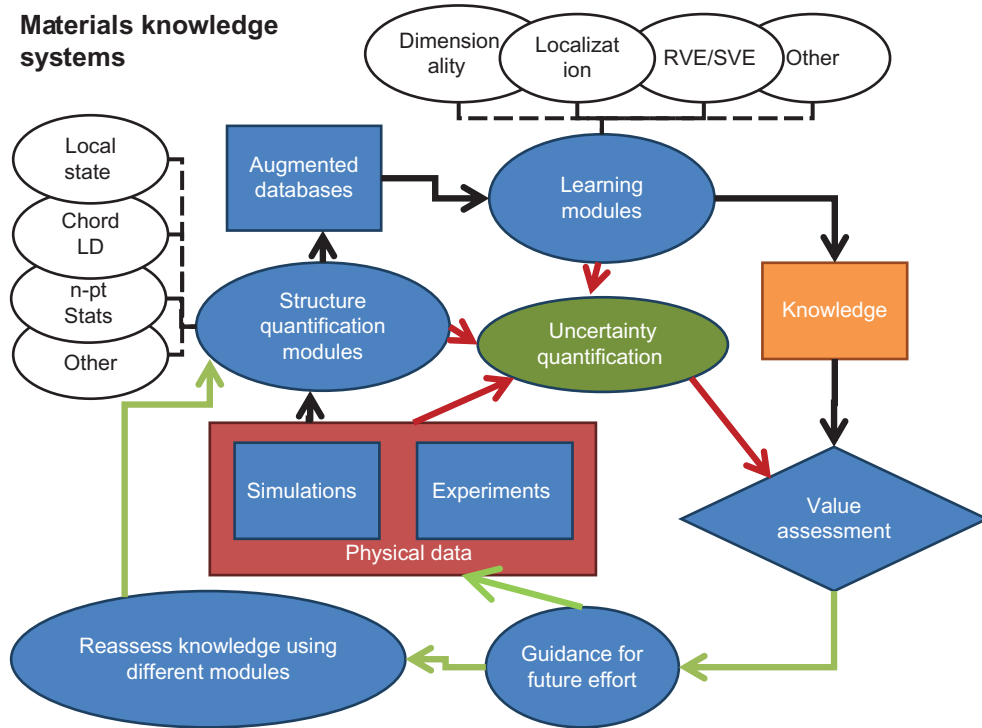


Figure 1.7 Schematic of the overall data flow cycles in the framework presented in this book.

Databases at the end of this step. The Augmented Databases are then mined using a set of Learning Modules that employ dimensionality reduction techniques such as principal component analyses (PCA), Kernel PCA, Isomap, Locally Linear Embedding (LLE), Hessian LLE, among others. The Learning Modules could also employ a variety of regression methods (including Bayesian Regression methods) to mine the underlying knowledge in the Augmented Databases and express the knowledge as computationally efficient PSP linkages. A salient feature of these relationships is that they allow exchange of information in both directions, that is, both for homogenization as well as for localization [78,94], and allow customized design of materials targeted to exhibit desired properties or performance characteristics [2]. Parallel to the above activities, we envision undertaking a rigorous quantification of uncertainty in the knowledge mined using the data flow described earlier. Uncertainty arises naturally in the physical datasets (both experimental and modeling datasets) and is augmented by the specific selections, approximations, and truncations made in

the Structure Quantification and Learning Modules used in the extraction of knowledge. The quantification of uncertainty is an important step in Value Assessment, the outcome of which will be used to direct future effort either into generation of additional physical datasets (this could include experimental or modeling datasets or both) in targeted regimes or into alternate options in the use of various Structure Quantification and Learning Modules used to extract the knowledge.

In the remaining chapters, the various concepts underlying the Structure Quantification and Learning Modules will be presented in a systematic manner. We will start with a theoretical framework for microstructure function in Chapter 2. We will then become familiar with the framework for a rigorous statistical quantification of the material internal structure in Chapter 3. These two chapters will therefore introduce the main Structure Quantification Modules. Following this, we will shift our attention to Learning Modules. We will start with objective dimensionality reduction in microstructure quantification in Chapter 4. As noted earlier, our primary interest is in formulating PSP linkages. Our strategy for accomplishing this will be to start with the existing (legacy) domain knowledge in the field and to supplement it with the new knowledge extracted using data science tools. We will therefore aim for a harmonious blend of the novel data science tools with previously established practices in the materials science and engineering domain. With this in mind, we will briefly remind ourselves of the most established composite theories available in literature in Chapter 5. In Chapters 6 and 7, we will augment these existing protocols with novel data-driven protocols and demonstrate new integrated protocols for extracting PSP linkages from available datasets. In Chapter 8, we will discuss various emerging trends and concepts in Data Management, Software Repositories, and e-Collaboration Platforms.

References

- [1] Friedel R. Materials that changed history. NOVA. 2010. Available from: <<http://www.pbs.org/wgbh/nova/tech/materials-changed-history.html>>.
- [2] Fullwood DT, et al. Microstructure sensitive design for performance optimization. *Prog Mater Sci* 2010;55(6):477–562.
- [3] Schwartz AJ, Kumar M, Adams BL. Electron backscatter diffraction in materials science. New York, NY: Kluwer Academic/Plenum Publishers; 2000.
- [4] Qidwai SM, et al. Estimating response of polycrystalline materials using sets of weighted statistical volume elements (WSVEs). *Acta Mater* 2012;60:5284–99.

- [5] Rowenhorst DJ, Lewis AC, Spanos G. Three-dimensional analysis of grain topology and interface curvature in a β -titanium alloy. *Acta Mater* 2010;58(16):5511–19.
- [6] Materials genome initiative for global competitiveness. National Science and Technology Council; 2011.
- [7] Pollock TM, et al. Integrated computational materials engineering: a transformational discipline for improved competitiveness and national security. Washington, DC: The National Academies Press; 2008.
- [8] McDowell DL, Story TL. New directions in materials design science and engineering (MDS&E). Report of a NSF DMR-sponsored workshop; October 19–21, 1998.
- [9] CES Edupack. Granta Design; 2005.
- [10] Calcagnotto M, et al. Deformation and fracture mechanisms in fine- and ultrafine-grained ferrite/martensite dual-phase steels and the effect of aging. *Acta Mater* 2011;59(2):658–70.
- [11] Yahyaoui H, et al. Effect of interlamellar spacing on the elastoplastic behavior of C70 pearlitic steel: experimental results and self-consistent modeling. *Mater Des* 2014;55:888–97.
- [12] Razmipoosh MH, Shamanian M, Esmailzadeh M. The microstructural evolution and mechanical properties of resistance spot welded Fe– ^{31}Mn – ^{3}Al – ^{3}Si TWIP steel. *Mater Des* 2015;67:571–6.
- [13] Larn RH, Yang JR. The effect of compressive deformation of austenite on the Widmanstätten ferrite transformation in Fe–Mn–Si–C steel. *Mater Sci Eng A* 1999;264(1–2):139–50.
- [14] Karlsson P, et al. Galling resistance and wear mechanisms for cold-work tool steels in lubricated sliding against high strength stainless steel sheets. *Wear* 2012;286–287:92–7.
- [15] Meurling F, et al. Influence of carbide and inclusion contents on the fatigue properties of high speed steels and tool steels. *Int J Fatigue* 2001;23(3):215–24.
- [16] Lee Y-J, et al. Effect of lath microstructure on the mechanical properties of flow-formed C-250 maraging steels. *Mater Sci Eng A* 2007;454–455:602–7.
- [17] McDowell DL. A perspective on trends in multiscale plasticity. *Int J Plast* 2010;26(9):1280–309 [special issue in honor of David L. McDowell].
- [18] Xie S, et al. Dislocation core structures in YAg, a ductile B2 CsCl-type intermetallic compound. *Scr Mater* 2008;58(12):1066–9.
- [19] Yasunaga K, et al. Electron energy-dependent formation of dislocation loops in CeO₂. *Nucl Instrum Methods Phys Res Sect B* 2008;266(12–13):2877–81.
- [20] Reed RC, et al. Creep of CMSX-4 superalloy single crystals: effects of rafting at high temperature. *Acta Mater* 1999;47(12):3367–81.
- [21] Levinson A, et al. Influence of deformation twinning on static annealing of AZ31 Mg alloy. *Acta Mater* 2013;61(16):5966–78.
- [22] Hirth JP, Lothe J. Theory of dislocations. New York, NY: McGraw Hill; 1968. p. 400–9.
- [23] Kocks UF. Polyslip in polycrystals. *Acta Metall* 1958;6(2):85–94.
- [24] Cottrell AH. Theory of dislocations. In: Chalmers B, editor. Progress in metal physics, vol. 4. London: Pergamon Press; 1953. p. 251–5.
- [25] ASTM International. E112 – 10: standard test methods for determining average grain size, West Conshohocken, PA, USA; 2010.
- [26] ASTM International. E1181-02: standard test methods for characterizing duplex grain sizes, West Conshohocken, PA; 2008.

- [27] Petch NJ. Cleavage strength of polycrystals. *Iron Steel Inst J* 1953;174 (Part 1):25–8.
- [28] Hall EO. The deformation and ageing of mild steel III. Discussion of results. *Proc Phys Soc London B* 1951;64:747–53.
- [29] Argon AS. Strengthening mechanisms in crystal plasticity. Oxford: Oxford University Press; 2008.
- [30] Reed-Hill RE, Abbaschian R. Physical metallurgy principles. 3rd ed. Boston, MA: PWS Publishing Company; 1994.
- [31] Panchal JH, Kalidindi SR, McDowell DL. Key computational modeling issues in integrated computational materials engineering. *J Comput Aided Mater Des* 2012. Available from: <http://dx.doi.org/10.1016/j.cad.2012.06.006>.
- [32] Kalidindi SR, Niegzoda SR, Salem AA. Microstructure informatics using higher-order statistics and efficient data-mining protocols. *JOM* 2011;63 (4):34–41.
- [33] Adams BL, Kalidindi SR, Fullwood D. Microstructure sensitive design for performance optimization. Waltham, MA, USA: Butterworth-Heinemann; 2012.
- [34] McDowell DL, et al. Integrated design of multiscale, multifunctional materials and products. Burlington, MA, USA: Elsevier; 2009.
- [35] Kalidindi SR. Microstructure informatics. Informatics for materials science and engineering: data-driven discovery for accelerated experimentation and application 2013;:443.
- [36] Shaffer JB, Knezevic M, Kalidindi SR. Building texture evolution networks for deformation processing of polycrystalline fcc metals using spectral approaches: applications to process design for targeted performance. *Int J Plast* 2010;26(8):1183–94.
- [37] Olson GB. Pathways of discovery designing a new material world. *Science* 2000;228(12):933–98.
- [38] Olson GB. Computational design of hierarchically structured materials. *Science* 1997;277(29):1237–42.
- [39] Stiénon A, et al. A new methodology based on X-ray micro-tomography to estimate stress concentrations around inclusions in high strength steels. *Mater Sci Eng, A* 2009;513–514:376–83.
- [40] Proudhon H, Buffière JY, Foutry S. Three-dimensional study of a fretting crack using synchrotron X-ray micro-tomography. *Eng Fract Mech* 2007;74 (5):782–93.
- [41] Tiseanu I, et al. 3D X-ray micro-tomography for modeling of Nb3Sn multifilamentary superconducting wires. *Fusion Eng Des* 2007;82 (5–14):1447–53.
- [42] Miller MK, Forbes RG. Atom probe tomography. *Mater Charact* 2009;60 (6):461–9.
- [43] Arslan I, et al. Towards better 3-D reconstructions by combining electron tomography and atom-probe tomography. *Ultramicroscopy* 2008;108 (12):1579–85.
- [44] Spowart JE. Automated serial sectioning for 3-D analysis of microstructure. *Scr Mater* 2006;5:5–10.
- [45] Spowart JE, Mullens HM, Puchala BT. Collecting and analyzing microstructures in three dimensions: a fully automated approach. *J Miner Met Mater* 2003;55(10):35–7.
- [46] Kirane K, et al. Grain level dwell fatigue crack nucleation model for Ti alloys using crystal plasticity finite element analysis. *J Eng Mater Technol-Trans ASME* 2009;131(2):1–14.

- [47] Przybyla CP, McDowell DL. Simulated microstructure-sensitive extreme value probabilities for high cycle fatigue of duplex Ti-6Al-4V. *Int J Plast* 2012; [special issue in honor or Nobutada Ohno].
- [48] McDowell DL, Dunne FPE. Microstructure-sensitive computational modeling of fatigue crack formation. *Int J Fatigue* 2010;32(9):1521–42 [special issue on emerging Frontiers in Fatigue].
- [49] Kalidindi SR, Bhattacharya A, Doherty R. Detailed analysis of plastic deformation in columnar polycrystalline aluminum using orientation image mapping and crystal plasticity models. *Proc R Soc Lond Math Phys Eng Sci* 2004;460(2047):1935–56.
- [50] Wang BL, et al. Systematic approach to microstructure design of Ni-base alloys using classical nucleation and growth relations coupled with phase field modeling. *Metall Mater Trans A* 2008;39A(5):984–93.
- [51] Wen YH, et al. Phase-field modeling of bimodal particle size distributions during continuous cooling. *Acta Mater* 2003;51(4):1123–32.
- [52] Ghosh S, Nowak Z, Lee K. Quantitative characterization and modeling of composite microstructures by Voronoi cells. *Acta Mater* 1997;45(6):2215–34.
- [53] Ghosh S, Lee K, Moorthy S. Multiple scale analysis of heterogeneous elastic structures using homogenization theory and voronoi cell finite element method. *Int J Solids Struct* 1995;32(1):27–62.
- [54] Kouznetsova VG, Geers MGD, Brekelmans WAM. Multi-scale second-order computational homogenization of multi-phase materials: a nested finite element solution strategy. *Comput Methods Appl Mech Eng* 2004;193(48–51):5525–50.
- [55] Kouznetsova V, Geers MGD, Brekelmans WAM. Multi-scale constitutive modelling of heterogeneous materials with a gradient-enhanced computational homogenization scheme. *Int J Numer Methods Eng* 2002;54(8):1235–60.
- [56] Kadewaki H, Liu WK. Bridging multi-scale method for localization problems. *Comput Methods Appl Mech Eng* 2004;193(30–32):3267–302.
- [57] McDowell DL, et al. Plasticity-related microstructure-property relations for materials design. *Key Eng Mater* 2007;340–341:21–30.
- [58] Choi HJ, et al. An inductive design exploration method for hierarchical systems design under uncertainty. *Eng Optim* 2008;40(4):287–307.
- [59] Luscher DJ, McDowell DL, Bronkhorst CA. A second gradient theoretical framework for hierarchical multiscale modeling of materials. *Int J Plast* 2010;26(8):1248–75.
- [60] Kalidindi SR. Data science and cyberinfrastructure: critical enablers for accelerated development of hierarchical materials. *Int Mater Rev* 2015;60(3):150–68.
- [61] Choi SH, et al. The effect of grain size distribution on the shape of flow stress curves of Mg—³Al—¹Zn under uniaxial compression. *Mater Sci Eng, A* 2008;488(1–2):458–67.
- [62] El-Danaf E, Kalidindi SR, Doherty RD. Influence of grain size and stacking-fault energy on deformation twinning in fcc metals. *Metall Mater Trans A* 1999;30(5):1223–33.
- [63] Dimiduk DM, et al. The role of grain size and selected microstructural parameters in strengthening fully lamellar TiAl alloys. *Metall Mater Trans A* 1998;29(1):37–47.
- [64] Morrison DJ, Moosbrugger JC. Effects of grain size on cyclic plasticity and fatigue crack initiation in nickel. *Int J Fatigue* 1997;20:S51–9.

- [65] Lasalmonie A, Strudel JL. Influence of grain size on the mechanical behaviour of some high strength materials. *J Mater Sci* 1986;21:1837–52 [Copyright 1986, IEE].
- [66] Hull D. Effect of grain size and temperature on slip, twinning and fracture in 3% silicon iron. *Acta Metall* 1961;9(3):191–204.
- [67] Adams BL, Gao X, Kalidindi SR. Finite approximations to the second-order properties closure in single phase polycrystals. *Acta Mater* 2005;53 (13):3563–77.
- [68] Fullwood DT, Niezgoda SR, Kalidindi SR. Microstructure reconstructions from 2-point statistics using phase-recovery algorithms. *Acta Mater* 2008;56 (5):942–8.
- [69] Niezgoda SR, Fullwood DT, Kalidindi SR. Delineation of the space of 2-point correlations in a composite material system. *Acta Mater* 2008;56 (18):5285–92.
- [70] Niezgoda SR, Kalidindi SR. Applications of the phase-coded generalized hough transform to feature detection, analysis, and segmentation of digital microstructures. *CMC Comput Mater Continua* 2009;14(2):79–97.
- [71] Niezgoda SR, et al. Optimized structure based representative volume element sets reflecting the ensemble-averaged 2-point statistics. *Acta Mater* 2010;58(13):4432–45.
- [72] Wargo EA, et al. Selection of representative volume elements for pore-scale analysis of transport in fuel cell materials. *J Power Sources* 2012;197:168–79.
- [73] Fullwood DT, et al. Gradient-based microstructure reconstructions from distributions using fast Fourier transforms. *Mater Sci Eng A* 2008;494 (1–2):68–72.
- [74] Bochenek B, Pyrz R. Reconstruction of random microstructures: a stochastic optimization problem. *Comput Mater Sci* 2004;31(1–2):93–111.
- [75] Roberts AP. Statistical reconstruction of three-dimensional porous media from two-dimensional images. *Phys Rev E* 1997;56(3):3203.
- [76] Niezgoda SR, Kanjrala AK, Kalidindi SR. Novel microstructure quantification framework for databasing, visualization, and analysis of microstructure data. *Integr Mater Manuf Innov* 2013;2:3.
- [77] Kalidindi SR. Computationally-efficient fully-coupled multi-scale modeling of materials phenomena using calibrated localization linkages. *ISRN Mater Sci* 2012.
- [78] Fast T, Kalidindi SR. Formulation and calibration of higher-order elastic localization relationships using the MKS approach. *Acta Mater* 2011;59:4595–605.
- [79] Fast T, Niezgoda SR, Kalidindi SR. A new framework for computationally efficient structure-structure evolution linkages to facilitate high-fidelity scale bridging in multi-scale materials models. *Acta Mater* 2011;59 (2):699–707.
- [80] Landi G, Niezgoda SR, Kalidindi SR. Multi-scale modeling of elastic response of three-dimensional voxel-based microstructure datasets using novel DFT-based knowledge systems. *Acta Mater* 2010;58(7):2716–25.
- [81] A national strategic plan for advanced manufacturing. National Science and Technology Council, Executive Office of the President; February 2012.
- [82] Echlin MP et al. A new TriBeam system for three-dimensional multimodal materials analysis. *Rev Sci Instrum* 2012;83(2): p. 023701-023701-6.
- [83] Kotula PG, Rohrer GS, Marsh MP. Focused ion beam and scanning electron microscopy for 3D materials characterization. *MRS Bull* 2014;39(04):361–5.

- [84] Villanova J, et al. Multi-scale 3D imaging of absorbing porous materials for solid oxide fuel cells. *J Mater Sci* 2014;49(16):5626–34.
- [85] Ebner M, et al. X-Ray tomography of porous, transition metal oxide based lithium ion battery electrodes. *Adv Energy Mater* 2013;3(7):845–50.
- [86] Betz O, et al. Imaging applications of synchrotron x-ray micro-tomography in biological morphology and biomaterial science. I. General aspects of the technique and its advantages in the analysis of arthropod structures. *J Microsc* 2007;227(1):51–71.
- [87] Bingert JF, et al. High-energy diffraction microscopy characterization of spall damage. *Dynamic behavior of materials*, vol. 1. Springer; 2014. p. 397–403.
- [88] Wang L, et al. Microstructural characterization of polycrystalline materials by synchrotron X-rays. *Front Mater Sci* 2013;7(2):156–69.
- [89] Pokharel R, et al. Polycrystal plasticity: comparison between grain-scale observations of deformation and simulations. *Annu Rev Condens Matter Phys* 2014;5(1):317–46.
- [90] Gulsoy EB, et al. Four-dimensional morphological evolution of an aluminum silicon alloy using propagation-based phase contrast x-ray tomographic microscopy. *Mater Trans* 2014;55(1):161–4.
- [91] Barwick B, et al. 4D imaging of transient structures and morphologies in ultrafast electron microscopy. *Science* 2008;322(5905):1227–31.
- [92] Panchal JH, Kalidindi SR, McDowell DL. Key computational modeling issues in integrated computational materials engineering. *Comput Aided Des* 2013;45(1):4–25.
- [93] Torquato S. Random heterogeneous materials. New York, NY: Springer-Verlag; 2002.
- [94] Kalidindi SR, et al. A novel framework for building materials knowledge systems. *Comput Mater Continua* 2010;17(2):103–25.

2

MICROSTRUCTURE FUNCTION

The previous chapter emphasized the importance of microstructure description and quantification, not only as a digital representation of the material itself but also as the main foundational block in establishing the high value PSP linkages needed to accelerate the materials development efforts. In this chapter, we now take a deep dive into a mathematically rigorous framework for the representation of the material microstructure. The reader is reminded that this framework has to necessarily address the hierarchy of material internal structure (spanning multiple length scales). As noted earlier, it is anticipated that most advanced materials used in emerging technologies will demand a tiered description of the material microstructure. In developing and presenting the fundamental concepts of such a framework, we will limit our attention in this chapter to two *well separated* length scales. It is assumed that the same overall philosophy can be applied repeatedly, as many times as needed, in describing materials whose microstructures exhibit salient features at multiple well separated length scales.

2.1 Length Scales

Let us now take a closer look at exactly what is meant by well separated length scales. This notion comes mainly from the concept of *homogenization* employed routinely in composite theories [1]. In both the hierarchical description of the material microstructure as well as in efficient scale-bridging, we need to first understand and identify the pertinent length scales. Figure 2.1 depicts an example for a hypothetical composite material system, where the length scales of interest are the macroscale and the mesoscale. In this figure, L and l implicitly define the length scales of a *material point* at the two scales being investigated in some pertinent multiscale material phenomenon (e.g., the failure properties of the composite system subjected to a specified macroscale loading condition for which it is well known that the mesoscale distribution of stress plays a dominant role).

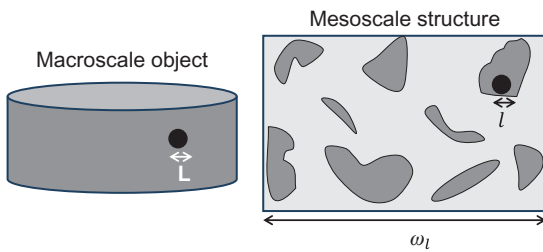


Figure 2.1 Schematic description of the length scales involved in hierarchical description of microstructure and the use of homogenization theories.

In the example in [Figure 2.1](#), L and l are selected such that they represent the smallest acceptable homogenization length scales for the macroscale and mesoscale, respectively. This essentially implies that it is possible (and reasonable) to formulate a sufficiently accurate homogenized material constitutive description at each of these length scales, by accounting for all of the salient (and often complex) features of the material structure that exist below that length scale. In other words, for the example shown in [Figure 2.1](#), it is implicitly assumed that a volume of material of the order of L^3 can be attributed with an effective value of a macroscale property of interest, denoted \mathbf{P}^* (generally a tensor, e.g., elastic stiffness, conductivity, coefficient of thermal expansion). It is deemed that this effective property allows a sufficiently accurate description of the material constitutive response for all considerations at the macroscale. For example, it is customary to describe the linear elastic response of a composite material as

$$\boldsymbol{\sigma}^* = \mathbf{C}^* \boldsymbol{\varepsilon}^* \quad (2.1)$$

where $\boldsymbol{\sigma}^*$ and $\boldsymbol{\varepsilon}^*$ are suitably defined second-rank stress and strain tensors (these will be introduced formally in later chapters) at the macroscale, and \mathbf{C}^* is the effective macroscale material property of interest called the elastic stiffness (a fourth-rank tensor; this will also be formally introduced in later chapters). It is extremely important to identify and define L such that it facilitates a sufficiently accurate description of the material constitutive response for all design considerations at the macroscale. Implicitly, this requirement also means that L is significantly smaller than the length scales associated with the gradients of the fields of interest at the macroscale, i.e., it is assumed that the macroscale quantities such as stress and strain themselves do not vary much over the length scale L (obviously, if the macroscale measures of stress or strain vary significantly over lengths of the order of L , it precludes the description of the homogenized

material response by Eq. (2.1)). It should be recognized that the actual value of L can vary dramatically depending on the specific application, from less than millimeters in small devices to centimeters or meters in larger structures.

The considerations at the mesoscale in Figure 2.1 are highly analogous to those described earlier for the macroscale. At the mesoscale, it is again assumed that there is a suitable length scale l , which allows us to describe the homogenized material constitutive response in a sufficiently accurate manner by accounting for all of the important material structure details at length scales much smaller than l . In other words, we expect the material structure to exhibit additional heterogeneity at length scales well below the length scale l (remember that we are dealing with hierarchical materials). In many ways, therefore, we are implicitly making the same assumptions in identifying length scale l , as we did earlier in identifying the length scale L (in a recursive manner).

In practice, the identification or selection of the length scales described above occurs quite naturally in most materials datasets generated by both experiments and models. In the experiments, the length scale is often set by the resolution limits of the specific machine used to acquire the datasets. For example, in any optical or electron micrograph, the length scale implicitly associated with a material point is the spatial resolution limit at which the image was acquired. Note the characterization machine implicitly provides information averaged at the spatial resolution limit. As another example, in any orientation map obtained by electron backscattered diffraction (EBSD), the length scale of each material point is typically associated with the measurement step size. Although the probe volumes in such measurements may be significantly smaller than the measurement step size, the lack of additional information forces us to adopt the step size as the appropriate length scale. In numerical simulations (e.g., using finite element methods or finite difference methods), each material point used in the computation is inherently associated with a specific length scale (e.g., the size of the element in the mesh or the computation grid) and the properties assigned to the material point are implicitly assumed to reflect averaged values over volumes defined by that length scale.

The concept of well separated length scales alluded to earlier implies that the hierarchical material being studied satisfies all of the requirements described above, while ensuring $l \ll L$. This is very important for virtually all of the considerations described in this book because it is the main requirement for invoking the concept of a representative volume element (RVE). The RVE concept

essentially allows us to identify volume element of size ω_l at the lower length scale in such a manner that it effectively captures all of the salient features of the material internal structure at the lower length scale (Figure 2.1), with $l < \omega_l \ll L$. Without this simplification, scale-bridging for multiscale investigation of any materials phenomena of interest would become computationally impractical, as we would be forced to consider RVEs of size L .

The most commonly adopted definitions of RVE size in the current literature [2–9] focus largely on the convergence in the prediction of selected macroscale (effective) properties (e.g., C^* in Eq. (2.1)) and do not explicitly consider whether or not the RVE has captured the desired microstructural details to sufficient accuracy. Incidentally, the classical definition of RVE provided by Hill [10] requires the RVEs to be large enough to capture both the representative microstructure as well as its homogenized effective properties. In this book, we will deviate from the current approaches in the literature and focus first on capturing the salient microstructure features in the RVE, and then subsequently address the convergence of the predictions of macroscale properties. The main motivation for this approach is the expectation that an RVE that already captures the salient microstructure features in the sample will also automatically capture all of the relevant macroscale properties that are influenced by the selected features. In this way, our central focus remains on understanding and quantifying the salient microstructure features of interest. Since we intuitively expect a class of microstructure features to influence a selected set of macroscale properties, in the approach advanced in this book, we will only need a limited number of RVEs (at most one for each class of microstructure features). On the contrary, in the traditional approach based on convergence of properties, we typically cannot even be sure that the RVE identified for one selected macroscale property in one selected direction would be adequate for the same macroscale property in any other selected direction in the same sample. In other words, one would need a very large number of RVEs, each validated for each property of interest (for each scalar component of a tensorial property).

It should also be clear from the above discussion that the use of the RVE concept in practice is bound to encounter some serious limitations. In some materials the separation of length scales is not practically achieved. For example, in thin films, this assumption might fail in considerations along the thickness direction. It should also be noted that the overall RVE shape does not have to be cuboidal. It can take any overall shape as long as the volume captures all of the important microstructural features present at the length scale of interest. In applications

where the microstructure features of interest are rare occurrences (e.g., features responsible for fatigue damage initiation), we are likely to need very large RVEs or other clever probability-based approaches.

Another difficulty arises from the need to capture accurately the role of interfaces. For example, in [Figure 2.1](#), there clearly are phase boundaries in the mesoscale structure of the material. If these interfaces are atomically sharp and exhibit special responses (e.g., transmit certain types of dislocations, attract certain types of defects), it would be inaccurate to capture such behavior in cuboidal volumes of selected length scale l . It would be necessary to design and use different shaped volumes at the lower length scale to capture their constitutive response (e.g., 2-D areal elements for interface regions, very thin 3-D volume elements in case of interphase regions). It should also be recognized that much of the discussion above was framed in the context of continuum descriptions of the material structure. Although the basic concepts described above should still apply at the lowest length scales where the continuum descriptions fail (e.g., atomistics), their application can be greatly hindered because of the need to treat discrete descriptions of the material structure in a mathematically rigorous framework.

We will limit our attention in this book to the simplest hierarchical material systems that exhibit well separated length scales with continuum descriptions of the material structure at least at two distinct length scales (as depicted in [Figure 2.1](#)). We will, however, be diligent in establishing the foundational framework in such a way that it allows future developments and enhancements needed to address the limitations mentioned above.

2.2 Local States and Local State Spaces

The discussion of length scales in the previous section leads naturally to the identification of the local states present in the material internal structure. It is important to recognize that the hypothesis of the existence of homogenized (effective) properties at each selected length scale implicitly leads to the definition of local states. As an example, imagine two different material points exhibiting distinct homogenized properties (e.g., consider one material point in each of the differently shaded regions in the material structure at the lower length scale shown in [Figure 2.1](#)). These differences in effective properties must arise from the fact the two material points are associated with distinct local states. As described earlier, in the study of hierarchical materials, we

assume that at any length scale there inherently exists significant heterogeneity at the lower length scales. Therefore, some salient measures of the material structure at the lower length scales must be different at the two material points being considered in order for these material points to exhibit different effective properties. Conversely, we also expect that if all of the salient material structure measures at the two different material points are identical, then the effective properties at the two material points should also be identical.

The above discussion leads us to hypothesize that structure–property relationships must exist at various length scales in the hierarchical material systems of interest with well separated length scales. In these relationships, it is implicitly assumed that only a limited number of measures of the highly heterogeneous and complex material structure present at the lower length scale affect the effective properties of interest at the higher length scale. The relevant set of measures of the ingrained material structure at any selected length scale constitutes the definition of the local state of the material at that length scale. By extension, the local state space defines the corresponding complete set of all theoretically possible local states one might expect to encounter in a given material system (this includes all the local states that may not even be present in a given sample of the selected material system).

It is important to understand that the local state in most cases is defined by a combination of multiple attributes. In most multiphase polycrystalline material systems, one might start with a description of the thermodynamic phase (see Figure 1.3) that implicitly identifies the crystal structure and certain thermophysical properties of the selected phase. Typically, the description of the individual phases in a multiphase system requires the specification of a phase identifier (typically a label assigned through historic practice in the field) and a chemical composition. For example, the most common thermodynamic phase in steels discussed in Chapter 1 is ferrite (also referred as α -Fe) which is essentially a pure form of Iron in a body-centered cubic crystal structure. However, in this state, ferrite is capable of dissolving very small amounts of carbon, which can in turn control certain properties exhibited by ferrite. More importantly, above 910°C, ferrite becomes unstable and changes into another thermodynamic phase called austenite (referred as γ -Fe), which exhibits a face-centered cubic structure. γ -Fe, on the other hand, is capable of dissolving much higher amounts of carbon (as much as 2.04 wt% at 1146°C), which can in turn have a dominant effect on the properties exhibited by this phase. It is hoped that the above

example has emphasized the need to identify both the thermodynamic phase identifier (e.g., α -Fe, γ -Fe) and the chemical composition (e.g., wt% C) in defining the local state at the mesolength scales where the morphology and distribution of the different thermodynamic phases in the material structure are expected to play a dominant role. There are abundant additional examples in the structural materials field. The reader is also encouraged to explore analogous concepts in identifying the local states in α - β Ti alloys and Ni-based superalloys as exercises.

If it is deemed that the combination of the phase identifier and its chemical composition is adequate for specifying the local state of the material, one might capture the corresponding definitions of the local state and the local state space in the following mathematical statements:

$$h = (\rho, c_i) \quad (2.2)$$

$$H = \{(\rho, c_i) | \rho \in \{\alpha, \beta, \gamma, \dots\}, c_i \in C_i^\rho\} \quad (2.3)$$

where (ρ, c_i) denotes an ordered combination of variables with ρ representing a phase identifier (which might take on values such as α or β or γ or ...) and c_i representing the chemical composition of the chemical species identified by i (which might take on values from a set C_i^ρ identifying the range of thermodynamically allowed solubility of the chemical species i in the phase ρ). Going back to the steels described earlier, the variable ρ can point to different thermodynamic phases that might be present (e.g., α -Fe, γ -Fe) and the variable i might point to different chemical elements that might be present in each phase (e.g., C, N, Al). Most importantly, Eqs. (2.2) and (2.3) introduce new symbols h and H for the local state and the local state space, respectively. We shall consistently use this notation for these entities throughout this book.

At this point, it is important to recognize that the definition of the local state described above is implicitly associated with a specific length scale of choice dictated by the hierarchical material system being studied. Furthermore, one might have to define and use the same local state definitions at multiple length scales. In other words, it is entirely possible that the material system depicted in Figure 2.1 exhibits additional hierarchy or lower length scales where the local state definition once again needs the specification of the thermodynamic phase identifier and its chemical composition. Therefore, one has to be always cognizant of the length scale implicitly associated with the definition of any local state variable and recognize that the values assigned to the local state reflect effective (suitably averaged) measures of

the heterogeneity of the material structure at the lower length scales. Such tiered representations are integral to the treatment presented in the book.

A second important feature of the definitions presented in [Eqs. \(2.2\) and \(2.3\)](#) is the fact that we are likely to require a combination of discrete and continuous variables to represent the local state. These then correspond to the respective discrete and continuous components of the local state spaces, as defined in [Eq. \(2.3\)](#). In the discussion above, it was also implicitly assumed that the local state is either measurable at the length scale of interest or is at least distinctly identifiable in digital representations of the microstructure, and exhibits the same local (effective) properties independent of its spatial location in the material internal structure. The reader should consult Ref. [11] for a more detailed discussion of the concepts of the local state and the local state space.

2.2.1 Local States and Local State Spaces in Polycrystalline Microstructures

The descriptions of the local state and the local state space presented in [Eqs. \(2.2\) and \(2.3\)](#) are fairly rudimentary and are intended as highly idealized descriptions of the hierarchical material systems. In practice, it will be necessary to include many other sophisticated attributes of the local state in dealing with most advanced material systems. In this section, we will digress a little and take a deeper look at the mesoscale microstructures in polycrystalline metals, so that the reader has a better appreciation of the complexity involved. In most polycrystalline materials ([Figure 2.2](#)), it becomes important to include attributes such as the crystal lattice orientation and suitable measures of defect densities (e.g., dislocation density) as they significantly impact the local properties defined at the mesolength scales. In this section, we will focus exclusively on the crystal lattice orientation as it demands a tensorial description of the local state variable.

A central challenge in the description of the polycrystalline microstructures is the inclusion of the crystal lattice orientation in the description of the local state. This need arises largely because the local properties exhibited at this length scale (significantly smaller than the individual crystals or grains shown in [Figure 2.2](#)) are often highly anisotropic. This anisotropy in the local properties leads naturally to highly complex interactions between the individual grains when accommodating an externally imposed load at the macroscale, and is expected to

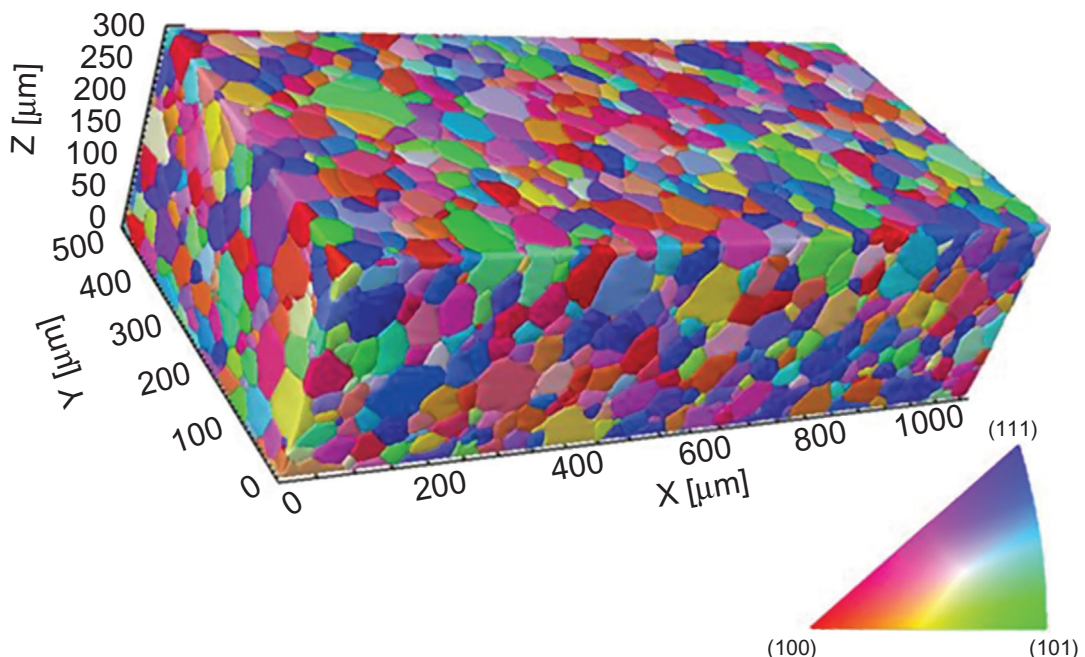


Figure 2.2 Mesoscale structure of β -Ti containing 4300 crystals (or grains) [12,13]. The size of the volume investigated is $1.115 \text{ mm} \times 0.516 \text{ mm} \times 0.3 \text{ mm}$ ($1670 \times 770 \times 200$ voxels). The three-dimensional crystal lattice orientation in each voxel is included in this experimental dataset. The color key corresponds to the stereographic projection of the crystallographic orientation parallel to the Z -axis.

produce localized deformation leading to failure (especially in fatigue and fracture conditions).

In a single phase polycrystalline microstructure (such as the one shown in Figure 2.2) the heterogeneity arises mainly because of the spatial placement of the differently oriented grains next to each other. Indeed, the local tensorial properties of the differently oriented crystals are quite similar or same (at least initially) in their own local crystal reference frames and are related to the properties in the sample reference frame through well-established coordinate transformation laws. However, since our interest in these materials is in defining the macroscale properties in the fixed sample reference frame, we need to account for the differences in the local properties of the different crystals in the sample reference frame. Consequently, it is important to include the crystal lattice orientation as an attribute of the local state in defining the mesoscale structure–property relationships in this important class of advanced structural materials.

Let $\{\mathbf{e}_1, \mathbf{e}_2, \mathbf{e}_3\}$ and $\{\mathbf{e}'_1, \mathbf{e}'_2, \mathbf{e}'_3\}$ represent two different Cartesian (orthogonal) reference frames that share the same

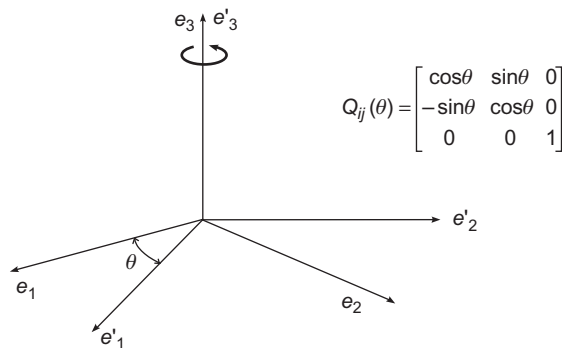


Figure 2.3 Two Cartesian reference frames that are related by a rotation of θ about the 3-axis and the corresponding coordinate transformation matrix.

origin. The transformation matrix $[Q_{ij}]$ that governs the relationships between the respective tensorial quantities defined in these two frames is expressed as

$$Q_{ij} = \mathbf{e}'_i \cdot \mathbf{e}_j \quad (2.4)$$

where the dot in Eq. (2.4) denotes a scalar dot product. Another way to interpret Eq. (2.4) is to recognize the components of the transformation matrix as simply the direction cosines of various basis vectors in one reference frame with respect to the basis vectors in the other reference frame. As a trivial example, the components of the transformation matrix for two Cartesian reference frames that are related to each other by a rotation about the \mathbf{e}_3 -axis by an angle θ are shown in Figure 2.3.

For our purposes, we need to describe the coordinate transformation matrix between two arbitrarily selected Cartesian reference frames (one associated with the crystal reference frame and the other with the sample reference frame) in the Euclidean 3-space. According to a formalism developed by Euler, one can describe this transformation uniquely by a sequence of three rotations taken about specific directions. These rotation angles are usually referred to as Euler angles. There exist a number of variants in the definitions of the Euler angles corresponding to different choices made in the selection of the three directions about which the rotations are defined. The particular definition of the Euler angles used extensively in the study of polycrystal mechanics is referred to as the *Bunge's Euler angles*.

Bunge's Euler angles are defined to describe a transformation from a sample Cartesian reference frame $\{\mathbf{e}_1, \mathbf{e}_2, \mathbf{e}_3\}$ to a local Cartesian crystal frame $\{\mathbf{e}_1^c, \mathbf{e}_2^c, \mathbf{e}_3^c\}$ as shown in Figure 2.4. The goal is to define a sequence of three transformations that would relate

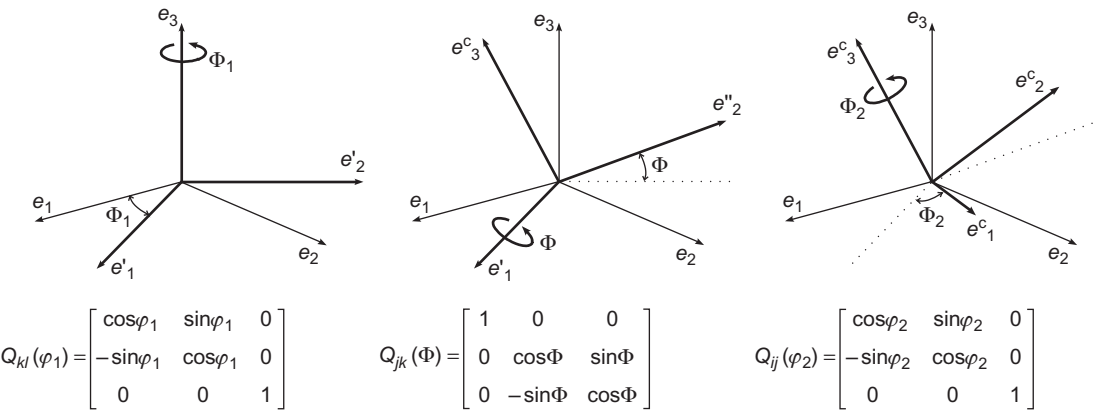


Figure 2.4 Schematic description of the Bunge's Euler angles used to establish the relationship between two arbitrarily defined Cartesian reference frames as a sequence of three rotations.

the sample reference frame to the crystal reference frame. In other words, our objective is to express the complete transformation matrix $Q_{ij} = \mathbf{e}_i^c \cdot \mathbf{e}_j^1$ in terms of a sequence of three (simplified) transformations, say $Q_{il} = Q_{ij}(\varphi_2)Q_{jk}(\Phi)Q_{kl}(\varphi_1)$, where $(\varphi_1, \Phi, \varphi_2)$ are called the Bunge–Euler angles that denote the angles associated with the three unit transformations involved in this process. In this formalism, one starts by rotating the sample frame about \mathbf{e}_3 by an angle of φ_1 so that the \mathbf{e}_1 -axis after the rotation is aligned with a direction \mathbf{e}'_1 that is perpendicular to both \mathbf{e}_3 and \mathbf{e}_3^c . After this first rotation, the sample reference frame $\{\mathbf{e}_1, \mathbf{e}_2, \mathbf{e}_3\}$ will form the intermediate reference frame $\{\mathbf{e}'_1, \mathbf{e}'_2, \mathbf{e}_3\}$, as shown in Figure 2.4. This new reference frame can now be rotated about the \mathbf{e}'_1 -axis by an angle Φ to bring \mathbf{e}_3 into perfect alignment with \mathbf{e}_3^c forming another intermediate reference frame $\{\mathbf{e}'_1, \mathbf{e}''_2, \mathbf{e}_3^c\}$, which is also shown in Figure 2.4. A final rotation by an angle φ_2 can then be applied about \mathbf{e}_3^c to bring $\{\mathbf{e}'_1, \mathbf{e}''_2, \mathbf{e}_3^c\}$ in perfect alignment with $\{\mathbf{e}_1^c, \mathbf{e}_2^c, \mathbf{e}_3^c\}$. In summary, the first unique (apart from several exceptions described in the subsequent section) rotation positions the \mathbf{e}'_1 -axis so it is perpendicular to both \mathbf{e}_3 and \mathbf{e}_3^c . Given this specific geometric relationship, a single and unique rotation about \mathbf{e}'_1 can align \mathbf{e}_3 and \mathbf{e}_3^c . Finally, a single unique rotation about \mathbf{e}_3^c aligns the reference frames. The components of each of the three transformation matrices are also shown in Figure 2.4.

The definition of the Bunge's Euler angles allows us to evaluate the overall coordinate transformation matrix between the

¹Summation on twice-repeated indices in a single product term is implied in this notation.

sample frame $\{\mathbf{e}_1, \mathbf{e}_2, \mathbf{e}_3\}$ and the crystal frame $\{\mathbf{e}_1^c, \mathbf{e}_2^c, \mathbf{e}_3^c\}$ as a product of the three transformation matrices shown in [Figure 2.4](#). This overall transformation matrix from the sample reference frame to the local crystal frame is denoted by $g^{s \rightarrow c}$ and is expressed as

$$\begin{aligned} g_{ij}^{s \rightarrow c} &= \begin{bmatrix} \cos \varphi_2 & \sin \varphi_2 & 0 \\ -\sin \varphi_2 & \cos \varphi_2 & 0 \\ 0 & 0 & 1 \end{bmatrix} \begin{bmatrix} 1 & 0 & 0 \\ 0 & \cos \Phi & \sin \Phi \\ 0 & -\sin \Phi & \cos \Phi \end{bmatrix} \begin{bmatrix} \cos \varphi_1 & \sin \varphi_1 & 0 \\ -\sin \varphi_1 & \cos \varphi_1 & 0 \\ 0 & 0 & 1 \end{bmatrix} \\ &= \begin{bmatrix} \cos \varphi_1 \cos \varphi_2 - \sin \varphi_1 \cos \Phi \sin \varphi_2 & \sin \varphi_1 \cos \varphi_2 + \cos \varphi_1 \cos \Phi \sin \varphi_2 & \sin \Phi \sin \varphi_2 \\ -\cos \varphi_1 \sin \varphi_2 - \sin \varphi_1 \cos \Phi \cos \varphi_2 & -\sin \varphi_1 \sin \varphi_2 + \cos \varphi_1 \cos \Phi \cos \varphi_2 & \sin \Phi \cos \varphi_2 \\ \sin \varphi_1 \sin \Phi & -\cos \varphi_1 \sin \Phi & \cos \Phi \end{bmatrix} \quad (2.5) \end{aligned}$$

A closer look at the definition of Bunge's Euler angles presented above reveals a redundancy in the definition. There are indeed two possible choices for the selection of \mathbf{e}'_1 while satisfying the requirement that this direction be perpendicular to both \mathbf{e}_3 and \mathbf{e}_3^c . The choices are \mathbf{e}'_1 and $-\mathbf{e}'_1$. To address this redundancy, the following limits are set for the three Bunge's Euler angles:

$$0 \leq \varphi_1 < 2\pi, \quad 0 \leq \Phi \leq \pi, \quad 0 \leq \varphi_2 < 2\pi \quad (2.6)$$

Even with the restricted range specified in [Eq. \(2.6\)](#) for the Bunge's Euler angles, there continue to be additional redundancies in their definition. For example, when $\Phi = 0$, we can uniquely specify only $(\varphi_1 + \varphi_2)$, and not φ_1 and φ_2 individually. Likewise, when $\Phi = \pi$, we can uniquely specify only $(\varphi_1 - \varphi_2)$. The $\Phi = 0$ and $\Phi = \pi$ redundancies are collectively known as gimbal lock, and present difficulties in as diverse fields as robotics, aeronautics and video-game design. Both of these redundancies are immediately apparent from [Eq. \(2.5\)](#). Except for the situations noted above, it is possible to select a unique set of Bunge's Euler angles to describe the relationship between any two arbitrarily selected Cartesian reference frames in the Euclidean 3-space. The Bunge–Euler angles and the transformation described in [Eq. \(2.5\)](#) will be used extensively in later chapters.

The interpretation of the coordinate transformation matrix described above further implies that the inverse transformation between the two selected reference frames is simply given by the transpose of the transformation matrix (see [Eq. \(2.4\)](#)). Particularly useful in later chapters is the fact that transformation from the crystal reference frame to the sample reference frame in the study of crystal mechanics is simply given by

$(g^{s \rightarrow c})^T$, with $g^{s \rightarrow c}$ being defined as in Eq. (2.5). In other words, the overall transformation matrix from the crystal reference frame to the sample reference frame can be expressed as

$$g_{ij}^{c \rightarrow s} = \begin{bmatrix} \cos \varphi_1 \cos \varphi_2 - \sin \varphi_1 \cos \Phi \sin \varphi_2 & -\cos \varphi_1 \sin \varphi_2 - \sin \varphi_1 \cos \Phi \cos \varphi_2 & \sin \varphi_1 \sin \Phi \\ \sin \varphi_1 \cos \varphi_2 + \cos \varphi_1 \cos \Phi \sin \varphi_2 & -\sin \varphi_1 \sin \varphi_2 + \cos \varphi_1 \cos \Phi \cos \varphi_2 & -\cos \varphi_1 \sin \Phi \\ \sin \Phi \sin \varphi_2 & \sin \Phi \cos \varphi_2 & \cos \Phi \end{bmatrix} \quad (2.7)$$

As mentioned earlier, the coordinate transformation matrices are needed to transform tensorial quantities from one reference frame to another reference frame. Some examples of the coordinate transformation laws for tensors of different ranks are summarized below.

$$\begin{aligned} a'_i &= Q_{ij} a_j \\ T'_{ij} &= Q_{ir} Q_{js} T_{rs} \\ C'_{ijkl} &= Q_{ip} Q_{jq} Q_{kr} Q_{ls} C_{pqrs} \end{aligned} \quad (2.8)$$

It is hoped that the discussion above has solidified the concept that the crystal lattice orientation in a polycrystalline microstructure can be conveniently represented as $g = (\varphi_1, \Phi, \varphi_2)$. Including this parameter in the local state description would imply extension of the previous definition of the local state and the local state space as

$$h = (\rho, c_i, g) \quad (2.9)$$

$$H = \{(\rho, c_i, g) | \rho = (\alpha, \beta, \gamma, \dots), c_i \in C_i^\rho, g \in FZ_\rho\} \quad (2.10)$$

where FZ_ρ denotes the *fundamental zone* (i.e., complete set) of all physically distinct crystal lattice orientations in the thermodynamic phase ρ that can theoretically occur in nature. Clearly, the identification of FZ_ρ depends on the symmetries inherent to the description of the crystal lattice structure (note that every element of FZ_ρ represents a potential distinct crystal lattice orientation of phase ρ).

Consideration of crystal symmetry will significantly influence the size of FZ_ρ . For example, a cubic crystal structure is known to have 24 symmetry elements. Therefore, we can expect the size of the fundamental zone for cubic crystals to be roughly about 1/24th of the orientation space identified in Eq. (2.6). In order to work out the size of the FZ_ρ , we consider in Figure 2.5 a sample reference frame, $\{\mathbf{e}_1, \mathbf{e}_2, \mathbf{e}_3\}$, and two equivalent crystal reference frames, $\{\mathbf{e}_1^c, \mathbf{e}_2^c, \mathbf{e}_3^c\}$ and $\{\mathbf{e}_1^a, \mathbf{e}_2^a, \mathbf{e}_3^a\}$. The crystal reference frames are considered equivalent because the descriptions of the crystal using either of these two frames are completely

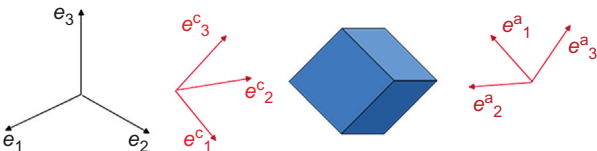


Figure 2.5 Illustration of crystal symmetry in the definition of lattice orientation.

identical in all aspects (i.e., completely indistinguishable). Let $Q_{ij}^{c \rightarrow s}$, $Q_{ij}^{a \rightarrow s}$, and $Q_{ij}^{a \rightarrow c}$ denote the related transformation matrices, where s denotes the sample reference frame. Using the concepts described earlier, it is easy to see that

$$Q_{ij}^{a \rightarrow s} = Q_{ik}^{c \rightarrow s} Q_{kj}^{a \rightarrow c} \quad (2.11)$$

Let $(\varphi_1, \Phi, \varphi_2)$ denote the Bunge–Euler angles describing the relationship between $\{e_1, e_2, e_3\}$ and $\{e_1^c, e_2^c, e_3^c\}$. In other words, $Q_{ij}^{c \rightarrow s}$ can be expressed in terms of the angles $(\varphi_1, \Phi, \varphi_2)$ using Eq. (2.7). Similarly, let $(\varphi_1^a, \Phi^a, \varphi_2^a)$ denote the Bunge–Euler angles describing the relationship between $\{e_1, e_2, e_3\}$ and $\{e_1^a, e_2^a, e_3^a\}$, i.e., express $Q_{ij}^{a \rightarrow s}$ also using Eq. (2.7) and $(\varphi_1^a, \Phi^a, \varphi_2^a)$. $Q_{ij}^{a \rightarrow c}$ can be computed based on the known symmetry of the selected crystal structure. Then, it should be possible to find the relationship between $(\varphi_1, \Phi, \varphi_2)$ and $(\varphi_1^a, \Phi^a, \varphi_2^a)$ using Eq. (2.11).

As a simple example, consider the crystal symmetry shown in Figure 2.5, which actually is an element of the cubic crystal symmetry. From this figure, we can express the symmetry transformation as

$$Q_{ij}^{a \rightarrow c} = \begin{bmatrix} -1 & 0 & 0 \\ 0 & -1 & 0 \\ 0 & 0 & 1 \end{bmatrix} \quad (2.12)$$

When this symmetry element is introduced into Eq. (2.11) in the manner suggested above, while using Eq. (2.7), leads to the following requirements: $\Phi^a = \Phi$, $\varphi_2^a = \pi + \varphi_2$, $\varphi_1^a = \varphi_1$. In other words, an important consequence of the symmetry element described in Eq. (2.12) is that the crystal orientations represented by $(\varphi_1, \Phi, \varphi_2)$ and $(\varphi_1, \Phi, \pi + \varphi_2)$ are essentially indistinguishable. Therefore, if one were to start with the orientation space defined in Eq. (2.6) and invoke the symmetry element shown in Eq. (2.12), the corresponding space of distinct orientations is reduced by half to $(0 \leq \varphi_1 < 2\pi, 0 \leq \Phi \leq \pi, 0 \leq \varphi_2 < \pi)$.

Cubic crystal lattices belong to the symmetry group O_h . There are 24 rotational symmetry elements in that group, which

means that there are 24 equivalent descriptions for any selected lattice orientation of a cubic crystal. These can be easily visualized by recognizing that there are six independent choices for selecting \mathbf{e}_1^c (corresponding to positive and negative directions along the edges of the cube), and for each of these choices there are four independent choices for the selection of \mathbf{e}_2^c . Note that \mathbf{e}_3^c is uniquely defined by the right-hand rule (i.e., $\mathbf{e}_3^c = \mathbf{e}_1^c \times \mathbf{e}_2^c$), after the selection of \mathbf{e}_1^c and \mathbf{e}_2^c . Indeed, the symmetry element illustrated in Figure 2.5 is one of the 24 cubic symmetry elements.

The FZ for cubic crystals, denoted by FZ_C , can be identified by repeating the analyses described above for all 24 elements of the cubic symmetry. A rigorous consideration of all 24 symmetry operations associated with the cubic crystal lattice identifies the fundamental zone as

$$FZ_C = \left\{ g = (\varphi_1, \Phi, \varphi_2) \mid 0 \leq \varphi_1 < 2\pi, \quad \cos^{-1} \left(\frac{\cos \varphi_2}{\sqrt{1 + \cos^2 \varphi_2}} \right) \leq \Phi \leq \pi/2, \quad 0 \leq \varphi_2 \leq \pi/4 \right\} \quad (2.13)$$

This space is depicted in Figure 2.6. The reader should note that FZ_C is not rectangular in shape.

The other most commonly encountered crystal structure in metals is the hexagonal close-packed structure (hcp), which exhibits 12 rotational symmetry elements. Consideration of these 12 symmetries using the approach described above leads to the identification of a fundamental zone for hcp crystal structures as

$$FZ_H = \{ g = (\varphi_1, \Phi, \varphi_2) \mid 0 \leq \varphi_1 < 2\pi, \quad 0 \leq \Phi \leq \pi/2, \quad 0 \leq \varphi_2 \leq \pi/3 \} \quad (2.14)$$

This fundamental zone is depicted in Figure 2.7, and is rectangular in shape.

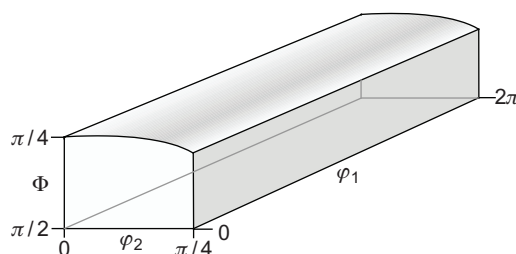


Figure 2.6 Fundamental zone for cubic crystal lattices.

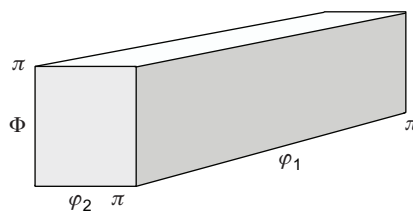


Figure 2.7 Fundamental zone for hexagonal crystal lattices.

It is acknowledged that the inclusion of the crystal lattice orientation in the local state description is particularly complicated by the fact this local state attribute is actually a proper orthogonal tensor, and the identification of the corresponding local state space demands consideration of the symmetry elements inherent to crystal lattice structures. As needed, additional attributes necessary to describe the local state can be appended following the approach described earlier in this chapter. For example, in mesoscale representation of polycrystalline microstructures, it may be necessary to add measures of suitable defect densities (e.g., dislocation density).

2.3 Microstructure Function

Quantitative description of the material microstructure essentially entails a rigorous description of the spatial and temporal distributions of the local states in the material internal structure. As noted earlier, such descriptions are inherently tied to a selected length scale, which reflects the size of the material point implicit in such definitions.

It is highly tempting and intuitive to seek a representation of the microstructure as $h(\mathbf{x}, t)$. In this representation, the microstructure would be described by a function that specifies the local state present at every spatial position \mathbf{x} and time t . Such an approach would lead to a deterministic approach because we would have to unambiguously specify the local state at every spatial point and at every instant of time in the sampled region. However, in practice, all microstructure characterization techniques probe the local state in the material over a finite volume and a finite time interval, both of which are dictated by the resolution limits inherent to the characterization technique/equipment used. Since the local state can only be characterized as an average measure over a finite probe volume and a finite time step, it becomes necessary to allow for the presence of mixed local states in the description of the microstructure function.

For example, such descriptions are essential in quantifying regions near grain boundaries or phase boundaries in multi-phase polycrystalline materials systems. Similar considerations are also unavoidable in the quantification of microstructure evolution in response to any dynamic loading conditions.

Recognition of the challenge described above has prompted Adams et al. [14] to cast the microstructure function in a statistical framework. In this novel approach, the microstructure is defined by the function $m(h,\mathbf{x},t)$, which reflects the probability density for finding local state h at the spatial location \mathbf{x} at time t . For convenience of representation, we will stop expressing explicitly the time dependence of the microstructure function for now, and pick it up in later chapters when we focus on linkages between processing (manufacturing steps) and the microstructure evolution. As discussed earlier, our initial focus is on the linkages between microstructure and properties, and for these we only need to concern ourselves with $m(h,\mathbf{x})$ for the most part.

Let us now remind ourselves of the important differences between the concepts of probability and probability density. Generally speaking, when a variable is only allowed discrete values, then it is appropriate to talk about the probability that the variable takes a specific discrete value of interest. For example, when tossing a coin, the expected results are discrete. So it is appropriate to talk about the probability of a specific result of tossing the coin. However, when the variable is allowed to take continuous values, then it is more appropriate to talk about probability densities. For example, variables h and \mathbf{x} are generally continuous variables, especially when the local state represents attributes such as chemical composition and crystal lattice orientation discussed earlier. In this situation, it is only meaningful to talk about the probability of realizing an outcome in a specific interval of values for the variable. In other words, for a continuous variable h , it is not very meaningful to ask about the probability of realizing a specific value of h at any selected spatial position \mathbf{x} . Instead, the right question to ask is “what is the probability of finding one of the local states that lie within a small interval dh centered around h at a selected \mathbf{x} ?” Defined in this manner, $m(h,\mathbf{x})dh$ would represent the probability and $m(h,\mathbf{x})$ the corresponding probability density. The treatment above can be extended to treat \mathbf{x} also as a continuous variable in which case $m(h,\mathbf{x})d\mathbf{h}d\mathbf{x}$ would represent the probability and $m(h,\mathbf{x})$ the corresponding probability density.

Although it is possible to continue the theoretical treatment of the microstructure function $m(h,\mathbf{x})$ in continuous spaces, it is far more practical to employ a discretized representation. It

should be noted that all materials structure characterization equipment exhibit inherent resolution limits in the measurements of the local state. For example, all measurements of material structure are implicitly tied to a certain probe volume (i.e., the measurements are from a certain $\text{d}x$ around x) and exhibit certain inherent uncertainty (i.e., the measurement only identifies a local state h to within a $\text{d}h$ around it). In other words, although one can theoretically formulate the microstructure function in continuous spaces, in practice we often have to live with discretized information about this function. In this book, we will mostly deal with a discrete (also referred as digital) representation of the microstructure function.

2.4 Digital Representation of Functions

It is essential to review some of the basic notions underlying the discrete representations of functions before we embark on a foundational framework for the digital representation of the microstructure function. Since we will be exploring digital representations for a variety of functions in this book, it would be very useful to discuss the main concepts in a general framework first, and subsequently apply them specifically to the microstructure function described above as our first application in this book. Readers already familiar with these topics can either skip this section or skim through it quickly.

Imagine that we are trying to establish an unknown function (i.e., mapping) denoted $f(x)$, where the independent variable x denotes a continuous variable. In the discussion below, for simplicity, we will treat both x and f as scalars. However, it should be noted that the discussion below applies just as well even when they are tensors of other (possibly different) ranks. Since x is a continuous variable, if we insist on establishing $f(x)$ completely and accurately, we would need to probe its value at an infinite number of locations corresponding to the distinct values of x (called the domain of the function). Note that this is true even when we confine our interest to only a finite interval in the domain, say $x \in (a, b)$, as there will still be an infinite number of distinct values that could be assigned to x . Therefore, it is impractical to fully establish the function of a continuous variable, unless it is a priori known that the function follows a certain analytical description. For example, if the function is known to describe exactly a linear mapping, then one can establish the function completely by probing its values only at two distinct locations in the domain.

However, in practice, we often do not know the functional relation (or mapping) of interest a priori (in fact establishing the relation is the central goal in many tasks). Furthermore, since each probing of the function value would be expected to incur a certain cost (generally probed using either experiments or numerical simulations), we need to develop optimized protocols for effectively recovering such functions using a reasonable number of function evaluations. Let $\{f_s = f(x_s); s = 1, 2, \dots, S\}$ denote a discrete set of function values evaluated at selected locations in the domain enumerated by the variable s . Given these values, our interest is in being able to “reconstruct” the function. In order to do this, we first need to express the function using suitable basis functions. Several different approaches, ranging from trivial basis functions to very sophisticated basis functions, are typically used for such reconstructions. If one were to use the simple indicator functions, the reconstructed function would exhibit “steps.” On the other hand if one were to use local interpolation functions, one would get a suitably interpolated description of the overall function. It should be noted that local interpolation functions are used extensively in numerical approaches such as finite element methods. A salient feature of these types of basis is that the evaluated function values only have a local influence on the reconstructed function. Consequently, these types of basis are said to provide local support. Note that these simple basis functions also work well even when the function evaluations are not conducted on a uniform tessellation of the domain.

Another alternative for the reconstruction of the function is the use of Fourier series or Fourier transforms, where the basis functions are selected to provide global support. These are particularly attractive when the function to be reconstructed is known or assumed to be periodic (i.e., the function essentially repeats itself in the domain with some known periodicity). In these approaches, the function is assumed to be represented by a series sum of harmonic functions (comprising both sine functions and cosine functions) covering a very broad range of frequencies. The basis used in these representations is usually an orthonormal basis and produces a one-to-one mapping of the function from the original space in which it is defined to a complementary frequency space. As a simple illustration, the Fourier representation of a periodic function using the classical harmonic basis can be expressed as

$$f(x) = \sum_{k=-\infty}^{\infty} F_k e^{ikx} \quad (2.15)$$

where the function is implicitly assumed to exhibit a periodicity of 2π (replacing x in Eq. (2.15) with $2\pi x/p$ will allow representation of functions with periodicity p , i.e., $f(x) = f(x + p)$) and $i = \sqrt{-1}$. Given that $e^{ikx} = \cos(kx) + i\sin(kx)$, it should be easy to see that F_k are simply the amplitudes of various frequencies enumerated by k (also referred to as the Fourier coefficients). Physically, k denotes the number of cycles over a length of 2π in x . If the variable x denotes time, k is usually referred to as the angular frequency, and the ordinary frequency (measured in Hz) is defined as $k/(2\pi)$. Although the terms angular and ordinary frequencies are commonly used to describe functions of time, the exact same concept extends to functions defined on other domains. For example, if x were to represent a dimension in the real physical space (i.e., the Euclidean space), then k would represent the spatial frequency. As noted earlier, Eq. (2.15) can be easily modified for arbitrary values of periodicity. In a suitably modified form of Eq. (2.15), k would represent the number of cycles over p . It is emphasized again that F_k provides an equivalent representation of the original function in the frequency space.

An important salient feature of the Fourier representations (arises from the use of orthonormal basis) is that the mapping between $f(x)$ and the Fourier coefficients F_k is one-to-one. In other words, given any one of the two representations, one can accurately reconstruct the other representation. Exploiting the orthonormal properties of the basis, one can compute any of the Fourier coefficients using the following expression:

$$F_k = \frac{1}{2\pi} \int_0^{2\pi} f(x) e^{-ikx} dx \quad (2.16)$$

Equation (2.16) also implies that one can compute any desired subset of the $\{F_k\}$ of interest independently as the computation of any of the Fourier coefficients does not need a priori knowledge of the values of any of the other coefficients (this is because of the orthonormal properties of the Fourier basis). The main disadvantage of using the Fourier series described above is the fact that the series expansion involves an infinite number of terms. Since it is generally not possible to ascertain a priori which of the terms in the series make dominant or important contributions, it typically requires a large number of evaluations to arrive at compact representations of the function.

Since our interest in this book is a digital representation of functions such as the microstructure function, our interest is mostly in a special variant of the concept of the Fourier series

called the discrete Fourier transforms (DFTs). The earlier discussion on Fourier series serves as a strong foundation for DFTs, as they share several properties with the Fourier series. More specifically, in the DFT representations, we start with a set of function values sampled uniformly in the domain of interest. For example, one could imagine tessellating the domain into uniformly sized and spaced bins. One of the main advantages of the DFT representations is that it starts with a finite number of discrete evaluations of the function and establishes its complementary representation in the discrete frequency space. Let $\{f_s | s = 0, 1, 2, \dots, S - 1\}$ represent the sampling of a function on a uniformly tessellated domain of interest (say, $x \in (a, b)$). The function is implicitly assumed to be periodic, i.e., the entire set of values of the function is assumed to repeat as a block (in the exact same sequence) outside of the domain of interest. This assumption of periodicity has its consequences, which we will explore in great detail later. For now, we will proceed assuming that the function of interest is indeed a periodic function. The DFT representation then provides a one-to-one mapping between the discrete function values in the real space and its representation in a discrete frequency space. This mapping (and the inverse mapping) can be expressed as

$$F_k = \mathfrak{F}(f_s) = \sum_{s=0}^{S-1} f_s e^{\frac{i2\pi ks}{S}} \quad (2.17)$$

$$f_s = \mathfrak{F}^{-1}(F_k) = \frac{1}{S} \sum_{k=0}^{S-1} F_k e^{-\frac{i2\pi ks}{S}} \quad (2.18)$$

It is important to recognize and understand several important features of the DFT and the inverse DFT mappings denoted as $\mathfrak{F}(\cdot)$ and $\mathfrak{F}^{-1}(\cdot)$, respectively, in Eqs. (2.17) and (2.18). The elements of the set $\{F_k | k = 0, 1, 2, \dots, S - 1\}$ are referred to as the DFTs of the discretized function of interest. Note that the number of DFTs is exactly same as the number of the discrete function values used to compute the DFTs. It is also important to notice that the value of the variable x does not enter either Eq. (2.17) or Eq. (2.18). In other words, $\{F_k\}$ depend only on the values of $\{f_s\}$ and vice versa, and there is no explicit dependence on the sampling bin size, i.e., Δx (the distance between two sequential sampling points in the domain on which the function is defined). Therefore, it might make more sense to define the periodicity of the function as S (i.e., the number of discrete function values) instead the domain size ($b - a$). Although we can

make this switch, it is important to always keep in the back of our mind that S (a dimensionless number) does indeed map to the domain size $(b - a)$, which might be associated with specific physical units of measurements. The physical meaning of F_k is essentially same as that of the Fourier coefficients described earlier. They represent the amplitudes of the discrete frequencies defined on S . As before, k denotes the number of cycles over the domain size associated with S . Note that the enumeration of the values has been chosen as $0, \dots, S - 1$ (as opposed to using $1, \dots, S$). This was done deliberately to assign a specific meaning to F_0 . Note that Eq. (2.17) assigns to F_0 the sum of $\{f_s\}$, which can be normalized by S to obtain the average value of the function. It should also be noted that the structure of Eqs. (2.17) and (2.18) would allow us multiple choices in terms of where and what factors we use in front of the summation sign in these mappings. In the version presented here, the factor $\frac{1}{S}$ was used in Eq. (2.18) and a factor of 1 (implied) was used in Eq. (2.17). We could have easily switched them (in fact several textbooks do this!) and still have accomplished the desired one-to-one mapping. In fact, there are other options. For example, one might have used $\frac{1}{\sqrt{S}}$ in both equations, and still be right. In fact, any combination whose product is $\frac{1}{S}$ works. In this book, we will use exclusively the mappings shown in Eqs. (2.17) and (2.18). The reader is strongly advised to check the specific versions used in any software packages, because this discrepancy can be (and has been) a source of major frustration in implementing some of the theoretical concepts described in this book.

Although Eqs. (2.17) and (2.18) are written for functions defined on a single variable, they are trivially extended for functions with multiple independent variables by simply performing the transform successively on each variable. For example, consider a function defined on two variables, say, x and y . Discrete sampling of this function produces a set of values that could be conveniently arranged as a rectangular matrix (allowing different sampling rates on the two variables). In order to obtain the DFTs of this function, one could perform a DFT on each row of the matrix and then subsequently perform the DFT again on each column of the resulting matrix. It should be noted that the size of the matrix remains the same. This is because the number of DFTs is always the same as the number of the discrete function values. Also, the sequence of the operations (rows first and then columns or columns first and then rows) has no influence on the final result.

The fact that the DFTs capture the frequency content of a discretely sampled function has led to many applications in the area of discrete signal processing. For example, in filtering the

noise in a digital signal, one usually has prior information on the expected frequency content in the original signal. In such situations, one can compute the DFTs, replace the amplitudes of all of the unwanted frequencies with zero values, and then simply reconstruct the signal. This operation essentially removes the undesired noise from the original signal. Of course, conversely, it is also very important to make sure the desired frequency content of the signal is well captured in the discrete sampling of the function. It can be shown that it is necessary to design the sampling rate such that the signal is sampled at least twice in one cycle for the highest frequency desired to be captured in the discretized function; this is usually referred as the Nyquist sampling rate. This would mean that for the spatial discretization of the microstructure, the spatial bin should be smaller than half the size of the smallest feature to be captured in the microstructure.

[Equations \(2.17\) and \(2.18\)](#) are generally used to convey the main concepts and representations behind DFTs. In practice, computation of the DFTs (or inverting from DFTs to real space) using either of these equations is computationally expensive. The reader should note that the equations presented involve approximately S^2 number of computations (e.g., computation of each F_k requires evaluation of S terms and there are S distinct values of F_k). In practice, DFTs are computed using a special algorithm that is generally referred as the fast Fourier transform (FFT) algorithm. The FFT algorithm takes advantages of the many redundancies implied in the brute force computations described by [Eqs. \(2.17\) and \(2.18\)](#) and reduces the number of computations involved to $S \log S$. This remarkable reduction in the computational cost (especially dramatic for large values of S) has made FFT algorithm widely popular and almost synonymous with DFT. However, it would be prudent to recognize that FFT refers to the specific computational algorithm, while DFT refers to the fundamental concept of the spectral representation of a discrete function with discrete Fourier transforms.

The reader is advised to review the many known relationships involving the DFTs. A few of these will be presented here without proofs. Indeed, the reader would be able to find proofs for these very easily in published literature. Interestingly, [Eqs. \(2.17\) and \(2.18\)](#) are applicable even when the function values $\{f_s\}$ are complex-valued. It can be shown that

$$\sum_{s=0}^{S-1} |f_s|^2 = \frac{1}{S} \sum_{k=0}^{S-1} |F_k|^2 \quad (2.19)$$

However, if the function values $\{f_s\}$ are all real-valued, then it is easy to show that approximately only one-half of the DFTs are unique²:

$$F_{S-k} = F_k^* \quad (2.20)$$

Note that Eq. (2.20) is not meant to be used for $k = 0$ because F_S has not been defined (recall that the DFTs are indexed $k = 0, 1, 2, \dots, S - 1$). However, Eq. (2.17) would actually imply that the DFTs are also periodic over S , just like the discrete values of the function (implied in Eq. (2.18)). Invoking the periodicity of DFTs would allow the application of Eq. (2.20) for $k = 0$.

For two discrete valued functions $\{f_s\}$ and $\{g_s\}$ defined on the same sampling grid (i.e., $s = 0, 1, 2, \dots, S - 1$), it can be shown that

$$\sum_{s=0}^{S-1} f_s g_s^* = \frac{1}{S} \sum_{k=0}^{S-1} F_k G_k^* \quad (2.21)$$

where $G_k = \Im(g_s)$. It should be noted that Eq. (2.19) can actually be inferred from Eq. (2.21) if one were to choose the two functions to be the same. Perhaps, the most valuable attribute of DFTs is in computing convolutions and correlations expressed as

$$\text{Conv}(f, g) \equiv h_r = \sum_{s=0}^{S-1} f_s g_{r-s} = \Im^{-1}(F_k G_k) \quad (2.22)$$

$$\text{Corr}(f, g) \equiv h_r = \sum_{s=0}^{S-1} f_{s+r} g_s = \Im^{-1}(F_k G_k^*) \quad (2.23)$$

It should be noted that the concepts of convolution and correlation are closely related as shown above. For most applications, one can cast their problems as either a convolution or a correlation. The main advantage of using DFTs is the remarkable computational advantage in utilizing either Eq. (2.22) or Eq. (2.23) in performing these operations. In particular, note the absence of a summation in the right-hand side of these equations. Consequently, the number of computations involved is reduced dramatically from order (S^2) to order (S). It is also important to recognize that the relationships described in Eqs. (2.22) and (2.23) are fairly special to DFTs. In particular, it should be noted that most other spectral representations do not result in these special relationships. Therefore, there is special

²Superscript * on complex numbers denotes its complex conjugate.

motivation for using DFTs in problems that involve convolutions or correlations.

Convolutions and correlations are used extensively in various image processing tasks. For example, if images of microstructure taken from a selected region are to be cross-registered, a correlation would be an excellent tool for the task. These concepts are also used extensively in composite theories based on Green's functions. Consequently, they are of tremendous utility in this book. In later chapters, we will use correlations extensively to quantify the neighborhoods in a given material system using the framework of n -point spatial correlations. We will also utilize convolutions in formulating a special class of structure–performance linkages that we shall refer as localization metamodels.

The description above transforms a set of discrete values of the function to a set of discrete frequencies defining the function. However, one of our real interests in using DFTs is that we hope to use them to reconstruct the function values at new points in the domain of interest (apart from the sampling points where the function values are already known). There do exist several options for recovering values of the functions at points other than the grid points [15]. We describe here an approach that we refer to as spectral interpolation, because it uses the DFTs to estimate the value of the function at any point in the domain of interest.

In using the spectral interpolation approach described here, it is assumed that the function was sampled adequately (see the discussion above on Nyquist sampling) such that the DFTs have already captured all of the important frequencies needed to describe the function of interest. In other words, it is presumed that a finer resolution sampling of the function would not reveal any new frequencies (i.e., new DFTs) or any significant changes in the amplitudes of the frequencies already identified. Under these circumstances, the DFT for a finer resolution grid on the same space can be obtained simply by padding the DFT for the original sampling grid with appropriately placed zeros. The DFT corresponding to the finer resolution grid can then be used to compute efficiently an interpolated value of the function at any of the grid points on the finer grid; this is the central idea behind spectral interpolation.

On the surface, the spectral interpolation approach described above sounds very complicated and computationally expensive. However, in practice, it will turn out that it is really quite simple to implement and is ideally suited for certain applications. First, we recognize that many of the functions of interest in capturing materials phenomena only require a relatively small number of

frequencies [11,16–18]. In other words, the number of dominant frequencies (assessed based on the magnitude of F_k) is typically much smaller than the number of function values (i.e., S). Let \tilde{K} denote the number of dominant DFTs in a function of interest (i.e., these specific DFTs possess significant values of F_k compared to the rest of the DFTs for the selected function). In general, we expect $\tilde{K} \ll S$. As explained above, it is necessary to invoke a finer resolution sampling grid to facilitate spectral interpolation as described here. The finer sampling grid may usually be designed such that the sampling rate is multiplied by an integer. This strategy will ensure that the original grid points are still included in the new grid. The increase in the sampling rate can be very large. This might be necessary to ensure that the interpolation point of interest (where the function value needs to be estimated) is at one of the grid points (or within an acceptable distance to the grid point) in the finer resolution grid. For example, the sampling rate can be multiplied by a million times or more to accomplish this requirement. Therefore the total number of sampling points on the finer resolution grid can be several orders of magnitude larger than S . Let $\tilde{S} \gg S$ denote the number of points in the finer resolution grid. The corresponding number of DFTs for the finer resolution grid would also be very large (i.e., \tilde{S}). However, only \tilde{K} of these would have dominant values as we have already ensured that all of the dominant frequencies were already captured in the original set of DFTs for the function. Therefore one can reconstruct the function value at any desired location on the finer resolution grid by simply evaluating \tilde{K} number of terms in a suitably formulated version of [Eq. \(2.18\)](#) for the new finer resolution grid. The most important concept to recognize here is that the number of terms will remain at \tilde{K} , completely independent of how large \tilde{S} might have to be selected to place the interpolation point of interest on the finer resolution grid.

The overall procedure described above is illustrated next with a simple example. As a simple example, consider the function shown in [Figure 2.8](#) (top) sampled at 9 points uniformly distributed on the periodic domain of the function (taken here as 2π). In the figure, the first point is repeated as the 10th point for easy visualization of the periodicity of the function, but this point is not included in the DFT computation. The corresponding complex-valued DFTs computed using [Eq. \(2.17\)](#) are shown in [Figure 2.8](#) (bottom). As explained earlier, F_0 is essentially the sum of all the function values. As expected, the dominant DFTs (not considering F_0) correspond to $k = (1,3)$ along with their corresponding complex conjugates at $k = (8,6)$ (see [Eq. \(2.20\)](#)). Note

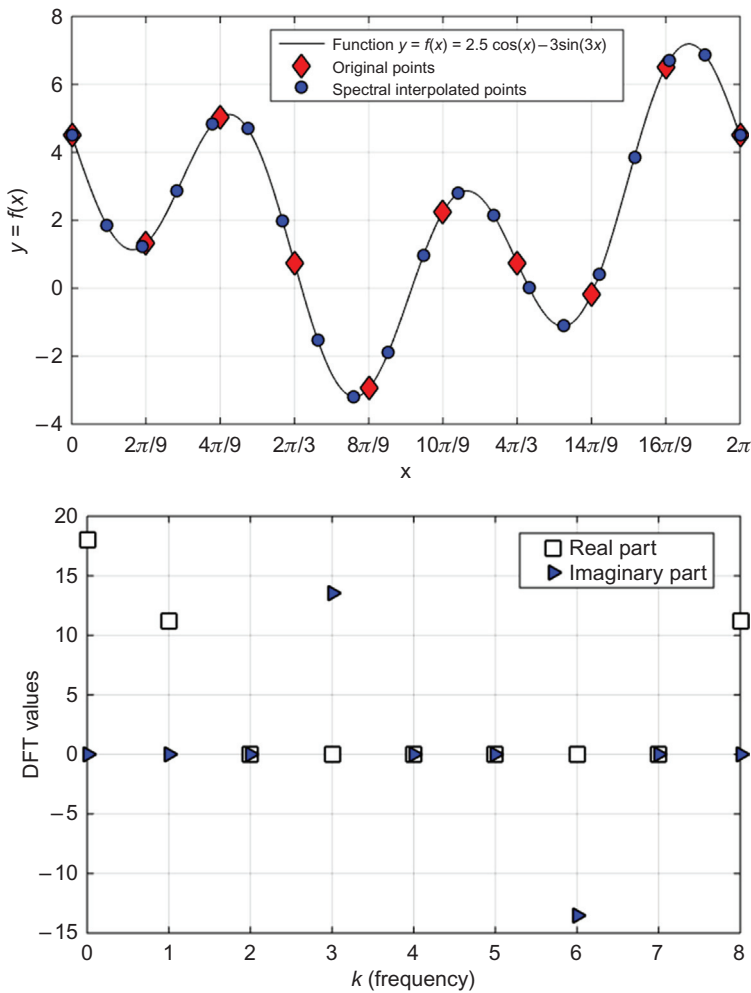


Figure 2.8 Top: Plots of the function selected to illustrate the spectral interpolation method, with the original sampling as well as the finer reconstruction. Bottom: DFT values corresponding to the original sampling.

also the enumeration of k from 0 to 8 (i.e., 0 to $(S - 1)$) and that F_1 is mainly real, while F_3 is mainly imaginary (as expected based on the selected function in Figure 2.8). Furthermore, the values of these DFTs are essentially the amplitudes of the corresponding terms in the selected function multiplied by $S/2$ (the factor S is a consequence of not having any normalization factors in Eq. (2.17), while the factor 2 arises because the amplitude is split into two complex conjugate DFTs for all real functions).

As a specific example of a spectral interpolation, let us assume that we wish to compute the values of the same function

at 19 points. In other words, we now wish to establish a DFT for the same function as if it was sampled at 19 points, without actually performing the DFT computations but using the previously established values (based on the sampling at 9 points). Let us denote this new DFT as \tilde{F}_k , and continue to denote the previously established DFT values as F_k . Since the DFT values are essentially the amplitudes of the frequencies multiplied by $S/2$ (with the value of S being different for \tilde{F}_k and F_k) it is easy to see that $\tilde{F}_k = \frac{19}{9} F_k$. However, the main challenge is that there are only 9 values of F_k , but we need to assemble 19 values of \tilde{F}_k . This challenge is easily addressed by reminding ourselves that k enumerates the frequencies (i.e., number of cycles) over the periodic domain (i.e., 2π) and that half of the DFTs have to the complex conjugates of the other half (because the function takes only real values). Therefore, we are obligated to take $\{F_k | k = 0, 1, \dots, 4\}$, scale them by $\frac{19}{9}$, and place them in $\{\tilde{F}_k | k = 0, 1, \dots, 4\}$. We also need to assign $\{\tilde{F}_{19-k} | k = 1, \dots, 4\}$ with the appropriate complex conjugates. Since we assume that no additional new frequencies will be uncovered with the higher sampling rate we assign the values of the rest of the DFTs in $\{\tilde{F}_k\}$ as zeros. The sample values reconstructed from an inverse DFT of \tilde{F}_k using Eq. (2.18) are also shown in Figure 2.8 (top) along with the original function and the original sampling. It is seen that the spectral interpolation provides excellent values for the new points.

Although an inverse DFT was used to reconstruct the values of the function at all new sampling points in the previous example, often this would incur high computational cost. In many situations, we are only interested in finding values of the function at specific selected points. In that situation, it might be computationally more economical to directly use Eq. (2.18) only on the dominant DFTs (it becomes necessary to maintain the list of the dominant DFTs along with their k values). We will see specific applications of these concepts in later chapters of this book.

2.5 Digital Representation of Microstructure Function

Armed with the concepts for digital representation of functions, we now get back to our earlier discussion of the microstructure function. We previously stipulated that the microstructure is best defined by the function $m(h, \mathbf{x})$, which reflects the probability density associated with finding local state h at the spatial location \mathbf{x} . We also hypothesized that it is only practical to capture this highly complex function with a

digital representation. Following the discussion above on DFTs, we will initially seek a digital representation of the microstructure function with a simple uniform sampling of the domain space. We will subsequently venture into more sophisticated representations using other basis.

The domain space for the microstructure function is the product space of the spaces defining the domains of the variables h and \mathbf{x} . The domain space for h is essentially the local state space (i.e., h can only take values from the local state space selected for the specific problem) discussed in detail earlier in [Section 2.1](#). The domain space for \mathbf{x} is essentially the physical space defining the volume of the microstructure of interest (presumably a representative volume of the microstructure). The simplest digital representation of the microstructure function therefore can be extracted by binning (typically a uniform tessellation using a suitable invariant measure) the physical space as well as the local state space [\[14\]](#). Let $s = 1, 2, \dots, S$ and $n = 1, 2, \dots, N$ enumerate the individual bins in spatial domain and the local state space, respectively. With these conventions, the discretized microstructure function can be denoted as m_s^n and represents the total volume fraction of all local states from bin n in the spatial bin s . As per this definition, the microstructure function is subject to the following constraints:

$$\sum_{n=1}^N m_s^n = 1, \quad 0 \leq m_s^n \leq 1 \quad (2.24)$$

As a simple example, consider the highly simplified two-dimensional microstructure volume element shown in [Figure 2.9](#). This particular microstructure volume is sampled very coarsely (using only a 4×4 sampling grid) and is therefore not at all representative of real microstructures (which would demand a higher sampling rate and/or a higher sampling volume to capture the rich heterogeneity exhibited by the material internal structure). Therefore, the microstructure volume shown in [Figure 2.9](#) is used here only for illustrating the main concepts. Since this specific example utilizes a two-dimensional domain, the sampling grid points need to be identified by a two-dimensional array, i.e., $s = (s_1, s_2)$. In order to allow a general multidimensional representation of the spatial grid points, we will henceforth use \mathbf{s} instead of s , i.e., $\mathbf{s} = (s_1, s_2)$. In [Figure 2.9](#), the indices for a 4×4 sampling grid are shown to correspond to the centers of each of the spatial bin (also referred as a voxel). Therefore, we are sampling the microstructure volume at only a finite number of grid points (a total of 16 grid points in [Figure 2.9](#)). The values sampled at these grid

(0,3)	(1,3)	(2,3)	(3,3)
(0,2)	(1,2)	(2,2)	(3,2)
(0,1)	(1,1)	(2,1)	(3,1)
(0,0)	(1,0)	(2,0)	(3,0)

Figure 2.9 Highly simplified small microstructure volume element used to illustrate the main concepts.

points would define m_s^n . The visualization of the microstructure volume shown in Figure 2.9 is a highly simplified reconstruction using the primitive indicator functions, where the entire spatial voxel is assigned the value sampled at the center of the voxel. In other words, what we see in Figure 2.9 is the reconstructed $m(h,\mathbf{x})$ based on the 16 values of m_s^n . Obviously, this is not the only reconstruction possible. However, this is the most typical reconstruction employed by most materials characterization equipment. The main reason for adopting this simple reconstruction is the fact that all materials characterization equipment inherently evaluate the material local state as an average over a finite probe volume. Consequently, it is only reasonable to assign the same local state to the entire probe volume, not just at the center of the probe volume. As mentioned earlier, the definition of a material point in hierarchical materials is implicitly tied to a specific length scale and is always associated with a small neighborhood volume. In the representation in Figure 2.9, this neighborhood volume is conveniently assumed to extend to include the entire volume of the spatial voxel surrounding the sampling point. It is also possible that the sampling interval was chosen such that the spatial voxel volume was significantly larger than the probe volume; this is very likely to happen when each measurement (at each sampling point) incurs substantial cost. In such situations, the reconstruction shown in Figure 2.9 is very primitive.

As an illustration, let us look at the specific values of the m_s^n for the microstructure in Figure 2.9. In this highly simplified microstructure, there are only two local states. These can be conveniently indexed by n , with $n = 1$ denoting the phase

represented white and $n=2$ denoting the phase represented gray in [Figure 2.9](#). With this assignment of local states, some example values for the digital representation of the microstructure shown in [Figure 2.9](#) would be $m_{(1,2)}^1 = 1$, $m_{(1,2)}^2 = 0$, $m_{(2,1)}^1 = 0$, and $m_{(2,1)}^2 = 1$. These specific values would capture the fact that the spatial voxel indexed as (1,2) is filled by the white phase and that the spatial voxel indexed as (2,1) is filled by the gray phase.

It is specifically noted that in the example shown in [Figure 2.9](#), we have assigned the local state at each sampling point exclusively to one of the two allowed local states in the material system. When one encounters material systems with a finite number of discrete local states and the local state at each of the sampling point is assigned fully to only one of the allowed local states (such as the one shown in [Figure 2.8](#)), discretized representation of the microstructure for such material systems can be binary (i.e., all values of m_s^n are either 0 or 1, while being subjected to the constraints specified in [Eq. \(2.24\)](#)). These special microstructures are referred to as *eigen microstructures*. Indeed, most advanced materials characterization equipment produce microstructure instantiations that can be strictly classified as eigen microstructures. This is for two reasons: (i) all characterization equipment inherently exhibit resolution limits in both spatial mapping (e.g., it is very difficult to resolve length scales below that of the probe volume) and in indexing the local state (e.g., in measuring the local composition in the probe volume there is always an implied resolution limit depending on the technique employed). Consequently if the spatial domain and the local state space are binned at the machine resolution limits, the machine always produces an eigen microstructure. Interestingly, even when the characterization process encounters a voxel with mixed local states (e.g., when measuring crystal lattice orientations in a voxel containing a grain boundary), the standard workflow in most modern characterization equipment is to identify the dominant local state in the voxel of interest and simply assign that local state fully to that voxel. Consequently, one can see why most microstructure datasets are amenable to representation as eigen microstructures. It should also be noted that the eigen microstructures are also generally preferred in modeling and simulation of materials phenomena wherever possible, because the effort required in establishing the local properties (at the scale of individual voxels) for mixed local states is much higher than for pure local states.

As mentioned earlier, in most real material systems, we anticipate encountering continuous local states (cf. [Section 2.2](#)).

As described earlier, it should be possible to define the corresponding local state space and bin it suitably, perhaps based on the resolution limit of the characterization equipment employed in mapping the microstructure. Consequently, we might end up with a large number of binned local states (i.e., the value of N might be very large). However, if we approach the representation of the microstructure as an eigen microstructure, then we expect a very sparse array (because each spatial voxel is assigned to only one of the local states from a very large list of potential local states). Therefore, we can take advantage of various modern computational tools available for efficient storage and manipulation of very large but sparse binary arrays.

It is emphasized again the framework for the description of the microstructure presented above is fairly general and can accommodate any combination of material features by simply enhancing the description of the local states and the corresponding local state space (cf. [Section 2.1](#)). This framework is also not limited to any specific length or time scales (because this is the description of material structure at a specified instant in time). The central challenge is really identifying the pertinent local states and their corresponding local state spaces. Obviously, if one wants to include a large number of local states, the representation does become unwieldy. However, with a smart choice of the local states for any selected application, one should be able to get a viable representation of the microstructure for any selected application. It should be noted one can define the local state to emphasize any complex aspect of the material structure, which might itself embed additional local spatial information. For example, in studying compositional fields (e.g., in spinodal decomposition) it might be very useful to include local compositional gradients in the definition of the local state, as it might carry the relevant information that controls the time evolution of the microstructure. The framework presented above does allow incorporation of such features. However, it is possible that a simple primitive binning of the local state space as described earlier may not represent the best strategy. We will explore later other Fourier basis to represent more efficiently the functions of interest over continuous local state spaces.

In summary for this section, it is pointed out that the discretized representation of microstructure is the most practical starting point in representation and quantification of microstructure data. In particular, this offers many advantages in fast computation of microstructure measures/metrics [\[16,19\]](#), automated identification of salient microstructure features in large

datasets [20], extraction of RVEs from an ensemble of datasets [21], reconstructions of microstructures from measured statistics [22,23], building of real-time searchable microstructure databases [24], and mining of high fidelity multiscale structure–performance–structure evolution linkages from physics-based models [25–29]. We shall explore all of these computations and analytics in coming chapters.

2.6 Spectral Representations of Microstructure Function

As mentioned earlier, the discretized representation of the microstructure presented above is essentially a primitive representation of the microstructure function. Mathematically, this relationship can be expressed as

$$m(h, \mathbf{x}) \approx \sum_{n=1}^N \sum_{s=0}^{S-I} m_s^n \chi_n(h) \chi_s(\mathbf{x}) \quad (2.25)$$

where the indicator function $\chi_i(x)$ is defined such that it is equal to 1 if x is included in the bin labeled i . Therefore, as long as the binning was accomplished such that there are no overlapping common elements in any two distinct bins and the union of all bins includes the entire space of interest, then we are guaranteed to have one of the coefficients equal to 1 and the rest will be 0 for any selected associated combination of (h, \mathbf{x}) .

A important take away from Eq. (2.25) is the distinction between the symbols h and n in Eq. (2.25). They are completely analogous to the use of \mathbf{x} and s for the spatial variables. It should be noted that h refers to a specific local state, while n is an index for the bins in the local state space. In the descriptions of the composite microstructures with a finite number of distinct constituents, the definitions of h and n merge to a single definition, and therefore the notation becomes somewhat redundant. However, for the more general case with continuous local states, these two variables can and will mean very different things. Therefore, proper attention has to be given to representing these variables differently as the need arises.

An important notation we have slipped in Eq. (2.25) is with regard to indexing the spatial bins. It was noted before that the variables h and \mathbf{x} needed to define the microstructure function can be quite complex and are likely to demand representation as tensors in specific applications. The need for treating \mathbf{x} as a

vector is obvious (see the example described in [Figure 2.9](#)), and we have previously discussed in [Section 2.2.1](#) the need for representing local states such as crystal lattice orientation as a part of h . In [Eq. \(2.25\)](#), we have chosen to treat h as a scalar variable, while allowing \mathbf{x} to be represented as a vector. Extensions of this representation that allow h to be represented as a vector are possible and will be introduced subsequently. In order to get a discretized representation that allows the treatment of \mathbf{x} as a vector, we simply have to allow the indices to be represented by arrays (i.e., as vector indices). Therefore, in the notation presented in [Eq. \(2.25\)](#) the spatial bin index is actually an array of integers. For example, for a three-dimensional microstructure volume, the values of \mathbf{s} will range from $\mathbf{0} = (0, 0, 0)$ to $\mathbf{S} - \mathbf{I} = (S - 1, S - 1, S - 1)$, where it is implicitly assumed that each dimension has S grid points. This notation can be easily adjusted for situations with unequal number of grid points along each of the spatial dimension. It is noted here that a similar strategy can be used when the representation of h demands a multivariate representation.

It should be obvious that [Eq. \(2.25\)](#) is only one of many possible spectral representations (the indicator functions described above form an orthogonal basis) of the microstructure that allows us to extract a discrete representation. As an example, for a multiphase composite, one might seek a representation of the microstructure function using classical harmonic series for the spatial component and the primitive indicator functions for the local state component. The spectral representation of such a function can be expressed as

$$m(h, \mathbf{x}) \approx \sum_{n=1}^N \sum_{\mathbf{k}=-\infty}^{\infty} M_k^n e^{\frac{i 2 \pi \mathbf{k} \cdot \mathbf{x}}{L}} \chi_n(h) \quad (2.26)$$

Implicit in [Eq. \(2.26\)](#) is the assumption of periodicity over L (in each of the spatial dimensions contained in the representation of \mathbf{x}) that is inherent to the use of harmonic basis. [Equation \(2.26\)](#) can be easily modified for situations with different periods along each of the spatial dimensions. Here we will proceed with [Eq. \(2.26\)](#) for simplicity of the mathematical representation. The reader should also note the use of an integer array for \mathbf{k} (a similar vector index was used earlier for \mathbf{s} for the exact same reasons) and that the dot product between \mathbf{k} and \mathbf{x} is essentially equivalent to using an independent Fourier basis for each dimension. The notation used in [Eq. \(2.26\)](#) allows compact descriptions of

multivariate functions (such as the microstructure function) using compounded Fourier basis (this includes every possible product of the terms that arise in the Fourier representations for each independent variable). As noted earlier, the main disadvantage with the use of harmonic series is that it requires an infinite number of terms. Therefore, it might be more practical to seek the equivalent DFT representation as

$$M_k^n = \Im(m_s^n) \quad (2.27)$$

In a similar manner, we can also seek other Fourier representations for the local state component of the microstructure function. As an example, let us consider the single phase polycrystalline microstructures we studied earlier in [Section 2.2.1](#), where the local state is captured by the crystal lattice orientation, i.e., $h = g$. For these microstructures, the microstructure function is suitably denoted as $m(g, \mathbf{x})$ and is usually referred to as the spatially resolved orientation distribution function. Physically, it captures the probability density associated with finding a specific orientation g of interest (to within a specified dg) at a spatial point of interest \mathbf{x} . As discussed earlier, one might seek a discrete representation of this microstructure function as shown in [Eq. \(2.25\)](#) by simply binning both the spatial domain as well as the local state space (i.e., the fundamental zone of orientations based on the symmetry of the selected crystal lattice). However, we can seek an efficient representation of the orientation component of the microstructure function through the use of generalized spherical harmonic basis (GSH) [\[30\]](#). The GSH basis, denoted as $T_l^{mn}(g)$, can be expressed as

$$T_l^{mn}(g) = T_l^{mn}(\varphi_1, \Phi, \varphi_2) = e^{im\varphi_1} P_l^{mn} e^{in\varphi_2} \quad (2.28)$$

where P_l^{mn} are certain generalizations of associated Legendre functions. Recall that $(\varphi_1, \Phi, \varphi_2)$ represent the ordered set of three Bunge–Euler angles introduced earlier to describe crystal lattice orientation, g . GSH functions form a complete orthonormal basis [\[30\]](#)

$$\oint T_l^{mn}(g) T_l^{m'n'*}(g) dg = \frac{1}{2l+1} \delta_{ll'} \delta_{mm'} \delta_{nn'} \quad (2.29)$$

where dg is the invariant measure of orientation space and $*$ denotes the complex conjugate. GSH functions can be modified to reflect any desired crystal and sample symmetries [\[11,30\]](#). For instance, symmetrized GSH functions for cubic-triclinic symmetry (in this notation the first symmetry refers to crystal

symmetry and the second one to the sample symmetry) are denoted as $\dot{T}_l^{\mu n}$, and can be found as a linear combination of GSH functions:

$$\dot{T}_l^{\mu n}(g) = \sum_{m=-l}^l \dot{A}_l^{m\mu} T_l^{mn}(g) \quad (2.30)$$

where $\dot{A}_l^{m\mu}$ are the coefficients that account for the cubic crystal symmetry in the GSH functions. The spectral representation of the microstructure function utilizing the GSH basis for the lattice orientation component can now be expressed as (by making use of the orthogonal properties of GSH)

$$m(g, \mathbf{x}) \approx \sum_{s=0}^{S-1} \sum_{\mu, n, l} M_{ls}^{\mu n} \dot{T}_l^{\mu n}(g) \chi_s(\mathbf{x}), \quad M_{ls}^{\mu n} = (2l+1) \int_{FZ} m(g, \mathbf{x}) \dot{T}_l^{\mu n*}(g) dg \quad (2.31)$$

where $M_{ls}^{\mu n}$ would be referred as the GSH coefficients. As a special case, when there is a single crystal of lattice orientation g_o in a spatial bin s , the corresponding GSH coefficients are simply given by

$$M_{ls}^{\mu n} = (2l+1) \dot{T}_l^{\mu n*}(g_o) \quad (2.32)$$

In the discretized representation of Eq. (2.31), we have utilized the primitive indicator basis for the spatial component and the GSH for the lattice orientation part. For reasons described earlier, we might be interested in a DFT representation for the spatial component. In such a situation, the discretized representation of the microstructure function can be expressed as

$$\tilde{M}_{lk}^{\mu n} = \Im(M_{ls}^{\mu n}) \quad (2.33)$$

It is emphasized here that the spatial and local state components of the microstructure function will usually demand different strategies. We will typically find that the DFT representations are usually very effective for describing the spatial component. This is because the spatial component is usually involved in a convolution computation. Prime examples of such computations are the spatial correlations (convolution of the microstructure function with itself) and the homogenization or localization linkages (convolution of a physics capturing Green's function with the microstructure function). These are the main subject of the

later chapters of this book. On the other hand, we will typically find that a Fourier series representation of the local state component of the microstructure is much more efficient in the applications described in this book. This is in spite of the fact that the Fourier series representations always produce an infinite number of terms in the series expansion. Note that this was the case with the GSH representations described above. For most applications described in this book, we will observe that properly selected Fourier representations for the local state component of the microstructure function will produce a compact representation (i.e., only a few terms will dominate the representation), and therefore we will be able to exploit the orthogonal properties of the Fourier series in arriving at computationally efficient homogenization and localization linkages [11,22,31–33] (these are the PSP linkages described in Chapter 1). The main reason for different treatment of the spatial component and the local state component in this book can therefore be attributed to the fact that the spatial component is often involved in a convolution computation whereas the local state component is often involved in an inner product computation.

As a final illustration of the concepts presented in this chapter, let us examine another class of archetypal microstructures where the local state in the material structure requires the treatment of the local chemical composition (c) as a continuous local state, i.e., $h = c$. For these microstructures, the microstructure function is suitably denoted as $m(c, \mathbf{x})$ and can be referred to as the spatially resolved composition distribution function. Physically, it captures the probability density associated with finding a specific composition of interest c (to within a specified dc) at a spatial point of interest \mathbf{x} . As discussed earlier, one might seek a discrete representation of this microstructure function by simply binning both the spatial domain as well as the local state space [28]. However, we can once again seek an efficient representation of the composition component of the microstructure function through the use of a suitable Fourier basis. Following essentially the same approach described earlier for polycrystalline microstructures but using Legendre polynomials (denoted as $P^n(\cdot)$) instead of the GSH as the Fourier basis, one can arrive at the following representation:

$$m(c, \mathbf{x}) \approx \sum_{s=0}^{S-1} \sum_n M_s^n P^n(c) \chi_s(\mathbf{x}) \quad (2.34)$$

where M_s^n would be referred as the Legendre coefficients. Employing a DFT representation for the spatial component results in the following discretized representation of the micro-structure function:

$$\tilde{M}_k^n = \Im(M_s^n) \quad (2.35)$$

One of the advantages of the Legendre polynomials is that they serve as an orthonormal basis for representations of non-periodic functions over a domain of $[-1,1]$. This feature may be of importance in representation of certain local states (such as the composition variable discussed above).

In all the examples discussed so far, the spatial voxels were defined at length scales that resulted in continuum scale descriptors of the local state. However, the same framework can also be applied to material structures at lower length scales. For example, this framework has recently been applied to results produced by molecular dynamics (MD) simulations. In the first example, this approach was applied to quantify the semi-crystalline polymer structure datasets produced by MD simulations [34]. In this example, a periodic volumetric domain comprising of many atoms was tessellated into voxels, where each voxel was large enough to have a finite number of atoms. It was necessary to define spatial voxels at this length scale in order to assign the local states of crystalline or amorphous to each voxel. The focus of the second application [35] was to critically evaluate the differences in the atomic structures predicted by various force fields used in the MD simulations for a selected material system. For this study, the center positions of the atoms were taken directly from the results of the MD simulations (as expected values) and a hard sphere of radius a was constructed around the center to denote the atom. The entire volumetric domain used in the simulation was then discretized into a uniform grid and the material structure was converted to a simple digital signal, denoted as m_s^n . The local state descriptor, n , was allowed only two discrete values: $n = 1$ was used to refer to the atomic species and $n = 2$ was used to refer to the empty space between the atomic species. The level of the spatial discretization employed in such studies is typically a parameter for the data-driven explorations. From past trials, a voxel size of approximately $a/5$ to $a/10$ is suggested. Although, in principle, the value of m_s^n can range between 0 and 1, it was decided to allow only a value of 0 or 1 for this variable. In other words, the structure was described as an eigen structure. It was demonstrated that the

approach described in this book is easily extended to the atomic structures predicted by MD simulations.

In closing this chapter, it is hoped that the reader is now acquainted with a generalized approach for the representation of the microstructure function that is broadly applicable to hierarchical material systems of interest in advanced technologies. It is cautioned that the representation is only the first step. Identification and extraction of the salient features of the microstructure is the next logical step. Our strategy will be to start with a comprehensive and extensible representation of the microstructure function. We will subsequently employ data-driven approaches that will objectively produce dramatically reduced representations of the microstructure for any selected application. Needless to say, the reduced-order representations for different applications demanding different performance criterion can be very different, even for the same material system.

References

- [1] Milton GW. The theory of composites. Cambridge Monographs on Applied and Computational Mathematics; 2001.
- [2] Gusev AA. Representative volume element size for elastic composites: a numerical study. *J Mech Phys Solids* 1997;45(9):1449–59.
- [3] Nemat-Nasser S, Hori M. Micromechanics: overall properties of heterogeneous materials. 2nd ed. Amsterdam: Elsevier; 1999.
- [4] Milton GW. The theory of composites. Cambridge monographs on applied and computational mathematics. Cambridge: Cambridge University Press; 2002.
- [5] Cherkaev A. Variational methods for structural optimization. Applied mathematical sciences, vol. 140. New York, NY, USA: Springer; 1991.
- [6] Drugan WJ, Willis JR. A micromechanics-based nonlocal constitutive equation and estimates of representative volume element size for elastic composites. *J Mech Phys Solids* 1996;44(4):497–524.
- [7] Kanit T, et al. Determination of the size of the representative volume element for random composites: statistical and numerical approach. *Int J Solids Struct* 2003;40(13–14):3647–79.
- [8] Ostoja-Starzewski M. Microstructural randomness and scaling in mechanics of materials. Boca Raton, FL: Chapman & Hall/CRC; 2008.
- [9] Willis JR. Variational and related methods for the overall properties of composites. *Adv Appl Mech* 1981;21.
- [10] Hill R. Elastic properties of reinforced solids: some theoretical principles. *J Mech Phys Solids* 1963;11(5):357–72.
- [11] Adams BL, Kalidindi SR, Fullwood D. Microstructure sensitive design for performance optimization. Waltham, MA, USA: Elsevier Science/Butterworth-Heinemann; 2012.

- [12] Rowenhorst DJ, Lewis AC, Spanos G. Three-dimensional analysis of grain topology and interface curvature in a β -titanium alloy. *Acta Mater* 2010;58(16):5511–19.
- [13] Qidwai SM, et al. Estimating response of polycrystalline materials using sets of weighted statistical volume elements (WSVEs). *Acta Mater* 2012;60:5284–99.
- [14] Adams BL, Gao X, Kalidindi SR. Finite approximations to the second-order properties closure in single phase polycrystals. *Acta Mater* 2005;53(13):3563–77.
- [15] Briggs WL, Henson VE. The DFT: an owner's manual for the discrete Fourier transform. Philadelphia, PA: Society for Industrial and Applied Mathematics; 1995.
- [16] Fullwood DT, et al. Microstructure sensitive design for performance optimization. *Prog Mater Sci* 2010;55(6):477–562.
- [17] Al-Harbi HF, Knezevic M, Kalidindi SR. Spectral approaches for the fast computation of yield surfaces and first-order plastic property closures for polycrystalline materials with cubic-triclinic textures. *Comput Mater Continua* 2010;15(2):153–72.
- [18] Knezevic M, Al-Harbi HF, Kalidindi SR. Crystal plasticity simulations using discrete Fourier transforms. *Acta Mater* 2009;57(6):1777–84.
- [19] Torquato S. Random heterogeneous materials. New York, NY: Springer-Verlag; 2002.
- [20] Niezgoda SR, Kalidindi SR. Applications of the phase-coded generalized hough transform to feature detection, analysis, and segmentation of digital microstructures. *CMC-Comput Mater Continua* 2009;14(2):79–97.
- [21] Niezgoda SR, et al. Optimized structure based representative volume element sets reflecting the ensemble averaged 2-point statistics. *Acta Mater* 2010;58:4432–45.
- [22] Fullwood DT, Niezgoda SR, Kalidindi SR. Microstructure reconstructions from 2-point statistics using phase-recovery algorithms. *Acta Mater* 2008;56(5):942–8.
- [23] Fullwood DT, et al. Gradient-based microstructure reconstructions from distributions using fast Fourier transforms. *Mater Sci Eng A Struct Mater* 2008;494(1–2):68–72.
- [24] Kalidindi SR, Niezgoda SR, Salem AA. Microstructure informatics using higher-order statistics and efficient data-mining protocols. *JOM* 2011;63(4):34–41.
- [25] Landi G, Kalidindi SR. Thermo-elastic localization relationships for multi-phase composites. *CMC—Comput Mater Continua* 2010;16(3):273–93.
- [26] Kalidindi SR, et al. A novel framework for building materials knowledge systems. *Comput Mater Continua* 2010;17(2):103–25.
- [27] Landi G, Niezgoda SR, Kalidindi SR. Multi-scale modeling of elastic response of three-dimensional voxel-based microstructure datasets using novel DFT-based knowledge systems. *Acta Mater* 2010;58(7):2716–25.
- [28] Fast T, Niezgoda SR, Kalidindi SR. A new framework for computationally efficient structure–structure evolution linkages to facilitate high-fidelity scale bridging in multi-scale materials models. *Acta Mater* 2011;59(2):699–707.
- [29] Fast T, Kalidindi SR. Formulation and calibration of higher-order elastic localization relationships using the MKS approach. *Acta Mater* 2011;59:4595–605.
- [30] Bunge HJ. Texture analysis in materials science: mathematical methods. London, UK: Butterworths; 1982.

- [31] Proust G, Kalidindi SR. Procedures for construction of anisotropic elastic–plastic property closures for face-centered cubic polycrystals using first-order bounding relations. *J Mech Phys Solids* 2006;54(8):1744–62.
- [32] Wu X, et al. Elastic–plastic property closures for hexagonal close-packed polycrystalline metals using first-order bounding theories. *Acta Mater* 2007; 55(8):2729–37.
- [33] Duvvuru HK, Wu X, Kalidindi SR. Calibration of elastic localization tensors to finite element models: application to cubic polycrystals. *Comput Mater Sci* 2007;41(2):138–44.
- [34] Dong X, et al. Dependence of mechanical properties on crystal orientation of semi-crystalline polyethylene structures. *Polymer* 2014;55(16):4248–57.
- [35] Kalidindi SR, et al. Application of data science tools to molecular dynamics datasets [in preparation].

3

STATISTICAL QUANTIFICATION OF MATERIAL STRUCTURE

In this chapter, we will shift our focus to the rigorous statistical quantification of the material internal structure. In other words, our interest lies in identifying and quantifying local patterns in the internal morphology of the material structure. Towards this end, we will build on the extensible framework presented in Chapter 2 for the discrete representation of the material structure as m_s^n . Although a number of different basis functions may be used to obtain a discretized representation of the material structure (see the discussion at the end of Chapter 2) and the treatment presented in this chapter is generally applicable to any choice of the basis functions, we will limit our discussion in this chapter to the simple indicator basis functions (i.e., simple binning of both the spatial domain and the local state space). We will come back to the use of the more sophisticated basis functions in later chapters. Consequently, in this chapter, m_s^n simply denotes volume fraction of the material local state belonging to the local state bin indexed by n in the spatial bin indexed by s . We will also find it useful to interpret m_s^n as the probability of finding the material local state n in the spatial bin s .

3.1 Spatial Correlations

The interpretation of m_s^n presented thus far allows one to define statistics on the structure representation. Indeed, our interest is not so much in any one instantiation of the material structure, but more on representing the ensemble of material structures that might have been taken from a given physical sample (or equivalently from an ensemble of samples produced by nominally the same processing or manufacturing route). [Figure 3.1](#) shows an example of such an ensemble of structures, enumerated as $j = 1, 2, \dots, J$. Let the discrete representation of the j th element of this ensemble be denoted as ${}^{(j)}m_s^n$. One can

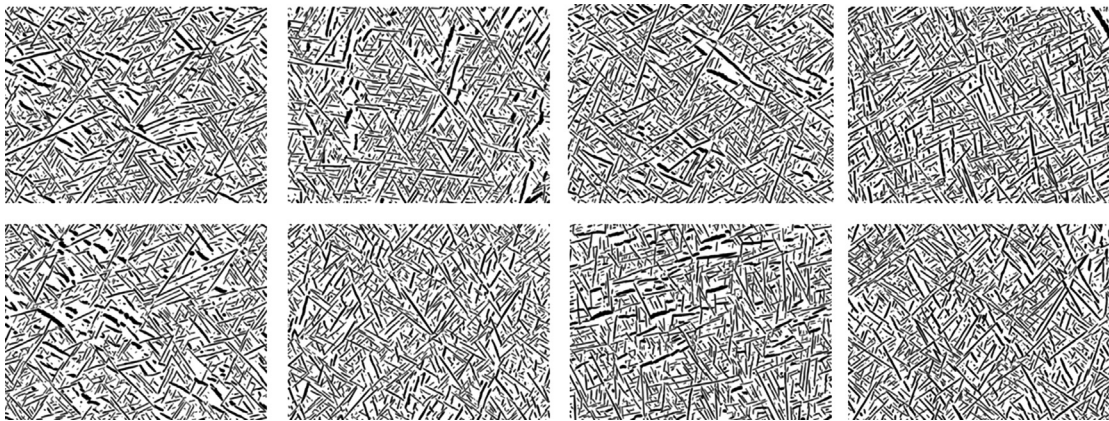


Figure 3.1 An example ensemble of microstructure extracted from samples nominally subjected to the same processing history. Note that there is some variance between the different microstructure elements of this ensemble.

then explore the statistics associated with ${}^{(j)}m_s^n$. For example, one might define a mean (expected value) as

$$f_s^n = \frac{1}{J} \sum_{j=1}^J {}^{(j)}m_s^n \quad (3.1)$$

Deeper reflection on Eq. (3.1) reveals some important features. First, since f_s^n reflects the expected value of m_s^n in the ensemble, and because of the specific meaning associated with m_s^n (discussed in Chapter 2), it should be clear that f_s^n is essentially the overall volume fraction of local states identified as n in the material internal structure. It is important to recognize that this physical interpretation of f_s^n was made possible because of the way we defined m_s^n in Chapter 2. Second, the value of f_s^n should be independent of s , if the material structure is *statistically homogeneous*. Indeed the independence of all averaged structure measures such as f_s^n on the spatial location s constitutes the definition of statistical homogeneity. In Chapter 2, we had previously assumed that the material hierarchical structure of interest exhibits well separated salient length (or structure) scales. We now further assume that the material structure exhibits statistical homogeneity at each salient length scale of interest. Invoking statistical homogeneity allows us to simply drop the spatial variable in the representation of the structure metric, i.e., we can replace f_s^n with just f^n with impunity. With this change, f^n can now be interpreted as the expected value of m_s^n in any arbitrarily selected spatial bin

in the material structure. Consequently, Eq. (3.1) can now be cast as

$$f^n = \frac{1}{S} \sum_s \sum_{j=1}^J {}^{(j)}m_s^n \quad (3.2)$$

In Eq. (3.2), S denotes the total number of spatial bins. Remember that the index s is treated here as a vector index (see the discussion at the end of Chapter 2). Most importantly, Eq. (3.2) introduces f^n as a *1-point spatial correlation* (or simply a *1-point statistic*). This is because this structure measure gives us information on what we might expect to see at any one randomly selected spatial bin in the material structure. Therefore, this particular structure metric is the most basic of all structure measures we can envision, and actually does not carry any information whatsoever on the relative spatial placement of local states in the material internal structure.

As a natural extension to the concept described above, one can start thinking of correlations between two arbitrarily placed points in the microstructure that are conditionally separated by a specified vector, r . Since we have already switched to a discrete representation of the microstructure, it should be noted that the vector r here is a vector index (allowed to take only integer values for its vectorial components). In other words, r indexes the vector space used to define the spatial correlations. Indeed, indices s and r share many common features. The main difference is that while the index s enumerates each of the spatial bins, the index r enumerates the vectors that can be thrown into the discretized microstructure (essentially as a difference between any two values of s). In other words, s indexes the discretized points in the microstructure and r enumerates the corresponding discretized vectors that can be thrown into the same microstructure (Figure 3.2).

Using the notation introduced above, one might define a mean (expected value) of a spatial correlation of two points separated by a vector index r as

$$f_{rs}^{np} = \frac{1}{J} \sum_{j=1}^J {}^{(j)}m_s^n {}^{(j)}m_{s+r}^p \quad (3.3)$$

If we stay with the simple interpretation of m_s^n (as volume fraction of local state n in spatial bin s), it should be clear that f_{rs}^{np} reflects the conditional probability of finding local state n at spatial bin s while simultaneously finding local state p at spatial bin $s+r$. As before, if we invoke statistical homogeneity of the microstructures studied, we can convince ourselves that f_{rs}^{np}

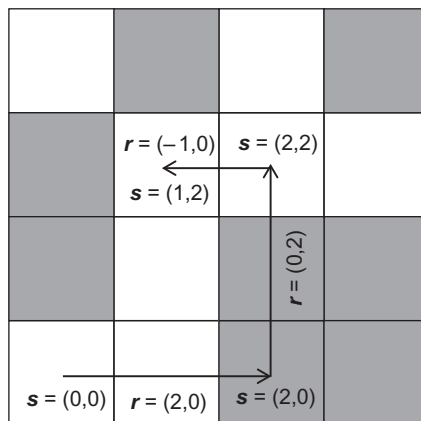


Figure 3.2 Illustration of the s and r indices used to label the discretized spatial bins and the corresponding discretized vector space. Note that both these indices are vector indices. See also Figure 2.10 for the indexing of spatial bins.

should be independent of s (provided we take an average over a sufficiently large ensemble of microstructures). In other words, we can simply drop the spatial variable in the representation of the structure metric, and define a *2-point spatial correlation* (or simply a *2-point statistic*) as

$$f_r^{np} = \frac{1}{S_r J} \sum_s \sum_{j=1}^J {}^{(j)}m_s^n {}^{(j)}m_{s+r}^p \quad (3.4)$$

In Eq. (3.4), we introduce the symbol S_r to denote the number of spatial bins that allow the placement of both s and $s+r$ with the microstructure element being studied. If the microstructure is assumed to be periodic, then $S_r = S$. If the microstructure is not assumed to be periodic, $S_r \leq S$. As a simple example, let S_1 , S_2 , and S_3 (i.e., $S = S_1 S_2 S_3$) denote the number of spatial bins in the three orthogonal reference directions of a rectangular parallelepiped microstructure element. Let $r = r_1 i + r_2 j + r_3 k$ provide the vectorial representation of the index r . Then, it would be easy to see that $S_r = (S_1 - |r_1|)(S_2 - |r_2|)(S_3 - |r_3|)$. Equation (3.4) further assumed that all microstructure elements had the same number of spatial bins (i.e., S was the same for all J microstructure elements). If this is not the case, the normalization factor used in Eq. (3.4) needs a suitable correction. One simple way to interpret Eq. (3.4) is to recognize that $S_r J$ denotes the total number of times the trials are conducted (where each trial denotes checking what local states exist at spatial bins marked s and $s+r$) and $\sum_s \sum_{j=1}^J {}^{(j)}m_s^n {}^{(j)}m_{s+r}^p$ is simply the number of trials

that were successful in finding the selected local states n and p at the two bins, respectively. Recognizing this allows one to make the needed corrections to Eq. (3.4) for different situations.

The structure metrics defined by Eq. (3.4) were called 2-point spatial correlations as they provide correlations between two points related by a fixed vector. Therefore, they can be interpreted as conditional probabilities. The 2-point correlations are the lowest order spatial measures of the microstructure that contain information regarding the relative internal placement of local states. It is also pointed out that the lower order correlations are generally embedded in the higher order correlations. For example, if one were to examine the 2-point correlations for the special case of $\mathbf{r} = \mathbf{0}$, one should be able to recover the 1-point correlations. More precise connections between these will be formulated later.

One can easily extend the concept described above to n -point spatial correlations through the placement of an n -vertex polyhedra. For example, 3-point correlations could be denoted as f_{rt}^{npq} and capture the conditional probability of simultaneously finding local state n at a randomly selected spatial bin s , local state p at the spatial bin $s + r$, and local state q at the spatial bin $s + t$. The three points involved in this definition can be visualized as a triangle. Consequently, the complete set of 3-point correlations would explore the placement of all triangles of all shapes and sizes in the material internal structure. One can therefore extend these concepts to visualize the extraction of a complete set of n -point correlations through the use of n -vertex polyhedra of all shapes and sizes. However, it is also clear that the complete set of n -point correlations for a composite material system with a large number of local states forms a vast and unwieldy data set containing a large amount of redundant information.

In an effort to understand these redundancies, let us first focus on 2-point correlations. If a 3-D microstructure of interest comprises N distinct local states, the complete set of its 2-point correlations contains N^2 correlations for each value of the three-dimensional (3-D) vector index \mathbf{r} . The full set of correlations is conveniently visualized as an $N \times N$ array:

$$f_r^{np} = \begin{bmatrix} f_r^{11} & \cdots & f_r^{1N} \\ \vdots & \ddots & \vdots \\ f_r^{N1} & \cdots & f_r^{NN} \end{bmatrix} \quad (3.5)$$

It has long been known that this set exhibits many interdependencies. Simple reflection on the definition of the

2-point correlations shown in Eq. (3.4) reveals the following redundancies:

$$f_r^{np} = f_{-r}^{pn}, \quad \sum_{p=1}^N f_r^{np} = f^n \quad (3.6)$$

The first redundancy in Eq. (3.6) simply states that the probability of finding ordered local states n and p in two spatial bins separated by r is the same as finding the same local states in the reverse order in two spatial bins separated by $-r$. The second redundancy implies that we sum up the row (an equivalent relation can be derived for summing up a column) of the correlations in Eq. (3.5) and we would recover the corresponding 1-point correlations (i.e., volume fractions). This can be easily reconciled by interpreting the sum of the row as the probability of finding the local state n in the first spatial bin and finding any local state in the second spatial bin. This redundancy also explicitly connects the 2-point correlations and the 1-point correlations. In other words, the information on the 1-point correlations is actually embedded in the 2-point correlations.

Using the simple redundancies expressed in Eq. (3.6), Frisch and Stillinger [1] showed that only one of the four correlations is independent for a two-phase material (i.e., if f_r^{11} is known then f_r^{12} , f_r^{21} , and f_r^{22} can be calculated). For the more general case, Gokhale et al. [2] showed that at most $\frac{1}{2}(N(N - 1))$ correlations are independent for a material system comprised of N distinct local states.

It is generally expected that there are more redundancies between the 2-point correlations than those expressed in Eq. (3.6). In order to identify these inherent redundancies, we need to exploit some of the advantages of the discrete Fourier transforms (DFTs) discussed in Chapter 2. In doing so, we have no choice but to assume that the microstructure element being studied exhibits periodicity. We will discuss later the implications of this assumption on the results derived using the DFTs. Exploiting the known properties of DFTs, Niezgoda et al. [3] demonstrate that the number of independent correlations is only $N - 1$. One can intuitively reconcile with this result by noting that the total degrees of freedom in the discretized microstructure function is $S(N - 1)$. Since the 2-point statistics are a derived quantity, the number of degrees of freedom must be less than or equal to that of the microstructure function. Since each correlation has S independent terms, only $(N - 1)$ correlations can be independent.

[Equation \(3.4\)](#) is particularly amenable to efficient computation using DFTs (see Chapter 2). The complex-valued DFT of the discretized microstructure function can be expressed as

$$M_{\mathbf{k}}^n = \Im(m_s^n) = \sum_{s=0}^{S-1} m_s^n e^{2\pi i s \cdot \mathbf{k}/S} = |M_{\mathbf{k}}^n| e^{i\theta_{\mathbf{k}}^n} \quad (3.7)$$

In [Eq. \(3.7\)](#), we have also dropped the use of the left superscript (j) to refer to a specific microstructure element (see [Eqs. \(3.1\)–\(3.4\)](#)). The derivation below applies to any single element of the microstructure ensemble, and therefore we do not need the superscript (j). The term $|M_{\mathbf{k}}^n|$ will be referred to as the amplitude of the DFT and $\theta_{\mathbf{k}}^n$ will be referred to as the phase of the DFT. Taking advantage of well-known properties of DFTs, the DFT representation of the set of 2-point statistics (f_r^{np}) can be expressed as (applying [Eq. \(2.23\)](#) on [Eq. \(3.4\)](#))

$$F_{\mathbf{k}}^{np} = \Im(f_r^{np}) = \frac{1}{S} M_{\mathbf{k}}^{n*} M_{\mathbf{k}}^p = \frac{1}{S} |M_{\mathbf{k}}^n| |M_{\mathbf{k}}^p| e^{-i\theta_{\mathbf{k}}^n} e^{i\theta_{\mathbf{k}}^p} \quad (3.8)$$

where $M_{\mathbf{k}}^{n*}$ denotes the complex conjugate of $M_{\mathbf{k}}^n$, and we have implicitly invoked the assumption of periodic microstructure (i.e., take $S_r = S$). Note specifically the use of a multidimensional integer array for \mathbf{k} introduced in Chapter 2 (see [Eq. \(2.26\)](#)). The set of correlations corresponding to $n = p$ in [Eq. \(3.8\)](#) are called the autocorrelations, while the others are called cross-correlations. The autocorrelations are real valued even functions (i.e., $f_r^{nn} = f_{-r}^{nn}$; cf. [Eq. \(3.6\)](#)), and therefore their DFTs are also real valued. The DFTs of the cross-correlations are generally complex-valued. Since all f_r^{np} are real valued, an implicit redundancy in their DFTs may be expressed as

$$F_{\mathbf{k}}^{np} = F_{(S-1)-\mathbf{k}}^{np*} \quad (3.9)$$

for all $\mathbf{k} \neq \mathbf{0}$. In other words, about one half of the DFTs are simply complex conjugates of the other half.

From [Eq. \(3.7\)](#), we can see that M_0^n is real valued and is simply equal to Sf^n , where f^n is the 1-point correlation (i.e., volume fraction of local state n in the microstructure). Consequently, one can derive the following requirements from [Eq. \(3.8\)](#):

$$F_{\mathbf{0}}^{np} = Sf^n f^p, \quad 0 \leq F_{\mathbf{0}}^{np} \leq S, \quad |F_{\mathbf{k}}^{np}| \leq S^2 \quad (3.10)$$

In order to rigorously derive the redundancies between the 2-point correlations, we start by recognizing that the

requirement $f_r^{np} = f_r^{pn}$ (Eq. (3.6)) translates in the DFT representations to

$$F_{\mathbf{k}}^{np} = \frac{1}{S} |M_{\mathbf{k}}^n| |M_{\mathbf{k}}^p| e^{-i\theta_{\mathbf{k}}^n} e^{i\theta_{\mathbf{k}}^p} = F_{\mathbf{k}}^{pn^*} \quad (3.11)$$

Next, we recognize that the product of two of the DFTs of the 2-point correlations exhibits the following property:

$$F_{\mathbf{k}}^{np} F_{\mathbf{k}}^{pq} = \frac{1}{S^2} |M_{\mathbf{k}}^p| |M_{\mathbf{k}}^q| |M_{\mathbf{k}}^n| e^{-i\theta_{\mathbf{k}}^n} |M_{\mathbf{k}}^q| e^{i\theta_{\mathbf{k}}^q} = F_{\mathbf{k}}^{pp} F_{\mathbf{k}}^{nq} \quad (3.12)$$

Using Eqs. (3.11) and (3.12), we can derive the desired result as

$$F_{\mathbf{k}}^{nq} = \frac{F_{\mathbf{k}}^{pn^*} F_{\mathbf{k}}^{pq}}{F_{\mathbf{k}}^{pp}} \quad (3.13)$$

Equation (3.13) is an important result from the work of Niezgoda et al. [3]. This equation implies that if $F_{\mathbf{k}}^{pn}$ (and by extension f_r^{pn}) are known for any one choice of p and all n or vice versa (i.e., either a column or a row in the array in Eq. (3.5) is known), then all of the other correlations can be calculated.

The $\sum_{p=1}^N f_r^{np} = f^n$ requirement expressed in Eq. (3.6) translates to the following requirements in the DFT representations (while making use of Eq. (3.10)):

$$\sum_{p=1}^N F_{\mathbf{k}}^{np} = \begin{cases} Sf^n = \sqrt{SF_{\mathbf{0}}^{nn}}, & \text{if } \mathbf{k} = \mathbf{0} \\ 0, & \text{if } \mathbf{k} \neq \mathbf{0} \end{cases} \quad (3.14)$$

The combination of Eqs. (3.13) and (3.14) now proves the claim made by Niezgoda et al. [3] that only $(N-1)$ correlations are independent.

It is noted that additional relations can be derived for eigen microstructures, where m_s^n are only allowed to take values of either 0 or 1. These have also been summarized by Niezgoda et al. [3] as

$$f_{\mathbf{0}}^{np} = \begin{cases} f^n, & \text{if } n = p \\ 0, & \text{if } n \neq p \end{cases} \quad (3.15)$$

$$\sum_{\mathbf{k}} F_{\mathbf{k}}^{np} = \begin{cases} \sqrt{SF_{\mathbf{0}}^{nn}}, & \text{if } n = p \\ 0, & \text{if } n \neq p \end{cases} \quad (3.16)$$

Equation (3.16) can be derived using Eq. (2.19) and recognizing that $\frac{1}{S} \sum_s (m_s^n)^2 = f^n$ and $\frac{1}{S} \sum_s (m_s^n + m_s^p)^2 = f^n + f^p$ for the eigen microstructures.

The reader should note that all of the ideas presented above can be extended to higher order spatial correlations [4].

3.2 Computation and Visualization of 2-Point Spatial Correlations

We now shift our focus and attention to the actual computations involved and the visualization of spatial correlations. We once again focus on 2-point statistics and hope the reader can make the necessary extensions for the higher order statistics. The computation of f_r^{np} directly from Eq. (3.4) for a specified combination of n and p essentially requires $O(S^2)$ (i.e., of the order of S^2) computations ($O(S)$ for each value of r and there are $O(S)$ different values of r). Such calculations are generally very expensive and are not easily scalable for datasets with high values of S . As mentioned earlier, our research group has recently demonstrated that these computations can be accomplished at $O(S \log S)$ using DFTs [3,5] (which allow the use of fast Fourier transform (FFT) algorithms) in very clever ways. One of the main benefits of these novel computational schemes is their excellent scalability to large microstructure datasets. We present below several variants of the DFT-based computational strategies and illustrate them with simple case studies.

The reader is reminded again that the computation of the spatial correlations can be interpreted in a simple manner by recognizing that the denominator represents the total number of trials conducted, while the numerator counts the number of successes (cf. Eq. (3.4) and its discussion). For the simplest case, where we assume the microstructure to be periodic, Eq. (3.8) provides the most computationally efficient strategy that takes full advantage of the FFT algorithm. As noted earlier, with the assumption of periodicity, S_r in Eq. (3.4) can be taken to be the same as S (the number of spatial bins used to describe the microstructure). This is because every spatial bin in the microstructure can be used to place the tail (or equivalently the head) of the vector in evaluating the 2-point statistics. Making use of Eq. (3.8), the computation of the 2-point statistics is reduced to computing the DFT of m_s^n , performing requisite products in the frequency space (where they are fully uncoupled), and performing an inverse DFT. For plotting the 2-point statistics, the most intuitive visualizations of 2-point statistics would result if $r = \mathbf{0}$ lies in the center of plot. This shift is accomplished trivially by making use of the periodicity implied in the DFT-based computations, as discussed next.

To further elaborate on the need to shift the 2-point statistics for better visualization, it is important to first recognize that the mathematical equations describing the DFTs are most conveniently expressed when enumerated from zero (see Eqs. (2.17) and (2.18)). Therefore, it is most beneficial to enumerate the spatial bins of the microstructure as $s = 0, 1, \dots, S - 1$ and to enumerate the vector space bins as $r = 0, 1, \dots, S - 1$. The reader is reminded that both s and r are expected to be multidimensional integer arrays in most applications of these protocols. Most importantly, the 2-point statistics computed using the strategy described in Eq. (3.8) are automatically enumerated $r = 0, 1, \dots, S - 1$. However, the most intuitive visualizations of 2-point statistics would result if $r = 0$ lies in the center of plot (Figure 3.3). Consequently, in presenting the 2-point statistics, it is customary (we will follow this practice throughout this book) to use the range $r = -(S - 1)/2, \dots, -1, 0, 1, \dots, (S - 1)/2$ (the range is adjusted to $r = -S/2, \dots, -1, 0, 1, \dots, S/2$ when S is even). This shift in range is accomplished trivially by making use of the periodicity implied (assumed) for all the functions involved (i.e., $m_s^n = m_{s+S}^n$, $f_r^{np} = f_{r+S}^{np}$). It is also pointed again that the indices used can themselves be arrays. Indeed, for the two-dimensional (2-D) microstructure shown in Figure 3.3, it is

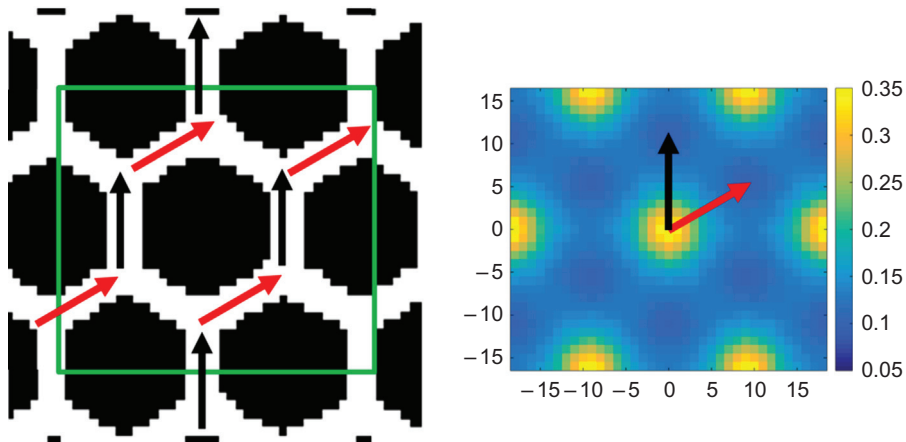


Figure 3.3 (Left) An example microstructure, shown in the green box in the center, which is extended beyond its boundaries by invoking periodicity. Note that this extension is only for visualization purposes (i.e., the actual microstructure dataset used in the calculation is confined to the green box). (Right) The 2-point statistics (white–white autocorrelation) plot computed using Eq. (3.8) and shifted for visualization as described in this chapter. In particular, it pointed out that although the number of black and red vectors that would fit within the green box is significantly different, with the invoking of the periodicity, they do actually become the same. As a consequence, the computed autocorrelation exhibits the expected hexagonal symmetry.

most convenient to express the spatial index as $\mathbf{s} = (s_1, s_2)$ and the index for the bins in the vector space as $\mathbf{r} = (r_1, r_2)$.

[Figure 3.3](#) illustrates the simple computations described above for a very simple periodic microstructure. The “honeycomb” eigen microstructure selected for this illustration has only two discrete local states—shown as black or white pixels. As noted earlier, for this case, only one of the autocorrelations is independent. [Figure 3.3](#) also depicts a plot of the computed white–white autocorrelation. The hexagonal symmetry, the feature shape, and the feature spacing are readily apparent in the autocorrelation. Furthermore, the periodicity implied in the use of DFTs resulted in the autocorrelations also exhibiting the same periodicity. Since the microstructure studied in an eigen microstructure, the autocorrelation for the zero vector (at the center of the plot) provides the phase volume fraction.

Let us now shift our attention to the computations of 2-point statistics for microstructures where we do not wish to invoke the periodicity assumption. In fact, this is likely to be the most common situation for all experimentally measured microstructures. For microstructures used in simulations, it is common to impose periodic boundary conditions. In such situations, it is actually more accurate to retain the periodicity assumption in the computations of the spatial correlations.

As a specific example, we will revisit the same structure illustrated earlier, but without invoking the assumption of periodicity. In other words, our interest will be to compute the autocorrelations as defined in [Eq. \(3.4\)](#), while accounting for the fact that $S_r \neq S$. A good strategy for performing these computations in an efficient manner (using FFT algorithms) would be to *pad* the microstructure such that only long vectors (larger than the vectors of interest in computing the 2-point statistics) can wrap around from one edge of the original image to the opposite edge. If we do this, even when the periodic assumption is implicitly invoked in the FFT algorithms, they do not affect the numerator (counts of success) in computing the spatial correlations of interest.

The padding strategy described above is illustrated in [Figure 3.4](#). Let $\mathcal{S} = (S_1, S_2)$ denote the grid of spatial bins in the original 2-D microstructure (shown in the inner green box). The padding now extends the microstructure function to $\tilde{\mathcal{S}} = (S_1 + T_1, S_2 + T_2)$, where $\mathbf{T} = (T_1, T_2)$ identifies the range of the vectors for which the 2-point statistics are to be computed. The reader is cautioned that use of very high values of \mathbf{T} can produce meaningless answers. As an example, if one chooses $\mathbf{T} = (S_1, S_2)$, then one can see that the number of trials

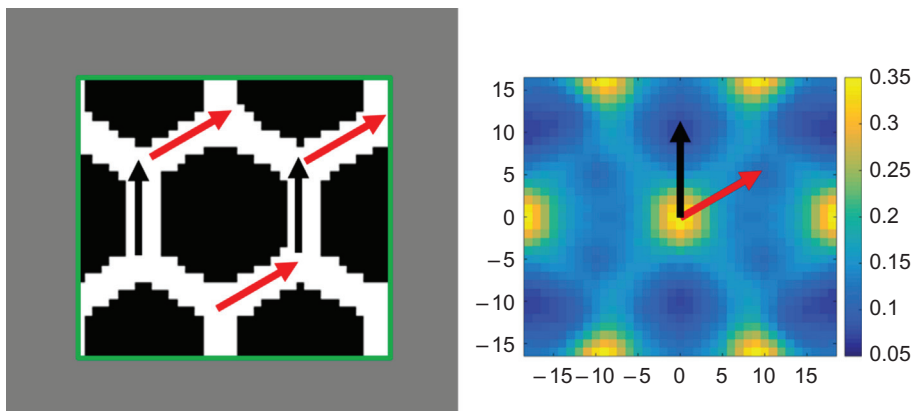


Figure 3.4 Illustration of the computations of 2-point spatial correlations using the padding strategy in order to avoid the periodicity assumption. A comparison of the autocorrelation plot to the one shown earlier in [Figure 3.3](#) indicates significant differences (compare the values corresponding to red and black vectors shown in these figures). These differences are a direct consequence of the assumptions made regarding periodicity in these computations.

conducted for the largest vector in computing the 2-point statistics is just one. Based on our experience, we recommend that $\mathbf{T} < (S_1/2, S_2/2)$. Let the padded microstructure be denoted as \tilde{m}_s^n . Let the corresponding DFT be denoted by $\tilde{M}_k^n = \mathfrak{F}(\tilde{m}_s^n)$. The spatial bins in the padded region of the microstructure may be assigned any of the local states that are not involved in the computation of the desired 2-point statistics. For example, if we are interested in computing f_r^{11} only, then the spatial bins in the padded region can be assigned a local state enumerated by 2 or a completely new local state enumerated by 3 (making the padded microstructure a 3-phase microstructure).

With the padded microstructures, we are now in a position to take advantage of FFT algorithms. Computation of $\mathfrak{F}^{-1}(\tilde{M}_k^{n^*} \tilde{M}_k^p)$ produces an accurate count of the number of successes in finding local states n and p separated by all vectors $\mathbf{r} \leq \mathbf{T}$. In fact, the computation described above produces results even for vectors $\mathbf{r} > \mathbf{T}$, but these results are corrupted by vectors wrapping around the padded region because of the periodicity assumption implicit in the DFT representations. However, since our interest here is exclusively in $\mathbf{r} \leq \mathbf{T}$, we will only take these results from the DFT computation described above. In order to compute the 2-point statistics of interest, we simply need to divide these numbers with a suitable denominator denoting the total number of trials involved; as discussed earlier, this is simply expressed as $(S_1 - |r_1|)(S_2 - |r_2|)$ for a 2-D microstructure. The padding in [Figure 3.4](#) is shown such that it equally envelopes all sides of the

original microstructure. This is just for easy visualization and interpretation. In reality, any placement of the original microstructure inside the overall padded region (i.e., any unequal distribution of the padding as long as the extended microstructure has the same overall size) will produce identical results for the computed 2-point statistics (this is, once again, a consequence of using DFTs).

Figure 3.4 depicts a plot of the f_r^{11} (white–white) autocorrelations that are not tainted by the periodicity assumptions implied in the use of DFTs. A comparison of the autocorrelations in Figures 3.3 and 3.4 reveals important consequences of the assumption of periodicity. For example, the hexagonal symmetry is no longer evident in the autocorrelations computed without invoking periodicity. This is mainly because the different vectors are no longer sampled the exact same number of times. Although this may not be as important when one deals with a very large image, it clearly has an effect for the relatively small image shown in Figure 3.4. In this simple example, one can easily reconcile the different values of the autocorrelations for the red and black vectors depicted in Figure 3.4, by noting that we can indeed place many more red vectors with both endpoints in a white pixel, when compared to the similar placement of the black vectors. It is therefore important to recognize that the assumption of periodicity can indeed influence significantly the computed 2-point statistics, especially when one has a limited number of features in the image.

Note that the strategy described above can be applied selectively in any direction of the image. In other words, one can decide to invoke periodicity assumption in certain directions and employ the padding strategy described above only in rest of the directions.

As an extension of the idea described above, we now demonstrate a general concept of *masks* that can be used advantageously in many situations related to computing the 2-point statistics. In fact, the padding strategy described above can be considered as a special case of using masks. As an example, consider the microstructure in Figure 3.5 which is essentially an extended version of the same microstructure shown in Figures 3.3 and 3.4. However, selected regions of the microstructure have been masked to hide certain irregularly shaped regions where the information is either not available or is of inferior quality (in other words, we do not wish to include that information in the computations of the 2-point statistics). As shown in Figure 3.5, these masked regions can be either on the boundary of the microstructure (e.g., the microstructure is

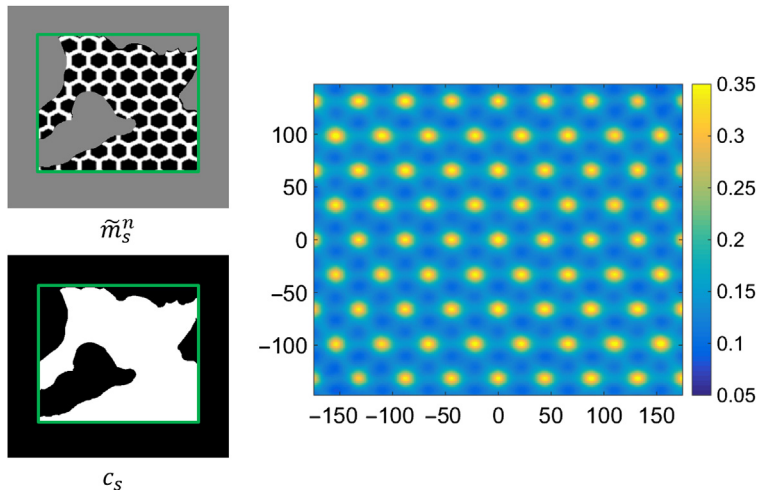


Figure 3.5 Illustration of the masking strategy to compute 2-point statistics for microstructures defined in irregular domains. The green outline box is only for visualization purposes and is not a part of the actual dataset.

measured in an irregular domain) or inside the microstructure (e.g., some regions of the micrograph may not be discernable or reliable). As demonstrated earlier, a mask can also be applied to produce a padded region to impose nonperiodic boundaries (Figure 3.4). In this situation, it is convenient to define two microstructure functions (Figure 3.5): (i) an extended microstructure function denoted as \tilde{m}_s^n , where we have introduced an additional fictitious local state (i.e., the third phase colored gray in Figure 3.5) in the masked region as well as the boundary padded regions, and (ii) a mask function denoted as c_s such that it takes a value of 0 for spatial bins (shown as black) in the masked regions and 1 (shown as white) everywhere else. It is pointed out that the extended \tilde{m}_s^n already contains the information in c_s . However, we choose to carry this information in the redundant manner described above for ease of discussion and computation.

Following the methodology described in the previous example, we compute $\tilde{M}_k^n = \Im(\tilde{m}_s^n)$ and then $\Im^{-1}(\tilde{M}_k^{n^*} \tilde{M}_k^p)$ to accurately count of the number of successes in finding local states n and p separated by all vectors of interest (i.e., the numerator). In order to compute the 2-point statistics of interest, we need to divide these numbers with the total number of trials involved (i.e., the denominator). For the masked microstructures described here, the denominator can be computed easily as $\Im^{-1}(C_k^* C_k)$, where $C_k = \Im(c_s)$. It should be noted once again that the padding scheme described in the previous case study is essentially a special case of the masking protocol described here. The overall

computations for the masked microstructures can be expressed as

$$f_r^{np} = \frac{\Im^{-1}(\tilde{M}_k^{n^*} \tilde{M}_k^p)}{\Im^{-1}(C_k^* C_k)} \quad \forall r \leq T \quad (3.17)$$

[Figure 3.5](#) depicts a plot of the f_r^{11} (white–white) autocorrelations where the computations were limited to the unmasked regions (the white region of the mask) using the computationally efficient DFT-based protocols developed and presented in this paper. Furthermore, there was no assumption of periodicity in this computation. However, it is seen that these autocorrelations are indeed very similar to the ones shown in [Figure 3.3](#) (performed assuming periodicity and limited to a much smaller range of vectors). This provides unambiguous confirmation that the protocols presented here are doing an excellent job of computing the 2-point statistics for irregular domains without invoking periodicity, while taking full advantage of the computational efficiency of the FFT algorithms.

3.3 Higher Order Spatial Correlations

Although much of the discussion above focused on 2-point spatial correlations, it is hoped that the reader can see the potential to extend the protocols to higher order spatial correlations. For example, the 3-point spatial correlations can be expressed as

$$f_{rr'}^{npq} = \frac{1}{S_r} \sum_s m_s^n m_{s+r}^p m_{s+r+r'}^q \quad (3.18)$$

The corresponding DFT representation for a periodic microstructure can be expressed as

$$F_{kk'}^{npq} = \Im(f_{rr'}^{npq}) = \frac{1}{S} M_k^{n^*} M_{k-k'}^p M_{k'}^q \quad M_k^n = \Im(m_s^n) \quad (3.19)$$

It should be apparent from these equations that both the actual number of statistics as well as the number of computations involved increase dramatically for the higher order spatial correlations. One is often interested in a subset of these higher order statistics. In the next chapter, we will explore data-driven approaches to identifying these subsets of salient spatial correlations for adoption as reduced-order measures of the microstructures.

Any specific local geometric pattern of interest in an image can be suitably expressed as a higher order spatial correlation. A particular measure that has gained broad adoption from the materials science community is the chord length distribution (CLD). A chord is defined as any line segment placed in a microstructure such that (i) the entire line segment lies in a selected local state and (ii) the ends of the line segment abut against a different local state. The CLD $p^i(l)$ denotes the probability density of finding a chord of length l within the phase of interest i . Thus, $p^i(l)dl$ provides the probability of finding a chord of length between $l \pm dl/2$ within phase i . One strategy for extracting the CLD is to recover it from another distribution called the lineal path function (LPF) [6,7]. Formally, the LPF, $L^i(l)$, denotes the probability that a line segment of length l thrown randomly into a given microstructure lies entirely within local state i . The main difference with respect to CLD is that the line segment does not have to end at the interfaces. An established relationship between the CLD and the LPF is expressed as [8]

$$p^i(l) = \frac{l_c}{V^i} \frac{d^2 L^i(l)}{dl^2}, \quad l_c = \int_0^\infty l p^i(l) dl \quad (3.20)$$

where V^i is the volume fraction of local state i and l_c is the mean chord length. When CLD and LPF are established using line segments in a prescribed direction, the corresponding distributions are referred to as angularly resolved distributions. Angularly resolved distributions serve as excellent measures of the anisotropy in a given microstructure.

An efficient method was recently presented [9] for calculating the angularly resolved LPF using the generalized Hough transform; in fact this approach is rather versatile and can be employed for automated identification of a large variety of either size-invariant or shape-invariant local geometric features in the microstructure. In short, a segmented image where the phase of interest i is marked by 1s and all other phases are marked by 0s may be convolved with an appropriate kernel filter to provide a map of all locations where a specific vector will lie completely in phase. For example, the filter to calculate $L^i(l=l^*, \theta=\theta^*)$ for a 2-D microstructure can be expressed as

$$\mathcal{O}_{r\theta} = \begin{cases} \frac{1}{r^*} & \text{if } r \leq r^* \text{ and } \theta = \theta^* \\ 0 & \text{otherwise} \end{cases} \quad (3.21)$$

The calculation of CLDs from the LPF is however not the most direct or efficient method. Line scan methods offer certain advantages. As an example, let us pretend that we are interested in the CLD in the horizontal direction on an image. For this case, the most direct way of identifying the chords is to start from one end of the image and simply scan the pixels in the horizontal direction. For each horizontal scan, by suitably starting and ending the count whenever an interface pixel is encountered, we can easily extract the lengths of all chords present in the image. The obvious advantage of a line scan approach is its computational efficiency. The main hurdle is their application to arbitrary directions of interest in an image (i.e., directions not necessarily aligned with the tessellation directions in the image). For this purpose, we have to identify efficient algorithms to either rotate the image or rotate the lines placed into the image.

Bresenham's line drawing algorithm [10] presents a computationally efficient approach for drawing an approximation of a line between two points in an n -dimensional, uniformly pixellated, image. Given the start and endpoint of the line in the image, Bresenham's algorithm determines the pixels lying on the line between these two points using only integer addition, subtraction, and bit shifting. Using only integer arithmetic is not only faster, but more accurate because it avoids the common drawbacks of accumulated floating point error. With Bresenham's algorithm, we can determine the pixels that correspond to a scan line through the image of any orientation. Once we have determined the pixels for a given scan line we can then simply translate this line such that it sweeps through the entire image. The use of translated Bresenham lines for extracting angularly resolved CLDs was demonstrated successfully in a range of applications [11].

3.4 Reconstructions of Microstructures from Spatial Correlations

One of the essential questions raised by the framework of the n -point spatial correlations described above is exactly how many spatial correlations are needed to capture all the details of the microstructure. One way to argue this would be to recognize that there exist only $(N - 1)S$ independent variables in the discretized representation of a microstructure denoted by m_s^n . So there can, in principle, be only $(N - 1)S$ independent spatial correlations defined using m_s^n . Earlier, in this chapter, we have

demonstrated that there indeed are only $(N - 1)$ independent spatial correlation functions (based on properties of the correlation functions in the DFT space). Keeping in mind that there are S variables in each correlation function, we can arrive at $(N - 1)S$ independent spatial correlations simply by choosing a row or column in the matrix of the 2-point spatial correlations shown in Eq. (3.5), and excluding one of the correlation functions in that row or column. Indeed, other combinations of spatial correlations might also serve the same purpose.

One needs to add some caveats to the argument presented above. The relationships derived earlier in this chapter were based on DFTs and therefore implicitly invoked periodicity assumptions. Therefore, it is entirely possible that only the 2-point spatial correlations computed using the periodicity assumptions are the only ones that capture the complete information on the microstructure in the relatively simple manner described above. Proving the relationships for the 2-point spatial correlations computed without using the periodicity assumption is rather messy. It is however clear from the examples presented in the previous section that certain interrelationships exist among the full set of 2-point spatial correlations computed without invoking the periodicity assumption. This is self-evident when one recognizes that the two sets of 2-point spatial correlations computed with and without invoking the periodicity assumptions can be related to each other (as already discussed in the example case studies presented in the previous section).

One simple way to answer the question on the adequacy of any selected subset of spatial correlations is to reconstruct the microstructure using the spatial correlations as the only input and then compare the reconstruction with the original microstructure to see what is missing in the reconstructions. The problem posed above is essentially an inverse problem that can be formulated as the minimization of the sum of the absolute (or squared) differences between the selected subset of targeted spatial correlations and their corresponding values from the reconstruction, subject to the conditions $m_s^n \geq 0$ and $\sum_n m_s^n = 1$.

Most efforts in the literature aimed at microstructure reconstructions from spatial correlations have formulated the problem as the minimization of an objective error function. However, one needs to perform this minimization over a very large number of variables. Note that the number of variables involved in the minimization is $(N - 1)S$ (this is the number of independent variables needed to define m_s^n subject

to $\sum_n m_s^n = 1$). In most practical applications S is fairly large, especially for 3-D microstructures. Consequently, the solution to this minimization problem is not trivial.

A large number of optimization techniques (for the minimization of the error measure between the reconstruction and the target statistics) have been applied to address this problem. These include Monte-Carlo methods [12–17], Gradient-based methods [4], Branch and bound methods [18], and simulated annealing methods [7,19–21]. Most of these approaches are not scalable to reconstructions of microstructures with sufficiently large numbers of spatial bins; large reconstructions are typically needed to establish practically useful 3-D representative volume elements (RVEs) of the material internal structure. Moreover, these approaches are typically hampered by the presence of multiple local minima. Efforts to speed up the optimization algorithms have explored the use of various techniques to update the 2-point statistics for specified perturbations in the trial function (rather than recalculate the complete set each time) [7,19,21], and confining the search to microstructures of a selected form, such as those defined using Gaussian random fields (GRFs).

In the digital signal processing field, phase recovery algorithms have been successfully developed and applied for rapid reconstruction of images/signals in various applications [22–24] from their correlation functions. These approaches are particularly well suited to taking advantage of the discretized representation of the microstructure function presented in this book, as well as the fast computation of the 2-point statistics using FFT algorithms presented earlier. One important idealization in the reconstructions comes from limiting them to eigen microstructures [25]. As mentioned earlier, m_s^n for these microstructures take values of 0 or 1. Although this sounds like a major limitation, it is not really that limiting. Philosophically, one may think of all non-eigen microstructures as being eigen microstructures at a finer discretization level; i.e., if one were to refine the spatial grid sufficiently one would eventually arrive at local neighborhoods that only contained a single distinct local state. Another way to look at this is to recognize that all non-eigen microstructures will naturally convert to eigen microstructures when we adopt a sufficiently fine binning of the local state space.

It is also important to recognize that the 2-point statistics described above automatically filter out translations and inversions of the microstructure. In other words, microstructure functions m_s^n and $m_{\pm s+a}^n$ (where a is an arbitrarily selected

index) produce identical sets of 2-point statistics (when computed using the DFT methods using periodic boundary assumptions). Therefore, any reconstruction from a given set of 2-point statistics can at best recover the original microstructure to within an arbitrary translation and/or an inversion.

For a microstructure with two phases, as noted earlier, the autocorrelation of one of the local states is the only independent correlation. From Eq. (3.8), one can see that it is fairly straightforward to compute the amplitude of the DFT of the microstructure function using

$$F_k^{nn} = \frac{1}{S} M_k^n M_k^{n*} = \frac{1}{S} |M_k^n|^2 \quad (3.22)$$

For a microstructure with multiple phases, Eq. (3.22) can be applied to each local state separately to compute the amplitudes of the DFT of the microstructure functions for all the local states. So the main challenge left is really recovering the phases of the DFT of the microstructure function for each local state. Consequently, the algorithms that focus on this problem are often referred to as the phase recovery algorithms [23,24,26–29].

In a typical phase recovery algorithm, $|M_k^n|$ are computed directly from the known 2-point statistics using Eq. (3.22). Following this, one starts with a guess of the microstructure. For convenience, let us identify the local state with the highest volume fraction as $n = 1$ (this can be accomplished simply by comparing the values of F_0^{nn} ; see Eq. (3.10)). The phase of M_k^1 is then taken from the guess of the microstructure. The phase of the other DFTs of the microstructure function can be computed using Eq. (3.8) as

$$e^{i\theta_k^p} = \frac{SF_k^{1p} e^{i\theta_k^n}}{|M_k^1||M_k^p|} \quad (3.23)$$

With the phases of the DFTs computed, one can reconstruct (essentially compute an inverse DFT) an improvement over the guessed microstructure, make necessary corrections to this improved guess (ensuring that $m_s^n \geq 0$ and $\sum_n m_s^n = 1$), and repeat the whole process again in an iterative scheme until one reaches convergence in the error (defined as the sum of the square of the difference between the target 2-point statistics and those of the reconstructed microstructure). It is generally observed that convergence is attained much more easily for eigen microstructures (i.e., m_s^n takes values of either 0 or 1) when compared to non-eigen microstructures. Various examples of the usage of this algorithm can be seen in Ref. [5].

3.5 Reconstructions from Partial Sets of 2-Point Statistics

Although the previous section describes a computationally efficient approach for the reconstruction of the microstructures from a complete knowledge of their 2-point spatial correlations, there are very few practical applications in materials science problems demanding the use of these protocols. This is because it is probably much harder to establish the full set of 2-point spatial correlations directly from experiments without actually characterizing 3-D microstructure datasets. Indeed, most commonly employed methods of microstructure characterization result in 2-D sampling of the inherently 3-D microstructure.

Recent years have witnessed tremendous advances in 3-D microstructure (and 4-D (four dimensional) when including information on time evolution) characterization, which have involved the use of automated serial sectioning combined with surface (2-D) scanning using suitable microscopy techniques [30–34] or high energy X-rays combined with computed tomography [35–42]. All of the 3-D material structure characterization techniques mentioned above require the use of highly specialized equipment and incur inordinate effort and cost. Moreover, the volumes of materials studied using some of these approaches are often very limited, which raise critical questions on their adequacy for statistically meaningful representation of the material structure.

A central premise of this book is that one should be seeking a statistical description of the material internal structure, as opposed to a fully deterministic description, especially for establishing reliable process–structure–property (PSP) linkages. In other words, any representation of an ensemble of microstructures has to be necessarily statistical in nature, i.e., it should facilitate a description of the average 3-D microstructure as well as its distribution within the sample [43–50].

Indeed, when the focus is shifted from a deterministic description of the material microstructure to a statistical description, it dramatically reduces the cost involved. This is because it is significantly easier and cheaper to extract 3-D statistics of the microstructure, as opposed to mapping out the complete 3-D internal structure of a selected subvolume in the material structure. The need for an inordinate effort in mapping the complete 3-D material structure arises largely from the requirement to precisely cross-register measurements from multiple 2-D planes into a single contiguous 3-D volume.

However, if one were able to extract statistical measures on 2-D planes, they can be trivially combined (or assembled) into 3-D statistics. Furthermore, collecting and assembling 3-D statistics from 2-D scans allow for examination of much larger material domains (i.e., large scan areas) at relatively low cost (both time and effort). Consequently, the acquired statistics are much more reliable and meaningful than those acquired from the fairly limited volumes investigated in direct 3-D mapping of the microstructure. This concept was explored extensively by Adams et al. [47,51,52], who have demonstrated that it is much easier to recover relevant microstructure statistics in 3-D in polycrystalline samples, when compared to the effort involved in measuring the material structure in 3-D contiguous volumes in the same class of samples [32,53–56]. These authors have also demonstrated that it is often possible to recover higher order distribution functions quantifying the material structure in 3-D using information gathered on 2-D sections using theories from stereology [57,58]. It is noted that these prior efforts were focused on collecting the 3-D microstructure statistics and using them directly to predict the macroscale properties of interest; there was no effort aimed at reconstructing a 3-D material microstructure from the assembled 3-D microstructure statistics.

It is sometimes useful to actually reconstruct an RVE from the 3-D microstructure statistics, especially for predictions of properties using numerical simulation tools (e.g., micromechanical finite element model). Unlike the homogenization theories that only require specification of the relevant microstructure statistics, the use of numerical tools such as the micromechanical finite element models requires the specification of the RVE as a 3-D microstructure. The difficulty associated with microstructure reconstructions from statistics depends on exactly what microstructure statistics are being used to drive the reconstructions. As a trivial example, if the microstructure statistics of interest are restricted to only the volume fractions of the constituent phases (also called 1-point spatial correlations), it is very easy to produce reconstructions that exhibit the specified microstructure statistics. In other words, such a simple specification typically results in a very large number of potential solutions. At the other end of the spectrum, it is also easy to see that specification of a very large number of microstructure statistics (e.g., involving multiple sets of higher order spatial correlations such as the n -point statistics [2,3,43,47,49,59–65]) will render the microstructure reconstruction in a specified single (finite) volumetric

domain without any potential solutions. Note that the reconstruction problem described above is essentially an inverse problem, and the features described above are typical of such problems.

Our interest in this section will be limited to reconstructions that aim to capture a prescribed partial set of measured higher order spatial correlations. Most prior efforts aimed at microstructure reconstructions from measured spatial correlations have employed various variants of the Monte-Carlo methods [12–17]. The general approach in these methods is to start from an initialization of spatial cells in the reconstruction (nucleation) and then guide the distribution and growth of those cells via minimization of some objective error function (typically formulated as a measure of the difference between the measured spatial correlations and those of the reconstructed microstructure).

In recent years, the field of computer graphics has successfully developed and implemented a set of algorithms that are aimed at problems that are very similar to the microstructure reconstruction problem described above. This new area, called solid texture synthesis [66], has adopted the term texture map (or simply texture¹) to refer to a color image that is applied to 3-D graphical objects to give them a more complex and real appearance. These textures are most commonly 2-D images that are mapped or interpolated across the surface of the 3-D object. However, when it is necessary to show the internal structure of a 3-D object with texture, a 3-D image or solid texture is needed. Solid texture synthesis algorithms are being used to create realistic 3-D images by utilizing 2-D exemplar textures (obtained when viewing the 3-D object from a particular direction). In other words, the 3-D solid texture is being reconstructed so that it will statistically resemble the expected 2-D exemplar texture when cut along any plane of a specified orientation; these algorithms can therefore be very valuable in addressing the microstructure reconstruction problem described earlier (see [Figure 3.6](#)).

One of the most computationally effective solid texture synthesis algorithms in the literature is an optimization-based approach presented by Kopf et al. [68]. The algorithm's inputs are a set of three input images that represent the desired appearance of the solid texture when cut anywhere along three orthogonal planes. The algorithm alternates between

¹Note that the use of the word texture in computer graphics is completely unrelated to the use of the same word in metallurgical practice.

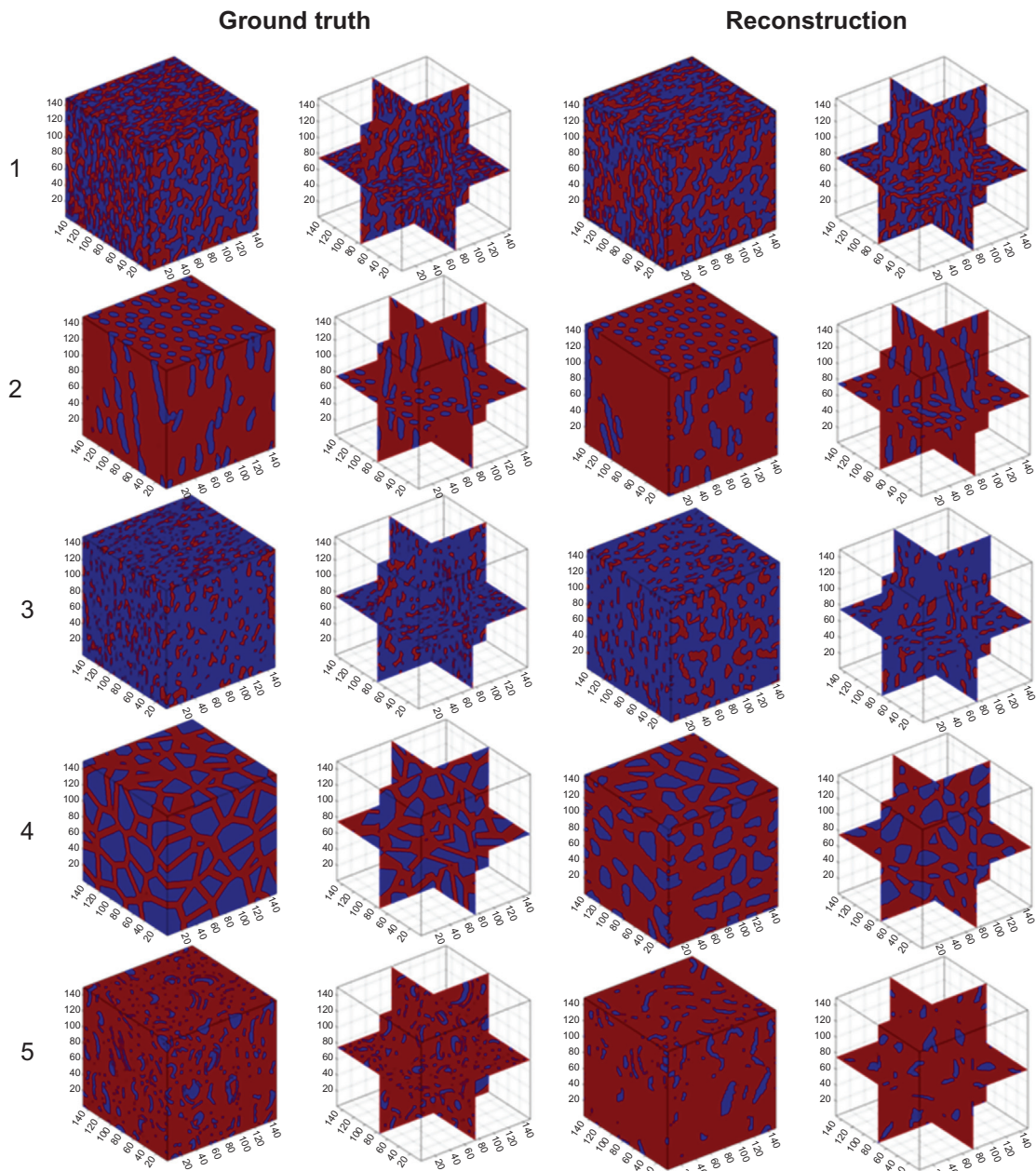


Figure 3.6 Examples of 3-D microstructure reconstructions demonstrated using a modified version of the solid texture synthesis approaches. Taken from Ref. [67].

search and optimization steps until the solid texture converges. The search step is relatively simple. The neighborhood of every pixel in the current iteration's solid texture is examined, and the three best matching neighborhoods from the exemplar input images are found. A neighborhood is defined as a small square region of pixels centered on a certain voxel. Since the algorithm's input is three orthogonal 2-D slices, we are only concerned with the three corresponding orthogonal neighborhoods centered on each voxel. The optimization step proceeds by assigning each pixel a value that minimizes the error between all best matching neighborhoods for which the pixel is involved.

At this point, it is useful to compare and contrast the texture synthesis algorithms and the Monte-Carlo based microstructure reconstruction algorithms. Although both algorithms target minimization of the error, they pursue dramatically different strategies. The search in the texture synthesis algorithms is restricted to the set of neighborhood exemplars taken directly from the measurements, whereas the Monte-Carlo methods do not impose any such restrictions. Although the term spatial correlation is not explicitly mentioned in the texture synthesis algorithms, it should be noted that each neighborhood exemplar carries information on higher order spatial correlations. In fact, if the neighborhoods are quantified by an $N \times N$ spatial grid, each exemplar actually represents an unbiased outcome in the evaluation of a specific N^2 -spatial correlation. Since each exemplar simply represents a potential outcome, it is important to sample correctly from all of the available exemplars; this is accomplished in the optimization step by seeking selected overall (global) microstructure statistics in the reconstruction. This strategy of balancing between local and global considerations in the iterative search and optimization steps, respectively, is the central distinctive feature of the highly successful solid texture synthesis algorithms. Towards this goal, Kopf et al. [68] present reweighting schemes which drive the reconstruction towards a compromise between the local and global requirements. Another more recent approach [69] uses a dual approach of position and neighborhood histogram matching. More specifically, a record is kept between iterations of which pixels and neighborhoods from the exemplars are copied to the reconstruction. The optimization weights are adjusted so that the exemplar images are sampled uniformly.

The Kopf et al. algorithm has recently been successfully demonstrated for microstructure reconstruction problems [67].

3.6 Representative Microstructures

We started this chapter by talking about microstructure statistics. Now that we have established a framework for computing spatial correlations and the associated statistics, we will briefly revisit the topic of microstructure statistics. Let $\{^{(j)}m_s^n; j = 1, 2, \dots, J\}$ denote an ensemble of microstructures extracted from samples subjected to nominally the same processing history (cf. [Figure 3.1](#)). It is also assumed here that each microstructure element of this set is of sufficient size. Within the framework of n -point statistics presented in this book, the important length scale to consider in deciding on the size of the microstructure element is the coherence length [7,47], defined as the length beyond which the n -point statistics (obtained on an ensemble of structures taken from a given sample) are completely uncorrelated. This length therefore depends on the specific sample being studied. For example, in a perfectly disordered structure, the coherence length is of the order of the individual spatial bin size. However, perfectly disordered structures are seldom realized in practice. Since one does not *a priori* know the coherence length in a given sample, one needs a few preliminary measurements (e.g., these could be long line scans) to establish the coherence length and then ensure that the scan size is larger than the coherence length of the structure in the given sample. Generally speaking, if the scan sizes are just about the order of the coherence length, one needs to acquire a sufficiently large number of scans in order to establish reliably the variance in the spatial correlations. The general practice in the field, however, has been to obtain very large scans (as large as practically feasible within available resources) and use a small number of these large scans instead of a large number of smaller scans from different locations in the physical sample. This practice is tantamount to subdividing the large scan into smaller regions and treating each smaller scan as an independent measurement (although in reality it is not!). From a statistics viewpoint, the preferred practice would be to obtain a large number of adequately sized scans (each approximately about twice the coherence length) from randomly selected regions in a given set of physical samples.

Once a suitable ensemble of microstructures has been assembled, the most natural question that arises next is if it is possible to identify an RVE that can be used as substitute for the entire ensemble. Instantiations of the RVE are essential to simulate performance characteristics of interest using numerical models. In this context, it is highly desired that the RVE reflects the expected values of the important structure measures (e.g., the spatial correlations deemed to be of import for the selected application). Within the framework of the n -point statistics presented earlier, in order to faithfully capture the material structure, the RVE should reflect as closely as possible the expected values of the salient set of n -point statistics. As an example, it might be desirable to construct an RVE for the ensemble of structures shown in [Figure 3.1](#).

In the framework presented in this book, the goal of an RVE construction essentially reduces to a reconstruction of an RVE from the ensemble-averaged n -point statistics, which are in fact the expected values targeted in the construction of the RVE. The reconstructions discussed in [Section 3.3](#) started with targeted 2-point statistics that actually came from a single microstructure. They may not work well for reconstructions for an ensemble-averaged set of 2-point statistics, as there is no guarantee that a microstructure matching these statistics can be reconstructed in a specified finite sized volume (with a fixed number of spatial bins). Therefore, one should expect this to be a nontrivial problem.

One trivial solution to the RVE construction problem described above is to think of the RVE as an equally weighted representation of all of the members of the selected ensemble of structures. This concept is already implied in [Eq. \(3.4\)](#), where $\frac{1}{j}$ can be considered as the weight. If one were to use this approach, each member of the ensemble would represent an SVE [\[86–89\]](#). In fact, if one were to follow this approach, the size of the SVEs can be significantly smaller than that of the RVE. The use of a set of SVEs of smaller volumes (instead of a single RVE) offers tremendous computational savings, especially when the macroscale properties need to be evaluated using sophisticated physics-based numerical simulations. The main disadvantage of using the equally weighted set of SVEs is simply the fact that one typically needs a fairly large number of SVEs to approximate the RVE [\[76\]](#), especially when SVEs are selected to be of relatively small volumes.

An alternate approach was presented by Niezgoda et al. [50], who introduced the concept of WSVEs. In this approach, the identification of a WSVE is approached as an optimization problem that searches through all weighted combinations of the available SVEs and minimizes the difference between the spatial statistics of the constructed WSVE and the ensemble-averaged spatial statistics from all available SVEs, while being subjected to the following constraints: (i) the number of SVEs used to build the WSVE is limited to the number prescribed by the user and (ii) the weights assigned to the individual members of WSVE have to be positive and sum up to 1. In other words, WSVE approximates the RVE as a set of optimally selected and weighted SVEs (from the available ensemble of SVEs) with the weights essentially representing the volume fractions of the selected SVEs in the RVE (Figure 3.7). Mathematically, the WSVE problem can be expressed as

$$\min_{w_j} \sum_r \left(\langle f_r \rangle - \sum_{j=1}^J w_j f_r^{(j)} \right)^2 \quad (3.24)$$

subject to

$$w_j \geq 0 \text{ for only } \tilde{J} \text{ values of } j; \quad w_j = 0 \text{ for all others}; \quad \sum_{j=1}^J w_j = 1 \quad (3.25)$$

In the above equations, $f_r^{(j)}$ denote the selected set of structure measures extracted from available SVEs enumerated by j , $\langle f_r \rangle$ is the set of ensemble-averaged target structure measures we wish to capture in the RVE, w_j are weights, and \tilde{J} is the number of elements used in the construction of the WSVE set (selected by the user as a number significantly smaller than J). Equations (3.24) and (3.25) can be solved using various nonlinear optimization toolsets [33,46,50]. In the above description, we have generalized $f_r^{(j)}$ to include whatever structure measures are deemed to be important for the problem at hand. These could include any selected subset of n -point spatial correlations combined with any other structure measures (e.g., CLDs). Indeed, these might even be the reduced-order representations of the structure measures discussed in the next chapter.

It was demonstrated that the WSVEs established using the concepts described above automatically approximated well the effective properties associated with the larger structure datasets,

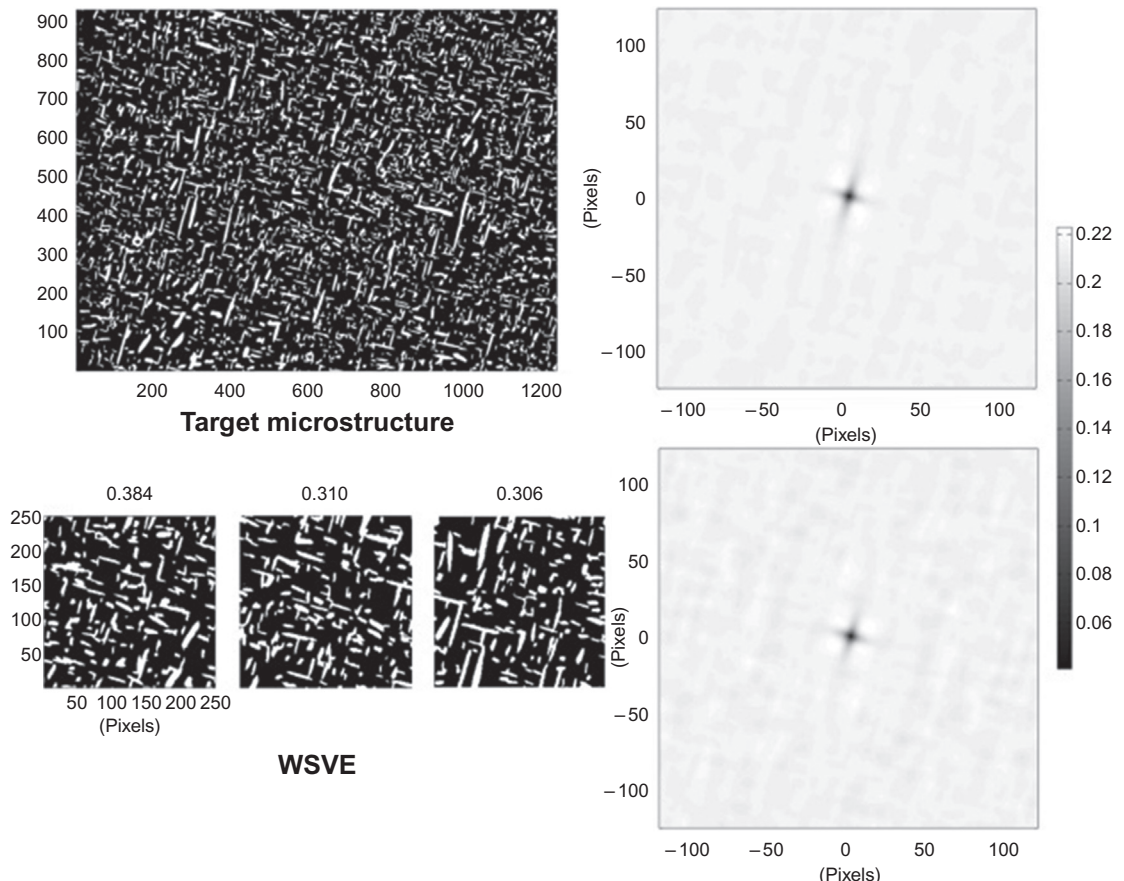


Figure 3.7 Illustration of the construction of a WSVE (weighted set of statistical volume element) set comprised of three weighted optimally selected SVEs (statistical volume elements) for an experimentally characterized precipitate structure [50,85]. The corresponding plots of 2-point statistics are shown on the right.

while providing major computational advantages because of the dramatic reduction in the sizes and numbers of the volume elements [33,46]. This is mainly because the WSVEs efficiently capture the spatial statistics in the ensemble of SVEs (or the RVE). The computational advantages of the WSVEs were particularly impressive when computationally expensive models (e.g., coupled multiscale models, crystal plasticity) were used to estimate the effective properties or performance associated with a given microstructure [46].

A trivial, but very useful in actual practice, application of the concepts described above lies in the reconstruction of a discrete set of crystal lattice orientations from a given orientation

distribution function (ODF). In Chapter 2, the concept of a spatially resolved ODF was introduced (cf. Eq. (2.31)). The one-point distribution function corresponding to this microstructure function is the well-known ODF [47,49,90], which captures the probability density associated with finding a specific orientation of interest in a given polycrystalline sample. As also discussed in Chapter 2, there are many advantages to seeking spectral representations of distributions. For the ODF, the most commonly used spectral representation utilizes generalized spherical harmonics (GSH; cf. Eq. (2.28)). The relationships between the ODF (denoted as $f(g)$) and its GSH coefficients denoted by $F_l^{\mu n}$ can be expressed as (cf. Eq. (2.31))

$$f(g) = \sum_{\mu, n, l} F_l^{\mu n} \dot{T}_l^{\mu n}(g), \quad F_l^{\mu n} = (2l + 1) \int_{FZ} f(g) \dot{T}_l^{\mu n*}(g) dg \quad (3.26)$$

Recognizing that ODF provides only information about the volume fractions of the various orientations present in the polycrystalline sample, we can formulate an alternate mathematical description as [91]

$$f(g) = \sum_{j=1}^J w_j \delta(g - g^{(j)}), \quad w_j \geq 0, \quad \sum_{j=1}^J w_j = 1 \quad (3.27)$$

The Dirac-delta function $\delta(g - g^{(j)})$ in Eq. (3.27) represents the ODF of a single crystal of orientation $g^{(j)}$, and w_j denotes its volume fraction in the polycrystal. The correspondence between the above two representations is important for many practical applications. For example, one often measures a large number of equally weighted discrete (single) orientations in a polycrystalline sample using techniques such as the electron backscattered diffraction (EBSD) and is interested in extracting the ODF. In that situation, Eqs. (3.26) and (3.27) result in

$$F_l^{\mu n} = \frac{1}{J} \sum_{j=1}^J (F_l^{\mu n})^{(j)}, \quad (F_l^{\mu n})^{(j)} = (2l + 1) \dot{T}_l^{\mu n*}(g^{(j)}) \quad (3.28)$$

Once one extracts an ODF, it is sometimes more useful to recover a small set of orientations that effectively represent the same texture. Note that this small set of orientations can be significantly smaller than the actual number of orientation measurements and might be needed to conduct numerical simulations (e.g., using crystal plasticity finite element models [92]). This inverse problem is very similar to the RVE problem

described earlier. As before, one hopes to approach the representative texture in the polycrystalline sample by performing a large number of individual (single crystal) measurements (analogous to getting a very large scan of the microstructure in the sample). One way to recover (or approximate) this representative texture with a finite number of orientations is to simply randomly select orientations from the large set of measurements (this would be akin to the SVE approach described earlier). Alternately, as described earlier, one can also approach the representative texture using a weighted set of orientations as (akin to the WSVE approach described earlier)

$$\min_{w_j} \int_{FZ} \left(f(g) - \sum_{j=1}^J w_j \delta(g - g^{(j)}) \right)^2 dg, \quad w_j \geq 0, \quad \sum_{j=1}^J w_j = 1 \quad (3.29)$$

Just as before, the extraction of a set of representative weighted orientations would entail the selection of specific orientations and then optimizing their weights. Therefore the same strategies and heuristics described above can be applied to this problem as well. In other words, one can first select a special set of single crystal orientations (these are the only ones whose weights are allowed to be non-zero; specifies the set of $g^{(j)}$) of a desired size (this specifies J) based on various heuristics (e.g., dominant peaks in the ODF, histograms of the measured orientations) and then solve the simple optimization problem stated in Eq. (3.29) to obtain the set of weights.

It is also pointed out that Eq. (3.29) can be cast in the GSH space to attain certain computational efficiency (effectively replacing the integral with a summation) as

$$\min_{w_j} \sum_{\mu,n,l} \left| F_l^{\mu n} - \sum_{j=1}^J w_j (F_l^{\mu n})^{(j)} \right|^2, \quad w_j \geq 0, \quad \sum_{j=1}^J w_j = 1 \quad (3.30)$$

References

- [1] Frisch HL, Stillinger FH. Contribution to the statistical geometric basis of radiation scattering. *J Chem Phys* 1963;38(9):2200–7.
- [2] Gokhale AM, Tewari A, Garmestani H. Constraints on microstructural two-point correlation functions. *Scr Mater* 2005;53:989–93.
- [3] Niezgoda SR, Fullwood DT, Kalidindi SR. Delineation of the space of 2-point correlations in a composite material system. *Acta Mater* 2008;56(18): 5285–92.
- [4] Fullwood DT, et al. Gradient-based microstructure reconstructions from distributions using fast Fourier transforms. *Mater Sci Eng A Struct Mater* 2008;494(1–2):68–72.

- [5] Fullwood DT, Niezgoda SR, Kalidindi SR. Microstructure reconstructions from 2-point statistics using phase-recovery algorithms. *Acta Mater* 2008;56(5):942–8.
- [6] Singh H, et al. Image based computations of lineal path probability distributions for microstructure representation. *Mater Sci Eng A* 2008;474(1–2):104–11.
- [7] Torquato S. Random heterogeneous materials. New York, NY: Springer-Verlag; 2002.
- [8] Torquato S, Lu B. Chord-length distribution function for two-phase random media. *Phys Rev E* 1993;47(4):2950.
- [9] Niezgoda SR, Kalidindi SR. Applications of the phase-coded generalized hough transform to feature detection, analysis, and segmentation of digital microstructures. *CMC-Comput Mater Continua* 2009;14(2):79–97.
- [10] Bresenham J. Algorithm for computer control of a digital plotter. *IBM Syst J* 1965;4(1):25–30.
- [11] Turner DM, Niezgoda SR, Kalidindi SR. Estimation of the angularly resolved chord length distribution for digital microstructures; 2012.
- [12] Garmestani H, et al. Semi-inverse Monte Carlo reconstruction of two-phase heterogeneous material using two-point functions. *Int J Theor Appl Multiscale Mech* 2009;1(2):134–49.
- [13] Li D, et al. 3D reconstruction of carbon nanotube composite microstructure using correlation functions. *J Comput Theor Nanosci* 2010;7(8):1462–8.
- [14] Baniassadi M, et al. Three-dimensional reconstruction and homogenization of heterogeneous materials using statistical correlation functions and FEM. *Comput Mater Sci* 2012;51(1):372–9.
- [15] Tabei S, et al. Microstructure reconstruction and homogenization of porous Ni-YSZ composites for temperature dependent properties. *J Power Sources* 2013;235:74–80.
- [16] Sheidaei A, et al. 3-D microstructure reconstruction of polymer nanocomposite using FIB–SEM and statistical correlation function. *Compos Sci Technol* 2013;80:47–54.
- [17] Yeong CLY, Torquato S. Reconstructing random media. II. Three-dimensional media from two-dimensional cuts. *Phys Rev E* 1998;58(1):224–33.
- [18] Hansen BL, et al. On the reconstruction of polycrystalline microstructures from two-point correlation statistics. *J Comput Aided Mater Des* 2003;10:163–73.
- [19] Yeong CLY, Torquato S. Reconstructing random media. *Phys Rev E* 1998;57(1):495–506.
- [20] Kumar H, Briant CL, Curtin WA. Using microstructure reconstruction to model mechanical behavior in complex microstructures. *Mech Mater* 2006;38:818–32.
- [21] Rozman MG, Utz M. Efficient reconstruction of multiphase morphologies from correlation functions. *Phys Rev E* 2001;63.
- [22] Fienup JR, Crimmins TR, Holsztynski W. Reconstruction of the support of an object from the support of its autocorrelation. *J Opt Soc Am* 1982;72(5):610–24.
- [23] Fienup JR. Phase retrieval algorithms: a comparison. *Appl Opt* 1982;21(15):2758–69.
- [24] Millane RP. Multidimensional phase problems. *J Opt Soc Am A* 1996;13(4):725–34.
- [25] Adams BL, Gao X, Kalidindi SR. Finite approximations to the second-order properties closure in single phase polycrystals. *Acta Mater* 2005;53(13):3563–77.

- [26] Bates RHT. Uniqueness of solutions to two-dimensional Fourier phase problems for localized and positive images. *Comput Vision Graph Image Process* 1984;25:205–17.
- [27] Millane RP. Redundancy in multidimensional deconvolution and phase retrieval. In: Digital image synthesis and inverse optics, vol. 1351; 1990. p. 227–36.
- [28] Hauptman H, Karle J. Solution of the phase problem. I: the centrosymmetric crystal. *Acta Cryst* 1954;7.
- [29] Gerchberg RW, Saxton WO. A practical algorithm for the determination of phase from image and diffraction plane pictures. *Optik* 1972;35: 237–46.
- [30] Spowart JE. Automated serial sectioning for 3-D analysis of microstructure. *Scr Mater* 2006;5:5–10.
- [31] Spowart JE, Mullens HM, Puchala BT. Collecting and analyzing microstructures in three dimensions: a fully automated approach. *J Miner Met Mater* 2003;55(10):35–7.
- [32] Echlin MP, et al. A new TriBeam system for three-dimensional multimodal materials analysis. *Rev Sci Instrum* 2012;83(2):. p. 023701-023701-6.
- [33] Wargo EA, et al. Selection of representative volume elements for pore-scale analysis of transport in fuel cell materials. *J Power Sources* 2012;197: 168–79.
- [34] Kotula PG, Rohrer GS, Marsh MP. Focused ion beam and scanning electron microscopy for 3D materials characterization. *MRS Bull* 2014;39(04):361–5.
- [35] Villanova J, et al. Multi-scale 3D imaging of absorbing porous materials for solid oxide fuel cells. *J Mater Sci* 2014;49(16):5626–34.
- [36] Ebner M, et al. X-Ray tomography of porous, transition metal oxide based lithium ion battery electrodes. *Adv Energy Mater* 2013;3(7):845–50.
- [37] Betz O, et al. Imaging applications of Synchrotron x-ray micro-tomography in biological morphology and biomaterial science. I. General aspects of the technique and its advantages in the analysis of arthropod structures. *J Microsc* 2007;227(1):51–71.
- [38] Stiénon A, et al. A new methodology based on X-ray micro-tomography to estimate stress concentrations around inclusions in high strength steels. *Mater Sci Eng A* 2009;513–514:376–83.
- [39] Proudhon H, Buffière JY, Fourny S. Three-dimensional study of a fretting crack using synchrotron X-ray micro-tomography. *Eng Fract Mech* 2007;74 (5):782–93.
- [40] Bingert JE, et al. High-energy diffraction microscopy characterization of spall damage. Dynamic behavior of materials, vol. 1. New York, NY, USA: Springer; 2014. p. 397–403.
- [41] Wang L, et al. Microstructural characterization of polycrystalline materials by synchrotron X-rays. *Front Mater Sci* 2013;7(2):156–69.
- [42] Pokharel R, et al. Polycrystal plasticity: comparison between grain-scale observations of deformation and simulations. *Annu Rev Condens Matter Phys* 2014;5(1):317–46.
- [43] Kalidindi SR. Data science and cyberinfrastructure: critical enablers for accelerated development of hierarchical materials. *Int Mater Rev* 2014.
- [44] Niezgoda SR, Kanjrala AK, Kalidindi SR. Novel microstructure quantification framework for databasing, visualization, and analysis of microstructure data. *Integrating Mater Manuf Innov* 2013;2:3.
- [45] Panchal JH, Kalidindi SR, McDowell DL. Key computational modeling issues in integrated computational materials engineering. *Comput Aided Des* 2013;45(1):4–25.

- [46] Qidwai SM, et al. Estimating response of polycrystalline materials using sets of weighted statistical volume elements (WSVEs). *Acta Mater* 2012;60: 5284–99.
- [47] Adams BL, Kalidindi SR, Fullwood D. Microstructure sensitive design for performance optimization. Butterworth-Heinemann; 2012.
- [48] Kalidindi SR, Niezgoda SR, Salem AA. Microstructure informatics using higher-order statistics and efficient data-mining protocols. *JOM* 2011;63(4): 34–41.
- [49] Fullwood DT, et al. Microstructure sensitive design for performance optimization. *Prog Mater Sci* 2010;55(6):477–562.
- [50] Niezgoda SR, et al. Optimized structure based representative volume element sets reflecting the ensemble-averaged 2-point statistics. *Acta Mater* 2010;58(13):4432–45.
- [51] Mason TA, Adams BL. Use of microstructural statistics in predicting polycrystalline material properties. *Metall Mater Trans A* 1999;30(4):969–79.
- [52] Gao X, Przybyla CP, Adams BL. Methodology for recovering and analyzing two-point pair correlation functions in polycrystalline materials. *Metall Mater Trans A* 2006;37(8):2379–87.
- [53] Uchic MD, Groeber MA, Rollett AD. Automated serial sectioning methods for rapid collection of 3-D microstructure data. *JOM* 2011;63(3):25–9.
- [54] Rowenhorst DJ, Lewis AC, Spanos G. Three-dimensional analysis of grain topology and interface curvature in a β -titanium alloy. *Acta Mater* 2010;58 (16):5511–19.
- [55] Xu W, et al. Techniques for generating 3-D EBSD microstructures by FIB tomography. *Mater Charact* 2007;58(10):961–7.
- [56] Van Boxel S, et al. Direct observation of grain boundary migration during recrystallization within the bulk of a moderately deformed aluminium single crystal. *Mater Trans* 2014;55(01):128–36.
- [57] Adams BL, Field DP. Measurement and representation of grain-boundary texture. *Metall Trans A* 1992;23A(9 pt 2):2501–13.
- [58] Adams BL. Orientation imaging microscopy: application to the measurement of grain boundary structure. *Mater Sci Eng A* 1993;166(1–2):59–66.
- [59] Kalidindi SR. Microstructure informatics. In: Informatics for materials science and engineering: data-driven discovery for accelerated experimentation and application; 2013. p. 443.
- [60] Hamedani HA, et al. Microstructure, property and processing relation in gradient porous cathode of solid oxide fuel cells using statistical continuum mechanics. *J Power Sources* 2011;196:6325–31.
- [61] Milhans J, et al. Statistical continuum mechanics analysis of effective elastic properties in solid oxide fuel cell glass-ceramic seal material. *J Power Sources* 2010;195(17):5726–30.
- [62] Li D, Garmestani D. Microstructure sensitive design and quantitative prediction of effective conductivity in fuel cell design. In: The 13th international symposium on plasticity and its current applications; 2007. Alaska.
- [63] Proust G, Kalidindi SR. Procedures for construction of anisotropic elastic–plastic property closures for face-centered cubic polycrystals using first-order bounding relations. *J Mech Phys Solids* 2006;54(8):1744–62.
- [64] Lin S, Garmestani H. Statistical continuum mechanics analysis of an elastic two-isotropic-phase composite material. *Compos Part B Eng* 2000;31 (1):39–46.
- [65] Garmestani H, Lin S, Adams BL. Statistical continuum theory for inelastic behavior of a two-phase medium. *Int J Plast* 1998;14(8):719–31.

- [66] Pietroni N, et al. Solid-texture synthesis: a survey. *IEEE Comput Graphics Appl* 2010;30(4):74–89.
- [67] Turner DM, Kalidindi SR. Statistical construction of 3-d microstructures from 2-d exemplars collected on oblique sections. In preparation, 2015.
- [68] Kopf J, et al. Solid texture synthesis from 2D exemplars. *ACM Trans Graph* 2007;26(3):2.
- [69] Chen J, Wang B. High quality solid texture synthesis using position and index histogram matching. *Visual Comput* 2010;26(4):253–62.
- [70] Gusev AA. Representative volume element size for elastic composites: a numerical study. *J Mech Phys Solids* 1997;45(9):1449–59.
- [71] Nemat-Nasser S, Hori M. *Micromechanics: overall properties of heterogeneous materials*. 2nd ed. Amsterdam: Elsevier; 1999.
- [72] Hornung U. ed. I.a. mathematics *Homogenization and porous media*, vol. 6. Springer; 1997.
- [73] Cherkaev A. Variational methods for structural optimization. *Applied mathematical sciences*, vol. 140. Springer; 1991.
- [74] Chen XL, Liu YJ. Square representative volume elements for evaluating the effective material properties of carbon nanotube-based composites. *Comput Mater Sci* 2004;29(1):1–11.
- [75] Drugan WJ, Willis JR. A micromechanics-based nonlocal constitutive equation and estimates of representative volume element size for elastic composites. *J Mech Phys Solids* 1996;44(4):497–524.
- [76] Kanit T, et al. Determination of the size of the representative volume element for random composites: statistical and numerical approach. *Int J Solids Struct* 2003;40(13–14):3647–79.
- [77] Shan Z, Gokhale AM. Representative volume element for non-uniform micro-structure. *Comput Mater Sci* 2002;24(3):361–79.
- [78] Sab K. On the homogenization and the simulation of random materials. *Eur J Mech A Solids* 1992;11(5):505–15.
- [79] Ostoja-Starzewski M. *Microstructural randomness and scaling in mechanics of materials*. Boca Raton, FL: Chapman & Hall/CRC; 2008.
- [80] Kröner E. Berechnung der elastischen Konstanten des Vielkristalls aus den Konstanten des Einkristalls. *Z Phys A Hadrons Nucl* 1958;151(4):504–18.
- [81] Milton GW. The theory of composites. In: Ciarlet PG, et al., editors. *Cambridge monographs on applied and computational mathematics*. Cambridge: Cambridge University Press; 2002.
- [82] Willis JR. Variational and related methods for the overall porperties of composite materials. *Adv Appl Mech* 1981;21:2–78.
- [83] McCoy JJ. Macroscopic response of continua with random microstructures. In: Nemat Nasser S, editor. *Mechanics today*, vol. 6. Oxford: Pergamon Press; 1981.
- [84] Hill R. Elastic properties of reinforced solids: some theoretical principles. *J Mech Phys Solids* 1963;11:357–72.
- [85] Kalidindi SR. Data science and cyberinfrastructure: critical enablers for accelerated development of hierarchical materials. *Int Mater Rev* 2015;60(3):150–68.
- [86] Jeulin D, Ostoja-Starzewski M. *Mechanics of random and multiscale microstructures*. New York, NY: Springer Wien; 2001.
- [87] McDowell DL, Ghosh S, Kalidindi SR. Representation and computational structure–property relations of random media. *JOM* 2011;63(3):45–51.
- [88] Przybyla CP, et al. Microstructure-sensitive modeling of high cycle fatigue. *Int J Fatigue* 2010;32(3):512–25 [special issue on Fatigue of Materials: Competing Failure Modes and Variability in Fatigue Life].

- [89] Przybyla CP, McDowell DL. Microstructure-sensitive extreme value probabilities for high cycle fatigue of ni-base superalloy IN100. *Int J Plast* 2010;26 (3):372–94.
- [90] Bunge H-J. Texture analysis in materials science. Mathematical methods. Göttingen: Cuvillier Verlag; 1993.
- [91] Fast T, Knezevic M, Kalidindi SR. Application of microstructure sensitive design to structural components produced from hexagonal polycrystalline metals. *Comput Mater Sci* 2008;43(2):374–83.
- [92] Al-Harbi HF, Kalidindi SR. Crystal plasticity finite element simulations using a database of discrete Fourier transforms. *Int J Plast* 2014.

REDUCED-ORDER REPRESENTATIONS OF SPATIAL CORRELATIONS

In Chapter 3, we presented a rigorous framework for the stochastic quantification of the material internal structure based on concepts of the n -point spatial correlations (sometimes simply referred to as n -point statistics). Although a number of different measures of the spatial correlations in the microstructure are possible (e.g., lineal-path functions and chord-length distributions), it is hoped the reader appreciates that only the n -point spatial correlations provide the most complete set of measures that are naturally organized by increasing amounts of microstructure information. The central practical difficulty of using the n -point spatial correlations is that they produce an extremely large number of structure metrics. In fact, one would be right in arguing that a large number of interdependencies must exist among the complete set of n -point spatial correlations (recall that the dependencies described in Chapter 3 are only for 2-point statistics). For most material systems of interest, the set of n -point statistics is an extremely large unwieldy set even for $n = 2$.

As a specific example, consider a simple two-phase microstructure. The number of independent 2-point spatial correlation functions for this microstructure is one. In other words, an autocorrelation for one of the constituent phases is adequate to capture all of the four different 2-point spatial correlations that could be defined between the constituent phases (Chapter 3). Even if we restrict our attention to a relatively small cuboidal neighborhood covering five spatial bins on either side in each of the three orthogonal directions, the corresponding number of discrete vectors from this truncated neighborhood would be

1331 ($=11^3$). In other words, the representation of the truncated set of 2-point correlations of interest in this example would require the use of a 1331-dimensional space. This continues to be an extremely large space for establishing PSP (process—structure—property) linkages. This simple example demonstrates clearly the critical need for a computationally efficient approach for establishing the linkages of interest.

Rigorous analyses of large materials datasets and the extraction of robust and reliable PSP linkages can only be accomplished in suitably defined low-dimensional representations of material structure. As mentioned earlier, this is the central challenge that lies before us. It was recently demonstrated that techniques such as principal component analysis (PCA) can be used to obtain objective low-dimensional representations of the 2-point spatial correlations needed to capture faithfully the salient details of the material hierarchical structure in the establishment of high-value PSP linkages [1–6].

4.1 Principal Component Analyses

In this section, we go over the main details involved in the PCA [7–9] and its physical significance in the data-driven reduction of high-dimensional representations (such as the use of a large number of n -point spatial correlations to represent the material structure). Let $\{x_r^{(j)}|r = 1, 2, \dots, R\}$ be a R -dimensional representation of a physical quantity of interest, where $j = 1, 2, \dots, J$ enumerates the number of available data points. In other words, the physical quantity itself requires specification of R values, and we assume that we have collected an ensemble comprising J data points. In a typical application of interest here, $J \ll R$. In such situations, we intuitively recognize that there is no need to carry the full information (i.e., all of the R values) in any subsequent analyses.

In PCA, we seek a linear, distance-preserving transformation of the data from its original frame (the reader would find it convenient to think of $\{x_r\}$ as a point in R -dimensional space) to a new orthogonal frame where the axes are aligned with the directions of the maximum variance between the data points within the considered ensemble of data points. This is schematically depicted in Figure 4.1 in a simple two-dimensional (2-D) illustration. It is obvious that the variance in the ensemble of data points is better captured in the new frame compared with the original frame. In other words, the new frame presents a better description of the data, where the axes now represent natural directions of high

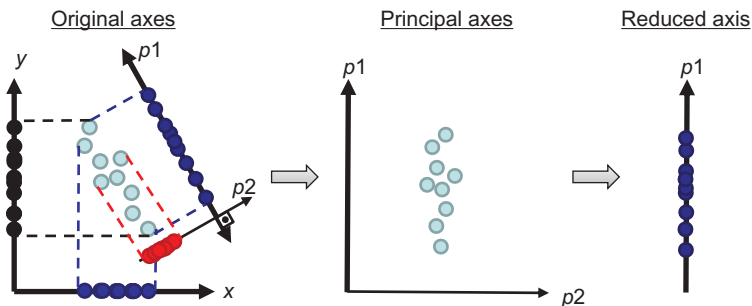


Figure 4.1 Illustration of dimensionality reduction using PCA approach.

orthogonal variance in the selected ensemble of data points. The utility of this concept is actually realized when the original data is in a very large number of dimensions and we only have a few data points (this is typically the case in virtually all considerations related to materials datasets discussed in this book). In such a situation, the new frame typically shows strongly decaying variance, that is, the data usually clusters in a lower dimensional subspace within the original high-dimensional space. As a simple example, consider a situation where the original data schematically shown in Figure 4.1 is actually in a three-dimensional (3-D) space, but all of the data is either within or very close to a specific plane in that 3-D space. The reader should note that this is very likely to happen in situations where $J \ll R$. In such situations, each of the data points in the ensemble can be approximately expressed in the new frame in a significantly lower number of dimensions, when suitably truncated based on the variance in the ensemble.

The linear, distance-preserving transformation underlying PCA can be mathematically expressed as

$$\tilde{x}_k^{(j)} = \sum_{r=1}^R Q_{kr} (x_r^{(j)} - \langle x_r \rangle) \quad (4.1)$$

In Eq. (4.1), $\langle x_r \rangle$ denotes a simple average of all data points, Q_{kr} represents an orthogonal transformation matrix, and $\tilde{x}_k^{(j)}$ represents of the j th data point in the new reference frame. Eq. (4.1) ensures that $\langle \tilde{x}_k \rangle$ is zero. Our interest of course is in finding the transformation matrix that would maximize the variance of $\tilde{x}_k^{(j)}$ for the selected ensemble of data points in a prioritized manner. In other words, we want $\tilde{x}_1^{(j)}$ to exhibit the highest possible variance, followed by $\tilde{x}_2^{(j)}$, and so on, while ensuring that

the transformation is linear and orthogonal (preserves the distances between points automatically).

With our attention on the variance in $\tilde{x}_1^{(j)}$, we can recast the set of equations obtained by applying Eq. (4.1) to every data point in the ensemble in the following way:

$$\{t\} = [X]\{q\} \quad (4.2)$$

where $t_j = \tilde{x}_1^{(j)}$, $X_{jr} = x_r^{(j)} - \langle x_r \rangle$, and $q_r = Q_{1r}$. The $[X]$ is the mean-centered data matrix. Maximizing the variance of $\tilde{x}_1^{(j)}$ then reduces to

$$\max_q |t|^2 = \{q\}^T [X]^T [X] \{q\} \quad (4.3)$$

where the superscript T denotes a transpose. As $\{q\}$ is required to be a unit vector (needed to ensure that $[Q]$ is an orthogonal matrix), the solution to Eq. (4.3) is obtained when $\{q\}$ is taken as the eigenvector corresponding to the largest eigenvalue of the symmetric matrix $[X]^T [X]$. Incidentally, $[X]^T [X]$ is the covariance matrix of the data matrix $[X]$, except for a multiplier. After finding the first direction, one would remove the first principal component (PC) from the data matrix as

$$[\tilde{X}] = [X] - [X]\{q\}\{q\}^T \quad (4.4)$$

and repeat the entire process on $[\tilde{X}]$. In fact, one would repeat this process as often as needed to find the additional directions of the new reference frame. This process of removing the PCs from the data matrix guarantees that the new direction is automatically perpendicular to all of the previously established directions of the new frame. The description above is mainly provided so that reader can understand the logic behind the PCA computations. In actual practice, there is no need to repeat the eigenvalue computations individually for each PC as described earlier. This is because the eigenvectors of the symmetric covariance matrix $[X]^T [X]$, when ordered by the magnitude of its eigenvalues, provide all of the directions of the new (transformed) frame identified in the PCA.

In general, the coordinates of the data point in the new frame, $\tilde{x}_k^{(j)}$, are called scores or weights of the PCs. The new directions identified by PCA (the eigenvectors of the data matrix) are referred to as the PCs. The eigenvalues computed in the PCA provide extremely useful information about the ensemble of data points studied. From Eq. (4.3), it is easy to see that the eigenvalue is actually the sum of the squared distances from the ensemble mean. In other words, the eigenvalue is essentially the variance in the dataset along the corresponding eigenvector, except for a

scaling factor. Indeed the sum of all eigenvalues is related to the total variance in the data ensemble, again except for a scaling factor.

One of the main consequences of PCA is that the data has been transformed into a new frame organized by variance (i.e., eigenvalues). Therefore, it is very likely that after the first few eigenvalues, the values of the rest of the eigenvalues drop to sufficiently low values, that it is possible to truncate the representations. In other words, we should expect to see significant drop in the values of $\tilde{x}_k^{(j)}$ with increasing values of k . It is emphasized here that the complete set $\{\tilde{x}_k^{(j)}|k = 1, 2, \dots, R\}$ denotes the full representation of the data point in the sense that we can fully recover the original representation of the data point, $x_r^{(j)}$ (this is because the $\langle x_r \rangle$ and Q_{kr} computed in the PCA are generally stored along with the data ensemble). However, a truncated (low-dimensional) representation $\{\tilde{x}_k^{(j)}|k = 1, 2, \dots, \tilde{R}\}$, where $\tilde{R} \ll R$ is only an approximate representation of the data point in that the original data point can no longer be fully recovered exactly. However, if the truncation is made judiciously (based on the decay in the eigenvalues), then the truncated representation should serve adequately for any future analysis with the data ensemble.

It should be clear from the above discussion that great caution needs to be exercised in selecting the level of truncation. As the eigenvalues are proportional to the variance, they provide valuable insight into the selection of the truncation level. One may decide on the truncation level based on the characteristics of decay in the eigenvalues. For example, one might want to ensure that the sum of the eigenvalues in the eliminated PCs is below a certain fraction of the total sum of all of the eigenvalues. Alternately, one may decide to keep only the PCs whose eigenvalues are above a certain small percentage of the largest eigenvalue. Sometimes, other factors can provide guidance on the truncation level. For example, irrespective of whether the data points were generated by experiments or simulations, there is inherently a certain level of uncertainty associated with the data points. The uncertainty in the data point can be used to decide on the truncation levels in PCA by ensuring that the contributions from the truncated components are well within the uncertainty associated with the elements of the data ensemble.

As noted earlier, PCA is particularly useful in situations where the number of data points is far lower than the number of dimensions needed to fully describe each data point, i.e., $J \ll R$. In such situations, PCA provides an objective (data-driven)

low-dimensional representation of the data ensemble. There is both an advantage and a disadvantage with this approach. The main advantage is that it is objective (as opposed to being based on the instincts of the analyst), i.e., unbiased. Therefore, it lends itself easily to automated analytics protocols. The primary disadvantage is that the representations (both the PC directions and weights) can change as more data is added to the ensemble. This is especially the case in the initial stages of the analyses when, in most cases, enough data is not available. After a large amount of data has been accumulated, one might reach a situation where the PCs do not change significantly. Because of this, there have been several reports in the literature on efficient algorithms to compute the eigenvalues and eigenvectors for PCA [10,11].

Also, from the computational perspective, the description provided above of computing the PCA transformation as the eigenvectors of $[X]^T[X]$ is not at all attractive, especially in the situation of interest to us where $J \ll R$. This is mainly because of the compute and memory requirements in the formation and storage of the very large $[X]^T[X]$. In general, one might find it computationally more stable to perform singular value decomposition of $[X]$ as $X = U\Sigma V^T$, while recognizing that the eigenvalues of $[X]^T[X]$ are the squares of the diagonal components of Σ and $Q = V^T$. If one proceeds in this way, $[X][V]$ produces the representation of the data points in the new PC frame.

One note of caution to the reader with respect to the use of PCA is to recognize its sensitivity to differential scaling of the dimensions of the data. In other words, if the components of the data represent disparate physical entities with different ranges in their numerical values (e.g., captured using different units of measurements, fundamentally different types of quantities), then differential scaling of the data components will produce very different PCA representations.

4.2 Application to Spatial Correlations

Let f_r denote the subset of n -point statistics of interest selected to quantify the material structure in any selected application. The reader should take note of the compaction in the notation here. In Chapter 3, we used f_r^{np} to denote the 2-point statistics. In the notation just introduced, we are compacting all of the spatial correlations of interest into a single vector. This vector could include any selected combination of n -point statistics (i.e., it might include some combination of

1-point statistics, 2-point statistics, 3-point statistics, etc.) as desired by the user. Let R denote the dimensionality of f_r , and further assume that we are analyzing an ensemble of microstructures, whose elements are enumerated $j = 1, 2, \dots, J$. Let $f_r^{(j)}$ denote the microstructure statistical measures of interest for a single element (microstructure) from the ensemble. It is once again emphasized that $J \ll R$ in most cases under consideration here. In such situations, PCA described earlier identifies a maximum of $(J - 1)$ orthogonal directions in the R -dimensional space that are arranged by decreasing levels of variance. It is $(J - 1)$ and not J because we need at least two points to define a direction (another way to look at this is to recognize that mean centering is equivalent to taking the same number of degrees of freedom as needed in the specification of one direction in the space of interest). From the output of the PCA, we can identify the new reference frame organized by the amount of variance observed in the data ensemble. In other words, the first direction of the new reference frame exhibits the direction of the highest variance in the given ensemble of microstructures, and the second direction exhibits the second highest direction of variance while being orthogonal to the first direction, and so on. Let φ_{kr} denote the components of the orthogonal set of directions identified by PCA. With respect to the general notation introduced earlier in Eq. (4.1), the $[\varphi]$ matrix is the same as the $[Q]$ matrix. Following the mathematical details presented in Section 4.1, it is convenient to express the PCA representation of any selected member of the microstructure ensemble as

$$f_r^{(j)} = \sum_{k=1}^{\min((J-1), R)} \alpha_k^{(j)} \varphi_{kr} + \bar{f}_r \quad (4.5)$$

where \bar{f}_r is simply the ensemble mean and $\alpha_k^{(j)}$ (referred as PC scores or weights) provide an objective representation of the microstructure in the new orthogonal reference frame identified by φ_{rk} . In Eq. (4.5), we make explicit note of the fact that there can only be a maximum of $\min((J - 1), R)$ dimensions in the new reference frame. In other words, the rest of the eigenvalues of the covariance matrix as well as the corresponding PC scores (or weights) will be identically equal to zero.

As discussed earlier, the eigenvalues obtained in the PCA carry important information that can aid in truncating the representations defined in Eq. (4.5). A suitable truncation (based on the eigenvalues), as discussed earlier, will result in an objective reduced-order representation of the microstructure

with only a handful of parameters. Mathematically, this reduced-order representation can be expressed as

$$f_r^{(j)} \approx \sum_{k=1}^{\tilde{R}} \alpha_k^{(j)} \varphi_{kr} + \bar{f}_r \quad (4.6)$$

where $\tilde{R} \ll \min(J - 1, R)$. Selection of \tilde{R} will depend on numerous considerations and will be explored later through a series of case studies. In summary, the PCA protocols described earlier will produce an objective (data-driven) representation of the material microstructure as $\{\alpha_k | k = 1, 2, \dots, \tilde{R}\}$. These descriptions are central to extracting the high-value PSP linkages of interest in materials development efforts.

In the rest of the chapter, we will discuss specific case studies that illustrate the application of the PCA protocols presented here.

4.3 Case Study: α - β Ti Micrographs

One of the earliest reported applications of PCA protocols described here on spatial statistics was on an ensemble of α - β Ti micrographs obtained from scanning electron microscopy [4]. The assembled database consisted of 150 high-resolution (1448×1923 pixels) segmented backscatter electron micrographs from five distinct heat treatments of Ti-5553 (Figure 4.2). As there are only two local states (corresponding to each phase) in this ensemble, we only need to compute the autocorrelations to establish a complete set of 2-point statistics. After computing the auto-correlations for all 150 micrographs, PCA was performed. In this particular exercise, note that $R = 1448 \times 1923 = 2,784,504$. This is indeed a very high-dimensional representation of the material structure (note that this set includes only the 2-point statistics).

After performing the PCA, the transformed representations in the new reference frame were truncated to three, i.e., $\tilde{R} = 3$. The 3-D plot shows the top three scores (PC weights) for each member of the ensemble, grouped by the heat treatment. It should be noted that the information on the heat treatment was not included in the PCA. In other words, this was a completely unsupervised dimensionality reduction. It is therefore remarkable that as few as three of PC scores are adequate to clearly distinguish microstructures both within and between each class (corresponding to a distinct heat treatment). This specific case study demonstrates that an extremely large dimensionality reduction is possible if our goal is to capture the variance among the micrographs both within each class and between the different classes.

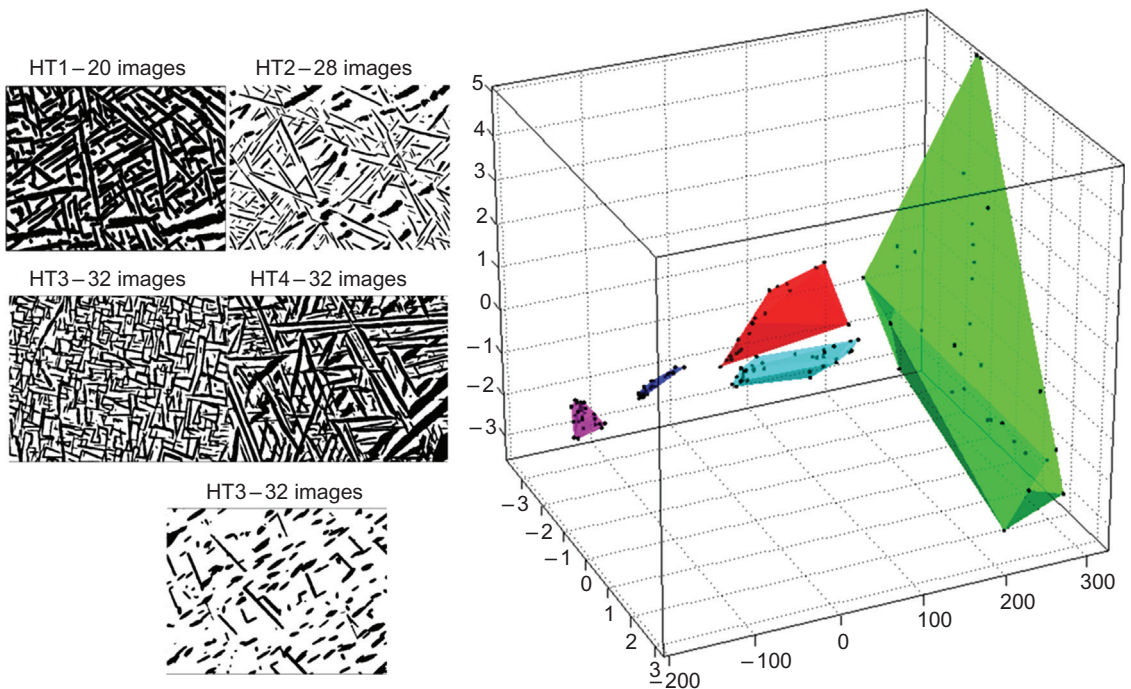


Figure 4.2 Visualization of an ensemble of α - β Ti micrographs [4,12]. Each point in the reduced-order 3-D PCA space represents a micrograph (examples shown on left) and each colored volume represents a structure class. The size of each colored region reflects the variance within the class. The axes in the 3-D plot correspond to the α_k in Eq. (4.6). The color key for the different heat treatments is as follows: HT1 = Red, HT2 = Blue, HT3 = Green, HT4 = Cyan, HT5 = Magenta.

Note the dramatic reduction in the PC scores between the first component and the other two components in Figure 4.2. As discussed earlier, this is expected and explains why we are successful in achieving such a high level of dimensionality reduction in this specific case study. The scores indicate that most of the variance in the ensemble is indeed captured by the first few PCs. It should also be noted that the volumes of the regions identified in Figure 4.2 provide an excellent measure of the inherent variance within each class of microstructures. In particular, note that HT2 (blue-colored class) and HT3 (green-colored class) exhibit the lowest and highest variance, respectively, among the five classes studied. This information is of tremendous value in the materials development efforts, where variance is one of the main impediments to scaling up from the laboratory scale to the industrial scale.

4.4 Case Study: Nonmetallic Inclusions/ Steel Composite System

As the next case study, we consider an ensemble of digitally created microstructures for a study of the salient structure–property linkages in an inclusion–matrix composite system. In this study [12,13], a large ensemble of 2-D synthetic microstructures were generated containing multiple hard or soft inclusions with different sizes, shapes, and spatial configurations in a steel matrix. For this purpose, a library of 500 particles (inclusions) was first generated such that this set exhibited a broad range of particle shapes and sizes seen in the published literature [14–17]. Circular, square, triangular, rhombic, and platelet (horizontal and vertical orientation) shapes were included in this particle library. A total of 900 microstructures were generated by randomly selecting the desired number of particles from the library and placing them in the steel matrix based on four different placement criteria—random arrangement, banded arrangements (i.e., horizontal or vertical bands), and clusters. Overlaps in the spatial placement of the particles were allowed to allow particles of complex shapes. The generated microstructures were restricted to be eigen microstructures (i.e., each pixel was completely filled by either the inclusion or the steel phase), and comprised 80×80 spatial bins or voxels. The area fraction of the inclusions in the microstructure ensemble was varied between 0% and 20% to reflect the local volume fraction of inclusions in the steel matrix encountered in practice.

Because the microstructures in this case study also have only two local states, the autocorrelations of the matrix phase is adequate to capture all of the independent 2-point statistics for each microstructure. Note that the dimensionality of this representation of the material microstructure is $R=80 \times 80=6400$. The 2-point autocorrelations were generated for all 900 microstructures in the ensemble, and PCA was performed following the protocols described earlier in this chapter.

Let us examine the efficacy of PCA in providing low-dimensional representations of the microstructures. In other words, if two microstructures look similar to each other, their PCA representations (i.e., values of α_k) should be close to each other. Also, if two microstructures look very different, their PCA representations should be far apart. Various 2-D projections of the PCA representations (for all of the 900 microstructures included in this study) are shown in [Figure 4.3a](#), where each

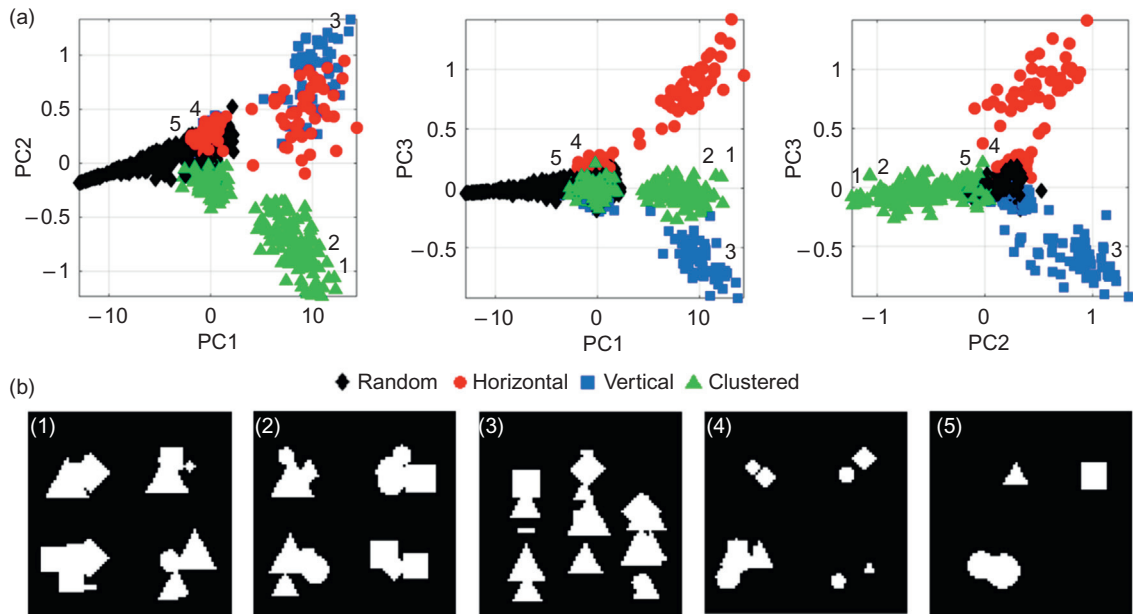


Figure 4.3 (a) Scatter plot of the entire dataset of 900 micrographs, plotted on the PCs, in different low-dimensional projections. Clusters corresponding to the four different methods of microstructure generation are identified by colors and markers. (b) Five example micrographs whose approximate locations on the first three PCA axes are shown in (a) [13].

point in the plot represents one microstructure. It is extremely important to note that all of the plots in Figure 4.3a are low-dimensional projections of the same PCA space. The microstructure representations in this plot are color-coded to distinguish four different classes included in this study (i.e., random, horizontally banded, vertically banded, and clustered). Careful examination of the plots shown in Figure 4.3a does demonstrate that the PCA representations of microstructures within a given class are indeed generally closer to each other compared with PCA representations of microstructures across the different classes. Note that the PCA performed here was completely unsupervised (i.e., the microstructures were not identified by their class in any way in the PCA). Therefore, the automatic classification of the microstructures seen in Figure 4.3a is actually an output from the PCA. As a further investigation of the efficacy of the PCA, we track the positions of five exemplar microstructures (labeled #1 through #5) shown in Figure 4.3b in the plots of Figure 4.3a. Microstructures #1 and #2 in Figure 4.3b are somewhat similar to each other, while

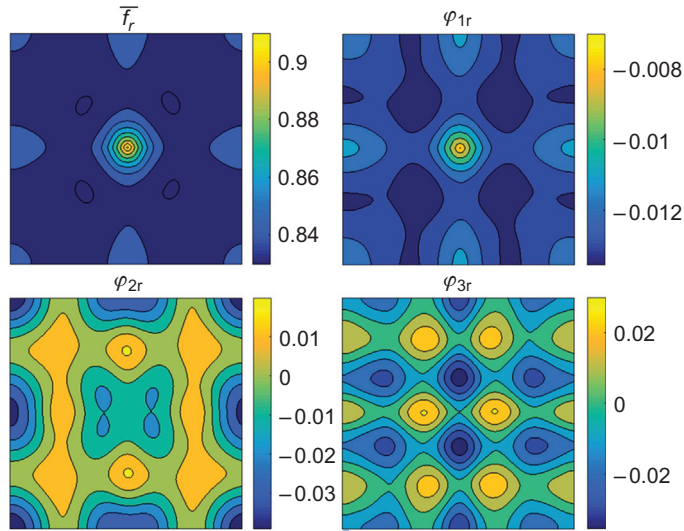


Figure 4.4 Plots of \bar{f}_r and φ_{kr} (for the first three values of k) obtained from the entire ensemble of 900 microstructures [13].

being distinctly different than either #4 or #5. Likewise, #4 and #5 are closer to each other compared to the rest. Also, microstructure #3 is distinctly different from the rest. All of these features are reflected fairly accurately in the distances between their corresponding representations in Figure 4.3a.

It is also informative to examine the information embedded in each of the PCs. Plots of \bar{f}_r and φ_{kr} (for different values of k ; see Eq. (4.6)) are presented in Figure 4.4 [13]. In these spatial correlation plots, the position of the each peak with respect to the center reflects the averaged length scale of features embedded in the spatial distribution of the matrix. This is because the PCA was performed on the autocorrelations of the matrix phase. The salient features in the spatial distribution of the matrix would correspond to features such as the directionally resolved averaged chord lengths (related to the averaged spacing of the inclusions), and the intensity of each peak reflects a certain probability of occurrence of that spacing.

The plot of \bar{f}_r simply reflects the averaged autocorrelations for the entire ensemble of 900 microstructures studied here. As expected, the averaged autocorrelation reflects a mostly random microstructure (produces a peak in the center that asymptotes quickly to a uniform value away from the center) with a few small peaks at the midpoints of the edges and the corners (these are presumably the contributions from the

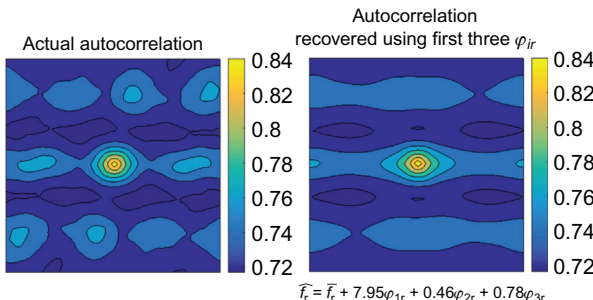


Figure 4.5 Comparison of the actual autocorrelation and the PCA-approximated autocorrelation for a selected exemplar horizontally banded microstructure [13].

banded microstructures). On the other hand, plots of φ_{kr} reflect a prioritized set of orthogonal deviations from the averaged autocorrelation. In other words, φ_{1r} reflects the most dominant deviation, φ_{2r} is the next most dominant deviation, and so on. The plot of φ_{1r} shows that it captures a certain scaled deviation in the intensities of the center peak (corresponds to volume fraction of the matrix in the microstructure) as well as the peaks at the midpoints of edges and the corners. Note also that the higher order φ_{kr} are in general more heterogeneous (i.e., they are trying to capture more subtle features in the microstructure). As implied in Eq. (4.6), one can construct the autocorrelation of any specific microstructure element of interest by starting with the averaged autocorrelation and adding weighted contributions from each of the PCs. This is illustrated in Figure 4.5, where the deviation of the autocorrelation of an exemplar microstructure from the ensemble average is decomposed into the individual weighted PCs. As shown in Figure 4.5, there will be a truncation error in the decomposition when the higher order PCs are ignored. However, since PCA provides a prioritized list of PCs, one can make the decision on the truncation level in a very objective manner.

4.5 Case Study: MD Simulation Datasets

The protocols described in this book for the quantification of the material structure are quite general and are expected to be broadly applicable to a diverse range of materials systems at a variety of length scales. As a specific illustration, the application of these protocols to results produced by molecular dynamics simulations was recently demonstrated [18].

A typical MD simulation dataset contains information on the expected center positions of the atoms. This information can then be easily transformed into a digital description of the entire volumetric domain used in the simulation, denoted in the usual manner as m_s^h . In this specific case study, the local state descriptor, h , was allowed only two values: $h = 1$ was used to refer to the atomic species and $h = 0$ was used to refer to the empty space between the atomic species. Furthermore, the description was restricted to an eigen microstructure description.

The protocols described in this book were applied on datasets simulated using 19 different potentials for Al at both 300 and 900 K. For each potential, the study included 20 atomic structures (taken at different times in the simulation after reaching an equilibrium state). Therefore, a total of 380 atomic structures (each comprising about 4000 atoms) were included in this analysis at each simulation temperature. The results are presented as PC plots in [Figure 4.6](#) and as dendrograms in [Figure 4.7](#). Each data point in [Figure 4.6a and b](#) represents the first three PC scores (or weights) for each MD-simulated atomic structure included in the analyses.

Keeping in mind the large dimensionality reduction implicit in the representation of [Figure 4.6](#) (from a description of the centers of about 4000 atoms to just three dimensions), it is indeed remarkable that this representation effectively captures both the intraclass and the interclass variations within the entire ensemble. This result is even more remarkable when one notes that this classification was performed in a completely unsupervised manner. In other words, the PCA computation was not informed in any way about the different potentials used in the MD simulations in producing the atomic structures included in the study. This is a clear testament to the power of the 2-point spatial correlations and PCA in capturing the salient features of the material structure in a rigorous framework. It is also very satisfying to note that the intraclass variance (reflected in the size of the cluster associated with each potential) in the simulated structures is significantly smaller than the interclass variance. Moreover, the intraclass variance seems to be of roughly the same order of magnitude for all the different potentials included in this study and is slightly higher for the datasets produced at the higher simulation temperature. All of these observations are consistent with expectations and provide strong support to the claim that the protocols presented in this book produce high-value, low-dimensional measures for diverse classes and types of material structures.

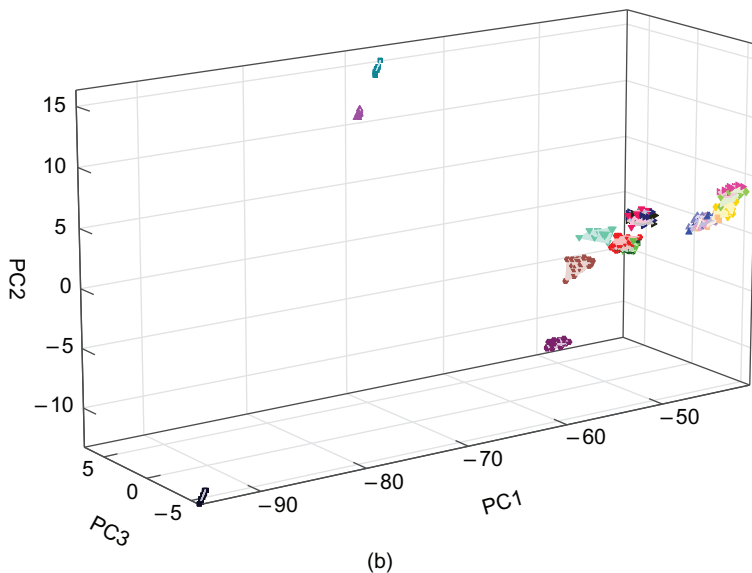
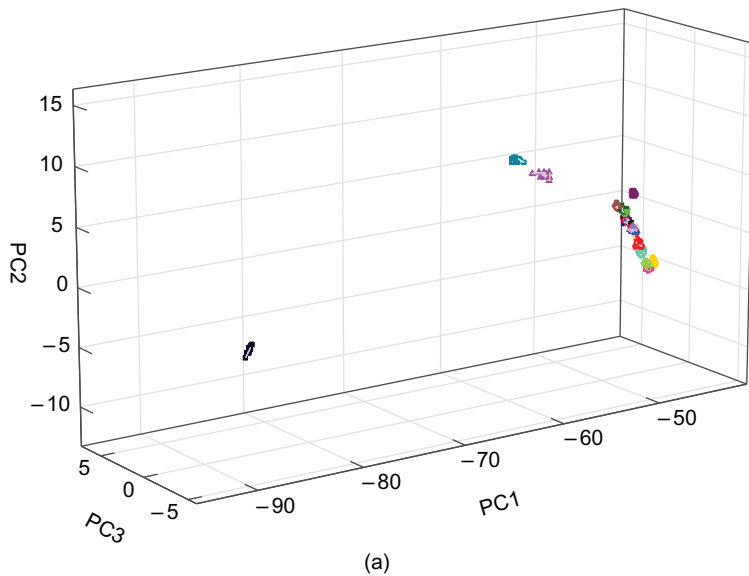


Figure 4.6 Unsupervised classification of the atomic structures predicted by MD simulations at 300 K (a) and 900 K (b) using different potentials using the protocols presented in this book [18].

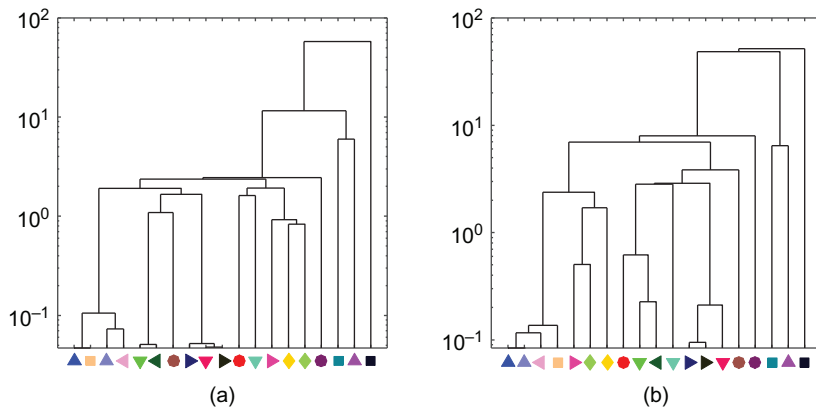


Figure 4.7 Dendograms of centroid distances corresponding to the data depicted in Figure 4.6 at (a) 300 K and (b) 900 K. The different symbols correspond to the different potentials included in the study [18].

An effective tool for visualizing distances in high-dimensional spaces is a dendrogram, which depicts the hierarchy of the distances between the data points. Figure 4.7a and b depict the interclass distances (between the cluster-means) as dendograms for the same datasets that were depicted in Figure 4.6a and b, respectively. This figure presents objective (unbiased) classification of the potentials included in the study, purely based on the predicted structures.

References

- [1] Suh C, et al. The application of principal component analysis to materials science data. *Data Sci J* 2002;1:19–26.
 - [2] Curtarolo S, et al. Predicting crystal structures with data mining of quantum calculations. *Phys Rev Lett* 2003;91(13):135503.
 - [3] CeCen A, et al. A data-driven approach to establishing microstructure-property relationships in porous transport layers of polymer electrolyte fuel cells. *J Power Sources* 2014;245:144–53.
 - [4] Kalidindi SR, Niezgoda SR, Salem AA. Microstructure informatics using higher-order statistics and efficient data-mining protocols. *JOM* 2011;63(4):34–41.
 - [5] Niezgoda SR, Kanjarla AK, Kalidindi SR. Novel microstructure quantification framework for databasing, visualization, and analysis of microstructure data. *Integr Mater Manuf Innov* 2013;2:3.
 - [6] Niezgoda SR, Yabansu YC, Kalidindi SR. Understanding and visualizing microstructure and microstructure variance as a stochastic process. *Acta Mater* 2011;59:6387–400.
 - [7] Halko N, et al. An algorithm for the principal component analysis of large data sets. *SIAM J Sci Comput* 2011;33(5):2580–94.

- [8] Rokhlin V, Szlam A, Tygert M. A randomized algorithm for principal component analysis. *SIAM J Matrix Anal Appl* 2009;31(3):1100–24.
- [9] Jolliffe I. Principal component analysis. Wiley Online Library; 2005.
- [10] Turk M, Pentland A. Eigenfaces for recognition. *J Cogn Neurosci* 1991;3(1):71–86.
- [11] Li Y. On incremental and robust subspace learning. *Pattern Recognit* 2004;37(7):1509–18.
- [12] Kalidindi SR. Data science and cyberinfrastructure: critical enablers for accelerated development of hierarchical materials. *Int Mater Rev* 2015;60(3):150–68.
- [13] Gupta A, et al. Structure-property linkages for non-metallic inclusions/steel composite system using a data science approach. *Acta Mater* 2015;91:239–54.
- [14] Dixin Y, et al. Numerical simulation of stress field in inclusions of large rudder arm steel castings. *Res Dev* 2009.
- [15] Ghosh A. Secondary steelmaking: principles and applications. Boca Raton, FL, USA: CRC Press; 2000.
- [16] Jacobi H, Rakoski F. High purity in steels as a criterion for materials development. *J Phys IV* 1995;5(C7): C7-3–C7-22.
- [17] Yu H-l, et al. Behavior of inclusions with weak adhesion to strip matrix during rolling using FEM. *J Mater Process Technol* 2009;209(9):4274–80.
- [18] Kalidindi SR, et al., Application of data science tools to quantify and distinguish between structures and models in molecular dynamics datasets. *Nanotechnology*. in press; 2015.

GENERALIZED COMPOSITE THEORIES

In this chapter, we shift our focus to currently existing theoretical frameworks for pursuing linkages between material structure and its associated properties. In particular, we will focus on the well-established homogenization theories [1–15] that are generally used for this purpose. It should be noted that the accuracy of these theories is largely dependent on the adequacy of the selected set of microstructure measures. For example, it is well known that when a material internal structure is quantified using only the volume fractions of the constituent phases, one can rigorously predict only the bounds of certain effective properties of the material. In general, one might expect to obtain better bounds and estimates of the effective properties, if one uses more information on the microstructure [1,16]. Nevertheless, the results of the homogenization theories, when expressed as computationally efficient structure–property linkages, serve a critical role in hierarchical multiscale materials models [17–19].

5.1 Conventions and Notations

The familiar 3D physical space is referred to as the Euclidean 3-space. Quantitative description of physical phenomenon in this space often requires selection of a reference point and reference directions, the combination of which is referred to as a reference frame. However, the phenomena themselves and the physical quantities involved are oblivious to the existence of the reference frame. In other words, the phenomenon occurs in the same way independent of the choice of the reference frame. Furthermore, the selection of the reference frame is not unique. Since an infinite number of choices exist for the selection of a reference frame (both the reference point

and the reference directions), it is necessary to develop a mathematical framework to reconcile the multiple descriptions of physical quantities arising from all of the possible choices of a reference frame. This is accomplished by the use of the mathematical concept of tensors. All quantities and processes encountered in physics-based multiscale materials modeling can be classified as tensors of different ranks, with the rank of the tensor identifying precisely the relationship between the multiple descriptions of the given physical quantity in any of the potential reference frames.

The simplest physical entities to describe are the tensors of rank 0, also referred to as scalars. The quantitative description of these physical quantities is completely independent of our choice for the reference frame. Energy, temperature, and density are all examples of physical quantities that can vary spatially and temporally in the Euclidean space, but can be represented as scalar functions. Tensors of rank 1 are also called vectors. Vectors are defined as a difference between an ordered pair of points. Vectors may be used to describe physical quantities such as displacement and its derivatives with respect to time such as velocity and acceleration. As another example, force is classically defined as the product of mass and acceleration. Since mass is a scalar (which is itself defined as a product of two scalars—density and volume) and acceleration is a vector, force has to be a vector.

Tensors of rank 2 and higher are often simply referred to as tensors. A convenient way of visualizing higher ranked tensors is to treat them as linear transformation mappings from a lower ranked tensor space into another lower ranked tensor space. For example, a tensor of rank 2 can serve as a linear mapping of all the vectors (tensors of rank 1) in the Euclidean space into itself.

It becomes necessary to define a reference frame in order to specify quantitatively any tensors of interest, except scalars. In mechanics studies, a reference frame is often defined by introducing a set of three orthonormal unit vectors $\{\mathbf{e}_1, \mathbf{e}_2, \mathbf{e}_3\}$, also called an orthonormal basis. The unit vectors in the basis are labeled following the right-hand convention. This definition yields the familiar rectangular Cartesian coordinate system and allows us to express any vector in the Euclidean 3-space as a weighted sum of the basis vectors. For example, a vector \mathbf{v} can be expressed as

$$\mathbf{v} = v_1 \mathbf{e}_1 + v_2 \mathbf{e}_2 + v_3 \mathbf{e}_3 = \sum_{i=1}^3 v_i \mathbf{e}_i \quad (5.1)$$

The quantities v_1 , v_2 , and v_3 are referred to as the components of the vector \mathbf{v} in the selected Cartesian reference frame.

At this point, it is important to recognize some of the important conventions used with tensors. Note that all tensors of rank higher than zero are shown with bold font style (e.g., \mathbf{v} in Eq. (5.1)). The components of the tensor in a specific reference frame are scalars and are shown using regular (not bold) font style. We have also introduced indicial notation in Eq. (5.1). The subscript i in v_i may refer to any one of the components of \mathbf{v} . Note also that we have used indicial notation in Eq. (5.1) to refer to the components of the orthonormal basis $\{\mathbf{e}_i\}$. It is important to recognize that while v_i refers to a scalar quantity, \mathbf{e}_i refers to a vector quantity (note the bold style), and most importantly that \mathbf{e}_i does not refer to i th component of vector \mathbf{e} . Another standard convention in indicial notation—the summation convention or Einstein summation convention—is that repeated indices in a single term automatically imply summation. In other words, one can drop the summation sign in Eq. (5.1) and simply express the equation as

$$\mathbf{v} = v_i \mathbf{e}_i \quad (5.2)$$

Finally, it is also a standard convention in tensor notation to use lower case symbols for vectors and upper case symbols for tensors of higher rank. All of these conventions will be used throughout this book. In Chapter 2, we already took a detailed look at the coordinate transformation laws associated with change of reference frames.

5.2 Review of Continuum Mechanics

When a body is subjected to force(s), it experiences internal stress. Stress at a material point is fundamentally defined as force per unit area in the neighborhood of that material point. However, this definition of stress requires specification of the orientation of the infinitesimal area element chosen at the material point. Since it is possible to choose an infinite number of area elements with different orientations at the material point, it follows that one can define an infinite number of stress-like quantities at the material point. The concept of a stress tensor helps us resolve this dilemma.

Figure 5.1 shows stresses on the surfaces of an infinitesimal cuboidal volume element taken around a material point of interest in the current loaded configuration. The stress vectors on each surface have been resolved into the three orthonormal basis directions giving a total of nine different stress components. Note that the stress vectors in this figure are depicted

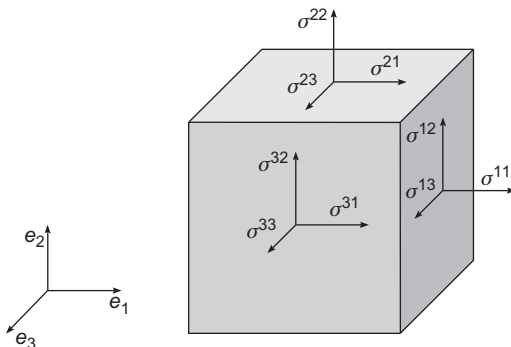


Figure 5.1 Description of the stress tensor at a material point.

only on the three positive surfaces (normals on these surfaces are along the positive directions of the orthonormal basis). It can be shown that the stress vectors on the negative surfaces (not shown in Figure 5.1) are exactly equal and opposite to the corresponding ones on the positive surfaces by virtue of force equilibrium. The nine stress components are labeled using two indices, with each index ranging from 1 to 3. The first index identifies the plane on which the stress component is described and the second index refers to the direction of the stress component. In the indicial notation, the stress components are simply referred to as σ_{ij} . Satisfying equilibrium of moments on the cuboid shown in Figure 5.1 yields the important result that the stress tensor defined here is symmetric.

$$\sigma_{ji} = \sigma_{ij} \quad (5.3)$$

As noted earlier, it is possible to define stress vectors on any plane passing through a material point. To avoid confusion between the definition of the stress tensor at a material point and the stress vectors on any plane passing through the material point, the later will henceforth be referred to as the traction vectors. The stress components shown in Figure 5.1 describe only the traction vectors on three specific (orthonormal) planes passing through the material point. However, once these nine components are specified, it is possible to uniquely determine the traction vector on any plane passing through the material point. Let \mathbf{n} denotes the unit normal of the plane of interest passing through the material point and \mathbf{t} the traction vector (force per unit area) on this plane.

Conditions of equilibrium can be used to establish the following relationship between these quantities:

$$\sigma_{ji} n_j = t_i \quad (5.4)$$

[Equation \(5.4\)](#) establishes clearly that the quantity defined by σ is indeed a second rank tensor because it describes a linear transformation mapping of all vectors in Euclidean vector space into itself. The physical quantity stress tensor is essentially defined through [Eq. \(5.4\)](#).

It is sometimes convenient to decompose a stress tensor into hydrostatic and deviatoric components as

$$\sigma_{ij} = \frac{1}{3} \sigma_{kk} \delta_{ij} + \sigma'_{ij} \quad (5.5)$$

where σ'_{ij} denotes the deviatoric stress tensor, δ_{ij} is the Kronecker delta, and $\frac{1}{3} \sigma_{kk}$ (note the use of summation convention for the repeated indices in this term) denotes the hydrostatic component of the stress tensor. We will find this decomposition particularly useful in studying plastic deformation in metals.

Application of equilibrium conditions to a body in static or quasistatic conditions (i.e., ignoring the inertia term) yields the following field equations:

$$\sigma_{ji,j} + b_i = \sigma_{ij,j} + b_i = 0 \quad (5.6)$$

where \mathbf{b} represents a body force per unit volume applied on the body. Note that in the absence of body forces, [Eq. \(5.6\)](#) takes the simple form $\sigma_{ij,j} = 0$. [Eq. \(5.6\)](#) is in effect an embodiment of the conservation of linear momentum principle.

Kinematics refers to a description of the changes in shape and size undergone by a given body as a function of time. Such descriptions are, by definition, independent of the material behavior since they simply describe the transformation from one shape of the body to another. In this context, it is useful to define a “configuration” of a given body. A configuration of a body is simply the collection of all positions (points in space) occupied by the body at any given time. For example, [Figure 5.2](#) shows two configurations of a body \mathbf{B} at two different instants, 0 and t , denoted as $\mathbf{B}(0)$ and $\mathbf{B}(t)$, respectively. In this figure, $\mathbf{B}(0)$ simply represents the collection of all spatial points occupied by the body at time 0 and is denoted as the initial configuration. $\mathbf{B}(t)$ represents a similar collection of all points occupied by the body at time t and is denoted as the deformed configuration.

In [Figure 5.2](#), \mathbf{x} represents the position occupied by a specific material point in the initial configuration $\mathbf{B}(0)$. The position

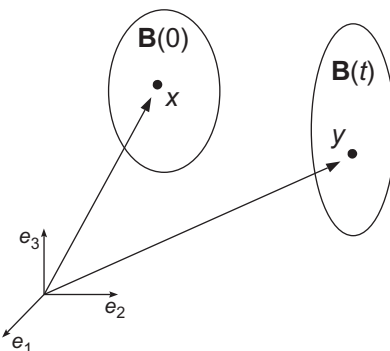


Figure 5.2 Schematic description of motion undergone by a body. $\mathbf{B}(0)$ represents the initial configuration and $\mathbf{B}(t)$ represents the deformed configuration at time t .

occupied by the same material point in the deformed configuration $\mathbf{B}(t)$ is shown as y in this figure. The main restriction we impose in defining different configurations of the body is that we allow one material point to occupy only one spatial position in a given configuration. This means that we assume that there exists a unique invertible mapping function that maps material points in one configuration to those in another configuration. Such a mapping function is called the motion of body \mathbf{B} and can be mathematically expressed as

$$\mathbf{y} = \mathbf{y}(\mathbf{x}, t) \quad (5.7)$$

Furthermore, we assume that the body is comprised of a set of continuous material points that remain continuous in the different deformed configurations. Physically, this implies that a specific material point sees the same material points in its neighborhood during the deformation. This is a reasonable assumption except when there are cracks developing in the material or phase transformations occurring in the material or there is material sliding such as in grain boundary sliding; these processes are excluded from consideration in the present discussion. Mathematically, the continuity assumption implies that the function described in Eq. (5.7) can be differentiated to yield

$$\mathbf{F}(\mathbf{x}, t) = \frac{\partial \mathbf{y}}{\partial \mathbf{x}} \quad (5.8)$$

$\mathbf{F}(\mathbf{x}, t)$ is a second rank tensor, as defined through Eq. (5.8), and is called the deformation gradient tensor. The deformation gradient tensor contains important information regarding the

strain experienced by the body. The difference between the position of a material point in the deformed configuration and its position in the initial configuration is defined as the displacement vector denoted as \mathbf{u} :

$$\mathbf{u} = \mathbf{y} - \mathbf{x} \quad (5.9)$$

The spatial gradient of the displacement vector is denoted by \mathbf{H} and is called the displacement gradient tensor. Mathematically, we can show

$$\mathbf{H}(\mathbf{x}, t) = \frac{\partial \mathbf{u}}{\partial \mathbf{x}} = \mathbf{F} - \mathbf{I} \quad (5.10)$$

Deformation and displacement gradients defined above contain the essential information about the strain experienced by a body. Rigid body translations, for example, do not involve any deformation gradients and therefore do not produce any strain in the body. Multiple definitions of strain are possible and have been proposed and used extensively in the literature. One frequently used strain measure is the Green's definition of strain expressed as

$$\mathbf{E}^G = \frac{1}{2}(\mathbf{F}^T \mathbf{F} - \mathbf{I}) \quad (5.11)$$

For deformations involving small strains, it can be shown that the strain tensor can be approximated as the symmetric component of the displacement gradient tensor as

$$\boldsymbol{\varepsilon} = \frac{1}{2}(\mathbf{H} + \mathbf{H}^T), \quad \varepsilon_{kl} = \frac{1}{2}(u_{k,l} + u_{l,k}) \quad (5.12)$$

In Eq. (5.12) we present the definition of strain in both the tensor notation as well as the indicial notation so that reader can appreciate the correspondence between these notations. In this book, we use both notations, depending on whichever one is more advantageous for the discussion. The reader should also note the introduction of commas in the subscript to denote derivatives in the indicial notation.

Elastic materials are generally defined as those materials that do not exhibit a permanent change of geometry in any closed loop loading/unloading cycle. For these materials, the linear elastic relationship between the stress and strain components can be expressed as

$$\sigma_{ij} = C_{ijkl}\varepsilon_{kl}, \quad C_{ijkl} = C_{jikl} = C_{ijlk} = C_{klji} \quad (5.13)$$

where C represents a positive-definite, fourth-rank, elastic stiffness tensor. Based on Eq. (5.13), the total number of independent elastic constants needed to describe the C tensors, in the most

general case, will be 21. It is often convenient to express the linear elastic stress-strain relations in the following matrix form:

$$\begin{Bmatrix} \sigma_{11} \\ \sigma_{22} \\ \sigma_{33} \\ \sigma_{23} \\ \sigma_{13} \\ \sigma_{12} \end{Bmatrix} = \begin{bmatrix} C_{1111} & C_{1122} & C_{1133} & C_{1123} & C_{1113} & C_{1112} \\ C_{1122} & C_{2222} & C_{2233} & C_{2223} & C_{2213} & C_{2212} \\ C_{1133} & C_{2233} & C_{3333} & C_{3323} & C_{3313} & C_{3312} \\ C_{1123} & C_{2223} & C_{3323} & C_{2323} & C_{2313} & C_{2312} \\ C_{1113} & C_{2213} & C_{3313} & C_{2313} & C_{1313} & C_{1312} \\ C_{1112} & C_{2212} & C_{3312} & C_{2312} & C_{1312} & C_{1212} \end{bmatrix} \begin{Bmatrix} \varepsilon_{11} \\ \varepsilon_{22} \\ \varepsilon_{33} \\ 2\varepsilon_{23} \\ 2\varepsilon_{13} \\ 2\varepsilon_{12} \end{Bmatrix} \quad (5.14)$$

The notation in Eq. (5.14) can be further simplified as

$$\begin{Bmatrix} \sigma_{11} \\ \sigma_{22} \\ \sigma_{33} \\ \sigma_{23} \\ \sigma_{13} \\ \sigma_{12} \end{Bmatrix} = \begin{bmatrix} C_{11} & C_{12} & C_{13} & C_{14} & C_{15} & C_{16} \\ C_{12} & C_{22} & C_{23} & C_{24} & C_{25} & C_{26} \\ C_{13} & C_{23} & C_{33} & C_{34} & C_{35} & C_{36} \\ C_{14} & C_{24} & C_{34} & C_{44} & C_{45} & C_{46} \\ C_{15} & C_{25} & C_{35} & C_{45} & C_{55} & C_{56} \\ C_{16} & C_{26} & C_{36} & C_{46} & C_{56} & C_{66} \end{bmatrix} \begin{Bmatrix} \varepsilon_{11} \\ \varepsilon_{22} \\ \varepsilon_{33} \\ 2\varepsilon_{23} \\ 2\varepsilon_{13} \\ 2\varepsilon_{12} \end{Bmatrix} \quad (5.15)$$

Most engineering materials exhibit additional symmetries that are attributable to the symmetry in their internal structure. The material symmetries (e.g., as a result of symmetries in the crystal lattice) have a profound influence on the number of independent terms in the elastic stiffness tensors. The stiffness matrix for a material exhibiting orthorhombic symmetry in its natural reference frame is expressed as

$$\begin{Bmatrix} \sigma_{11} \\ \sigma_{22} \\ \sigma_{33} \\ \sigma_{23} \\ \sigma_{13} \\ \sigma_{12} \end{Bmatrix} = \begin{bmatrix} C_{11} & C_{12} & C_{13} & 0 & 0 & 0 \\ C_{12} & C_{22} & C_{23} & 0 & 0 & 0 \\ C_{13} & C_{23} & C_{33} & 0 & 0 & 0 \\ 0 & 0 & 0 & C_{44} & 0 & 0 \\ 0 & 0 & 0 & 0 & C_{55} & 0 \\ 0 & 0 & 0 & 0 & 0 & C_{66} \end{bmatrix} \begin{Bmatrix} \varepsilon_{11} \\ \varepsilon_{22} \\ \varepsilon_{33} \\ 2\varepsilon_{23} \\ 2\varepsilon_{13} \\ 2\varepsilon_{12} \end{Bmatrix} \quad (5.16)$$

The elastic stiffness matrix for a material exhibiting transverse isotropy or hexagonal crystal symmetry in its natural reference frame is expressed as

$$\begin{Bmatrix} \sigma_{11} \\ \sigma_{22} \\ \sigma_{33} \\ \sigma_{23} \\ \sigma_{13} \\ \sigma_{12} \end{Bmatrix} = \begin{bmatrix} C_{11} & C_{12} & C_{13} & 0 & 0 & 0 \\ C_{12} & C_{11} & C_{13} & 0 & 0 & 0 \\ C_{13} & C_{13} & C_{33} & 0 & 0 & 0 \\ 0 & 0 & 0 & C_{44} & 0 & 0 \\ 0 & 0 & 0 & 0 & C_{44} & 0 \\ 0 & 0 & 0 & 0 & 0 & (C_{11} - C_{12})/2 \end{bmatrix} \begin{Bmatrix} \varepsilon_{11} \\ \varepsilon_{22} \\ \varepsilon_{33} \\ 2\varepsilon_{23} \\ 2\varepsilon_{13} \\ 2\varepsilon_{12} \end{Bmatrix} \quad (5.17)$$

The stiffness matrix for a material exhibiting cubic crystal symmetry in its natural reference frame is expressed as

$$\left\{ \begin{array}{l} \sigma_{11} \\ \sigma_{22} \\ \sigma_{33} \\ \sigma_{23} \\ \sigma_{13} \\ \sigma_{12} \end{array} \right\} = \left[\begin{array}{cccccc} C_{11} & C_{12} & C_{12} & 0 & 0 & 0 \\ C_{12} & C_{11} & C_{12} & 0 & 0 & 0 \\ C_{12} & C_{12} & C_{11} & 0 & 0 & 0 \\ 0 & 0 & 0 & C_{44} & 0 & 0 \\ 0 & 0 & 0 & 0 & C_{44} & 0 \\ 0 & 0 & 0 & 0 & 0 & C_{44} \end{array} \right] \left\{ \begin{array}{l} \varepsilon_{11} \\ \varepsilon_{22} \\ \varepsilon_{33} \\ 2\varepsilon_{23} \\ 2\varepsilon_{13} \\ 2\varepsilon_{12} \end{array} \right\} \quad (5.18)$$

Equation (5.18) can also be expressed as

$$C_{ijkl} = C_{12}\delta_{ij}\delta_{kl} + C_{44}(\delta_{ik}\delta_{jl} + \delta_{il}\delta_{jk}) + (C_{11} - C_{12} - 2C_{44}) \sum_{r=1}^3 \delta_{ir}\delta_{jr}\delta_{kr}\delta_{lr} \quad (5.19)$$

As the final example, the elastic stiffness matrix for materials that exhibit isotropic properties can be expressed as

$$C_{ijkl} = C_{12}\delta_{ij}\delta_{kl} + C_{44}(\delta_{ik}\delta_{jl} + \delta_{il}\delta_{jk}) \quad (5.20)$$

Comparison of Eqs. (5.19) and (5.20) allows us to define an anisotropy ratio for cubic crystals as

$$A = \frac{2C_{44}}{C_{11} - C_{12}} \quad (5.21)$$

Note that for the isotropic case, $A = 1$. The deviation of A from a value of one serves as a measure of the degree of elastic anisotropy in the cubic crystal.

5.3 Concept of Homogenization

As already stated at the beginning of Chapter 2, it is generally assumed that the composite material structures of interest exhibit at least two well separated length scales. Furthermore, we will assume that the lower length scale is significantly larger (by several orders of magnitude) than the atomic length scales and that the concepts of continuum mechanics described above are applicable at this length scale. Averaging methods underlie a variety of homogenization methods. There is a vast literature in this general area that the reader might refer (Refs. [15,20–23]). These homogenization methods might include the rule of mixtures (Voigt [24]), the inverse rule of mixtures [25], the Mori–Takana method [26], Kerner’s method [27], the dilute distribution model [28], the self-consistent model [29], etc. Excellent treatment of the overall subject may be found in Refs. [30,31]. The general

framework resulting from this approach may be applied to a range of material responses with similar types of governing field equations; these include fluid flow, diffusion, electromagnetism, and elasticity [31].

To define the concept of effective properties more precisely, we hypothesize that the continuum theories developed at the mesoscale are also correct at the RVE scale. For example, in the theory of elasticity we require that an effective stiffness tensor satisfies

$$\bar{\sigma} = \mathbf{C}^{\text{eff}} \bar{\varepsilon} \quad (5.22)$$

at the RVE scale, where the volume averaged values of stress and strain are used as the homogenized quantities:

$$\bar{\sigma} = \frac{1}{V(\Omega)} \int_{\Omega} \sigma(\mathbf{x}) d\mathbf{x}, \quad \bar{\varepsilon} = \frac{1}{V(\Omega)} \int_{\Omega} \varepsilon(\mathbf{x}) d\mathbf{x} \quad (5.23)$$

The reader should note that we are using a bar on the top of a quantity to denote its volume average. The reader will also note that, in general, $\mathbf{C}^{\text{eff}} \neq \bar{\mathbf{C}}$. In fact, taking the average stiffness as the effective stiffness is equivalent to assuming the commonly used rule of mixtures. An alternative homogenization method that is often used is the inverse rule of mixtures. For most material structures neither of these approaches yields an accurate effective property tensor, but in certain cases they are good estimates.

5.4 Higher Order Homogenization Theory

We now shift our focus to a sophisticated higher order homogenization framework based on the statistical continuum theories developed by Kröner [21,32]. Our interest in this specific framework comes from the fact that this theory allows one to account for the details of the material hierarchical structure in the form of the n -point spatial correlations discussed in the earlier chapters of this book.

We start with the notion that a representative volume element of a composite can be identified. We then invoke an additive decomposition of the strain field in the RVE into an average quantity and a perturbation from the average as

$$\varepsilon(\mathbf{x}) = \bar{\varepsilon} + \varepsilon'(\mathbf{x}), \quad \bar{\varepsilon}' = \mathbf{0} \quad (5.24)$$

In the rest of this chapter, we will continue to denote the perturbed quantities with a prime as the superscript. Without

loss of generality, the local perturbation in the strain field can be expressed in terms of a fourth-rank polarization tensor, \mathbf{a} , as

$$\boldsymbol{\varepsilon}'(\mathbf{x}) = \mathbf{a}(\mathbf{x})\bar{\boldsymbol{\varepsilon}}, \quad \bar{\mathbf{a}} = \mathbf{0} \quad (5.25)$$

Using Eqs. (5.13), (5.22), and (5.23), we can derive an expression for the effective stiffness tensor as [1]

$$\mathbf{C}^{\text{eff}} = \bar{\mathbf{C}}\bar{\mathbf{a}} + \bar{\mathbf{C}} = \mathbf{C}^r + \bar{\mathbf{C}}' + \bar{\mathbf{C}}'\bar{\mathbf{a}}, \quad \mathbf{C}(\mathbf{x}) = \mathbf{C}^r + \mathbf{C}'(\mathbf{x}) \quad (5.26)$$

where \mathbf{C}^r denotes a reference value and \mathbf{C}' denotes the perturbation from the reference stiffness tensor.

The central challenge in the homogenization theory can now be formulated as the derivation of a suitable expression for the polarization tensor \mathbf{a} relating the averaged strain tensor to the perturbation of the local strain tensor from the averaged quantity (Eq. (5.25)). The perturbation in the strain field can be related to a perturbation in the displacement field (Eq. (5.12)) as

$$\varepsilon'_{kl} = \frac{1}{2}(u'_{k,l} + u'_{l,k}) \quad (5.27)$$

The field equation for the perturbed displacement field can be derived from the equilibrium conditions (Eq. (5.6) with no body forces) as [1]

$$\sigma_{ij,j} = [(C_{ijkl}^r + C'_{ijkl})(\bar{\varepsilon}_{kl} + \varepsilon'_{kl})]_j = C_{ijkl}^r \varepsilon'_{kl,j} + C'_{ijkl,j} \bar{\varepsilon}_{kl} + (C'_{ijkl} \varepsilon'_{kl})_j = 0 \quad (5.28)$$

$$C_{ijkl}^r u'_{k,lj} + F_i = 0, \quad F_i = C'_{ijkl,j} \bar{\varepsilon}_{kl} + (C'_{ijkl} \varepsilon'_{kl})_j \quad (5.29)$$

The field equation in Eq. (5.28) was complicated by the fact that it expresses the equilibrium requirements in the original heterogeneous composite material structure. The greatest benefit of Eq. (5.29) is that allows us to interpret the governing field equation in (5.29) as a stress analyses problem on a homogeneous material exhibiting the reference stiffness tensor as its property and being subjected to a heterogeneous body force per unit volume of F_i . Since Eqs. (5.28) and (5.29) are mathematically completely equivalent, the solution for Eq. (5.29) will also serve as the solution for Eq. (5.28).

Furthermore, Eq. (5.29) allows for a solution using the Green's function method. The main strategy in this method will be to first solve the governing partial differential equation in (5.29) for a unit body force and then to obtain the solution for

u'_i as a convolution integral over the body force distribution defined in the governing field equation (5.29). In other words, the strategy here can be summarized through the following equations:

$$C_{ijkl}^r G_{km,lj}(x - x') + \delta(x - x')\delta_{im} = 0 \quad (5.30)$$

$$u'_k(x) = \int_V G_{ki}(x - x') F_i(x') dx' \quad (5.31)$$

Eq. (5.30) defines the fundamental Green's function solution, G_{km} , as the k th component of the displacement field at location \mathbf{x} in a material whose elastic stiffness is defined by C_{ijkl}^r when a unit body force with a single m th component is applied at position \mathbf{x}' . If C_{ijkl}^r is selected to be isotropic, the solution for Green function, G_{km} , can be derived as [1]

$$G_{km}(\tilde{\mathbf{x}}) = \frac{1}{8\pi \mu^r(\lambda^r + 2\mu^r)} \left\{ \frac{(\lambda^r + 3\mu^r)}{|\tilde{\mathbf{x}}|} \delta_{km} + \frac{(\lambda^r + \mu^r)}{|\tilde{\mathbf{x}}|^3} \tilde{x}_k \tilde{x}_m \right\} \quad (5.32)$$

where $\tilde{\mathbf{x}} = \mathbf{x} - \mathbf{x}'$ and λ^r and μ^r are the Lame moduli used in the description of the isotropic elastic stiffness components of the reference tensor C_{ijkl}^r . The corresponding perturbation in the strain field can be computed from Eq. (5.31) as

$$\begin{aligned} \varepsilon'_{kl}(\mathbf{x}) &= \int_V \frac{1}{2} (G_{ki,l}(\mathbf{x} - \mathbf{x}') + G_{li,k}(\mathbf{x} - \mathbf{x}')) F_i(\mathbf{x}') d\mathbf{x}' \\ &= \int_V \frac{1}{2} (G_{ki,l}(\mathbf{x} - \mathbf{x}') + G_{li,k}(\mathbf{x} - \mathbf{x}')) \\ &\quad [C'_{ijmn}(\mathbf{x}')_j \bar{\varepsilon}_{mn} + (C'_{ijmn}(\mathbf{x}') \varepsilon'_{mn}(\mathbf{x}'))_j] d\mathbf{x}' \end{aligned} \quad (5.33)$$

Substituting Eq. (5.33) into Eq. (5.25) and employing $\tilde{\mathbf{x}} = \mathbf{x} - \mathbf{x}'$ permits the extraction of the following recursive expression for \mathbf{a} :

$$\mathbf{a}_{klmn}(\mathbf{x}) = \int_V \frac{1}{2} (G_{ki,l}(\tilde{\mathbf{x}}) + G_{li,k}(\tilde{\mathbf{x}})) [C'_{ijmn}(\mathbf{x}') + C'_{ijpq}(\mathbf{x}') \mathbf{a}_{pqmn}(\mathbf{x}')]_j d\mathbf{x}' \quad (5.34)$$

Note that the Green function has a singularity ($G_{km}(\tilde{\mathbf{x}}) \rightarrow \infty$ as $\tilde{\mathbf{x}} \rightarrow 0$), and therefore the integral in Eq. (5.34) needs particular attention. Mathematically, this integral is said to have a principal value in the neighborhood of $\tilde{\mathbf{x}} = 0$. Moreover, since the equation is recursive in \mathbf{a} , repeated substitution of the expression in itself produces an infinite series.

Addressing these issues properly, one can show that Eq. (5.34) can be cast as the following infinite series [1]:

$$a_{klmn}(\mathbf{x}) = - \int_V \Gamma_{klkj}(\tilde{\mathbf{x}}) \left[C'_{ijmn}(\mathbf{x}') + C'_{ijpq}(\mathbf{x}') \left(- \int_V \Gamma_{pquv} \left[C'_{uvmn}(\mathbf{x}'') + C'_{uvrs}(\mathbf{x}'') \int_V \dots \right] d\mathbf{x}'' \right) \right] d\mathbf{x}' \quad (5.35)$$

with

$$\begin{aligned} \Gamma_{klkj}(\tilde{\mathbf{x}}) &= E_{klkj} \delta(\tilde{\mathbf{x}}) + I_{klkj}^\infty \delta(\tilde{\mathbf{x}}) + \Phi_{klkj}(\tilde{\mathbf{x}}) \\ E_{klkj} &= \text{Lim}_{|\mathbf{x} - \mathbf{x}'| \rightarrow 0} \left(\int_S \frac{1}{2} (G_{ki,l}(\tilde{\mathbf{x}}) + G_{li,k}(\tilde{\mathbf{x}})) n_j dS \right) \\ I_{klkj}^\infty &= \text{Lim}_{|\mathbf{x} - \mathbf{x}'| \rightarrow \infty} \left(\int_S \frac{1}{2} (G_{ki,l}(\tilde{\mathbf{x}}) + G_{li,k}(\tilde{\mathbf{x}})) \left[C'_{ijmn}(\mathbf{x}') \right] n_j dS \right) \\ \Phi_{klkj}(\mathbf{x} - \mathbf{x}') &= \frac{1}{2} (G_{ki,lj}(\tilde{\mathbf{x}}) + G_{li,kj}(\tilde{\mathbf{x}})) \end{aligned} \quad (5.36)$$

where $\delta(\tilde{\mathbf{x}})$ is 1 if $\tilde{\mathbf{x}} = \mathbf{0}$ and 0 otherwise. Substitution of Eq. (5.35) in Eq. (5.26) produces the desired series expression for the effective stiffness [1]

$$\mathbf{C}^{\text{eff}} = \overline{\mathbf{C}} - \overline{\mathbf{C}' \mathbf{T} \mathbf{C}'} + \overline{\mathbf{C}' \mathbf{T} \mathbf{C}' \mathbf{T} \mathbf{C}'} - \dots \quad (5.37)$$

It should be noted that the bars on the top of the different terms denote very complex volume averages or ensemble averages (invoking the assumptions of ergodicity and statistical homogeneity at the lower length scale). In particular the bars on the higher order terms denote multiple nested volume integrals (Eq. (5.35)) or multivariate ensemble averages. Therefore, the evaluation of these terms is nontrivial. Some details of these computations are presented in Ref. [1]. It is also worth noting that Eq. (5.37) can be recast as [33]

$$\mathbf{C}^{\text{eff}} = \mathbf{C}^r + \overline{\mathbf{C}' (\mathbf{I} + \mathbf{\Gamma} \mathbf{C}')^{-1}} \quad (5.38)$$

References

- [1] Adams BL, Kalidindi SR, Fullwood D. Microstructure sensitive design for performance optimization. Waltham, MA, USA: Butterworth-Heinemann; 2012.
- [2] Adams BL, Olson T. Mesostructure—properties linkage in polycrystals. *Prog Mater Sci* 1998;43(1):1–88.

- [3] Castañeda PP, Telega JJ, Gamin B. Nonlinear homogenization and its applications to composites, polycrystals and smart materials. Springer; 2004.
- [4] Fullwood DT, Adams BL, Kalidindi SR. A strong contrast homogenization formulation for multi-phase anisotropic materials. *J Mech Phys Solids* 2008;56(6):2287–97.
- [5] Luscher DJ, McDowell DL, Bronkhorst CA. A second gradient theoretical framework for hierarchical multiscale modeling of materials. *Int J Plast* 2010;26(8):1248–75.
- [6] McDowell DL, et al. Plasticity-related microstructure-property relations for materials design. *Key Eng Mater* 2007;340–341:21–30.
- [7] McDowell DL, Olson GB. Concurrent design of hierarchical materials and structures. *Sci Model Simul* 2008;15:207–40.
- [8] Milton GW. The theory of composites. Cambridge Monographs on Applied and Computational Mathematics; 2001.
- [9] Ponte Castañeda P. Second-order homogenization estimates for nonlinear composites incorporating field fluctuations: I—theory. *J Mech Phys Solids* 2002;50(4):737–57.
- [10] Ponte Castañeda P. Second-order homogenization estimates for nonlinear composites incorporating field fluctuations: II—applications. *J Mech Phys Solids* 2002;50(4):759–82.
- [11] Roters F, et al. Overview of constitutive laws, kinematics, homogenization and multiscale methods in crystal plasticity finite-element modeling: Theory, experiments, applications. *Acta Mater* 2010;58(4):1152–211.
- [12] Talbot DRS, Willis JR. Upper and lower bounds for the overall response of an elastoplastic composite. *Mech Mater* 1998;28(1–4):1–8.
- [13] Talbot DRS, Willis JR. Upper and lower bounds for the overall properties of a nonlinear composite dielectric. II. Periodic microgeometry. *Proc Math Phys Sci* 1994;447(1930):385–96.
- [14] Talbot DRS, Willis JR, Nesi V. On improving the Hashin–Shtrikman bounds for the effective properties of three-phase composite media. *IMA J Appl Math* 1995;54(1):97–107.
- [15] Willis JR. Variational and related methods for the overall properties of composites. *Adv Appl Mech* 1981;21:1–78.
- [16] Fullwood DT, et al. Microstructure sensitive design for performance optimization. *Prog Mater Sci* 2010;55(6):477–562.
- [17] Bouvard J, et al. Review of hierarchical multiscale modeling to describe the mechanical behavior of amorphous polymers. *J Eng Mater Technol* 2009;131(4):041206.
- [18] Elliott J. Novel approaches to multiscale modelling in materials science. *Int Mater Rev* 2011;56(4):207–25.
- [19] Hao S, et al. Multi-scale constitutive model and computational framework for the design of ultra-high strength, high toughness steels. *Comput Methods Appl Mech Eng* 2004;193(17):1865–908.
- [20] Hill R. The elastic behavior of a crystalline aggregate. *Proc R Soc Lond A Math Phys Sci* 1952;65:349–54.
- [21] Kröner E. Bounds for effective elastic moduli of disordered materials. *J Mech Phys Solids* 1977;25:137–55.
- [22] Hashin Z, Shtrikman S. A variational approach to the theory of the elastic behaviour of multiphase materials. *J Mech Phys Solids* 1963;11(2):127–40.
- [23] Suquet P. Elements of homogenization for inelastic solid mechanics Lecture Notes in Physics 272 In: Sanchez-Palencia E, Zaoui A, editors. Homogenization techniques for composite media. Berlin: Springer Verlag; 1987. p. 193–278.

- [24] Voigt W. Lehrbuch der Krystallphysik. Teubner xxiv, 1910.
- [25] Reuss A. Berechnung der Fliebgrenze von Mischkristallen auf Grund der Plastizitätsbedingung für Einkristalle. Z. Angew. Math. Mech. 1929;9:49–58.
- [26] Mori T, Tanaka K. Average stress in matrix and average elastic energy of materials with misfitting inclusions. Acta Metall 1973;21:571–4.
- [27] Kerner EJ. The elastic and thermo-elastic properties of composite media. Proc Phys Soc Ser B 1956;69(8):808–13.
- [28] Eshelby JD. The determination of the elastic field of an ellipsoidal inclusion, and related problems. Proc R Soc Lond A 1957;241:376–96.
- [29] Hill R. A self-consistent mechanics of composite materials. J Mech Phys Solids 1965;13:213–22.
- [30] Nemat-Nasser S, Hori M. Micromechanics: overall properties of heterogeneous materials. 2nd ed. Amsterdam: Elsevier; 1999.
- [31] Milton GW. Cambridge Monographs on Applied and Computational Mathematics The theory of composites. Cambridge: Cambridge University Press; 2002.
- [32] Kroner E. Statistical modelling. In: Gittus J, Zarka J, editors. Modelling small deformations of polycrystals. London: Elsevier Science Publishers; 1986. p. 229–91.
- [33] Torquato S. Random heterogeneous materials. New York, NY: Springer-Verlag; 2002.

STRUCTURE–PROPERTY LINKAGES

It is hoped that the reader appreciates from the prior discussion the importance and promise of multiscale modeling [1–4] as the key ingredient in our plans for dramatically accelerating the design, development, and deployment of new/improved materials in emerging technologies [5–9]. A number of recently announced national research strategic initiatives (e.g., [5,8,9]) are being built on the premise that an increased use of multiscale materials modeling can dramatically reduce the need for extensive (and often expensive) experimentation that dominates the current materials development efforts. However, the main factors impeding the highly desired increased utilization of multiscale modeling have been discussed already in Chapter 1. Briefly, they can be collected into three groups [10]: (i) Model Maturity (i.e., the accuracy and reliability of available models), (ii) Model Interoperability (i.e., ability of the models covering multiple scales and physics to be strung together to work seamlessly), and (iii) Model Inversion (i.e., ability to address high value problems of interest in materials and process design that target improvements in specific performance targets). It should be noted that tremendous progress has indeed been made in being able to numerically simulate a broad range of materials phenomena using sophisticated physics-based modeling approaches [1–4,11–15]. However, it is essential to address the main impediments described earlier, if we are to realize the full benefits from these modeling approaches in advanced materials development efforts.

It has already been mentioned several times in this book that modern data-science tools and concepts offer a promising new avenue for addressing most of the impediments described earlier. In the context of advanced materials development efforts, the central goal of Data Analytics is the extraction of robust and reliable process–structure–property (PSP) linkages that capture quantitatively the roles of different unit manufacturing

(or processing) steps on the salient measures of the material hierarchical structure that in turn control the properties of interest (or performance characteristics desired in service). In this regard, it is extremely important to cast the desired PSP linkages in computationally efficient forms that allow direct integration into the tools typically employed by practitioners in the product design and manufacturing fields. In other words, the PSP linkages of interest are not likely to be employed in the forms developed in the advanced numerical tools [1–4] or the sophisticated homogenization theories [16–21], but more likely in the reduced-order forms (also called surrogate models or metamodels) that allow practical solutions to inverse problems of materials and process design. In recent years, a data-centered framework has emerged for capturing highly accurate PSP linkages relevant to a broad range of materials phenomena [22–33].

Figure 6.1 depicts schematically the philosophy described earlier. The top row of boxes and arrows in this figure depict the current workflows typically employed when utilizing multiscale materials simulations in the materials development efforts. The focus in these efforts is generally on numerical strategies for solving accurately the governing field equations (e.g., using finite element approaches), while satisfying the lower length scale material constitutive laws and the imposed boundary and initial conditions. Not surprisingly, the computational requirements of such multiscale materials models are usually very high for most advanced materials with rich hierarchical internal structures. Furthermore, there is significant uncertainty associated with the predictions of these models as a number of

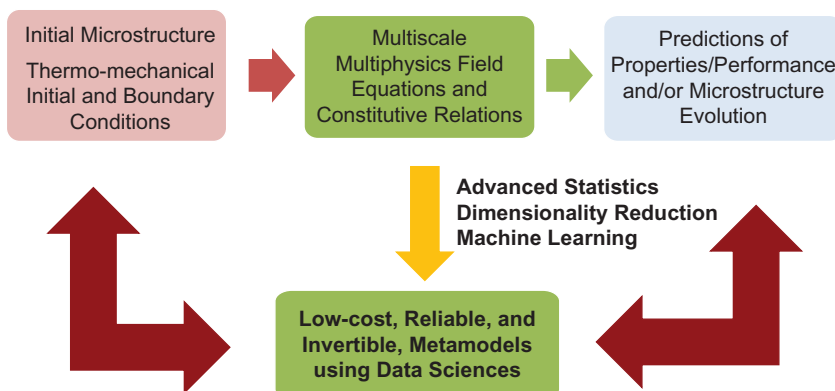


Figure 6.1 Schematic depiction of the promise and potential role of data sciences in facilitating accelerated in silico explorations of materials design.

assumptions had to be made in building these models. Therefore, the best way to utilize these multiscale models is to employ them to provide reliable guidance to the materials development efforts. In other words, the focus needs to be shifted from accuracy of predictions to the reliability of guidance. This is where the data-centered, invertible, surrogate models are likely to play an important role.

It should also be pointed out that there isn't enough attention paid to systematic learning from the multiscale simulations in the currently employed protocols. In other words, in any typical design and optimization effort, solutions of the governing field equations are generally obtained for multiple trials of the material structures. However, most of the solutions are routinely discarded as that particular trial did not produce the desired property or performance. It is important to recognize that even when the trial did not produce the desired solution, there is a great deal of information in the solution obtained. In other words, we should be actively learning from failed attempts at materials design and optimization. Since a significant computational cost was expended in arriving at the solution, it only behooves us to learn as much as we can from the solution obtained. Machine learning techniques and data-driven methods are ideally suited for this task, and can lead to dramatic savings in both time and effort, when integrated properly into the materials development efforts.

This chapter demonstrates the integration of all of the foundational concepts and notions described in the previous chapters in an effort to demonstrate the utility and promise of data-science approaches in arriving at high value, low computational cost, robust, and reliable structure–property linkages (formulated as metamodels or surrogate models). In doing so, we also aim to integrate high value information already available in the form of validated physics-based models, wherever possible. Indeed, our goal will be to judiciously fuse the legacy domain knowledge already available (e.g., the homogenization theories presented in Chapter 5) with the data-driven approaches (presented in Chapters 2, 3, and 4).

6.1 Data-Driven Framework for Homogenization Linkages

Let us start with homogenization linkages. As described in earlier chapters, the concept homogenization inherently seeks to replace the heterogeneous (but statistically homogeneous)

material structure at the lower length scale with an equivalent homogenized material whose properties mimic the properties of the actual material as closely as possible. Homogenization plays a critical role in communicating high value information from the lower length scale to the higher length scale. Obviously, as one might expect this will involve some sort of averaging. As specific examples, see Eqs. (5.37) and (5.38), where the bars on the top of the various terms indicate nested volume averages or multivariate ensemble averages.

As a specific example, let us examine the second term in the series of Eq. (5.37) in detail

$$\overline{\mathbf{C}'\mathbf{T}\mathbf{C}'} = \frac{1}{V} \int_V \int_V \mathbf{C}'(\mathbf{x}) \Gamma(\mathbf{t}) \mathbf{C}'(\mathbf{x}') d\mathbf{x}' d\mathbf{x} \quad (6.1)$$

where $\mathbf{C}'(\mathbf{x})$ denotes the perturbation in the local property (compared to a selected reference property) at spatial position \mathbf{x} in the microstructure volume V , $\mathbf{t} = (\mathbf{x} - \mathbf{x}')$, and $\Gamma(\mathbf{t})$ is a symmetric second derivative of a suitably defined Green's function for the underlying physics of the problem at hand (cf. Chapter 5). Note that for convenience, we switched the symbol $\tilde{\mathbf{x}}$ to \mathbf{t} in writing Eq. (6.1) from Eq. (5.37). This is because we specifically want to treat \mathbf{t} as a vector (i.e., difference between two spatial points) and not be confused with spatial points (such as \mathbf{x}' and \mathbf{x}). Although Eqs. (5.37) and (5.38) were derived for the elastic response of composites, several reports in literature have shown that they could be applied to nonlinear material response [19,34,35] with appropriate reinterpretation of the terms in the series.

As noted earlier, the evaluation of the integral in Eq. (6.1) is nontrivial. In an effort to simplify this, we make use of the statistical measures we have developed in Chapter 3. It becomes highly beneficial to recognize that the integral in Eq. (6.1) can be reinterpreted using 2-point spatial correlations as

$$\overline{\mathbf{C}'\mathbf{T}\mathbf{C}'} = \langle \mathbf{C}'(\mathbf{x}) \Gamma(\mathbf{t}) \mathbf{C}'(\mathbf{x}') \rangle = \iint_{HH\Psi(\mathbf{t})} f(h, h') |\mathbf{t}| \mathbf{C}'(h) \Gamma(\mathbf{t}) \mathbf{C}'(h') dh dh' dt \quad (6.2)$$

A large number of things have transpired in going from Eq. (6.1) to Eq. (6.2). Let us examine these in detail slowly. First, we imply that the volume average (see Eq. (6.1)) can be replaced with the ensemble average denoted by $\langle \cdot \rangle$. In the ensemble average, each sampling involves a random selection of a pair of spatial points $(\mathbf{x}, \mathbf{x}')$ from the volume V , and the

evaluation of the term $\mathbf{C}'(\mathbf{x})\Gamma(\mathbf{t})\mathbf{C}'(\mathbf{x}')$, with $\mathbf{t} = (\mathbf{x} - \mathbf{x}')$. Of course, the ensemble average will equal the volume average shown in Eq. (6.1) only when a sufficiently large number of samples have been evaluated and averaged. This is often referred to as the ergodic assumption.

Next, we recognize that the ensemble average can be naturally expressed using the spatial correlations as shown in Eq. (6.2). In this expression, $f(h, h'|\mathbf{t})$ reflects the probability density associated with finding local states h and h' separated by vector \mathbf{t} . Essentially this is the description of the 2-point spatial correlations where the variables h , h' , and \mathbf{t} are all treated as continuous variables. In other words, the f_r^{np} we studied in Chapter 3 is the discretized version of $f(h, h'|\mathbf{t})$. Also, the reader might note that $f(h, h'|\mathbf{t})$ reflects the probability densities, while f_r^{np} reflects the corresponding probabilities (as a consequence of binning both the local state spaces denoted by H as well as the vector space denoted by $\Psi(\mathbf{t})$; discussed in Chapter 3). Furthermore, note that \mathbf{C}' at any spatial point \mathbf{x} depends only on the local state at that point. Therefore, each sampling of local states h and h' separated by vector \mathbf{t} contributes exactly $\mathbf{C}'(h)\Gamma(\mathbf{t})\mathbf{C}'(h')$ to the ensemble total, which when factored by $f(h, h'|\mathbf{t})dh dh' dt$ (denoting the number fraction of the samples that realize this particular combination of conditions) yields the exact contribution to the ensemble average from all such instances (i.e., local states h and h' separated by vector \mathbf{t}). Therefore, one can see that the integral in Eq. (6.1) can be conveniently expressed as shown in Eq. (6.2) making use of the 2-point spatial correlations. Furthermore, it should be noted that the product $\mathbf{C}'(h)\Gamma(\mathbf{t})\mathbf{C}'(h')$ is completely independent of the specific material structure being studied. In other words, this product can be precomputed for every possible combination of the local states of interest separated by every possible vector of interest, and provided as a database (or a library of values) that can be readily accessed by any multiscale material modeling effort. Of course, serious thought has to be given on how to organize this database (likely to include a very large number of values because of the combinatorial nature of the term of interest) so that it can be accessed and utilized with the least computational cost. That will become our main focus in the later sections of this chapter.

Indeed, the most important and remarkable feature of Eq. (6.2) is that the influence of the material structure on the effective property of interest comes exclusively from the 2-point spatial correlations. Furthermore, it can be shown that every term in the series shown in Eq. (5.37) can be expressed similarly

where the role of the material structure enters the homogenization relationship exclusively through a specific set of n -point spatial correlations [36]. For example, the third term in the series of Eq. (5.37) only needs 3-point spatial correlations as input from the material structure. Note also that the 1-point statistics enter Eq. (5.37) through the first term.

Next, let us take advantage of the digital representations of the n -point spatial correlations we have learnt in Chapter 3. Employing these concepts, Eq. (6.2) can be rewritten as

$$\langle \mathbf{C}' \Gamma \mathbf{C}' \rangle = \sum_{r,n,p} \aleph_r^{np} f_r^{np} \quad (6.3)$$

where the microstructure-independent \aleph_r^{np} capture the underlying physics governing the multiscale phenomenon being investigated.

Although the expression in Eq. (6.3) looks very simple, there are a few impediments to using it in multiscale materials modeling efforts. As discussed in Chapters 2 and 3, it is possible to experimentally estimate f_r^{np} for a large number of hierarchical material systems. In fact, some authors have proposed very clever schemes to assemble the requisite material structure statistics in 3-D using 2-D measurements on a limited number of oblique sections into the sample [37]. The central complexity in the practical implementation of Eq. (6.3) is in the computation of the \aleph_r^{np} coefficients. Not only does this require the computation of a very large number of the coefficients (corresponding to all combinations of n, p , and r), it also needs a rigorous treatment of the principal value problem mentioned toward the end of Chapter 5. Furthermore, it is also known that the series in Eq. (5.37) exhibits good convergence properties only for small to moderate contrast in local properties. The strong dependence of the convergence of the series with the contrast can be reconciled at least qualitatively by noting that the product $\Gamma \mathbf{C}'$ is being appended to each term to get to the next higher-order term, and that this term approximately scales with $\mathbf{C}'^{-1} \mathbf{C}'$, which essentially is a measure of the contrast. This also explains why the answers from the homogenization theory are very sensitive to the selection of \mathbf{C}' , and why the use of a simple average of the properties of the different constituents for the reference value of the property often constitutes a good choice in this theory [38].

In the approach presented in this book, we address these challenges using emerging concepts in data sciences. First we recognize that there could be a large number of redundancies in the expression of the n -point spatial correlations [39,40] (discussed also in Chapter 3). Indeed, the PCA techniques

presented in Chapter 4 can be used to identify any linear dependencies among the spatial correlations in a computationally effective manner. Protocols for this have been already described in Chapter 4. Since PCA is essentially a linear transformation, one can see that its usage will lead to recasting [Eq. \(6.3\)](#) as

$$\langle \mathbf{C}' \mathbf{T} \mathbf{C}' \rangle \approx A_o + \sum_i A_i \alpha_i \quad (6.4)$$

where α_i denote the weights (or scores) of the principal components of the spatial correlations (cf. Chapter 4) and A_i denote their corresponding influences on the effective property of interest. Physically, α_i capture the most salient information on the microstructure in a given ensemble of microstructures of interest, selected in an objective (data-driven) approach. Because [Eq. \(6.4\)](#) represents essentially a remapping of the linkages in [Eq. \(6.3\)](#), the influence coefficients A_i would still be independent of the details of the material structure. Also implicit in [Eq. \(6.4\)](#) is the truncation of the series to include only the dominant terms arising from PCA.

Although [Eq. \(6.4\)](#) shows the treatment for 2-point statistics, it is hoped that the reader can see that the above treatment can be applied in the exact same manner to all of the terms in the series in [Eq. \(5.37\)](#). Of course, in the higher-order terms of the series, we need to include higher-order spatial statistics. Since α_i are being used here to denote the weights of the principal components arising from a consideration of all of the n -point spatial correlations included in the analyses, the low-dimensional data-driven form of [Eq. \(5.37\)](#) looks identical to that shown in [Eq. \(6.4\)](#):

$$C^* \approx A_o + \sum_i A_i \alpha_i \quad (6.5)$$

where C^* now denotes a specific tensorial component of the effective property of interest.

The goals of the data-science approach are to identify the important terms that make dominant contributions to [Eq. \(6.5\)](#) and estimate the corresponding values of the influence coefficients, A_i . Our goal is to keep the structure of [Eq. \(6.5\)](#) relatively simple with a small number of terms so that we can produce computationally low-cost structure–property linkages. It is also important to note that the relatively simple algebraic structure of [Eq. \(6.5\)](#) allows us to potentially invert the relationships, where we seek to identify specific material structures that correspond to a targeted value of the effective property.

As noted earlier, one of the limitations of Eq. (6.5) is that it is derived from the weak contrast expansion of the homogenization theory expressed in Eq. (5.37). In an effort to alleviate this limitation, we could alter the structure of Eq. (6.5) as [41]

$$C^* \approx \tilde{A}_o + \sum_i \tilde{A}_i \tilde{\alpha}_i \quad (6.6)$$

where $\tilde{\alpha}_i$ denote certain polynomial combinations of α_j . In other words, we will allow the inclusion of different polynomial groupings of α_j in the surrogate model to be extracted, if they produced significant contributions to the effective property of interest. This extension of Eq. (6.5) was partially motivated by the fact that the higher-order spatial correlations can be seen as products of lower-order spatial correlations in the limiting case of perfectly disordered materials. Since our interest here extends far beyond perfectly disordered materials, we are hypothesizing that simple polynomials of the weights of the principal components would capture these complex interdependencies to a certain extent.

It is important to note the sequence of operations in the proposed approach. In this approach, the PCA is first applied on the spatial correlations without any consideration of the information on the properties. In other words, this is an unsupervised dimensionality reduction based exclusively on structure metrics. Since there was no consideration of properties in the PCA step, there is no implicit assumption of a linear dependence between PC scores and properties. That is why we are seeking nonlinear linkages between PC scores (representing structure) and the properties of interest through Eq. (6.6). It is also entirely possible to employ other approaches that combine these two steps in a single supervised, nonlinear, dimensionality reduction step. This could be a focus for future efforts in this emerging area.

6.2 Main Steps of the Data-Driven Framework for Homogenization Linkages

Successful implementation of the framework presented in the previous section would require objective evaluation of the importance of a large number of structure measures in controlling the value of a selected effective property of interest and identifying the specific terms that make the strongest

contributions. This is accomplished by performing a large number of regressions to calibration dataset, which is often produced using a numerical simulation tool (e.g., finite element models). The novel data-science approach described here would involve three main steps: (i) generating a calibration dataset comprising an ensemble of representative microstructures of interest and simulating their mechanical responses using suitable physics-based numerical models, (ii) extracting objective, reduced-order, quantitative measures of the microstructures used as input to (i), and (iii) establishing validated structure–property linkages using the measures identified in (ii). These steps are described in more detail as follows.

The first step involves the creation of an ensemble of microstructures that are representative of the specific application, and evaluating their performance characteristics using suitable tools (e.g., finite element models). The microstructures can either be extracted from measurements or generated synthetically. Either way, the microstructure needs to be discretized and digitized suitably, resulting in m_s^n introduced in Chapter 2. The properties of interest corresponding to each microstructure can be obtained either from direct measurements or from mathematical/numerical models.

For the second step, we compute the spatial correlation of interest for each microstructure used in the first step using the methods described in Chapter 2, and perform a PCA following the protocols outlined in Chapter 4. Consequently, at the end of the second step, we would have assembled a dataset. Each data point in this dataset captures the important structure measures as well as the properties of interest for each microstructure studied in the first step. Each data point may be expressed as $(P_1^{(k)}, P_2^{(k)}, \dots, P_M^{(k)}, \alpha_1^{(k)}, \alpha_2^{(k)}, \dots, \alpha_{\tilde{R}}^{(k)})$, where (k) indexes the microstructures included in the analyses, $P_i^{(k)}$ denotes a specific macroscale property of interest (we assume that there are M macroscale properties of interest), and $\alpha_i^{(k)}$ denote the reduced-order representation of microstructure (i.e., PC weights). Consider a dataset with K (i.e., $k = 1, 2, \dots, K$) such data points. We now explore robust methods to extract high fidelity structure–property linkages from such a dataset. In the examples presented here, we utilize simple polynomial functions and ordinary least squares linear regression techniques [42]. Other functional descriptions and regression techniques may also be employed as needed.

For simplicity of notation, in the equations below, we drop the subscript on the property of interest and refer to it

generically as $P^{(k)}$. Let a normalized error associated with each data point in the linear regression be defined as

$$E^{(k)} = \frac{|P^{(k)} - f^p(\alpha_1^{(k)}, \alpha_2^{(k)}, \dots, \alpha_{\tilde{R}}^{(k)})|}{\frac{1}{K} \sum_{k=1}^K P^{(k)}} \quad (6.7)$$

where $f^p(\alpha_1^{(k)}, \alpha_2^{(k)}, \dots, \alpha_{\tilde{R}}^{(k)})$ denotes a p^{th} -order polynomial function, and the normalization factor is selected as the mean value of the property. The polynomial coefficients are then established using standard protocols of minimizing the sum of the squares of the residuals in the entire dataset (including all K data points). Note that the extracted polynomial linkage depends critically on the selection of both p and \tilde{R} as well as the error measure.

Critical selection of parameters p and \tilde{R} is central to the extraction of high-fidelity structure–property linkages. Although higher values of p and \tilde{R} will always produce a lower value of the error, they do not necessarily increase the fidelity of the extracted linkages. This is because the higher values of p and \tilde{R} may lead to over-fitting of the linkages, and can produce erroneous estimates in any subsequent application of the linkages to new microstructures (those not included in the regression analyses).

The following specific measures are suggested to critically evaluate the robustness of the polynomial-fits:

i. Mean absolute error of fit defined as

$$\bar{E} = \frac{1}{K} \sum_{k=1}^K E^{(k)} \quad (6.8)$$

ii. Standard deviation, σ , of error of fit with respect to mean absolute error, defined as

$$\sigma = \sqrt{\frac{1}{K} \sum_{k=1}^K (E^{(k)} - \bar{E})^2} \quad (6.9)$$

iii. Mean absolute error \bar{E}_{CV} , and standard deviation σ_{CV} , of Leave-One-Out Cross Validation (LOOCV) error. This model selection method involves the training of a polynomial fit K times, while leaving one data point out of the test set each time. Cross validation error for a single instance $E_{cv}^{(k)}$ is thus defined as:

$$E_{cv}^{(k)} = \frac{|P^{(k)} - f_{[k]}^p(\alpha_1^{(k)}, \alpha_2^{(k)}, \dots, \alpha_{\tilde{R}}^{(k)})|}{\frac{1}{K} \sum_{k=1}^K P^{(k)}} \quad (6.10)$$

where $f_{[k]}^p$ is the polynomial fit obtained by ignoring the k^{th} data point. Given a large K , for an over-fitted polynomial, the exclusion of a single data point will cause significant change in the coefficients, whereas for a good fit this change will be negligible. The measures \bar{E}_{CV} and σ_{CV} are defined as the mean and standard deviation of the set defined as $\{E_{cv}^{(k)} \forall k \in 1..K\}$.

The first two measures of error of fit defined above will show improvement of fit with higher values of p and \tilde{R} , whereas the last two measures of error of CV are expected to show decline in robustness of fit with higher values of p and \tilde{R} (indicating over-fit of data). Therefore, a compromise can be made in choosing the best fit based on the values of the above four measures. If multiple viable fits exist, one might select the least complex one (the one with the lowest number of terms).

It should be noted that the procedure described earlier is different from the traditional practice of splitting the data into a calibration (or training) component and a validation component. The conventional approach of hard-splitting of the data is usually a good practice for situations where the number of data points far exceeds the number of parameters involved in the training. In many applications involving the establishment of PSP linkages, because of the high cost of generating data (each numerical simulation for a given microstructure using a physics-based model generally incurs a significant cost); the earlier described approach of cross validation may be preferred to maximize the utilization of the available information in establishing the surrogate model. Given the unimaginably large space of all theoretically possible microstructures and the relatively small number of available datasets, effective utilization of all available datasets takes precedence in many of data-science tasks. However, when a sufficiently large dataset becomes available, one might want to switch to the strategy of hard-splitting the data into a calibration (or training) set and a validation set.

6.3 Case Study: Microstructure–Property Relationships in Porous Transport Layers

There exist a number of technological applications where porous solids are used to transport various chemical species of interest. Prime examples include the gas diffusion layer (GDL) and micro-porous layer (MPL) in Polymer electrolyte fuel cells

(PEFCs). Essentially, porous materials represent a new class of materials with complex hierarchical internal structures (i.e., microstructures). As a specific example, Cecen et al. [22] examined the gas diffusivity in porous media using the data-driven protocols presented in this book. At the present time, the majority of the structure-diffusivity correlations established for porous materials are in the form of simplified correlations between intuitively selected microstructure features and the effective gas diffusivity.

More specifically, it was demonstrated that a high-fidelity microstructure-diffusivity metamodel can be established using the protocols described earlier. As described earlier, the first step generally involves the generation of a dataset that can be used both for the calibration and the validation tasks. For this purpose, a Fickian diffusivity simulation model was set up. A total of 300 microscale volumes of $100 \times 100 \times 100$ voxels from MPL and 200 microscale volumes of $50 \times 50 \times 151$ voxels from GDL were sampled from previously generated experimental observations. The effective diffusivity of each volume was predicted using a numerical implementation of the Fick's model to generate the dataset for this case study [22]. Therefore, consideration of each digital microstructure produced one data point which can be expressed as $(D_{str}^{(k)}, \alpha_1^{(k)}, \alpha_2^{(k)}, \dots, \alpha_{\tilde{R}}^{(k)})$, where $D_{str}^{(k)}$ denotes the effective structural diffusivity coefficient of the microstructure labeled (k) . The complete dataset contained $K = 500$ data points.

In this case study, the 2-point correlations for each microstructure included in the study were computed to include vectors contained in a $41 \times 41 \times 41$ volume, that is, $R = 41^3 = 68,921$. This constitutes a very large dimensional representation of the microstructure that is not easily amenable to traditional methods of establishing microstructure–property correlations. Application of the PCA protocols described in Chapter 4 produces an objective low-dimensional representation of the entire ensemble of microstructures. Figure 6.2 [22] depicts a visualization of the ensemble of microstructures in the first two-dimensions of the PCA space (i.e., $\tilde{R} = 2$). It is seen clearly that the two sets of microstructures corresponding to the MPL and the GDL automatically separate in these visualizations. In other words, two PCs are adequate to confidently associate any of the members of the entire ensemble to either the MPL or the GDL set. This example, once again, demonstrates the remarkable effectiveness of PCA in unsupervised classification of the microstructures.

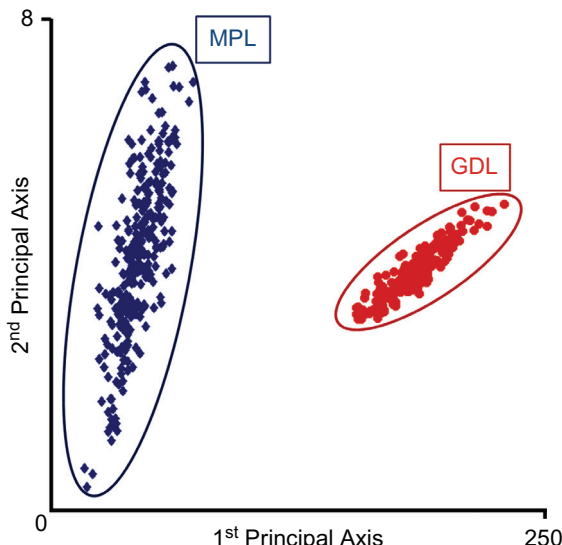


Figure 6.2 The ensemble of microstructures studied are visualized in the first two principal component axes [22]. The clustering of the datasets is clearly visible.

A dataset of 500 data points (each combination of the estimated effective diffusivity and the PCA weights of the microstructure constitute one data point) was then produced and subsequently mined for microstructure-effective diffusivity correlations using the protocols described earlier. Increasing degrees of polynomials ($1 \leq p \leq 5$) and increasing numbers of PCs ($\check{R} (1 \leq \check{R} \leq 5)$) were explored in the regression analyses conducted in this study. The results of the regression analyses are summarized in Figure 6.3 [22]. As expected, the mean and median measures of the error decrease with an increase in either p or \check{R} . It is also seen that the values of both parameters should be at least two for a reasonable fit. The LOOCV analyses (see Figure 6.3b) indicates a discernible loss of fidelity with over-fitting of the data points at high values of both p and \check{R} . For example, the E_{CV} value for quintic fits starts to increase with the inclusion of more than two PC weights. Hence, the error measures from LOOCV are effective indicators of over-fitting.

Based on a thorough consideration of the plots in Figure 6.3, the authors [22] decided to go with the cubic fit with two PCs (principal components). The predictions from this fit are

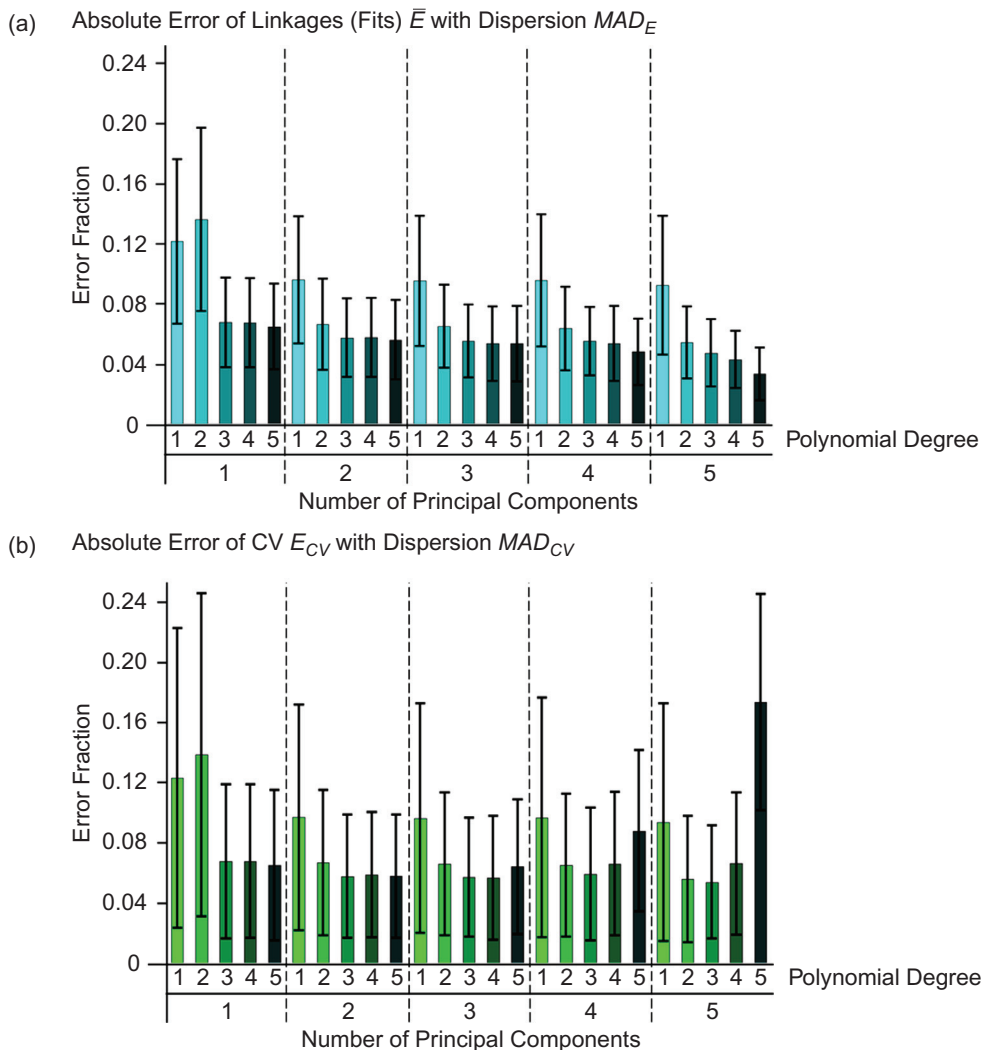


Figure 6.3 (a) The mean absolute error as a function of the degree of the polynomial and the number of principal components used in the regression. (b) The mean absolute error of cross validation as a function of the degree of the polynomial and the number of principal components used in the regression [22].

compared with the predictions from the original dataset (including both GDL and MPL) in Figure 6.4. If the fit was perfect, then all points would lie on the diagonal dashed line. Clearly, the protocols provided an excellent single linkage that captured the structure–property linkage in the diverse ensemble of porous microstructures included in the study.

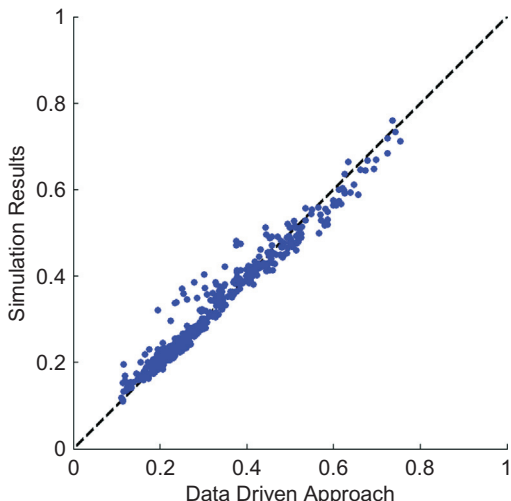


Figure 6.4 Comparison of the predictions of effective structural diffusivity for the ensemble of 500 microstructures from the data-driven approach with those from the physics-based simulations [22].

6.4 Case Study: Structure–Property Linkages in Inclusions/Steel Composites

Performance and properties of a steel sheet are strongly influenced by the size, shape, composition, type (hard or soft), and distribution of nonmetallic inclusions in the steel sheet. Prior studies [43–47] aimed at extracting structure–property linkages for nonmetallic inclusions/steel composites have largely relied on experiments, aided by analytical and numerical models. More importantly, all of the prior linkages have utilized highly simplified measures of microstructure such as the volume fraction of inclusions, the average inclusion size, and the average inclusion spacing in establishing the desired linkages. In a recent study, Gupta et al. [41] successfully employed the data-centered methods described earlier in this chapter to establish structure–property linkages for the nonmetallic inclusions/steel composite system.

In the first step, an ensemble of 900 two-dimensional (2-D) synthetic microstructures was generated, where the microstructures contained multiple hard or soft inclusions with different sizes, shapes, and spatial configurations in a steel matrix [41]. This ensemble of microstructures was already discussed in Section 4.4. A 2-D micromechanical finite element (FE) model was then developed to evaluate the properties of interest associated with each of

Table 6.1 Material parameters used in the FE simulations of the steel-inclusion system [41]

Definitions	Case 1 (hard inclusions)	Case 2 (soft inclusions)
Temperature (T)	900°C	1000°C
Strain rate ($\dot{\epsilon}$)	5 s ⁻¹	5 s ⁻¹
Inclusion: Young's Modulus (E)	136.93 GPa	10.27 GPa
Inclusion: Poisson's ratio (ν)	0.3	0.3
Inclusion: Yield Strength (σ_0)	273.86 MPa	20.54 MPa
Steel : Young's Modulus(E)	29.77 GPa	21.39 GPa
Steel : Poisson's ratio (ν)	0.3	0.3
Steel : Yield Strength (σ_0)	56.99 MPa	44.73 MPa
Steel : Hardening Exponent (N)	0.23	0.23

the 900 microstructures in this ensemble. The FE model simulated plane strain compression of the inclusion-steel composite system using the commercial software ANSYS. Four-noded structural solid elements were utilized in this model. Periodic boundary conditions were applied to simulate a plane strain compression of 15% reduction. Both the inclusion and steel were treated as isotropic, with the inclusion being elastic-perfectly plastic and the matrix being elastic-plastic (with hardening). Some of the material parameters used to define the properties of the steel matrix and the precipitates are summarized in Table 6.1.

The inclusion/steel matrix interface was modeled using 2-D, 2-noded, surface to surface contact elements on the inclusion side of the interface, and 2-D target elements on the steel matrix side. It was assumed that interface is initially bonded, and that sliding occurs with friction after debonding. A bilinear cohesive zone model (CZM) with mode I debonding was used [48]. Values of the CZM parameters used in this study included maximum normal contact stress (σ_{max}) = 0.01 MPa, contact gap at the completion of debonding (δ_n^c) = 0.1 μm , and artificial damping coefficient (η) = 1e - 5 [49,50]. Coefficient of friction was taken as 0.4 [51].

A total of three macroscale performance parameters of interest were selected for the case study. In other words, for each microstructure, these properties would be extracted from the micro-mechanical FE models and linked with the microstructure measures. The macroscale parameters selected are (i) the effective (composite) yield strength (σ_0), (ii) effective strain hardening exponent (N), and (iii) localization propensity (LP). σ_0 and N

are examples of bulk properties (i.e., volume averaged values), while LP quantifies the degree of the heterogeneity of the local response. These parameters are extracted as follows [41]:

- i. σ_0 : Effective yield strength of the composite material system is computed from averaged (overall) true stress-strain response. σ_0 is defined as the macroscale stress at 0.2% offset macroscale plastic strain.
- ii. N: Effective strain hardening exponent is computed by fitting the averaged true stress-strain response to a power hardening law [49].

$$\sigma_y = \sigma_0 \left(1 + \left(\frac{3G}{\sigma_0} \right) \bar{\varepsilon}_p \right)^N \quad (6.11)$$

In this study, N was computed only for the case of soft inclusions. For the case of hard inclusions, the range of parameter N was negligibly small when computed for all microstructures in the selected ensemble.

- iii. LP: Localization propensity was defined to capture strain localization in the system during plane strain compression (to be used as an indicator of potential damage accumulation). It was defined as the area fraction of the matrix elements experiencing an equivalent strain greater than a prescribed cut-off strain (ε_c). The cut-off strain was chosen as 1.25 times the macroscale equivalent strain ($\bar{\varepsilon}$) applied to the composite material system. It was observed that the predicted values of LP produced a significant variation only for the hard inclusions.

Separate simulations were performed for (Case 1) hard and (Case 2) soft inclusions (see Table 6.1), that is, 900 simulations were performed for each case [41]. As expected, strain localization and void formation at inclusion/matrix interface were observed in the simulations with hard inclusions. No void formation was observed in case of soft inclusions; instead inclusions just got elongated.

The next step after generating calibration dataset is to establish objective reduced-order quantification of each synthetic microstructure used in the study. Autocorrelations of the matrix phase were used to capture all of the independent 2-point statistics for each microstructure. For this case study, $\{f_r | r = 1, 2, \dots, 6400\}$ denotes the complete set of 2-point statistics for one microstructure, as each microstructure had 80×80 spatial bins. PCA was performed to obtain reduced-order representations for this set of autocorrelations.

Structure–property linkages were generated using both the conventional and the data-science approaches to allow for a critical comparison. Structure–property linkages using conventional approaches were established using the following sequence of

steps: (i) Volume fraction of inclusions and the average inclusion size were computed as structure measures for each synthetic microstructure generated in this study. Volume fraction was computed by dividing the total area of inclusions by total area (inclusion + matrix) and average inclusion size was computed as a simple average of the equivalent diameters of all inclusions present in a microstructure. (ii) Macroscale performance parameters were computed using the micromechanical FE model (same as for the data-science approach). (iii) Power-law functional forms of the type $y = a^*x^\lambda$, where y = property of interest and x = empirical structure measure, were established using standard regression analysis. Following the typical current practice in the field, only one structure parameter was explored at a time in the conventional fits.

Structure–property linkages using data-science approach were established using regression analysis and validated using LOOCV as described earlier in this chapter. Increasing degrees of polynomial ($1 \leq p \leq 5$) and increasing numbers of PCs ($1 \leq \tilde{R} \leq 5$) were explored in the regression analysis. As described earlier, macroscale parameters σ_0 , N , and LP were chosen as properties of interest, $P_i^{(k)}$. For the case of hard inclusions (Case 1) parameters σ_0 and LP were computed, and for the case of soft inclusions (Case 2) parameters σ_0 and N were computed. Data-driven structure–property linkages for each parameter were then established by objective selection of p and \tilde{R} such that the most robust (i.e., accurate without risking over-fitting) linkages were established (after evaluating a large number of regression analyses involving different combinations of p and \tilde{R}).

[Figure 6.5](#) and [Table 6.2](#) summarize the results of all the fits produced in this study using both the conventional approaches and the data-science approaches. It is clear from these results that for all three macroscale parameters studied here, the data-science protocols produced robust and reliable linkages. This is evidenced in the values of the errors and their standard deviations for all 900 microstructures (see [Table 6.2](#)) evaluated in this study. As expected, the linkages are much more accurate for macroscale parameters that reflect bulk averaged values (such as yield strengths) when compared to macroscale parameters that are strongly weighted by local responses (such as LP).

Even though [Figure 6.5](#) and [Table 6.2](#) have clearly demonstrated a higher accuracy of the surrogate models obtained from the data-science approaches compared to the conventional approaches, this is not the main point of this comparison. Indeed, one can argue that the effort involved in establishing the data-science linkages presented here is

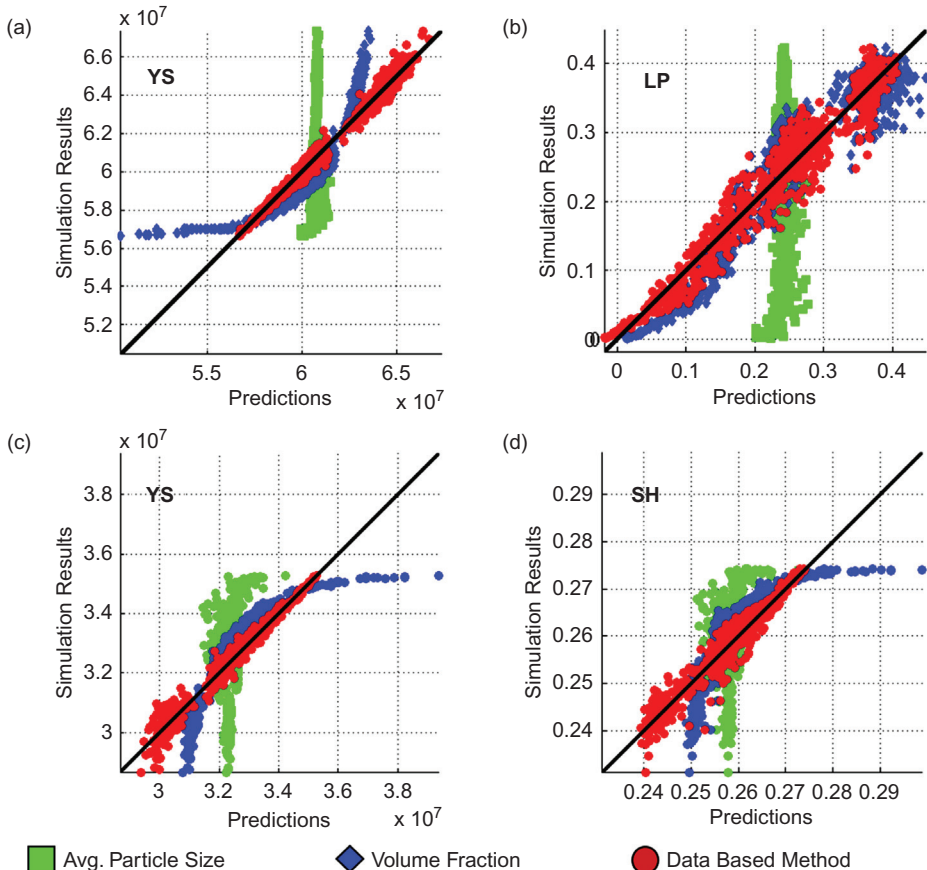


Figure 6.5 Comparison of the structure–property linkages using the conventional methods and the data-science approaches for the properties/performance characteristics of interest. (a) and (b) present results for hard inclusions, while (c) and (d) present the results for soft inclusions. The black line represents a perfect match between the estimates from the different surrogate models (extracted using both traditional and data-sciences approaches) and the corresponding simulation results [41].

substantially higher compared to the effort expended in the highly simplified conventional approaches. One might even argue that if a stronger effort was spent on the conventional approaches presented here (e.g., by combining the different traditional structure measures into new polynomial terms), they might have resulted in equally good (or perhaps even better) surrogate models. However, the main difficulty in extending the conventional approaches to much richer regression analyses comes from the lack of guidance in the objective selection of the structure measures. The data-science approach described here, based on the systematic use of n -point statistics for

Table 6.2 Summary of the performances of the conventional and data science approaches for establishing structure—property linkages [41]

	Data based method				Conventional linkages (volume fraction)				Conventional linkages (average particle size)			
	# PCs	Degree	R ²	Ē %	σ %	R ²	Ē %	σ %	R ²	Ē %	σ %	
Hard inclusions	σ_0	1	2	0.9847	0.38	0.34	0.7370	1.68	1.25	0.0068	3.36	2.31
	LP	2	3	0.9503	8.18	6.64	0.9004	12.48	8.18	0.0111	39.98	24.74
Soft inclusions	σ_0	1	2	0.9708	0.58	0.55	0.7563	1.82	1.43	0.0370	3.93	2.41
	N	3	2	0.9451	0.60	0.59	0.6794	1.62	1.24	0.0593	2.91	1.94

structure measures, presents an approach that can be largely automated using computer codes.

It is also worth noting some of the limitations of data-science approach presented here. It should be noted that the linkages developed here are data-driven in the sense that they are established using a specific set of 900 microstructures. The central assumption in the data-driven approach presented here is that this set of 900 microstructures is inclusive of all of the different types of microstructures encountered in the actual application. Keeping in mind that the number of theoretically possible distinct microstructures in a composite system is unimaginably large, it is unlikely that the specific set of 900 microstructures selected here would represent every theoretically possible microstructure. In other words, it is highly likely that one will encounter a new microstructure that is distinctly different from the microstructures included in the study. In such a situation, the framework presented earlier presents the following opportunities: (i) One can quantify rigorously the difference between the new microstructure and the elements of the ensemble used in generating the linkages using the n -point spatial correlations as the measures of the microstructure. It would then be possible to decide objectively if the new microstructure constitutes an interpolation or an extrapolation of the microstructures included in the analyses (cf. see Figure 4.3). This is important because an interpolation in the microstructure space

would impart much more confidence in the predicted value of the property compared to an extrapolation. (ii) If it is deemed that the new microstructure is distinctly different than the microstructures included in the prior analyses, one can then decide to extend the analyses with minimal additional effort by adding new sets of microstructures. The data-science framework and algorithms presented here allow easy addition of new data points with minimal redundant work. This is because both the principal component analyses and the regression methods allow updates with the addition of new data points.

6.5 MKS: Data-Driven Framework for Localization Linkages

The focus in this chapter thus far has been on homogenization, that is, in communicating the salient information from the lower length scale to the higher length scale. In many situations, it is critical to pass salient information in the opposite direction, that is, localization. As an example, localization might capture the spatial distribution of the response field of interest (e.g., stress or strain rate fields) at the lower length scale for an imposed loading condition at the higher length scale. Of course, localization is substantially more complicated than homogenization. This can be easily seen by comparing the corresponding theories for homogenization and localization in Eqs. (5.35) and (5.37), respectively. The challenge in localization is that it has to be accomplished by satisfying the governing field equations at the lower length scales. In several materials design problems (e.g., in simulating thermo-mechanical processes on materials where there is macroscale heterogeneity in the evolution of the underlying microstructure) localization is just as important as homogenization, if not more important. Furthermore, if localization is addressed with adequate accuracy, it implicitly results in much higher accuracy for homogenization.

Eq. (5.35) described a polarization tensor which related the perturbation in local strain tensor to the macroscale imposed strain tensor (see Eq. (5.25)). In practice, we are more interested in the local strain tensor (not just the perturbation) and therefore it is more useful to cast the localization problem for elastic response of a composite material system as

$$\boldsymbol{\varepsilon}(\mathbf{x}) = \mathbf{a}(\mathbf{x})\langle\boldsymbol{\varepsilon}(\mathbf{x})\rangle = (\mathbf{I} + \mathbf{a}(\mathbf{x}))\langle\boldsymbol{\varepsilon}(\mathbf{x})\rangle \quad (6.12)$$

where $\mathbf{a}(\mathbf{x})$ continues to denote the polarization tensor introduced in Eq. (5.25). The localization tensor $\mathbf{a}(\mathbf{x})$ introduced in Eq. (6.12)

is only different from $\mathbf{a}(\mathbf{x})$ by a fourth-rank identity tensor, \mathbf{I} . Accounting for this difference, the theoretical expression for the localization tensor can be expanded from Eq. (5.35) as

$$\mathbf{a}(\mathbf{x}) = (\mathbf{I} - \langle \Gamma(\mathbf{x}, \mathbf{x}') \mathbf{C}'(\mathbf{x}') \rangle + \langle \Gamma(\mathbf{x}, \mathbf{x}') \mathbf{C}'(\mathbf{x}') \Gamma(\mathbf{x}', \mathbf{x}'') \mathbf{C}'(\mathbf{x}'') \rangle - \dots) \quad (6.13)$$

where the rest of the variables continue to have the same meaning as they had in Chapter 5.

In the data-driven framework for homogenization presented earlier in this chapter, we took advantage of the statistical descriptions of the microstructure in transforming the complex volume integrals in the composite theory to the more practical forms (see Eqs. (6.1) and (6.2)). We now undertake a similar exercise to transform Eq. (6.13) into a more computationally useful form by utilizing the concept of microstructure function $m(h, \mathbf{x})$ introduced in Chapter 2. Recall that this function reflects the probability density associated with finding the local state h (to within an invariant measure dh) at the spatial location \mathbf{x} (note that $m(h, \mathbf{x})dh$ reflects the corresponding probability; see Chapter 2). Further, recall that the complete set of all distinct local states that are possible in a given material system is referred to as the local state space, denoted by H (i.e., $h \in H$). As before, introducing this function, invoking the ergodic hypothesis, and substituting $\mathbf{t} = \mathbf{x} - \mathbf{x}'$, one can recast Eq. (6.12) as [52,53]:

$$\begin{aligned} \boldsymbol{\varepsilon}(\mathbf{x}) = & \left(\mathbf{I} - \int_{\Psi} \int_H \alpha(h, \mathbf{t}) m(h, \mathbf{x} + \mathbf{t}) dh d\mathbf{t} \right. \\ & + \int_{\Psi} \int_{\Psi} \int_H \int_H \tilde{\alpha}(h, h', \mathbf{t}, \mathbf{t}') m(h, \mathbf{x} + \mathbf{t}) \right. \\ & \left. m(h', \mathbf{x} + \mathbf{t} + \mathbf{t}') dh dh' d\mathbf{t} d\mathbf{t}' - \dots \right) \boldsymbol{\varepsilon}(\mathbf{x}) \end{aligned} \quad (6.14)$$

The details of deriving Eq. (6.14) from Eq. (6.13) are identical to the steps involved in deriving Eq. (6.2) from Eq. (6.1). As before, the structure of Eq. (6.14) offers many computational advantages. First, the terms $\alpha(h, \mathbf{t})$ and $\tilde{\alpha}(h, h', \mathbf{t}, \mathbf{t}')$ are independent of the microstructure function. In other words, they capture the microstructure-independent physics governing the elastic localization in a composite material. Second, the terms in Eq. (6.14) are indeed convolutions (notice the products of terms defined at $\mathbf{x} + \mathbf{t}$ and \mathbf{t}). Consequently, these can be most efficiently computed using discrete Fourier transforms (DFTs; see Chapter 2). Because of this feature, the terms $\alpha(h, \mathbf{t})$ and $\tilde{\alpha}(h, h', \mathbf{t}, \mathbf{t}')$ are referred to as first-order and second-order localization kernels (or influence functions), respectively. Note that

[Eq. \(6.14\)](#) represents an infinite series expansion of a highly nonlinear function, where each term of the series can be interpreted as a linearized contribution from a specific topological feature in the microstructure.

Because of the tremendous difficulties involved in evaluating the kernels analytically (these are the same as those discussed earlier for the coefficients in the homogenization linkages), we seek data-driven approaches for establishing their values. The framework for accomplishing this task has been called Materials Knowledge System (MKS) approach [24–29,33]. In the MKS approach, localization kernels are obtained by a calibration procedure that involves matching the predictions of [Eq. \(6.14\)](#) to the corresponding predictions from previously validated numerical models (e.g., finite element models) for a broad range of exemplar microstructures. The central advantage of the MKS methodology lies in its computational efficiency. Once the localization kernels are calibrated, they can be applied to new microstructures with very little computational cost, often orders of magnitude lower than what is needed to execute the previously established numerical model. The viability and the computational advantages of the MKS approach have been successfully demonstrated for thermo-elastic deformation fields in composites [25], rigid-viscoplastic deformation fields in composites [24], the evolution of the composition fields in spinodal decomposition of binary alloys [27], and the elastic deformation fields in polycrystalline aggregates [29].

In the MKS approach, we first seek a computationally efficient form of [Eq. \(6.14\)](#) using spectral (Fourier) representations. Specifically, we seek representations of the following type for the various functions in [Eq. \(6.14\)](#) (only the functions in the first term are shown below; these representations can be extended to higher-order terms in the series):

$$m(h, \mathbf{x}) = \sum_L \sum_s M_s^L Q_L(h) \chi_s(\mathbf{x}), \quad \alpha(h, \mathbf{t}) = \sum_L \sum_r A_r^L Q_L(h) \chi_r(\mathbf{t}) \quad (6.15)$$

In [Eq. \(6.15\)](#), $Q_L(h)$ is a suitably selected Fourier basis for functions defined on the continuous local state space (see Section 2.5) with the following orthonormal properties:

$$\int_H Q_L(h) Q_{L'}^*(h) dh = \frac{\delta_{LL'}}{N_L} \quad (6.16)$$

where the superscript * denotes a complex conjugate, $\delta_{LL'}$ is the Kronecker delta, and N_L is a constant that might depend on L . $\chi_s(\mathbf{x})$ in [Eq. \(6.15\)](#) defines an indicator basis which essentially

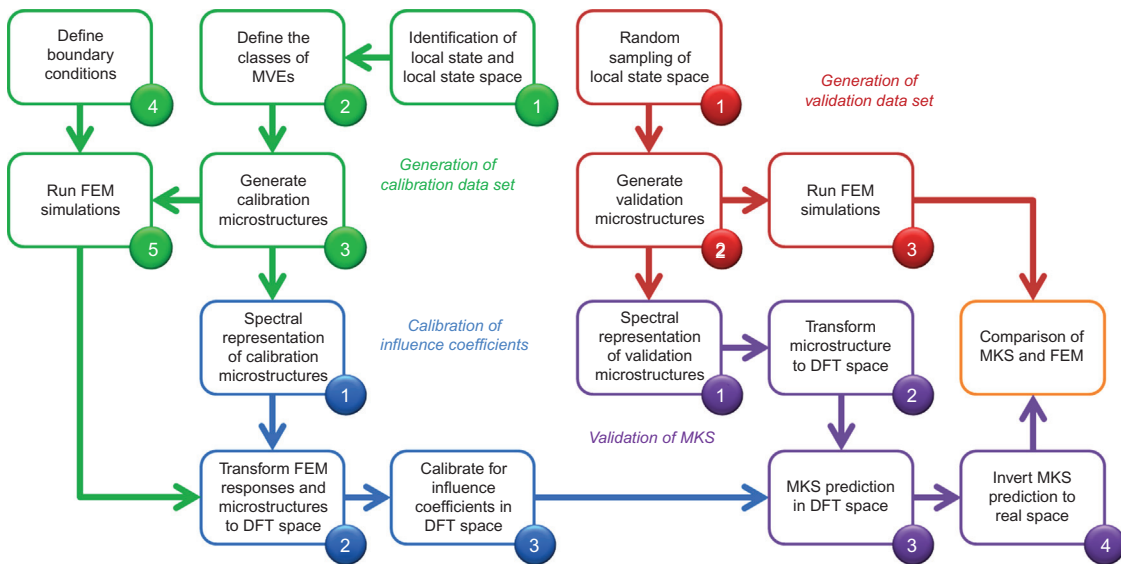


Figure 6.6 An example workflow template for establishing the localization kernels in the generalized MKS formulation [29].

tessellates the spatial domain into a uniform grid [54] (see also Chapter 2). This function is defined such that its value is one for all points belonging to spatial bin s , and zero for all points outside. In a completely analogous manner, $\chi_r(t)$ denotes an indicator basis for tessellating (simple binning) of the vector space (very similar to what we did in Chapter 3 when computing spatial correlations using DFTs). The choice of the indicator basis for the spatial variables in Eq. (6.15) is primarily motivated by the fact that it allows for the use of DFTs in performing the convolutions in the integrals in Eq. (6.14) in computationally efficient ways. Using the orthogonal properties of both bases, we can show

$$\begin{aligned} M_s^L &= \frac{N_L}{\Delta} \int_{H,V} m(h, \mathbf{x}) Q_L^*(h) \chi_s(\mathbf{x}) dh d\mathbf{x} \\ A_r^L &= \frac{N_L}{\Delta} \int_{H,R} \alpha(h, t) Q_L^*(h) \chi_r(t) dh dt \end{aligned} \quad (6.17)$$

where Δ is the volume of the spatial bin.

Introducing these spectral representations into Eq. (6.14), we derive here a generalized form of the MKS:

$$\begin{aligned} \mathbf{p}_s = & \left(\sum_L \sum_r \frac{\Delta}{N_L} A_r^L M_{s+r}^{L*} \right. \\ & \left. + \sum_L \sum_{L'} \sum_r \sum_{r'} \frac{\Delta^2}{N_L N_{L'}} A_{rr'}^{LL'} M_{s+r}^{L*} M_{s+r+r'}^{L'*} + \dots \right) \langle \mathbf{p} \rangle \end{aligned} \quad (6.18)$$

As before, the main challenge is the estimation of the microstructure-independent influence coefficients (such as A_t^L). The overall workflow involved in building the MKS databases mirrors the workflows described earlier for the homogenization linkages. This workflow is shown in Figure 6.6 as a broadly usable template. This procedure involves four different main tasks (color coded in Figure 6.6) with several subtasks. The template will be illustrated next with a specific case study.

6.6 Case Study: MKS for Elastic Response of Composites

The first successful applications of the MKS framework focused on elastic response of multiphase composites, where each constituent phase was assumed to exhibit isotropic response. This, however, does not restrict the overall response of the composite to be isotropic. Indeed, the preferential placement of the constituent phases can produce an anisotropic effective response at the macroscale. For the multiphase composites, the local state space is already discrete and naturally binned. In other words, $Q_L(h)$ could just be $\chi_n(h)$ (see Eq. 2.25). With this choice, M_s^L can be simply substituted with the familiar m_s^n , and Eq. (6.18) can be recast as

$$\mathbf{p}_s = \left(\sum_n \sum_{\mathbf{r}} \alpha_{\mathbf{r}}^n m_{\mathbf{s}+\mathbf{r}}^n + \sum_n \sum_{n'} \sum_{\mathbf{r}} \sum_{\mathbf{r}'} \alpha_{\mathbf{r}\mathbf{r}'}^{nn'} m_{\mathbf{s}+\mathbf{r}}^n m_{\mathbf{s}+\mathbf{r}+\mathbf{r}'}^{n'} + \dots \right) \langle \mathbf{p} \rangle \quad (6.19)$$

Note that some of the constants in Eq. (6.18) have now been absorbed into the influence kernels. $\alpha_{\mathbf{r}}^n$ and $\alpha_{\mathbf{r}\mathbf{r}'}^{nn'}$ are essentially the first- and second-order influence kernels that are independent of the details of the microstructure. Note also that for elasticity, both these kernels are fourth-rank tensors. $\alpha_{\mathbf{r}}^n$ captures the contribution of the placement of the local state n in a spatial location indexed by $\mathbf{s} + \mathbf{r}$ on the local strain tensor in the spatial cell indexed \mathbf{s} . In an analogous manner, the second-order influence coefficient $\alpha_{\mathbf{r}\mathbf{r}'}^{nn'}$ captures the additional contribution (over the first-order contribution) to the same local strain tensor in the spatial cell indexed \mathbf{s} arising from the simultaneous placement of local state n' in spatial cell indexed $\mathbf{s} + \mathbf{r} + \mathbf{r}'$ and the placement of local state n in the spatial cell indexed by $\mathbf{s} + \mathbf{r}$.

As already noted several times before, the main challenge with Eq. (6.19) is the estimation of the numerical values of the unknown influence kernels. It should be noted that the number of parameters in the localization linkages is far higher than the number of parameters in the homogenization linkages discussed earlier. For example, the total numbers of first- and second-order coefficients are SN and $(SN)^2$, respectively, where S denotes the number of spatial bins used in the description of the microstructure and N is the number of distinct local states expected in the composite system. In particular, it is important to note the dramatic increase in the number of influence coefficients with the higher-order terms. Indeed, the number of first-order influence coefficients is itself quite substantial for most microstructure datasets, because S is typically very large. As an example, if the microstructure is defined on a $20 \times 20 \times 20$ grid, then $S = 8000$. This is where the use of DFTs offers a special advantage, especially since the basic mathematical operation involved in Eq. (6.19) is a convolution. In the DFT space, Eq. (6.19) truncated to the first term can be recast as:

$$\mathbf{P}_k = \left[\left(\sum_{n=1}^N \beta_k^{n*} \mathcal{M}_k^n \right) \right] \bar{\mathbf{p}} \quad (6.20)$$

$$\beta_k^n = \Im(\alpha_s^n), \quad \mathbf{P}_k = \Im(\mathbf{p}_s), \quad \mathcal{M}_k^n = \Im(m_s^n) \quad (6.21)$$

where $\Im(\cdot)$ denotes the familiar DFT operator that transforms datasets from the s or r space to the k space, and the star in the superscript continues to denote the complex conjugate. Also, we have restricted our initial attention to only the first term in the series of Eq. (6.19). We will revisit the higher-order terms subsequently as they pose significant additional challenges. As explained already, the higher-order terms become important as the contrast in the local properties in the composite system increases. So, our initial focus will be restricted to low and medium contrast composites where the first-term dominates the local response.

The most important consequence of the DFT representation shown in Eq. (6.20) is the uncoupling of the first-order influence coefficients. Note that the number of coupled first-order coefficients in Eq. (6.20) is only N (the number of distinct local states in the composite system of interest), although the total number of first-order coefficients still remains as SN . Because of this dramatic uncoupling of first-order coefficients into smaller sets,

it becomes fairly easy to estimate the values of influence coefficients β_k^n in the DFT space by calibrating them to results from FE models.

It is emphasized here that establishing β_k^n is a one-time computational task for a selected composite material system, because these coefficients are independent of the details of the microstructure (defined by m_s^n). As such, they offer a compact representation of the underlying knowledge for elastic strain fields for all possible topologies that could be defined in the given composite material system. The simplicity of Eq. (6.20) also presents a computationally efficient procedure for computing the elastic fields in any new microstructure dataset, after the corresponding influence coefficients are established and stored.

Landi et al. [26] have demonstrated the viability of the MKS framework capturing the elastic response of low to moderate contrast composites. In their case study, they used a composite of two phases that exhibit isotropic elastic properties. The values of the Young's moduli for the two phases were taken as 200 and 300 GPa, respectively. The value of the Poisson's ratio, however, was assumed to be 0.3 for both phases.

The first step in the implementation of the MKS framework is the generation of the calibration dataset (green colored parts of the workflow shown in Figure 6.6). Landi et al. [26] employed “delta” microstructures (all but one central spatial bin assigned to one local state and the central bin assigned a different local state; see Figure 6.7). This is particularly beneficial for calibrating first-order terms, because a delta function in m_s^n produces nonzero values for all M_k^n . In other words, a delta microstructure implicitly contains all spatial frequencies possible in the dataset, and therefore requires contributions from all first-order terms in Eq. (6.19). For a two-phase material system, only two distinct delta microstructures (one black element surrounded completely by white and vice-versa) can be defined. Consequently, these two delta microstructures were employed to calibrate all of the influence coefficients in Eq. (6.20).

Finite element FE meshes corresponding to the delta microstructures were produced and analyzed using the commercial FE software ABAQUS®. The calibration FE models used in this study comprised of $21 \times 21 \times 21 = 9261$ cuboid-shaped, three-dimensional, eight-noded, solid elements (C3D8). Since α_r^n , and its DFT β_k^n are both fourth-rank tensors and elasticity allows superposition, the determination of the complete fourth-ranked tensor requires application of a total of six different boundary conditions. As an example, let us consider the estimation of the

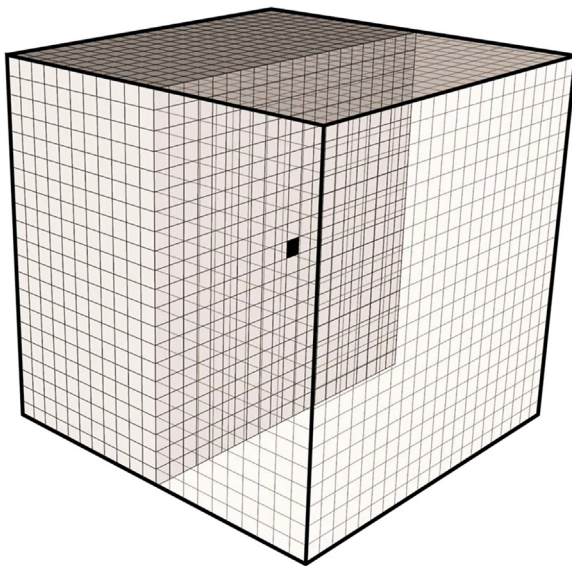


Figure 6.7 An example of a delta microstructure used in the calibration of the first-order influence coefficients. In this microstructure a central element is assigned to phase 2 (shown black). All other elements are assigned to phase 1 (shown white) [26].

$(\beta_{ij11}^n)_k$ components. For estimating these coefficients, we need to apply a uniaxial strain at the higher length scale and document the spatial variation of the different strain components at the microscale. In other words, we need to apply a nonzero $\bar{\varepsilon}_{11}$, while keeping other components of the macroscale strain tensor equal to zero. It should be noted that $\bar{\varepsilon}_{11}$ corresponds to the volume average, which in the equal volume cuboidal elements based FE models used here, is simply the numerical average over all the elements in the model. Periodic boundary conditions were applied in all of the FE model simulations. Imposing periodic boundary conditions entails setting up equations that relate displacements of nodes on opposite faces to each other. For example, for establishing $(\beta_{ij11}^n)_k$, the following boundary conditions are employed between corresponding node sets on opposite faces of the FE model shown in Figure 6.8.

$$u_i^{3+} = u_i^{3-}, \quad u_i^{2+} = u_i^{2-}, \quad u_{i \neq 3}^{1+} = u_{i \neq 3}^{1-}, \quad u_3^{1+} - u_3^{1-} = \bar{\varepsilon}_{11} L, \quad u_i^B = 0. \quad (6.22)$$

In the notation used in Eq. (6.22), u_i denote the components of the displacement vector, L is the length of the side of the

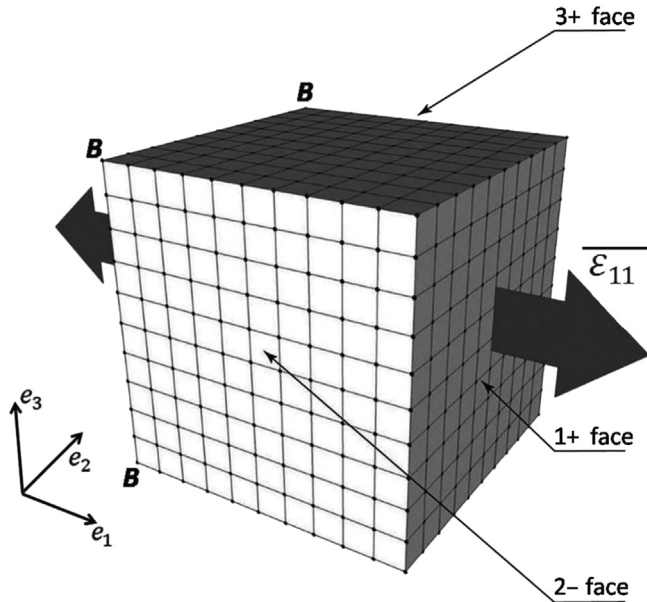


Figure 6.8 Illustration of the periodic boundary conditions applied on the FE models. As examples, all nodes on the 1+, 2– and 3+ faces are highlighted in the picture. Consequently, opposite faces will have the same shape after deformation [26].

cuboidal FE mesh, the superscripts $n+$ and $n-$ refer to the subset of nodes on faces whose outward normals are oriented along the positive n and the negative n directions, respectively, and the superscript B refers to the nodes at the four corners of the 1– face (see Figure 6.8).

Next we proceed to the calibration step (blue colored components of Figure 6.6). As an example, consider the procedure used for establishing $(\beta_{ij11}^n)_k$. For these coefficients, Eq. (6.20) with only the first-order coefficients takes the form

$$(e_{ij})_k = \left(\sum_{n=1}^N (\beta_{ij11}^{n*})_k \mathcal{M}_k^n \right) \bar{\varepsilon}_{11} \quad (6.23)$$

where $\mathbf{e}_k = \Im(\varepsilon_s)$ (see Eq. (6.21)). The constraints on the micro-structure signal, m_s^h , described in Eq. (2.24) translate to the following constraints in the DFT space:

$$\sum_{n=1}^N \mathcal{M}_0^n = S, \quad \sum_{n=1}^N \mathcal{M}_{k \neq 0}^n = 0 \quad (6.24)$$

Introducing Eq. (6.24) into Eq. (6.23) leads to the following condensed equations:

$$(e_{ij})_{\mathbf{k} \neq 0} = \left(\sum_{n=1}^2 (\beta_{ij11}^{n*})_{\mathbf{k}} \mathcal{M}_{\mathbf{k}}^n \right) \bar{\varepsilon}_{11} = ((\beta_{ij11}^1)_{\mathbf{k}} - (\beta_{ij11}^2)_{\mathbf{k}})^* \mathcal{M}_{\mathbf{k}}^1 \bar{\varepsilon}_{11} \quad (6.25)$$

$$= (\gamma_{ij11}^1)_{\mathbf{k}} \mathcal{M}_{\mathbf{k}}^1 \bar{\varepsilon}_{11}$$

$$(e_{ij})_0 = [((\beta_{ij11}^1)_0 - (\beta_{ij11}^2)_0)^* \mathcal{M}_0^1 + (\beta_{ij11}^2)_0^* S] \bar{\varepsilon}_{11} \quad (6.26)$$

The requirement that $(\mathbf{e})_0 = S\bar{\varepsilon}$ (the zero frequency term in DFT) is simply the product of the average value and the number of spatial cells) for any and every microstructure subjected to any choice of the macroscale strain tensor requires $(\beta_0^1)^* = (\beta_0^2)^* = \mathbf{I}$, where \mathbf{I} is the symmetric fourth-rank identity tensor. In addition, for each component of the local strain tensor, the remaining $(S-1)$ influence coefficients are fully uncoupled but not independent (one half of these are complex conjugates of the other half because all components of α are expected to take on only real values [55]).

The FE results from the two delta microstructures (i.e., the calibration dataset) were used to calibrate the values of $(\gamma_{ij11}^1)_{\mathbf{k}}$ in Eq. (6.25) using standard regression methods. Note that the redundancies implicit in Eq. (6.25) preclude the independent estimation of values of β_k^1 and β_k^2 . In other words, we can only estimate the values of γ_k^1 . Likewise, from the best estimates for $(\gamma_{ij11}^1)_{\mathbf{k}}$, we can only recover the values of $(\tilde{\alpha}_{ij11}^1)_{\mathbf{r}} = (\alpha_{ij11}^1)_{\mathbf{r}} - (\alpha_{ij11}^2)_{\mathbf{r}}$. This function is expected to decay rapidly as $|\mathbf{r}|$ increases. The same procedures described earlier can be used to establish the other components of $(\tilde{\alpha}_r^1)$ using other suitable periodic boundary conditions, which also entailed establishing the other components of (γ_k^1) .

The next step in the MKS framework is the generation of a validation dataset (the red colored components in Figure 6.6). For this purpose, one generates a new set of microstructures for the same composite material system being studied. In this case study, a set of random microstructures (where the black and white phases were placed randomly in the microstructure) were employed for the validation task. The random microstructures with their rich diversity of local neighborhoods produce the most heterogeneous microscale strain fields in the composite, and therefore offer an excellent opportunity to evaluate the localization relationships most critically. The validation microstructures were simulated using the same FE approaches that were used in the calibration step.

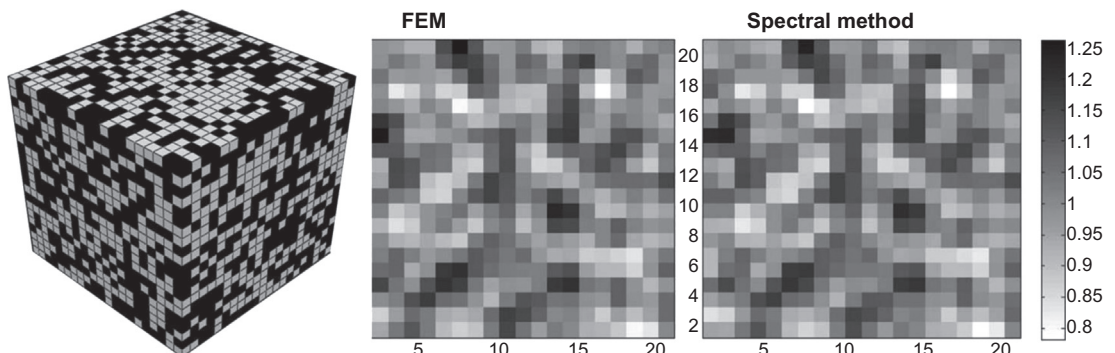


Figure 6.9 Comparison of contour maps of the local ε_{11} component of strain (normalized by the macroscopic applied strain) for the mid-plane of a 3-D random microstructure (left), calculated using the FEM analysis (center) and the MKS spectral method (right). The ratio of the Young's moduli for the two phases was 1.5 [26].

The final step of the MKS framework is the actual validation of the calibrated MKS kernels (the purple colored components of Figure 6.6). Figure 6.9 provides an example of a comparison of the microscale strain fields predicted by the MKS linkages and FE methods for a mid-section through one of the validation microstructures. It is seen that the two predictions are in excellent agreement with each other. It should also be noted that the MKS predictions for the new microstructure are obtained with very minimal computational effort by using Eq. (6.25) and performing an inverse DFT. The MKS predictions for the validation microstructure in Figure 6.9 took only 0.4 sec on a standard desktop computer (2.00 GHz CPU and 4 GB RAM), while the FE method on the same machine took 116 sec. It is therefore clear that there is tremendous gain in computational efficiency in using the MKS calibrated localization metamodels.

The error between the predictions shown in Figure 6.9 from the MKS spectral linkages and the FE methods can be quantified as

$$Err = \max_{s \in S} \left(\frac{|((\varepsilon_{11})_s)_{FEM} - ((\varepsilon_{11})_s)_{MKS}|}{\bar{\varepsilon}_{11}} \right) \cdot 100\% \quad (6.27)$$

where the subscripts FEM and MKS indicate that the predictions were made using FEM and MKS, respectively. Based on the above definition, the value of Err in the results shown in Figure 6.9 was approximately 1%.

One of the central benefits of the MKS framework is that the MKS kernels can be calibrated on smaller volume elements and applied to much larger volume elements. In general, one has to approach this scaling very carefully. However, for the case study presented earlier, where there is no inherent length scale in the

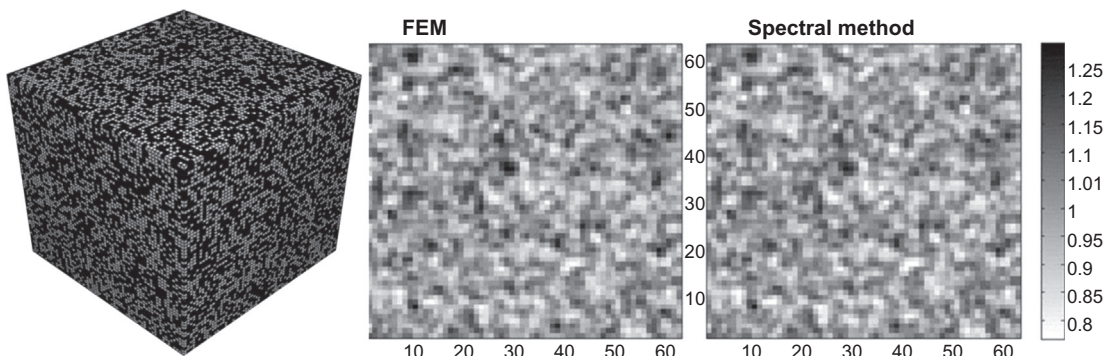


Figure 6.10 Comparison of contour maps of the local ε_{11} component of strain normalized by the macroscopic applied strain for a random 3-D microstructure discretized in a $63 \times 63 \times 63$ grid (left), calculated using the FEM analysis (center) and the MKS spectral linkages (right). The set of influence coefficients for the spectral method are recovered from the set obtained on a coarser $21 \times 21 \times 21$ grid. The strain maps shown in the middle and right are for the mid-plane of the microstructure. The ratio of the Young's moduli between the two phases is 1.5 [26].

physics-based model (i.e., the local elastic properties did not depend on the voxel size or any other inherent length scale in the model), this scaling can be accomplished in a trivial manner. As a specific example, Landi et al. [26] simply pad the $21 \times 21 \times 21$ array of $(\hat{\alpha}_r^1)$ established in the case study described earlier with zeros to an array size of $63 \times 63 \times 63$ and take the DFT to establish the new (γ_k^1) for the larger grid.

The influence coefficients established for $63 \times 63 \times 63$ microstructure grid were then validated using another random microstructure. Figure 6.10 shows the 3-D microstructure used for this purpose along with the predictions from both the MKS spectral linkages as well as the direct FE methods. The error in the predictions (defined using Eq. (6.27)) is still about 1%, validating the simple strategy described earlier for extending the localization relationships to larger microstructure datasets. It is also worth noting that the DFT-based approach took 10.4 sec on a desktop computer, while the FE method took approximately 1 h on the same machine.

The methods described earlier have also been successfully demonstrated for thermoelastic deformations in multiphase composites [25].

6.7 Case Study: MKS for Elastic Response of Higher Contrast Composites

As mentioned earlier, it was generally observed that the first-order terms in the MKS series expansion were adequate to

capture accurately the microscale distribution of response fields of interest as long as the contrast between the respective properties of the local states in the microstructure was limited to moderately low values. It has also been observed that the higher order terms are essential for improving the accuracy of the MKS metamodels for material systems with moderate to high contrast. The main impediment to including the higher order terms arises from the fact that the number of influence coefficients in the higher order terms is extremely large. Although some decoupling is accomplished by the use of DFTs (details presented in the previous section), the numbers of even the second-order coefficients for most problems are so large that it is not practical to simply extend and employ the same heuristics described in the previous section.

In recent work [28], it was pointed out that the higher-order terms in Eq. (6.19) can be collapsed to look similar to the first-order term for specific choices of the additional vectors. As an example, consider the second term in the series of Eq. (6.19). If one chooses a specific value for the index r' , then the second term has the exact same features as the first term in terms of the variable spatial indices. In other words, we can continue to use the DFT transformation we used earlier to uncouple the influence coefficients. This should not be surprising, as it essentially amounts to selection of specific numbers (or selection of specific terms) from the very large number of potential higher-order terms. The selection can of course be guided by systematically increasing the number of near neighbors included for each higher order term in the series [28]. More specifically, it was demonstrated that Eq. (6.19) retains the simple form as before, even when the higher order terms are included:

$$\mathbf{p}_s = \left(\sum_{i=1}^I \sum_{r \in S} \alpha_r^i m_{s+r}^i \right) \bar{\mathbf{p}} \quad (6.28)$$

In Eq. (6.28), the index i now enumerates all of the distinct local configurations, each specified by a selected set of local vectors and the associated local states. The series in Eq. (6.28) is truncated after the consideration of a finite number of such local configurations (denoted by I). As a specific illustration, the case study of the previous section was repeated with a contrast of 10 in the ratio of the values of the Young's moduli of the two phases (the Poisson ratios were once again kept the same for the two phases). The results from this case study are summarized in Figure 6.11 [28]. The MKS predictions using only the first-order term (Case 1 in Figure 6.11) exhibited an error of

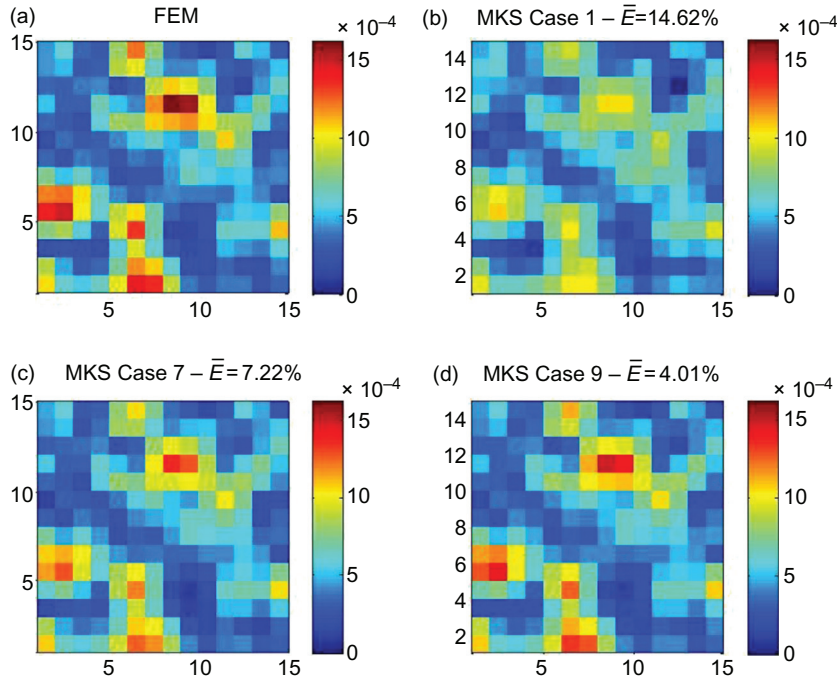


Figure 6.11 MKS and FE predictions of the strain fields in an example 3-D composite microstructure with a contrast ratio of 10 between the Young's moduli of the constituent phases. The strain fields shown are from a section perpendicular to the loading direction and containing the highest local strain in the microstructure in the FE predictions.

14.62%. However, the inclusion of second-order coefficients involving up to sixth neighbors (Case 7 in Figure 6.11) reduced the error in the MKS predictions to 7.22%. Furthermore, the inclusion of seventh-order coefficients (seventh-term in the series shown in Eq. (6.19) involving first neighbors along with the second-order coefficients involving second to sixth neighbors reduced the error to 4.01%. Clearly the higher order terms play an important role in the MKS metamodels for composite with high contrast.

6.8 Case Study: MKS for Elastic Response of Polycrystals

We now examine the application of the MKS framework to a more complex material system such as a polycrystalline material system with a continuous local state. We encountered these

materials in Chapter 2, where we recognized that the definition of the local state now has to include a description of the crystal lattice orientation in the form of Bunge–Euler angles, that is, $h = g = (\varphi_1, \Phi, \varphi_2)$. We have also briefly discussed the fact that the symmetrized generalized spherical harmonic basis (GSH) [56] denoted as $\dot{T}_l^{\mu n}(g)$ serves an excellent Fourier basis for functions defined on the orientation space (see Eq. (2.28)).

With the use of the GSH as the Fourier basis, the microstructure and the influence functions take the following specific forms [29]

$$m_s(g) = \sum_{\mu,n,l} M_{ls}^{\mu n} \dot{T}_l^{\mu n}(g), \quad M_{ls}^{\mu n} = (2l+1) \int_{FZ} m_s(g) \dot{T}_l^{\mu n*}(g) dg \quad (6.29)$$

$$\alpha_r(g) = \sum_{\mu,n,l} A_{lr}^{\mu n} \dot{T}_l^{\mu n}(g), \quad A_{lr}^{\mu n} = (2l+1) \int_{FZ} \alpha_r(g) \dot{T}_l^{\mu n*}(g) dg \quad (6.30)$$

In writing the microstructure and the influence functions earlier, we have already binned the spatial variables because we anticipate using the DFTs for their computational efficiency in carrying out the convolutions involved in the MKS series. Therefore, only the local state variable is being shown in the Fourier representations in these equations. $M_{ls}^{\mu n}$ and $A_{lr}^{\mu n}$ are the Fourier coefficients of the functions $m_s(g)$ and $\alpha_r(g)$, respectively. As a special case, when there is a single crystal of lattice orientation g_o in a spatial bin s , the corresponding GSH coefficients of $m_s(g)$ are simply given by

$$M_{ls}^{\mu n} = (2l+1) \dot{T}_l^{\mu n*}(g_o) \quad (6.31)$$

The orthonormality of the GSH basis functions allows us to derive the following expression for the first-order MKS (i.e., the higher-order terms are truncated) [29]

$$\mathbf{p}_s = \sum_L \sum_{\mathbf{r}} \frac{1}{(2l+1)} \mathbf{A}_r^L M_{s+r}^{L*} \bar{\mathbf{p}} \quad (6.32)$$

where L enumerates each distinct combination of (μ, n, l) in the GSH series expansion. In prior work [52,53,57,58], it was seen that kernel functions in elastic statistical continuum theories (which have exactly the same physical meaning as the influence functions described here) had nonzero coefficients only for a few of the terms in the series ($l = 0, 4$ for cubic-triclinic and

$l = 0, 2, 4$ for hexagonal-triclinic). Herein, lies the tremendous potential of the GSH representations for the MKS formulation. If the GSH representations of the influence coefficients, A_r^L , were successfully captured in a limited number of terms, it would lead to tremendous computational benefits in the calibration of the MKS linkages.

The hypothesis stated earlier was validated recently with a specific case study focused on the elastic deformation of polycrystals [29]. As noted earlier, the first step in establishing the MKS metamodels involves the generation of a calibration dataset. In this specific study, three different types of microstructures were used in the training set: (i) delta, (ii) equi-axed, and (iii) random microstructures (see Figure 6.12). As noted earlier, delta microstructures are very efficient in capturing accurately the fundamental interactions between the two local states represented in them. However, since we can explore only two orientations at a time in a delta microstructure, they are not efficient in quickly exploring the interactions between all possible local states (note that a very large number of local states are possible in this case study). Conversely, the random microstructures (where each volume element is assigned a distinct crystal lattice orientation) permit efficient exploration of the interactions between a large numbers of crystal lattice orientations. Note also that the random microstructures produce the most heterogeneous stress (and strain) fields in the microscale volume elements (MVEs). The equi-axed microstructures were added to the calibration dataset as they reflect the type of microstructures encountered in real applications.

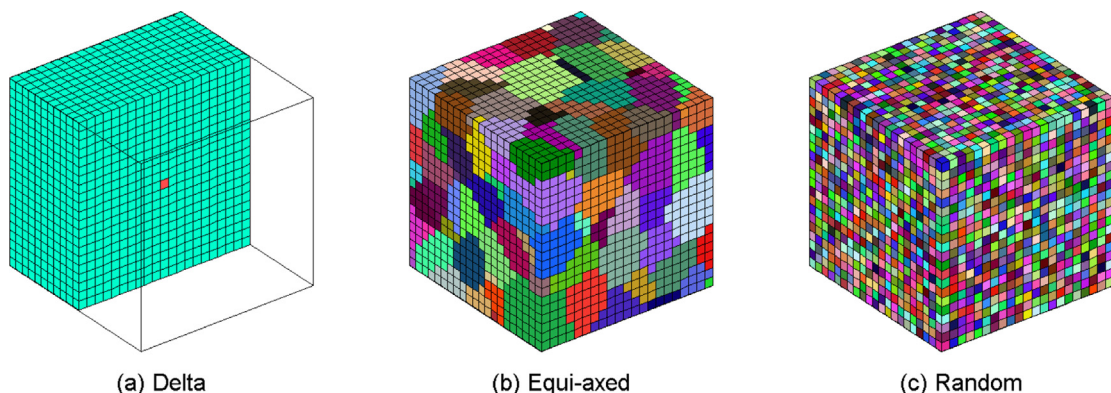


Figure 6.12 Examples of MVEs (of size $21 \times 21 \times 21$) used for the calibration of influence coefficients for polycrystalline material systems studied in this work: (a) delta microstructures, (b) equi-axed microstructures, and (c) random microstructures [29].

The assignment of crystal orientations to each microstructure in the calibration set must be accomplished in such a way that it permits efficient exploration of the very large range of potential spatial interactions between all possible local states [53]. Since the local state space for the problems at hand is a continuous space, the number of distinct orientations making up the local state space is essentially infinite. A strategy that has been successfully used in other studies is to identify a set of principal orientations that exhibit the extremes in the local responses (or properties) of interest. The central hypothesis is that using these principal orientations in the calibration process ensures that the MKS linkages are employed largely as interpolations as opposed to extrapolations. It was previously shown that the principal orientations can be identified as the vertices of a texture hull in the GSH space [59,60], which were also observed to correspond with the orientations on the bounding surfaces of the fundamental zone [53]. For this case study, the set of principal orientations were sampled from the bounding surface of the fundamental zone in the orientation space.

The calibration dataset for the case study was then established by executing micromechanical FE simulations using commercial software ABAQUS [61], using protocols very similar to those used in the previous case studies. Two material systems were selected for this study: (i) copper with elastic stiffness constants $C_{11} = 168.4 \text{ GPa}$, $C_{12} = 121.4 \text{ GPa}$ and $C_{44} = 75.4 \text{ GPa}$ [62] (this corresponds to cubic anisotropy ratio of $A = 3.21$), (ii) α -Ti with elastic stiffness constants $C_{11} = 154 \text{ GPa}$, $C_{12} = 86 \text{ GPa}$, $C_{44} = 46 \text{ GPa}$, $C_{13} = 67 \text{ GPa}$ and $C_{33} = 183 \text{ GPa}$ [63]. Micromechanical finite element simulations were executed on a total of 3600 microstructures or MVE.

The next step, calibration of the influence kernels, was accomplished by casting the linkages of interest (Eq. (6.32)) in the DFT space (following the same approach as in the previous examples):

$$\mathbf{P}_k = \left[\left(\sum_L \mathbf{A}_k^{L*} \mathcal{M}_k^L \right) \right] \bar{\mathbf{p}} \quad (6.33)$$

$$\mathbf{A}_k^L = \Im(\mathbf{A}_r^L), \quad \mathbf{P}_k = \Im(\mathbf{p}_s), \quad \mathcal{M}_k^L = \Im(M_s^{L*})$$

where \mathbf{A}_k^L and \mathcal{M}_k^L are the Fourier coefficients of influence functions and the microstructure function in the DFT space. As usual, the values of \mathbf{A}_k^L are established using standard regression methods on the calibration dataset.

The next step involves the validation of the MKS kernels established. Following protocols similar to those described

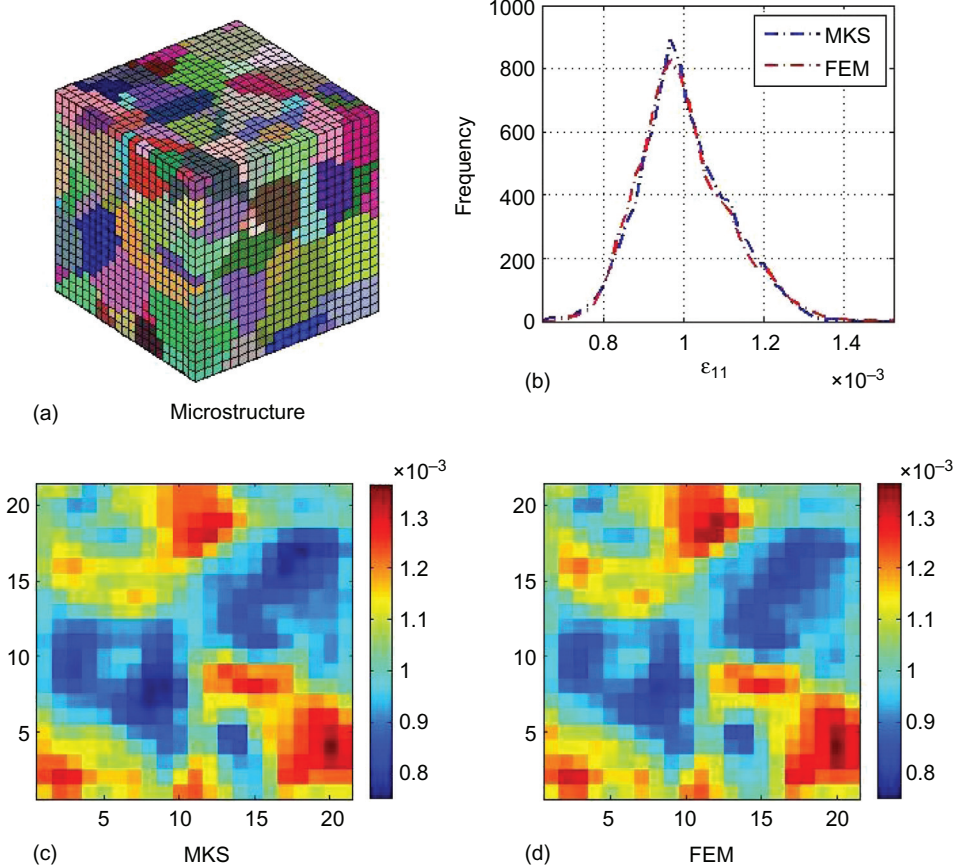


Figure 6.13 Comparison of strain fields predicted with MKS and FEM approaches. (a) An example Copper polycrystal microstructure selected for the validation. (b) Frequency plots of the predictions of ε_{11} from MKS and FEM. (c) and (d) Middle slices of strain fields predicted by MKS and FEM, respectively [29].

earlier, it was determined that only ten values of L (corresponding to $l = (0, 4)$ as expected) produced dominant contributions for cubic polycrystals. Similarly, only 15 values of L (corresponding to $l = (0, 2, 4)$) produced dominant values for the hexagonal polycrystals. It is emphasized that the tremendous dimensionality reduction obtained as a consequence of using the GSH representations results in major computational advantages.

The accuracy of the MKS linkages established in this case study was critically evaluated by computing the mean, minimum, and maximum errors for a selected validation dataset. It was observed that the MKS kernels exhibited remarkable accuracy for both classes of polycrystals (the maximum error was

less than 0.5% for hexagonal polycrystals, while it was less than 2% for cubic polycrystals). As expected, the error increases with increased contrast (the anisotropy in Copper polycrystals is substantially larger than in α -Titanium). As a specific example, Figure 6.13 shows the strain field predicted by the MKS models along with the corresponding prediction from FEM for a selected equi-axed microstructure of Copper. The plots shown in Figure 6.13(c) and 6.13(d) correspond to the strain distributions of a middle slice of the three dimensional MVE shown in Figure 6.13(a). Figure 6.13(b) compares the distributions of the strains present in the two predictions (for the entire MVE). It is seen that there is an excellent agreement between the FEM and MKS predictions.

It is also important to note the computational efficiency of the MKS approach. For example, the FEM prediction of a $21 \times 21 \times 21$ MVE took 25 sec with 2 processors (each 3.0 GHz) on a supercomputer, while prediction with MKS took only 2 sec with only 1 processor (3.0 GHz) on a standard desktop computer.

6.9 Case Study: MKS for Perfectly Plastic Response of Composites

In this case study, we will demonstrate the applicability of the MKS framework to the rate-independent rigid-plastic deformation of a two-phase MVE, with no strain hardening. The two phases are assumed to exhibit isotropic plasticity with yield strengths of 200 MPa and 250 MPa, respectively. The stress-strain relationships for both phases are assumed to be described by the Levy–Mises equations [64] as

$$\dot{\varepsilon} = \lambda \sigma', \quad (6.34)$$

where $\dot{\varepsilon}$ is the symmetric strain rate tensor, σ' is the symmetric deviatoric Cauchy stress tensor, and λ is a proportionality parameter that can be related to the yield strength of the material, the equivalent plastic strain rate and the equivalent stress. Although, it is not directly apparent from Eq. (6.34), this constitutive relation described implies a rate-independent plastic response. The goal of the localization linkage is to compute the local strain rate field in the MVE of the two-phase composite. For simplicity, we shall consider the case of an applied isochoric simple compression strain rate tensor at the macroscale, with equal extension in lateral directions, expressed as

$$\dot{\bar{\varepsilon}}_{ij} = \begin{bmatrix} \dot{\bar{\varepsilon}} & 0 & 0 \\ 0 & -0.5\dot{\bar{\varepsilon}} & 0 \\ 0 & 0 & -0.5\dot{\bar{\varepsilon}} \end{bmatrix} \quad (6.35)$$

For this example, the local state space is discrete (only two local states). Therefore, we can revert back to our earlier formulation in Eqs. (6.25) and (6.26), modified for the present case study, as

$$(\dot{\boldsymbol{e}})_{k \neq 0} = \left(\sum_{n=1}^2 \beta_k^{n*} \mathcal{M}_k^n \right) \dot{\bar{\varepsilon}} = (\beta_k^1 - \beta_k^2)^* \mathcal{M}_k^1 \dot{\bar{\varepsilon}} = \gamma_k^1 \mathcal{M}_k^1 \dot{\bar{\varepsilon}} \quad (6.36)$$

$$(\dot{\boldsymbol{e}})_0 = S \dot{\bar{\varepsilon}} \quad (6.37)$$

The main difference compared to earlier formulation is that in this case study β_k^{n*} are expressed as a second-rank tensor. The second obvious difference is that the MKS linkage is now between macroscopically imposed strain rate tensor and the local strain rate tensor in each spatial bin.

As before, the values of γ_k^1 are established by regression analysis using calibration datasets produced by FE models on selected microstructures. Once again, for this case study, we employ two delta microstructures. The MVE contained 804,357 ($93 \times 93 \times 93$) cuboid-shaped three-dimensional eight-noded solid elements. The values of γ_k^1 were established as the best-fit values for the FE results on the two delta microstructures, using standard linear regression analyses methods [65].

As a validation of the MKS kernels, we demonstrate their predictive capability on a completely different MVE in Figure 6.14. This figure compares the local $\dot{\varepsilon}_{11}$ component of the strain rate field for the validation microstructure using both the FE analysis and the calibrated MKS kernels. The average error over all of the spatial bins for the microstructure shown in Figure 6.14 is only 2.2%. The FE analyses could not be performed on a regular desktop PC. It was executed on an IBM e1350 supercomputing system (part of The Ohio Supercomputer Center), and required 94 processor hours. In contrast, the MKS method took only 32 sec on a regular laptop (2 GHz CPU and 2 GB RAM).

In the case study presented here, MKS was developed for a very specific loading condition (i.e., simple compression strain rate tensor; see Eq. (6.35)). In order to extend the MKS framework presented here to general loading conditions, we need to generalize Eq. (6.36) as

$$(\dot{\boldsymbol{e}})_{k \neq 0} = \gamma_k^1(\dot{\bar{\varepsilon}}) \mathcal{M}_k^1 \dot{\bar{\varepsilon}} \quad (6.38)$$

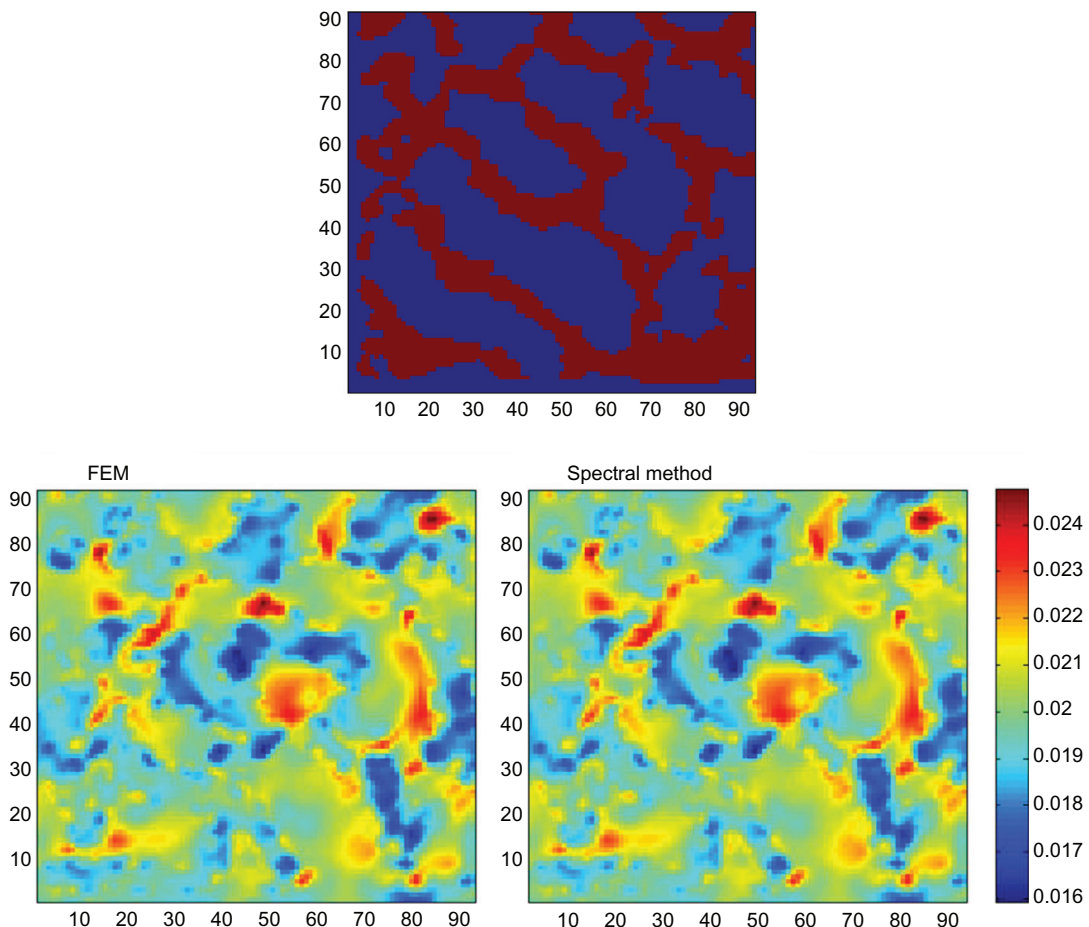


Figure 6.14 Comparison of the contour maps of the local $\dot{\varepsilon}_{11}$ component of the strain rate tensor for a 3-D microstructure. The middle section of the 3-D MVE used in the calculation is shown at the top (a), while the predicted strain rate contours by the FE method (b), and the MKS established in this work (c) are shown below. Both phases are assumed to exhibit isotropic plasticity with yield strengths of 200 MPa and 250 MPa, respectively. The macroscopic simple compression strain rate applied is 0.02 s^{-1} .

where the dependence of γ_k^1 on the macroscale imposed strain rate tensor, $\dot{\varepsilon}$, is explicitly noted. We therefore need to establish the functional dependence of γ_k^1 in the space of symmetric second rank tensors, which is a six-dimensional space. However, if we elect to solve the problem in the principal frame of $\dot{\varepsilon}$ (i.e., the microstructure signal needs to be appropriately rotated), then the domain of interest for describing γ_k^1 reduces to a three-dimensional space. If we further exploit the fact that the magnitude of $\dot{\varepsilon}$ has no effect on the localization (a consequence

of the rate-independence of the plastic response) and we require $\dot{\varepsilon}$ to be traceless (to reflect volume conservation during plastic deformation), then the domain of interest for describing γ_k^1 can be expressed using a single angular variable [66,67]. The functional dependence of γ_k^1 on this single angular variable can be expressed conveniently using DFTs [67]. These strategies will be expounded in the next chapter.

References

- [1] Ghosh S, Lee K, Moorthy S. Multiple scale analysis of heterogeneous elastic structures using homogenization theory and voronoi cell finite element method. *Int J Solids Struct* 1995;32(1):27–62.
- [2] Kouznetsova VG, Geers MGD, Brekelmans WAM. Multi-scale second-order computational homogenization of multi-phase materials: a nested finite element solution strategy. *Comput Methods Appl Mech Eng* 2004;193(48-51):5525–50.
- [3] Kadewaki H, Liu WK. Bridging multi-scale method for localization problems. *Comput Methods Appl Mech Eng* 2004;193(30-32):3267–302.
- [4] Luscher DJ, McDowell DL, Bronkhorst CA. A second gradient theoretical framework for hierarchical multiscale modeling of materials. *Int J Plas* 2010;26(8):1248–75.
- [5] Materials Genome Initiative for Global Competitiveness., National Science and Technology Council, Executive Office of the President, 2011.
- [6] Pollock TM, et al. Integrated computational materials engineering: a transformational discipline for improved competitiveness and national security. Washington DC: The National Academies Press; 2008.
- [7] McDowell DL, Story TL. New directions in Materials Design Science and Engineering (MDS&E). Report of a NSF DMR-Sponsored Workshop. 1998, October, p. 19–21.
- [8] A National Strategic Plan for Advanced Manufacturing, National Science and Technology Council, Executive Office of the President, Feb 2012.
- [9] Schmitz GJ, Prahl U. ICMEg—the Integrated Computational Materials Engineering expert group—a new European coordination action. *Integr Mater Manuf Innov* 2014;3(1):2.
- [10] Kalidindi SR. Data science and cyberinfrastructure: critical enablers for accelerated development of hierarchical materials. *Int Mater Rev* 2015;60(3):150–68.
- [11] Kirane K, et al. Grain level dwell fatigue crack nucleation model for Ti alloys using crystal plasticity finite element analysis. *J Eng Mater Technol-Trans Asme* 2009;131(2):23–37.
- [12] Przybyla CP, McDowell DL. Simulated microstructure-sensitive extreme value probabilities for high cycle fatigue of duplex Ti-6Al-4V. *Int J Plast*, Special Issue in Honor of Nobutada Ohno 2012;27(12):1871–95.
- [13] Wang BL, et al. Systematic approach to microstructure design of Ni-base alloys using classical nucleation and growth relations coupled with phase field modeling. *Metall Mater Trans a-Physical Metall Sci* 2008;39A(5):984–93.
- [14] Wen YH, et al. Phase-field modeling of bimodal particle size distributions during continuous cooling. *Acta Mater* 2003;51(4):1123–32.

- [15] Kalidindi SR, Bhattacharya A, Doherty R. Detailed analysis of plastic deformation in columnar polycrystalline aluminum using orientation image mapping and crystal plasticity models. *Proc R Soc London: Math, Phys Eng Sci* 2004;460(2047):1935–56.
- [16] Adams BL, Olson T. Mesostructure - properties linkage in polycrystals. *Progress Mater Sci* 1998;43(1):1–88.
- [17] Castañeda PP, Telega JJ, Gambin B. Nonlinear homogenization and its applications to composites, polycrystals and smart materials. Springer; 2004.
- [18] Fullwood DT, Adams BL, Kalidindi SR. A strong contrast homogenization formulation for multi-phase anisotropic materials. *J Mech Phys Solids* 2008;56(6):2287–97.
- [19] Milton GW, et al. The theory of composites Cambridge monographs on applied and computational mathematics. New York, NY, USA: Cambridge University Press; 2001.
- [20] Roters F, et al. Overview of constitutive laws, kinematics, homogenization and multiscale methods in crystal plasticity finite-element modeling: theory, experiments, applications. *Acta Mater* 2010;58(4):1152–211.
- [21] Willis JR. Variational and related methods for the overall poroperties of composite materials. *Adv Appl Mech* 1981;21:2–78.
- [22] CeCen A, et al. A data-driven approach to establishing microstructure-property relationships in porous transport layers of polymer electrolyte fuel cells. *J Power Sources* 2014;245:144–53.
- [23] Kalidindi SR, Niezgoda SR, Salem AA. Microstructure informatics using higher-order statistics and efficient data-mining protocols. *JOM* 2011;63(4):34–41.
- [24] Kalidindi SR, et al. A novel framework for building materials knowledge systems. *Comput Mater Continua* 2010;17(2):103–25.
- [25] Landi G, Kalidindi SR. Thermo-Elastic localization relationships for multi-phase composites. *Cmc-Comput Mater Continua* 2010;16(3):273–93.
- [26] Landi G, Niezgoda SR, Kalidindi SR. Multi-scale modeling of elastic response of three-dimensional voxel-based microstructure datasets using novel DFT-based knowledge systems. *Acta Mater* 2010;58(7):2716–25.
- [27] Fast T, Niezgoda SR, Kalidindi SR. A new framework for computationally efficient structure–structure evolution linkages to facilitate high-fidelity scale bridging in multi-scale materials models. *Acta Mater* 2011;59(2):699–707.
- [28] Fast T, Kalidindi SR. Formulation and calibration of higher-order elastic localization relationships using the MKS approach. *Acta Mater* 2011;59:4595–605.
- [29] Yabansu YC, Patel DK, Kalidindi SR. Calibrated localization relationships for elastic response of polycrystalline aggregates. *Acta Mater* 2014;81:151–60.
- [30] Shaffer JB, Knezevic M, Kalidindi SR. Building texture evolution networks for deformation processing of polycrystalline fcc metals using spectral approaches: applications to process design for targeted performance. *Int J Plast* 2010;26(8):1183–94.
- [31] Al-Harbi HF, Kalidindi SR. Crystal plasticity finite element simulations using a database of discrete Fourier transforms. *Int J Plast* 2015;66:71–84.
- [32] Al-Harbi HF, Landi G, Kalidindi SR. Multi-scale modeling of the elastic response of a structural component made from a composite material using the materials knowledge system. *Model Simul Mater Sci Eng* 2012;20(5):055001.
- [33] Kalidindi SR. Computationally efficient, fully coupled multiscale modeling of materials phenomena using calibrated localization linkages. *ISRN Mater Sci* 2012;2012:13.

- [34] Garmestani H, Lin S, Adams BL. Statistical continuum theory for inelastic behavior of a two-phase medium. *Int J Plast* 1998;14(8):719–31.
- [35] Garmestani H, et al. Statistical continuum theory for large plastic deformation of polycrystalline materials. *J Mech Phys Solids* 2001;49(3):589–607.
- [36] Adams BL, Kalidindi SR, Fullwood D. Microstructure sensitive design for performance optimization. Waltham, MA, USA: Butterworth-Heinemann; 2012.
- [37] Gao X, Przybyla CP, Adams BL. Methodology for recovering and analyzing two-point pair correlation functions in polycrystalline materials. *Metall Mater Trans A* 2006;37(8):2379–87.
- [38] Kalidindi SR, et al. Elastic properties closures using second-order homogenization theories: Case studies in composites of two isotropic constituents. *Acta Mater* 2006;54(11):3117–26.
- [39] Fullwood DT, et al. Microstructure sensitive design for performance optimization. *Progress Mater Sci* 2010;55(6):477–562.
- [40] Gokhale AM, Tewari A, Garmestani H. Constraints on microstructural two-point correlation functions. *Scr Mater* 2005;53:989–93.
- [41] Gupta A, et al. Structure-property linkages for non-metallic inclusions/steel composite system using a data science approach. *Acta Mater* 2015;91:239–54.
- [42] Rao CR. Linear statistical inference and its applications, vol. 22. Hoboken, NJ, USA: John Wiley & Sons; 2009.
- [43] Baker T, Gave K, Charles J. Inclusion deformation and toughness anisotropy in hot-rolled steels. *Met Technol* 1976;3(1):183–93.
- [44] Garrison Jr WM, Wojcieszynski AL. A discussion of the effect of inclusion volume fraction on the toughness of steel. *Mater Sci Eng: A* 2007;464 (1–2):321–9.
- [45] Gupta A, et al. Integrated modeling of steel refining, casting and rolling operations to obtain design set points for quality steel sheet production. In: The 11th International Conference On Numerical Methods In Industrial Forming Processes: Numiform 2013. 2013. AIP Publishing.
- [46] Lankford J. (E) Effect of oxide inclusions on fatigue failure. *Int Met Rev* 1977;22(1):221–8.
- [47] Murakami Y. Metal fatigue: effects of small defects and nonmetallic inclusions: effects of small defects and nonmetallic inclusions. Atlanta, GA, USA: Elsevier; 2002.
- [48] Alfano G, Crisfield M. Finite element interface models for the delamination analysis of laminated composites: mechanical and computational issues. *Int J Numer Methods Eng* 2001;50(7):1701–36.
- [49] ANSYS Release 14.0, Help System, Mechanical APDL, ANSYS, Inc.
- [50] Luo C. Evolution of voids close to an inclusion in hot deformation of metals. *Comput Mater Sci* 2001;21(3):360–74.
- [51] Stienon A, et al. A new methodology based on X-ray micro-tomography to estimate stress concentrations around inclusions in high strength steels. *Mater Sci Eng: A* 2009;513:376–83.
- [52] Duvvuru HK, Wu X, Kalidindi SR. Calibration of elastic localization tensors to finite element models: Application to cubic polycrystals. *Comput Mater Sci* 2007;41(2):138–44.
- [53] Kalidindi SR, Landi G, Fullwood DT. Spectral representation of higher-order localization relationships for elastic behavior of polycrystalline cubic materials. *Acta Mater* 2008;56(15):3843–53.
- [54] Adams BL, Gao X, Kalidindi SR. Finite approximations to the second-order properties closure in single phase polycrystals. *Acta Mater* 2005;53 (13):3563–77.

- [55] Oppenheim AV, Schafer RW, Buck JR. Discrete time signal processing. Upper Saddle River, NJ, USA: Prentice-Hall; 1999.
- [56] Bunge HJ. Texture analysis in materials science: mathematical methods. London, UK: Butterworths; 1982.
- [57] Proust G, Kalidindi SR. Procedures for construction of anisotropic elastic–plastic property closures for face-centered cubic polycrystals using first-order bounding relations. *J Mech Phys Solids* 2006;54(8):1744–62.
- [58] Wu X, et al. Elastic–plastic property closures for hexagonal close-packed polycrystalline metals using first-order bounding theories. *Acta Mater* 2007;55(8):2729–37.
- [59] Adams BL, et al. Microstructure-sensitive design of a compliant beam. *J Mech Phys Solids* 2001;49(8):1639–63.
- [60] Kalidindi SR, et al. Microstructure sensitive design of an orthotropic plate subjected to tensile load. *Int J Plast* 2004;20(8–9):1561–75.
- [61] Hibbit D, Karlsson B, Sorensen P. ABAQUS/Standard Analysis User’s Manual. Providence, RI, USA: Hibbit, Karlsson, Sorensen Inc; 2007.
- [62] Meyers MA, Chawla KK. Mechanical behavior of materials. New York, NY, USA: Cambridge University Press; 2009.
- [63] Welsch G, Boyer R, Collings EW. Materials properties handbook: titanium alloys. Materials Park, OH, USA: ASM International; 1993.
- [64] Khan AS, Huang S. Continuum theory of plasticity. New York: Wiley; 1995.
- [65] Montgomery DC, Peck EA, Vining GG. Introduction to linear regression analysis. Hoboken, NJ: Wiley-Interscience; 2006.
- [66] Van Houtte P. Application of plastic potentials to strain rate sensitive and insensitive anisotropic materials. *Int J Plast* 1994;10(7):719–48.
- [67] Knezevic M, Al-Harbi HF, Kalidindi SR. Crystal plasticity simulations using discrete Fourier transforms. *Acta Mater* 2009;57(6):1777–84.

PROCESS–STRUCTURE LINKAGES

We now shift our focus to the other challenge in establishing process–structure–property (PSP) linkages, i.e., establishing process–structure linkages. In many situations, we will find that the process–structure linkages are more conveniently cast as process–structure evolution linkages that capture the instantaneous time derivatives of the structure for an imposed process condition. This would then mean that the information on the structure evolution then needs to be properly integrated in time (or over the entire process route) to predict the final structures achieved in a given process. When these linkages are suitably combined with the structure–property linkages described in the last chapter, we have the opportunity to establish the high-value PSP linkages needed for accelerated design, development, and deployment of new/improved materials in advanced technologies.

7.1 Mathematical Framework

The mathematical framework for process–structure linkages follows the same framework that was presented in Chapter 6, but with differences in the output variables. In the structure–property linkages, the salient measures of the microstructure were used as inputs and the properties of interest associated with the microstructure served as the outputs. In the process–structure linkages, we are interested in capturing the details of the microstructure evolution as a function of the process parameters. Consequently, we have to treat the initial microstructure and the process parameters as inputs to the linkages, and the rate of change in the microstructure as the output. One can see right away that the process–structure linkages are, in general, significantly more challenging than the structure–property linkages we discussed in the previous chapter. This is mainly because we need to include potentially a very

large-dimensional representation of the structure in both the input and the output lists of variables.

As a simple illustration, let us consider the microstructure evolution predicted by a selected phase-field model in a selected material system. Even when the physics of the problem is fixed (i.e., the governing field equations of the model are fixed), different initial microstructures will produce different final microstructures. This can be visualized conveniently using the protocols described in Chapters 3 and 4. As an illustration, we capture in [Figure 7.1](#) the salient details of the microstructure evolution in the principal component analyses (PCA) space (using the protocols presented earlier in this book) for 10 different initial microstructures. It is important to note that only the first three principal components (PCs) are shown in this plot. As each microstructure is represented as a point in this space, each pathline shown in [Figure 7.1](#) captures the details of the microstructure evolution for one initial microstructure. It is interesting that the 10 initial microstructures produced 10

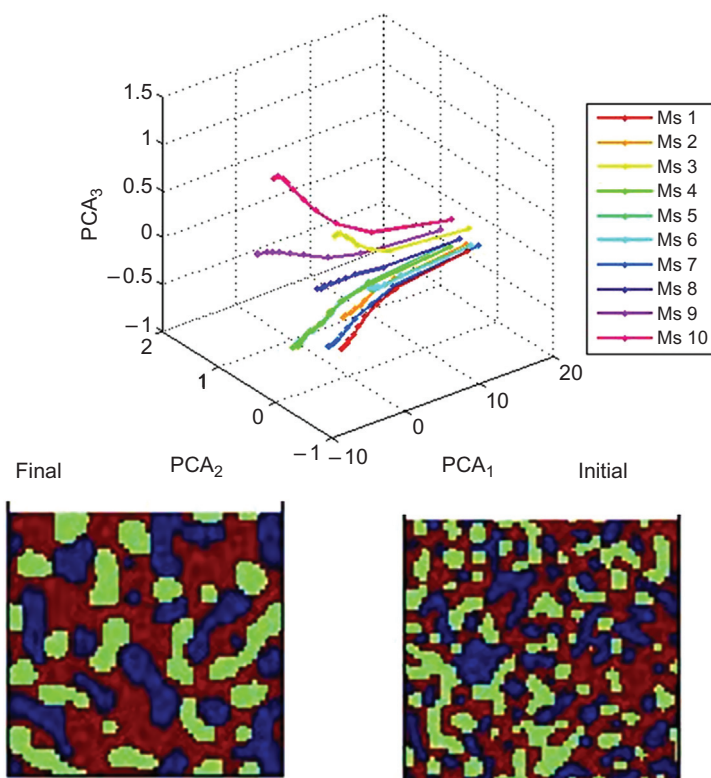


Figure 7.1 Illustration of pathlines capturing salient details of the microstructure in the PCA space. As each point in this space represents a microstructure, each pathline captures the details of the evolution of the microstructure from its initial state to its final state. Representative examples of initial and final microstructures are also presented. The microstructure is a three-phase microstructure, and the data was generated using a phase-field model.

nonintersecting pathlines. This is one again a testament to the power of the techniques presented in this book, as intersecting pathlines would imply that a given microstructure (at the point of intersection) can produce two different microstructures at the next time step and therefore would be nonphysical. In the context of the low-dimensional PCA representations, intersecting pathlines would imply that we lost important information in the dimensionality reduction step. That is why it is remarkable that only three PCs produce nonintersecting pathlines for this ensemble of data.

Going back to [Figure 7.1](#), if one was to overlay pathlines from a different process (e.g., different driving forces or model parameters), then the pathlines from the other process would be expected to intersect these pathlines. In fact, the overlaying of pathlines from different processes and finding these intersections points (or nodes) are critical to successfully addressing inverse problems in process design. Indeed, such a process network superimposed with property contours was schematically introduced in [Figure 1.5](#) at the beginning of this book. We have now identified a specific set of protocols in Chapters 6 and 7 to accomplish this tremendous challenge. We will revisit this concept later in a specific case study.

Mathematically, a single data point for mining the process-structure linkages of interest for considerations at the higher length scale (i.e., in the homogenization direction) can be expressed in a general form as $(\{\dot{\alpha}_i^{(k)}|i=1,2,\dots,\tilde{R}\}, \{\theta_i|i=1,2,\dots,I\}, \{\alpha_i^{(k)}|i=1,2,\dots,\tilde{R}\})$, where (k) indexes a specific microstructure, and θ_i denote the process parameters. If we seek simple polynomial linkages (analogous to [Eq. \(6.6\)](#)), we could express the desired linkages as

$$\dot{\alpha}_j \approx \tilde{A}_o(\theta_k) + \sum_i \tilde{A}_{ij}(\theta_k) \tilde{\alpha}_i \quad (7.1)$$

where $\tilde{\alpha}_i$ denote polynomial combinations ([Chapter 6](#)). Note that the coefficients of the polynomials are expected to depend strongly on the process parameters. As noted earlier, establishing the process-structure linkages is indeed significantly more challenging than establishing structure-property linkages. Furthermore, we need to ensure that the linkages produce non-intersecting pathlines within the range of the microstructure space of interest.

In a very similar manner, one can also address localization linkages connecting the processing conditions with the details of microstructure evolution. As an example, one could suitably modify [Eq. \(6.18\)](#) for this purpose as

$$\begin{aligned}\dot{M}_s^K = & \left(\sum_L \sum_r \frac{\Delta}{N_L} A_{\mathbf{r}}^{KL}(\theta_k) M_{s+r}^{L^*} \right. \\ & \left. + \sum_L \sum_{L'} \sum_r \sum_{r'} \frac{\Delta^2}{N_L N_{L'}} A_{\mathbf{r} \mathbf{r}'}^{KLL'}(\theta_k) M_{s+r}^{L^*} M_{s+r+r'}^{L'^*} + \dots \right) \quad (7.2)\end{aligned}$$

Once again, it is reiterated that it is indeed quite challenging to implement these because of the very high dimensionality of representations involved in these linkages. In order to obtain practically useful linkages, one has to resort to suitable heuristics. In the rest of this chapter, we describe two specific applications where we have enjoyed some success.

7.2 Case Study: Microstructure Evolution Using Phase-Field Models

The tools developed in this book have been demonstrated on selected phase-field models. As a specific example, microstructure evolution during spinodal decomposition was targeted for the first demonstration [1]. Spinodal decomposition occurs when a homogeneous mixture separates into regions of distinct chemical compositions (or phases). Phase separation of a binary alloy into two phases can be described by the well-known Cahn–Hilliard equation [2,3] as

$$\dot{c}(\mathbf{x}) = \nabla^2 D \left(\frac{df(c(\mathbf{x}))}{dc} - \nabla^2 K c(\mathbf{x}) \right) \quad (7.3)$$

where \mathbf{x} is the spatial variable, c is a conserved order parameter that defines the atomic fraction of one of the phases, D is the diffusion coefficient, f is the free energy expressed as a function of c , and K gives information about the interface between the two phases. The free energy, f , is classically assumed to be a double-well potential and is often approximated as a fourth-order polynomial as [4]

$$f(c(\mathbf{x})) = 4F(c(\mathbf{x})^2 - 1)^2 \quad (7.4)$$

where F is the height of the energy barrier between the minima in the potential. [Equation \(7.4\)](#) implicitly identifies the atomic fractions where spinodal decomposition will occur. For the present case study, the parameters in [Eqs \(7.3\) and \(7.4\)](#) were assigned the following values: $D = 0.1 \mu\text{m}^2/\text{s}$, $F = 211$, and $K = 0.3 \mu\text{m}^2$. For these parameters, the compositions can be shown to lie in the range, $c \in [0.15, 0.23]$. For the present case

study, $c(\mathbf{x})$ constitutes the local state, and therefore the local state space is trivially identified as $c(\mathbf{x}) \in [0.15, 0.23]$.

The basis employed for describing the functions on the local state space were the indicator functions (i.e., employing simple binning of the local state space just like the binning of the spatial domain). Using the concepts and protocols described in earlier chapters, the average atomic fraction in a spatial bin, c_s , is mapped into the discretized microstructure function, m_s^h . The response variable of interest in the spinodal decomposition problem described above is the time derivation of atomic fraction, $\dot{c}(\mathbf{x})$. In the discretized representations used in the Materials Knowledge System (MKS) framework, the response variable would be the time derivative of the averaged atomic fraction in a spatial bin, \dot{c}_s . In other words, we seek to establish MKS linkages between signals \dot{c}_s (output signal) and m_s^h (input signal). Once such a linkage is established, it will be necessary to evolve the microstructure using an appropriate time-integration procedure. As noted earlier, it is envisioned that the MKS framework will be applied recursively in microstructure evolution problems in order to march forward in time, thereby capturing the path dependence of the phenomenon studied.

Because of the similarity of the expressions sought here to those already described in Chapter 6, the same calibration and validation protocols were employed. Twenty different two-dimensional (2-D) initial microstructures spatially resolved into 20×20 bins and reflecting a random perturbation in average atomic fraction that lies within the spinodal points identified earlier were constructed for this case study. Equations (7.3) and (7.4) were numerically integrated for the direct computations, wherein each selected initial microstructure was evolved using the Euler Forward method with a time step of $\Delta t = 0.1$ s [5]. This time step, for the selected model parameters, assured that the numerical integration was well within the stability criterion for the finite difference method [6]. Periodic boundary conditions were maintained by imposing the minimum image convention on the system [7]. Several intermediate datasets, each including both the spatial distribution of the atomic fraction and its time derivative in the entire microstructure, were extracted. A total of about 2000 datasets were extracted from the simulations on the 20 different initial microstructures described earlier. These datasets were grouped into two groups: a calibration group, R , and a validation group, Q , with $R \cap Q = \emptyset$. The calibration and validation protocols were already described in Chapter 6.

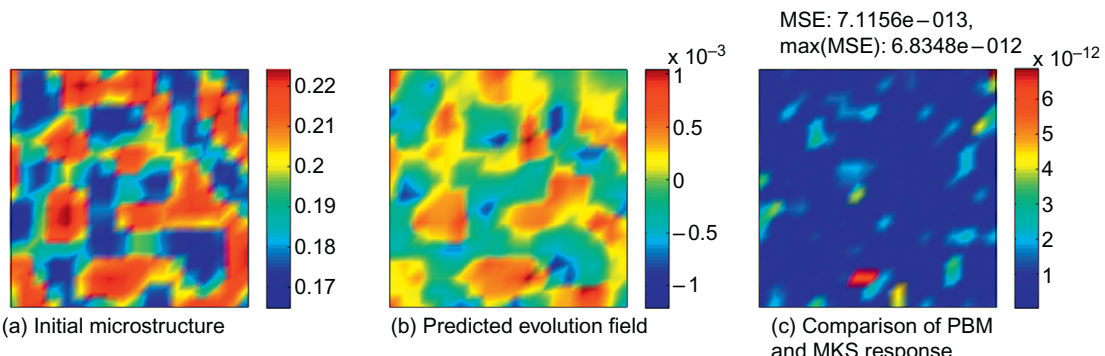


Figure 7.2 The predicted time derivatives of the atomic fraction by the MKS approach developed and the error in this prediction (in comparison to values computed directly from the physics-based model) for an example microstructure. MSE refers to mean squared error.

Figure 7.2 shows an example initial microstructure from the validation set, the corresponding predicted response (i.e., the time derivative of the atomic fraction), and the error in the predicted response (i.e., the absolute difference between the predicted responses by the MKS and the direct computation using the physics-based model). This prediction was obtained using $H = 125$ (number of bins in the local state space). It is seen that the MKS approach predicts the response field with very high accuracy.

As before, it was observed that the calibrated influence kernels decay to zero values for large vectors indicating that the same kernels can be applied on large microstructure datasets [1] with the potential for significant computational advantages, especially for the larger microstructures. In recent work from our research group, a similar case study was successfully demonstrated with the use of Legendre polynomials as the Fourier basis for functions on the continuous local state space. Indeed, it was observed that the use of the Legendre polynomials resulted in a much more compact representation of the kernel functions.

7.3 Case Study: DFT Databases for Crystal Plasticity Computations

As mentioned earlier, process-structure linkages typically need to include and track a number of variables that influence the material constitutive response. The example above was relatively simple in that we could seek direct correlations between

the microstructure function and its time derivative. In many materials phenomena of interest, this may not be possible. As a specific example, we discuss here the application of some of the data science approaches described in this book to tracking microstructure evolution during plastic deformation of polycrystalline materials.

As noted earlier in this book, crystallographic texture and its evolution are known to be major sources of anisotropy in polycrystalline metals. Physics-based models such as crystal plasticity theories have demonstrated remarkable success in predicting the anisotropic mechanical response in polycrystalline metals and the evolution of underlying texture in finite plastic deformation. These theories aim to predict the plastic anisotropy of polycrystalline materials by accounting for the fundamental mechanism of plastic deformation at the scale of the constituent single crystals by taking into account the details of slip system geometry in each individual crystal. To predict the response of the overall polycrystalline aggregate, one needs to use one of the homogenization models that can be classified based on the assumptions made with regard to the local interactions between grains, such as Taylor-type (also known as full constraints) Taylor [8], relaxed constraints [9], LAMEL [10], self-consistent [11–14], and crystal plasticity finite element [15–21] models. The simplest and the most widely used approach is the Taylor-type model. In this method, the applied velocity gradient tensor at the microscale is assumed to be the same as the one applied at the macroscale (on the polycrystal). The macroscopic stress for the polycrystal is obtained by volume averaging the stresses inside the polycrystal. The Taylor-type model usually provides good predictions of the overall anisotropic stress–strain response and the averaged texture evolution for single-phase, high stacking faulty energy, cubic metals [22]. However, it usually lacks good predictions at the scale of individual crystals and it fails to show the development of heterogeneities within the grains [10,23,24].

Implementation of crystal plasticity theories in designing and manufacturing simulation tools generally demands very large computational resources because of the high computational time required to solve the highly nonlinear, numerically stiff, crystal plasticity constitutive equations at every integration point. This makes the use of these physics-based multiscale material models impractical, especially when the size of the polycrystalline aggregate is very large. It is therefore not surprising that these novel approaches have not been yet been adopted broadly by the advanced materials development community.

There is a critical need to speed up solutions to the crystal plasticity constitutive equations in order to use crystal plasticity theories within reasonable computation cost in a number of advanced metals development efforts. Utilizing techniques similar to those described earlier in this book, our research group has established a new strategy to speed up the crystal plasticity computations at the crystal level through the use of a compact database of discrete Fourier transforms (DFTs) [25–28]. This spectral database is used to efficiently reproduce the solutions for the main functions of the crystal plasticity theory for any given crystal orientation subjected to arbitrary deformation mode. The spectral database approach has been successfully applied in both face-centered and body-centered cubic polycrystalline metals that deform by crystallographic slip. This approach was found to be able to speed up the crystal plasticity computations by two orders of magnitude compared with the conventional crystal plasticity model. Another special advantage of the spectral database is that trade-offs can be made by the user in terms of the desired accuracy and computation speed in any simulation through the selection of the truncation levels in the number of dominant DFTs used.

We start here with a concise description of the crystal plasticity theory. For finite deformations, the total deformation gradient tensor \mathbf{F} on a crystalline region can be decomposed into elastic and plastic components as [29]

$$\mathbf{F} = \mathbf{F}^* \mathbf{F}^P \quad (7.5)$$

where \mathbf{F}^* contains deformation gradients due to elastic stretching and lattice rotation, while \mathbf{F}^P denotes the deformation gradient due to plastic deformation. The constitutive equation in the crystal can be expressed as

$$\mathbf{T}^* = \mathcal{L} \mathbf{E}^* \quad (7.6)$$

where \mathcal{L} is the fourth-order elasticity tensor, \mathbf{T}^* and \mathbf{E}^* are a pair of work conjugate stress and strain measures defined using the elastic deformation gradient tensor as

$$\mathbf{T}^* = \mathbf{F}^{*-1} [(\det \mathbf{F}^*) \mathbf{T}] \mathbf{F}^{*-T}, \quad \mathbf{E}^* = \frac{1}{2} (\mathbf{F}^{*T} \mathbf{F}^* - \mathbf{I}) \quad (7.7)$$

where \mathbf{T} is the Cauchy stress in the crystal and \mathbf{I} is the second-order identity tensor. The evolution of \mathbf{F}^P can be expressed as

$$\dot{\mathbf{F}}^P = \mathbf{L}^P \mathbf{F}^P, \quad \mathbf{L}^P = \sum_{\alpha} \dot{\gamma}^{\alpha} \mathbf{m}_0^{\alpha} \otimes \mathbf{n}_0^{\alpha} \quad (7.8)$$

where \mathbf{L}^p is the plastic velocity gradient tensor, $\dot{\gamma}^\alpha$ is the shearing rate on the slip system α , and \mathbf{m}_0^α and \mathbf{n}_0^α denote the slip direction and the slip plane normal of the slip system α , respectively, in the initial configuration. In the rate-dependent formulation, the shearing rate on each slip system depends on the resolved shear stress τ^α and the slip resistance s^α of that slip system. It can be expressed in a power-law relationship as [15,16,30,31]

$$\dot{\gamma}^\alpha = \dot{\gamma}_0 \left| \frac{\tau^\alpha}{s^\alpha} \right|^{\frac{1}{m}} \text{sgn}(\tau^\alpha), \quad \tau^\alpha \approx \mathbf{T}^* \cdot \mathbf{m}_0^\alpha \otimes \mathbf{n}_0^\alpha \quad (7.9)$$

where $\dot{\gamma}_0$ is the reference value of the shearing rate, and m is the strain rate sensitivity parameter. For most metals at room temperature, the value of m is usually taken to be very small (~ 0.01). The evolution of the slip resistance can be described phenomenologically by a saturation-type law as [32]

$$\dot{s}^\alpha = h_o \left(1 - \frac{s^\alpha}{s_s} \right)^a \sum_\beta |\dot{\gamma}^\beta| \quad (7.10)$$

where h_o , s_s , and a denote the slip hardening parameters. It should be noted that Eq. (7.11) implies that slip on one system hardens all other systems equally. Finally, the lattice spin tensor \mathbf{W}^* (and the related lattice rotation tensor, \mathbf{R}^*) in the crystalline region is given by

$$\mathbf{W}^* = \dot{\mathbf{R}}^* \mathbf{R}^{*\text{T}} = \mathbf{W} - \mathbf{W}^p, \quad \mathbf{W}^p = \frac{1}{2} (\mathbf{L}^p - \mathbf{L}^{p\text{T}}) \quad (7.11)$$

where \mathbf{W} is the applied spin tensor, and \mathbf{W}^p is the plastic spin tensor.

A detailed description of the implementation of the above crystal plasticity constitutive equations with the implicit version of the FE package ABAQUS is described by Kalidindi et al. in Ref. [15]. The crystal plasticity framework described above demands significant computational resources. This is a direct consequence of the fact that most metals have a very weak dependence on the strain rate at room temperature, which demands the use of a small value for the strain rate sensitivity parameter in the flow rule used in the rate-dependent crystal plasticity formulations (see Eq. (7.9)) [16,30,31]. Our research group [26,28,33] has developed a new database approach to obtain the solutions involved in these computations at dramatically reduced computational cost. In this approach, a DFT-based database is used to reconstruct directly the solutions for the main functions of the conventional crystal plasticity theory for any given crystal orientation under any applied deformation

mode. In this method, spectral representations are established for the following three main functions: (i) the deviatoric stress tensor $\sigma'(g,L)$, (ii) the lattice spin tensor $\mathbf{W}^*(g,L)$, and (iii) the total shear rate $\sum_\alpha |\dot{\gamma}^\alpha|(g,L)$. In these functions, the independent variable, g , denotes the crystal lattice orientation defined using the Bunge–Euler angles $(\varphi_1, \phi, \varphi_2)$ [34], and L represents the velocity gradient tensor applied at the crystal level. In any time step, in the simulation of the deformation process, the stress function gives the values of the deviatoric stress components at the crystal level, the spin tensor predicts the crystal rotation, and the total shear rate determines the slip hardening rates as defined in Eq. (7.10).

The domain of the functions described above is the product space of the orientation space and the deformation mode space. The deformation mode space includes the complete set of all velocity gradient tensors which can be efficiently described as [35]

$$\begin{aligned} \mathbf{L} &= \dot{\varepsilon} \mathbf{D}_o + \mathbf{W}, \quad \mathbf{D}_o = \sum_{j=1}^3 D_j \mathbf{e}_j^p \otimes \mathbf{e}_j^p, \quad \dot{\varepsilon} = \frac{1}{2} |\mathbf{L} + \mathbf{L}^T| \\ D_1 &= \sqrt{\frac{2}{3}} \cos\left(\theta - \frac{\pi}{3}\right), \quad D_2 = \sqrt{\frac{2}{3}} \cos\left(\theta + \frac{\pi}{3}\right), \quad D_3 = -\sqrt{\frac{2}{3}} \cos(\theta) \end{aligned} \quad (7.12)$$

where $\{\mathbf{e}_i^p, i = 1, 2, 3\}$ denotes the principal frame of the unit, traceless, \mathbf{D}_o , and the range of angular variable θ that defines all possible diagonal matrices is $[\frac{\pi}{6}, \frac{\pi}{2}]$. The spectral databases are built in the $\{\mathbf{e}_i^p\}$ reference frame using two primary variables, g^p and θ , where g^p denotes the crystal lattice orientation with respect to the $\{\mathbf{e}_i^p\}$ reference frame. The spectral representations of the functions of interest are then expressed as [26]

$$\mathbf{W}_{rq}^* = \dot{\varepsilon} \frac{1}{N_{g^p} N_\theta} \sum_k \sum_n \mathbf{B}_{kn} e^{\frac{2\pi i k r}{N_{g^p}}} e^{\frac{2\pi i n q}{N_\theta}} + \mathbf{W} \quad (7.13)$$

$$\sigma'_{rq} = s \dot{\varepsilon}^m \frac{1}{N_{g^p} N_\theta} \sum_k \sum_n C_{kn} e^{\frac{2\pi i k r}{N_{g^p}}} e^{\frac{2\pi i n q}{N_\theta}} \quad (7.14)$$

$$\left(\sum_\alpha |\dot{\gamma}^\alpha| \right)_{rq} = \dot{\varepsilon} \frac{1}{N_{g^p} N_\theta} \sum_k \sum_n G_{kn} e^{\frac{2\pi i k r}{N_{g^p}}} e^{\frac{2\pi i n q}{N_\theta}} \quad (7.15)$$

where r and q enumerate the grid points in the orientation space g^p and the deformation mode space θ , respectively. The corresponding total numbers of grid points in the periodic orientation and deformation mode spaces are denoted by N_{g^p} and N_θ , respectively. The spectral databases for the function of interest described above are stored in the form of Fourier coefficients \mathbf{B}_{kn} , \mathbf{C}_{kn} , and G_{kn} (referred to as the DFTs), where k and n represent frequencies in the DFT space, \mathbf{B} and \mathbf{C} denote second-rank tensors, and G is a scalar.

In order to compute the DFTs of interest, we first need to compute the values of the functions of interest on a uniform grid in their respective periodic domains. In prior works [26,28], these values were computed using the crystal plasticity theory described earlier on a uniform three-degree grid in each of the angular variables involved. The periodic Bunge–Euler space of interest in computing DFTs for orientation-dependent functions in cubic crystals is identified as $(\phi_1 \in [0, 2\pi], \Phi \in [0, 2\pi], \phi_2 \in [0, 2\pi])$ [26,33]. The periodic space of interest in defining the deformation mode is identified as $\theta \in [0, 2\pi]$. It should be noted that there exist several redundancies in the space identified above; in fact, there exist at least 48 equivalent orientations based on the crystal symmetry alone. These equivalent representations have been exploited in the computations of the function values.

For the functions studied in this work, it is typically observed that only a small fraction of the DFTs are numerically significant compared to the others. In other words, although the number of DFTs computed is as large as the discrete dataset of the function values that was used in computing the transform, only a relatively small fraction of the terms in the computed transform need to be stored; ignoring the rest of the terms in the transform has only a small influence on the reconstructed values. The number of numerically significant DFTs (henceforth referred to as dominant DFTs) varies for the different field variables. It was seen that as few as 200 DFTs dominated the representations of the various functions of interest for fcc polycrystals [26]. Keeping a minimal set of dominant DFTs is critical for gaining computational speed in the spectral approach to the crystal plasticity computations described in this paper. Taking into account more of the DFTs will improve the accuracy at the expense of computational cost.

A characteristic feature of the DFTs is that they reproduce exactly the values of the functions at the grid points that were used in evaluating the DFTs (here the uniform three-degree grid), when all of the DFTs are utilized. In order to recover the function values at any other location of interest (not on the

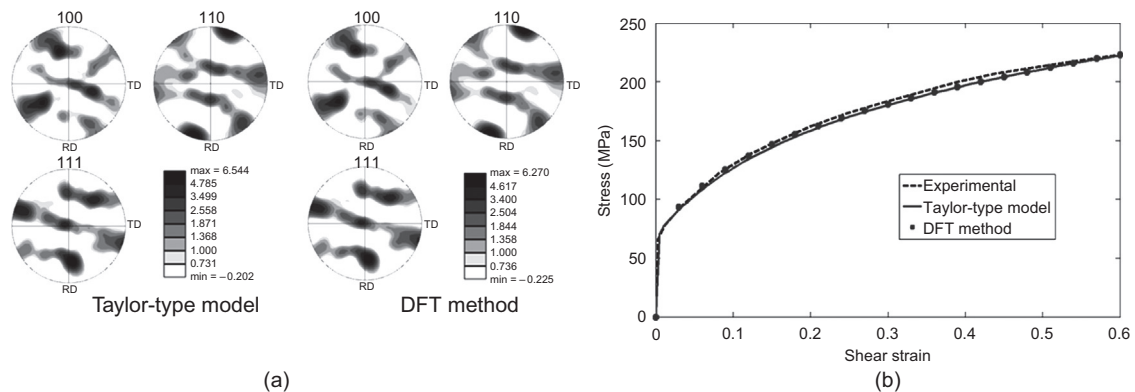


Figure 7.3 Comparison of the predictions from the spectral method (using 500 DFTs for the stress, the shearing rate, and the lattice spin components) against the corresponding predictions from the conventional approach for simple shear of IF steel: (a) pole figures and (b) stress-strain curves, including the experimental result [36].

selected grid) in their respective domains, we use the spectral interpolation technique [27] described in Chapter 2. One example of the validation of the spectral database for bcc crystal plasticity calculations is presented in Figure 7.3. In this figure, we compare the predictions of the stress-strain curves and the deformed textures against the corresponding predictions from the conventional crystal plasticity computations for selected deformation processes. Both of these predictions are based on the simple Taylor model. The slip hardening parameters used in these simulations were those established previously for interstitial-free (IF) steel by curve fitting the Taylor predictions to experimental measurements [36]. The predicted texture and stress-strain curves for a polycrystalline IF steel deformed by simple shear to a shear strain of $\gamma = 0.6$ using the conventional computational approach and the DFT spectral approach presented earlier are shown in Figure 7.3. The initial texture in the sample was captured using a set of 1200 discrete crystal orientations [36]. The DFT-based predictions used 500 dominant DFTs for the stress, the shearing rate, and the lattice spin components. It is clear that the DFT-based databases produce excellent predictions, and these are obtained at a significant faster computational speed. The simulation time was 130 s for the conventional calculations and only 2.9 s for the spectral approach using dominant DFTs. All of the computations were performed on a regular Pentium 4 desktop PC.

In much more recent work, the DFT database approach has been successfully implemented in a commercial finite element

code to permit computationally efficient simulations of heterogeneous deformations using crystal plasticity theories. To accomplish this, the spectral database approach to crystal plasticity solutions was successfully integrated with the commercial finite element package ABAQUS through a user materials subroutine, UMAT. This new crystal plasticity spectral database–FE approach was demonstrated and validated through a few example case studies for selected deformation processes on face-centered and body-centered cubic metals [37].

References

- [1] Fast T, Niezgoda SR, Kalidindi SR. A new framework for computationally efficient structure-structure evolution linkages to facilitate high-fidelity scale bridging in multi-scale materials models. *Acta Mater* 2011;59(2):699–707.
- [2] Cahn JW, Hilliard JE. Free energy of a nonuniform system. I. Interfacial free energy. *J Chem Phys* 1958;28(2):258–67.
- [3] Novick-Cohen A, Segel L. Nonlinear aspects of the Cahn-Hilliard equation. *Phys D* 1984;10(3):277–98.
- [4] Sander E, Wanner T. Monte Carlo simulations for spinodal decomposition. *J Stat Phys* 1999;95(5):925–48.
- [5] Wang Y, Chen LQ, Khachaturyan AG. Kinetics of strain-induced morphological transformation in cubic alloys with a miscibility gap. *Acta Metall Mater* 1993;41(1):279–96.
- [6] Incropera F, DeWitt D. Fundamentals of heat and mass transfer. 5th ed. Hoboken, NJ, USA: Wiley; 2001.
- [7] Hloucha M, Deiters UK. Fast coding of the minimum image convention. *Mol Simul* 1998;20(4):239–44.
- [8] Taylor GI. Plastic strain in metals. *J. Inst. Metals.* 1938;LXII:307–24.
- [9] Kocks UF, Mecking H. Physics and phenomenology of strain hardening: the FCC case. *Prog Mater Sci* 2003;48(3):171–273.
- [10] Van Houtte P, et al. Deformation texture prediction: from the Taylor model to the advanced Lamel model. *Int J Plast* 2005;21(3):589–624.
- [11] Molinari A, Canova GR, Ahzi S. A self-consistent approach of the large deformation polycrystal viscoplasticity. *Acta Metall* 1987;35(12):2983–94.
- [12] Lebensohn RA, Liu Y, Ponte Castañeda P. On the accuracy of the self-consistent approximation for polycrystals: comparison with full-field numerical simulations. *Acta Mater* 2004;52(18):5347–61.
- [13] Lebensohn RA, Tomé CN. A self-consistent anisotropic approach for the simulation of plastic deformation and texture development of polycrystals: application to zirconium alloys. *Acta Metall Mater* 1993;41(9):2611–24.
- [14] Lebensohn RA, Tome CN, Castaneda PP. Self-consistent modelling of the mechanical behaviour of viscoplastic polycrystals incorporating intragranular field fluctuations. *Philos Mag* 2007;87(28):4287–322.
- [15] Kalidindi SR, Bronkhorst CA, Anand L. Crystallographic texture evolution in bulk deformation processing of FCC metals. *J Mech Phys Solids* 1992;40(3):537–69.
- [16] Needleman A, et al. Finite element analysis of crystalline solids. *Comput Methods Appl Mech Eng* 1985;52(1–3):689–708.

- [17] Peirce D, Asaro RJ, Needleman A. An analysis of nonuniform and localized deformation in ductile single crystals. *Acta Metall* 1982;30(6):1087–119.
- [18] Peirce D, Asaro RJ, Needleman A. Material rate dependence and localized deformation in crystalline solids. *Acta Metall* 1983;31(12):1951–76.
- [19] Kalidindi SR, Schoenfeld SE. On the prediction of yield surfaces by the crystal plasticity models for fcc polycrystals. *Mater Sci Eng A Struct Mater* 2000;293(1–2):120–9.
- [20] Bachu V, Kalidindi SR. On the accuracy of the predictions of texture evolution by the finite element technique for fcc polycrystals. *Mater Sci Eng A Struct Mater* 1998;257(1):108–17.
- [21] Kalidindi SR, Anand L. Macroscopic shape change and evolution of crystallographic texture in pre-textured fcc metals. *J Mech Phys Solids* 1994;42(3):459–90.
- [22] Bronkhorst CA, Kalidindi SR, Anand L. Polycrystalline plasticity and the evolution of crystallographic texture in FCC metals.. *Philos Trans R Soc Lond A* 1992;341:443–77.
- [23] Kalidindi SR, Bhattacharyya A, Doherty RD. Detailed analysis of grain-scale plastic deformation in columnar polycrystalline aluminum using orientation image mapping and crystal plasticity models. *Proc R Soc A* 2004;460:1935–56.
- [24] Bhattacharyya A, et al. Evolution of grain-scale microstructure during large strain simple compression of polycrystalline aluminum with quasi-columnar grains: OIM measurements and numerical simulations. *Int J Plast* 2001;17(6):861–83.
- [25] Kalidindi SR, Duvvuru HK, Knezevic M. Spectral calibration of crystal plasticity models. *Acta Mater* 2006;54(7):1795–804.
- [26] Knezevic M, Al-Harbi HF, Kalidindi SR. Crystal plasticity simulations using discrete Fourier transforms. *Acta Mater* 2009;57(6):1777–84.
- [27] Knezevic M, Kalidindi SR, Fullwood D. Computationally efficient database and spectral interpolation for fully plastic Taylor-type crystal plasticity calculations of face-centered cubic polycrystals. *Int J Plast* 2008;24(7):1264–76.
- [28] Al-Harbi HF, Knezevic M, Kalidindi SR. Spectral approaches for the fast computation of yield surfaces and first-order plastic property closures for polycrystalline materials with cubic-triclinic textures. *CMC-Comput Mater Continua* 2010;15(2):153–72.
- [29] Asaro RJ, Needleman A. Overview no. 42 texture development and strain hardening in rate dependent polycrystals. *Acta Metall* 1985;33(6):923–53.
- [30] Hutchinson JW. Bounds and self-consistent estimates for creep of polycrystalline materials. *Proc R Soc Lond A Math Phys Sci* 1976;348(1652):101–27.
- [31] Pan J, Rice JR. Rate sensitivity of plastic flow and implications for yield-surface vertices. *Int J Solids Struct* 1983;19(11):973–87.
- [32] Brown SB, Kim KH, Anand L. An internal variable constitutive model for hot working of metals. *Int J Plast* 1989;5(2):95–130.
- [33] Kalidindi SR, et al. Representation of the orientation distribution function and computation of first-order elastic properties closures using discrete Fourier transforms. *Acta Mater* 2009;57(13):3916–23.
- [34] Bunge H-J. Texture analysis in materials science. Mathematical methods. Göttingen: Cuvillier Verlag; 1993.
- [35] Van Houtte P. Application of plastic potentials to strain rate sensitive and insensitive anisotropic materials. *Int J Plast* 1994;10(7):719–48.

- [36] Peeters B, et al. Work-hardening/softening behaviour of b.c.c. polycrystals during changing strain paths: I. An integrated model based on substructure and texture evolution, and its prediction of the stress-strain behaviour of an IF steel during two-stage strain paths. *Acta Mater* 2001;49(9):1607–19.
- [37] Al-Harbi HF, Kalidindi SR. Crystal plasticity finite element simulations using a database of discrete Fourier transforms. *Int J Plast* 2014.

MATERIALS INNOVATION CYBERINFRASTRUCTURE

In this final chapter, the emerging paradigms in materials innovation online platforms or cyberinfrastructure are discussed. It is hoped that reader appreciates the embryonic state of the entire field of Data Science, which essentially only recently established itself as an independent discipline (initially was considered as an extension of the statistical sciences) [1–4]. It is also hoped that the preceding chapters have been clarified to the reader, the distinction between data science (with a focus on extracting high value information or knowledge from available data) and computational science (with a focus on solution methodologies to rigorously formulated problems).

At its core, data science is comprised of two primary components. The first component can be broadly identified as Data Management and includes robust and reliable storage, aggregation, archival, retrieval, and sharing protocols. This is a critical and necessary first step as it would be impossible to pursue data science without easy access to reliable data. It is also important to embrace a very broad definition of data in this context. For example, when one does experiments in materials science, data can include not just the files produced by the instruments used but also various other pertinent details about the experiment (e.g., environmental conditions, details of how the test specimens were prepared, instrument settings, and so on). It is customary in the field of data science to refer to salient data about data as metadata. Metadata might include key information such as the file type or format, file size, time of creation, and its central purpose is to enhance the utility of the data by providing important information on the context and content, thereby allowing it to be discovered in appropriate searches by potential users. In this regard, metadata might even include keywords, categories, and other relevant metrics that describe the essential content of the data. Carefully designed metadata and metadata databases are crucial to ensuring and improving data longevity and usefulness [5].

The second task in data science centers around Data Analytics, which has been the main focus of this book thus far in as much as it applies to hierarchical material datasets. The focus in this component of data science is usually on mining the embedded high value information via noise or background filtering, data fusion, uncertainty analyses, statistical analyses, dimensionality reduction, pattern recognition, regression analyses, machine learning, and statistical learning.

Increasingly, in recent years, there has been a strong recognition for the critical need of a third component of data science: e-Collaboration Science. This component deals with the online tools designed specifically to seed and nurture cross-disciplinary research collaborations between application domain experts and data scientists. Through such collaborations, one aims to achieve a synergistic integration of specific disciplinary workflows with emerging data science tools and the concomitant enhancement of the overall research productivity. e-Collaborations also have the potential to dramatically accelerate the processes of multidisciplinary research team formation with a desired and otherwise unachievable combination of expertise. As a simple illustration of the importance of e-collaboration tools, consider the impact of e-mail on the research productivity of individual researchers in all domains of science and technology. One can make similar observations regarding the prevalent use of Dropbox (<http://www.dropbox.com>) and Github (<https://github.com/>) by researchers worldwide. HUBzero (<https://hubzero.org/>) and nanoHUB (<https://nanohub.org/>) serve as early examples of successful new online scientific communities that share data and tools. These examples attest to the positive impact that e-collaboration platforms can have in enhancing and accelerating the cross-disciplinary collaborations needed to integrate emerging data science protocols into existing disciplinary workflows.

Several recent vision-setting documents for the materials community [6,7] have emphasized the critical need for open-access materials databases that capture, curate, and archive the critical information needed to facilitate accelerated development of new/improved materials and their deployment in emerging technologies. While these reports do not provide a clear road map, they do emphasize the anticipated benefits from the availability of these new databases. One of the immediate benefits is that they have the potential to minimize the unintended repetition of effort from multiple groups of researchers, possibly over multiple generations.

As noted multiple times in this book, core materials knowledge is often expressed in the form of PSP linkages, and the

main challenge in designing and building the desired knowledge databases stems from the fact that most materials of interest exhibit rich internal structures that span multiple length scales. Because of the tremendous challenge inherent to this task, most current efforts at building materials databases have either focused on a single length scale and/or restricted their attention to a limited number of structure measures. It is generally anticipated that these smaller databases can be effectively fused in the future to provide more comprehensive databases.

When materials databases are focused on PSP linkages at a single length scale, they only need to address a limited amount of variety in the datasets. Consequently, it is possible to design and build valuable databases that focus on physical properties of specific chemical elements or compounds that do not depend on microstructure (see <http://www.citrination.com>, <http://cleanenergy.molecularspace.org>, <http://www.materialsproject.org/>, <http://oqmd.org>, <http://www.aowlib.org/>, <http://srdata.nist.gov/gateway/gateway?dblist=1>, <http://www.calphad.org/>, <http://www.ctcms.nist.gov/potentials/>). There currently also exist several materials databases that focus on macroscale physical properties of various commercially available materials without a rigorous description of the associated material microstructure. These databases serve a valuable purpose for the product design community to facilitate deployment of advanced materials available today in emerging technologies (see <http://www.matweb.com/>, <http://www.grantadesign.com/products/ces/>, http://mits.nims.go.jp/index_en.html). However, more often than not, it is likely that the materials available today will need some additional tweaking in their manufacturing process, so that they can be optimized for a selected application. To undertake such a tweaking in a cost-effective manner, it is essential to document and track the evolution of the material's hierarchical structure throughout the various unit manufacturing processes employed. Nevertheless, the property-centered databases described above serve an important role in materials development efforts.

The recognition of the important role of microstructure has led to the design and deployment of novel microstructure-centered materials databases and tools. Examples of such resources include DREAM3D (<http://dream3d.bluequartz.net/>), the Materials Atlas (<https://cosmicweb.mse.iastate.edu/wiki/display/home/materials+atlas+home>), and the Computational Materials Data Network (<http://www.asminternational.org/web/cmdnetwork/about>). These newer generation microstructure-centered materials innovation cyberinfrastructure platforms offer exciting avenues for accelerated materials development efforts.

The practical realization of the vision embodied in the recent national strategic initiatives [6,7] is only feasible with the accumulation of very large libraries of materials data that capture the relevant multiscale spatio-temporal information on material internal structures covering a very broad range of material classes. Given the amount of information needed, it is impossible for any one research group or even a single organization to assemble all this information. Furthermore, even if one were to somehow assemble these libraries, the expertise needed to efficiently mine them and curate the core materials knowledge needed to advance the accelerated development of new and improved materials lies well outside the traditional skillsets of the materials practitioners and experts; this is actually the central focus of emerging e-collaboration platforms. It is therefore imperative to develop online collaboration platforms that are specifically designed to facilitate intimate collaborations between distributed (geographically, organizationally, and based on expertise) team members.

Integrated workflows are foundational to the successful realization of the vision articulated above. These workflows would efficiently integrate high value information and knowledge gleaned from different sources. It should be recognized that data is the essential currency of all transactions in such workflows. Note that these integrated workflows are just emerging at this time [8]. The materials development community is poised to undertake the massive effort needed to design and validate such workflows in a systematic manner. This effort can be helped in significant ways if it is undertaken within a supporting Big Data cyberinfrastructure which would allow us to digitally capture the numerous trials undertaken in the development and validation of workflows (in both successful and failed trials). This database of workflows can then provide guidance for the design of new and improved workflows in the future, thereby allowing us to learn from successes and failures of past attempts in a highly objective manner.

Examples of such collaboration platforms are just emerging and are becoming increasingly popular with the scientific research community. However, they currently tend to focus largely on the individual subtasks involved in the overall research enterprise. Prime examples include Google Docs (<https://docs.google.com/>), Authorea (<https://www.authorea.com/>) and ShareLaTex (<https://www.sharelatex.com/>) for collaborative writing, Mendeley (<http://www.mendeley.com/>) and ResearchGate (<http://www.researchgate.net/>) for collaborative annotation and sharing

of research documents, GitHub (<https://github.com/>) and SourceForge (<http://sourceforge.net/>) for collaborative software development, Plot.ly (<https://plot.ly/>) for collaborative data analysis and visualization, and Google + (<https://plus.google.com/>) and LinkedIn (<https://www.linkedin.com/>) for e-teaming and networking. Within the materials community, there have also been several attempts at creating e-collaborative sites (see <http://web.ornl.gov/sci/doe2k/micsreview/99/tools.html>, <http://prisms.engin.umich.edu//prisms>, <http://tpm.amc.anl.gov>, <https://www.linkedin.com/groups/mgidigital-data-community-7459917>). Clearly the landscape of collaborative materials innovation platform is still very nascent.

While the above-mentioned collaboration platforms support specific subtasks involved in a collaborative research environment, there have also been efforts aimed at integrating one or more of these functionalities into comprehensive research collaboration platforms that allow development of emergent open-access research communities. Given the central role computer codes play in any kind of data transformations, it is only natural that the collaboration platforms pay major attention to central functionalities related to code versioning, sharing, and curation. In this regard, several successful collaboration platforms have been built and deployed using the HUBzero software mentioned earlier. One of the best known examples is nanoHUB (<https://nanohub.org/>), focused on sharing and providing access to nanoscale science and engineering simulation tools. These platforms address the many challenges of code sharing by providing access to executable versions of highly sophisticated software on centralized computational resources (such as cloud computing resources, campus clusters, and national high-performance computing facilities).

As another alternative, a number of recent efforts have focused on building collaboration communities [9] using GitHub. These efforts focus more on the transparency of the codes (through code versioning) and allow the users to utilize their own independent computational resources for executing the codes. Approaches centered around open-source code sharing present tremendous flexibility and agility to the individual researcher in pursuing a wide range of new research avenues, many of which may not have been envisioned by the original code producer. Github-based research collaboration platforms also allow one to integrate other web services as needed (e.g., for enabling sharing and annotating of data and results, discussions, and tracking workflows). One such example is the

recently launched MATIN environment at Georgia Tech (www.mined.gatech.edu/matin) which involves collaborative research and education cutting across materials, manufacturing, and data sciences.

References

- [1] Cleveland WS. Data science: an action plan for expanding the technical areas of the field of statistics. *Int Stat Rev* 2001;69(1):21–6.
- [2] Dhar V. Data science and prediction. *Commun ACM* 2013;56(12):64–73.
- [3] Hey T, Tansley S, Tolle K. *The fourth paradigm. Data-intensive scientific discovery*. Microsoft Research; 2009.
- [4] Anderson C. The end of theory: the data deluge makes the scientific method obsolete. *Wired Magazine*. 2008. Updated 6/23/2008). Available at: <http://www.wired.com/science/discoveries/magazine/16-07/pb_theory>.
- [5] Kalidindi SR, Graef MD. Materials data science: current status and future outlook. *Annu Rev Mater Res* 2015 (in press).
- [6] Pollock TM, et al. Integrated computational materials engineering: a transformational discipline for improved competitiveness and national security. Washington, DC: The National Academies Press; 2008.
- [7] Materials genome initiative for global competitiveness. National Science and Technology Council, Office of the President, Council, 2011.
- [8] Salem AA, et al. Workflow for integrating mesoscale heterogeneities in materials structure with process simulation of titanium alloys. *Integrating Mater Manuf Innov* 2014;3(1):1–22.
- [9] Dabbish L, et al. Social coding in GitHub: transparency and collaboration in an open software repository. In: Proceedings of the ACM 2012 conference on computer supported cooperative work. 2012. p. 1277–286.

INDEX

Note: Page numbers followed by “*f*” and “*t*” refer to figures and tables, respectively.

A

- ABAQUS, 181, 199–200, 202–203
- Acceleration in materials innovation, 130
- ad hoc* approaches in materials development, 11–12
- Al alloys, 1–2
- Amplitudes of discrete frequencies, 53–54
- Angular frequency, 51–52
- Anisotropy ratio for cubic crystals, 137
- Augmented Databases, 25–27
- Austenite, 8, 38–39
- Autocorrelations, 81, 85
- Automated documentation of standardized workflows, 18–19

B

- Big data era, 16
- Body-centered cubic (bcc) structure, 8–10
- Body-centered tetragonal crystal structure, 8–10
- Body force per unit volume, 133
- Bresenham’s line drawing algorithm, 91
- Bunge–Euler angles, 42–43, 43*f* angles associated with three unit transformations, 42–43
- crystal symmetry, 46
- Bunge–Euler space of interest, 201

C

- Cahn–Hilliard equation, 194–195

Cartesian crystal frame, 42–43

- Cauchy stress, 198–199 tensor, 182–184
- Cementite, 8
- Chemical composition, 1
- Chord, defined, 90
- Chord length distribution (CLD), 90 from LPF, 91
- Collaboration platforms support, 210–212
- Composites, study of elastic responses, 169–176
- Configuration of a body, 133
- Conservation of linear momentum principle, 133
- Coordinate transformation matrix, 42–43, 43*f* inverse transformation, 44–45 for studying crystal mechanics, 44–45 of tensorial quantities, 45
- Copper polycrystals, MKS linkages of, 182
- Cross-feed multiscale structure-sensitive materials models, 22–23
- Cross validation error, 154–155
- Crystal plasticity models, 22–23
- Cubic crystal structure, 45–46, 46*f* anisotropy ratio for, 137 fundamental zone for, 45–47, 47*f* lattice orientation, 46–47 stiffness matrix of, 137 symmetry transformation, 46
- Cyberinfrastructure, 21, 25, 207, 210

D

- Data analytics, 208
- Data-driven approach, 18 for homogenization linkages, 147–152
- for localization linkages, 165–169
- Data-driven protocols, 20–21
- Data management, 207
- Data transformations, 16–17, 16*f*
- Deformation gradient tensor, 134–135
- Deformation mode space, 200–201
- “Delta” microstructures, 171
- Dendrogram, 126 of centroid distances, 126*f*
- Digital recording of workflows, 21
- Digital representation of function, 50–60 assumption of periodicity, 52–53
- DFT representations, 52–54
- of material microstructure, 18–19
- of microstructure function, 60–65 assignment of local states, 62–63 eigen microstructures, 63
- microstructure volume, 61–62, 62*f*
- of *n*-point spatial correlations, 150
- Digital signal representation of microstructure, 18–19
- Digitization, 17–20
- Dilute distribution model, 137–138

Dirac-delta function, 104
 Discrete Fourier transforms (DFTs), 52–54, 80, 167–168, 170–171
 Bunge–Euler space of interest, 201
 complex-valued, 58–59
 discretized microstructure function, 81
 computation of, 55
 in computing convolutions and correlations, 56
 databases for crystal plasticity computations, 196–203
 of discretely sampled function, 54–55
 of discretized function of interest, 53–54
 discretized function of interest, 53–54
 of dominant frequencies, 57–60
 example of a spectral interpolation, 59–60
 for a finer resolution grid, 57–58
 function values, 55–56
 inverse, 83
 known relationships involving, 55–56
 main advantage of, 56–57
 $O(S \log S)$ using, 83
 padded microstructure, 85–87
 periodicity of, 56, 86–87
 phase of, 81, 94
 uses of, 57
 Discretization, 17–18
 Discretized microstructure, 77
 Discretized spatial bins, spatial correlations of, 77, 78f
 Dislocations, 10
 Displacement, 130
 Displacement gradient tensor, 135
 Dropbox, 208

E
 E-Collaboration Science, 208, 210
 Effective properties, concept of, 138
 Eigen microstructures, 63, 82, 94
 Elastic deformation gradient tensor, 198–199
 Elastic materials, 135–136
 Elastic response of multiphase composites, study of, 169–176
 Elastic responses, study of of composites, 169–176
 of higher contrast composites, 176–178
 of polycrystals, 178–182
 Elastic stiffness, 33–35
 Elastic stiffness matrix, 136–137
 Electron backscattered diffraction (EBSD), 35, 104
 Ensemble of material structures, 75–76, 76f, 157f
 ensemble averages using 2-point spatial correlations, 148–149
 in study of structure-diffusivity correlations, 156–157, 157f
 Ensemble of $\alpha\text{-}\beta$ Ti micrographs, case study, 118–119, 119f
 Euclidean space, 51–52
 Euclidean 3-space, 129–130
 Euler angles, 42
 Euler Forward method, 195

F
 Face-centered cubic (fcc) structure, 8–10
 Fast Fourier transform (FFT) algorithms, 83, 85
 Ferrite, 8
 Ferrite phase, 8–10

Fickian diffusivity simulation model, 156
 Force, 130
 Fourier coefficients, 51–54
 Fourier representation of a periodic function, 51–52
 Free energy, 194–195
 Fundamental zone, 45
 for cubic crystals, 45–47, 47f
 hexagonal close-packed structure (hcp), 47, 48f

G
 Generalized spherical harmonic basis (GSH), 67–68, 102–103, 105, 179–180
 Github, 208, 211–212
 “Goal-means” approach, 22–23
 Green function, 57, 68–69, 139–141

H
 Hall–Petch rules, 12
 Hexagonal close-packed structure (hcp), 47
 fundamental zone, 47, 48f
 Hierarchical internal structures of the materials.
See Microstructure
 Hierarchical Materials Informatics, 20–27
 Higher contrast composites, study of elastic responses, 176–178
 Higher order homogenization theory, 138–141
 Higher order spatial correlations, 89–91
 of chord length distribution (CLD), 90
 DFT representation, 89
 3-point, 89
 Higher-order spatial statistics, 151–152
 Homogenization, 137–138
 of higher order, 138–141
 significance, 147–148

Homogenization linkages, data-driven approach for, 147–152, 170
 steps in, 152–155
 computing polynomial coefficients, 153–154
 creation of an ensemble of microstructures, 153
 establishing validated structure–property linkages, 153–154
 evaluating robustness of polynomial-fits, 154–155
 extracting objective, reduced-order, quantitative measures of microstructures, 153
 splitting of data into calibration (or training) component and validation component, 155
 technological applications
 microstructure–property relationships in porous transport layers, 155–157
 structure–property linkages for nonmetallic inclusions/steel composite system, study of, 158–165
 “Honey-comb” eigen microstructure, 85
 HUBzero, 208, 211

I

Integrated workflows, 210
 Inverse problems in materials and process design, 13–15
 Inverse rule of mixtures, 137–138

K

Kerner’s method, 137–138
 Kinematics, 133
 Knowledge databases, 25–27
 Kronecker delta, 167–168

L

Lame moduli, 140
 Lattice spin tensor, 198–199
 Leave-One-Out Cross Validation (LOOCV) error, 154–157
 Legendre coefficients, 69–70
 Legendre polynomials, 70, 196
 Length scales, 33–37, 48
 in any optical or electron micrograph, 35
 concept of well separated, 35–36
 elastic stiffness, 33–35
 of ingrained material structure, 38
 linear elastic response of a composite material, 33–35
 local states and local state spaces, 37–48
 combination of discrete and continuous variables, 40
 definition, 39
 mathematical statements, 39
 in polycrystalline microstructures, 40–48
 macroscale, 33–36
 material internal structure
 in, 8
 of a material point, 33, 34f
 mesoscale, 35
 in numerical simulations, 35
 representative volume element (RVE), 35–36
 volume of material, 33–35
 Length scales local states and local state spaces
 in polycrystalline microstructures, 40–48
 Lineal path function (LPF), 90
 angularly resolved, 90–91
 Linear elastic response of a composite material, 33–35

Linear elastic stress–strain relations, 135–136
 Localization linkages, 165–169 challenges, 165
 localization tensor, 165–166 polarization tensor, 165–166
 Localization propensity (LP), 161–162
 Localization tensor, 165–166
 Local states and local state spaces, 37–48
 combination of discrete and continuous variables, 40
 definition, 39
 mathematical statements, 39
 in polycrystalline microstructures, 40–48

M

Macroscale, 33–35
 Martensite, 8
 Martensite phase, 8–10
 Masking protocol, 88–89
 Masks, 87–88
 Material internal structure, 1–2, 6–12
 Material microstructure.
See Microstructure
 Materials
 in advanced technologies, 1–2
 development, 21
 informatics, 16–17
 knowledge, 16–17
 for structural applications, 1–2
 Materials databases, 209
 Computational Materials Data Network, 209
 DREAM3D, 209
 Materials Atlas, 209
 Materials Knowledge Systems (MKS), 25–27, 26f, 195
 methodology, 167
 for elastic response of composites, 169–176
 for elastic response of higher contrast composites, 176–178

Materials Knowledge Systems (MKS) (*Continued*)
 for elastic response of polycrystals, 178–182
 generalized form of, 168–169
 for perfectly plastic response of composites, 182–186
 workflow template for establishing localization kernels, 168*f*
 MATIN environment, 211–212
 MD simulation datasets, case study, 123–126, 125*f*
 PCA computation, 124
 protocols used, 123–124
 Mean absolute error of fit, 154–155, 158*f*
 Mesoscale, 35
 diversity of structures in, 8–10
 role of interfaces, 37
 of steel grades, 9*f*
 Metadata, 207
 Mg alloys, 1–2
 Microscale volume elements (MVEs), 180, 180*f*, 182
 Microstructure, 1–2, 11, 33
 characterization techniques, 48–49
 evolution, 14–15
 function, 48–50
 of an independent and continuous variable, 50
 in continuous spaces, 49–50
 digital representation, 60–65
 domain space for, 61
 functional relation (or mapping) of interest a priori, 51
 local state, specification of, 48–49
 microstructure volume, 61–62
 reconstruction of, 51–52

spectral representation, 65–71
 as a statistical framework, 49
 theoretical treatment of, 49–50
 time dependence of, 49
 metrics (microstructure measures), 18
 volume, 61–62, 62*f*
 Microstructure–property relationships, in porous transport layers, 155–157
 Model Interoperability, 22–23
 Model Inversion, 22–23
 impediment in, 22–23
 Model Maturity, 22–23
 Molecular dynamics (MD) simulations, 70–71
 Monte-Carlo based microstructure reconstruction algorithms, 99
 Mori–Takana method, 137–138
 Motion of body, 133–134, 134*f*
 Multiscale measurements, 22–23
 Multiscale physics-based models, 22–23

N

NanoHUB, 208
 National Science and Technology Council, 21–22
 National Strategic Plan for Advanced Manufacturing, 21–22
 Neighborhood, defined, 97–99
 Normalized error, 153–154
n-point spatial correlations, 24–25
n-point statistics, 100
n-vertex polyhedra, 79
 Nyquist sampling, 57

O
 1-point spatial correlations, 77, 81

Ordered local states, 80
 Ordinary frequency, 51–52
 Orientation distribution function (ODF), 102–105
 Orthonormal basis, 130

P

Padding strategy, 85–86, 86*f*
 of masked regions, 87–88
 Perfectly plastic response of composites, MKS for, 182–186
 Perturbation of local strain tensor, 138–139, 148
 Plastic response of polycrystalline metals, modeling of, 22–23
 Poisson’s ratio, 171
 Polarization tensor, 165–166
 Polycrystalline materials, 40–48
 crystal lattice orientation, 41
 coordinate transformation matrix for Cartesian reference frames, 41–43, 42*f*, 43*f*
 fundamental zone, 45
 mesoscale structure, 41*f*
 microstructures, 40–41
 quantifying regions, 48–49
 Polycrystalline microstructures, 69–70
 Polycrystals, study of elastic responses, 178–182
 Polymer electrolyte fuel cells (PEFCs),
 microstructure–property relationships in, 155–157
 Principal component analysis (PCA), 112–116, 150–152, 156–157, 161, 192–193
 computing transformation, 116
 consequences of, 115
 dimensionality reduction using, 113*f*

- eigenvalues computed in, 114–115, 117–118
 linear, distance-preserving transformation, 113
 variance observed in data ensemble, 116–117
- Principal components (PCs), 114–116, 152, 192–193
- Probability and probability density, 49, 166
 of a chord, 90
 of realizing an outcome, 49
- Process—structure—property (PSP) linkages, 2–6, 12, 13*f*, 17, 21–22, 68–69, 95, 145–146, 208–209
 for crystal plasticity computations, 196–203
 data-centered framework for, 145–147, 146*f*
 mathematical framework for, 191–194
 on selected phase-field models, case study, 194–196
- Protocols for establishing materials knowledge and wisdom, 22–23
 impediments for establishing, 22–23
- Q**
 Quantitative description of material microstructure, 48
 Quantization, 17–18
- R**
 Rectangular Cartesian coordinate system, 130
 Reduced-order models, 2
 Reduced-order representations of the material structure, 2
 Reference frame, 130
 Reference stiffness tensor, 139
 Representative volume element (RVE), 35–37
- microstructure features in, 36
 Rigid body translations, 135
 Rule of mixtures, 137–138
- S**
 Saturation-type law, 198–199
 Scalars, 130
 Scientific research platforms, 210–211
 Authorea, 210–211
 GitHub, 210–211
 Google +, 210–211
 Google Docs, 210–211
 LinkedIn, 210–211
 Mendeley, 210–211
 Plot.ly, 210–211
 ResearchGate, 210–211
 ShareLaTex, 210–211
 Self-consistent model, 137–138
 Slip, 10
 Slip resistance, 12
 Solid texture synthesis algorithms, 97–99
 Spatial correlations
 application of, 116–118
 of discretized spatial bins, 77, 78*f*
 ensemble of material structures, 75–76, 76*f*
 ensemble of α – β Ti micrographs, case study, 118–119, 119*f*
 higher order, 79, 89–91
 inclusion-matrix composite system of steel, case study, 120–123
 lower order, 79
 MD simulation datasets, case study, 123–126, 125*f*
 normalization factor in, 78–79
n-point, 79
 1-point, 77, 81
- ordered local states in, 80
 principal component analysis (PCA), 112–116
 reconstructions of microstructures from, 91–94
 from correlation functions, 93
 3-D representative volume elements (RVEs), 93
n-point spatial correlations, 91–92
 optimization techniques, 93
 from partial sets of 2-point spatial correlations, 95–99, 98*f*
 2-point spatial correlations, 92
 using Gaussian random fields (GRFs), 93
 representation of the structure metric, 76–77
 of spatial bins, 78–79
 structure metrics, 79
 3-point, 79
 2-point, 77–82
 between two points separated by a specified vector, 77
 visualization of, 83–89
- Spatial distributions, 1–2
 Spectral representation of microstructure function, 65–71
 for continuous local state, 69–70
 Fourier representations, 67–68
 mathematical representation, 65–67
 molecular dynamics (MD) simulations, 70–71
 three-dimensional microstructure volume, 65–66

- Spectral representation of microstructure function (*Continued*)
- using classical harmonic series, 66
 - using generalized spherical harmonic basis (GSH), 67–68
- Spinodal decomposition, 194–195
- Standard deviation of error of fit, 154
- Standardization and automation of workflows, 21
- Statistical homogeneity, 76–78
- Statistical measures of microstructures, 19–20
- representative microstructures, 100–105
- spatial correlations, 75–83, 76f
- higher order, 89–91
 - reconstructions of microstructures from, 91–94
 - visualization of, 83–89
- Statistical volume elements (SVEs), 101–102
- Steels, 1–2
- crystal plasticity calculations for interstitial-free (IF), 201–202, 202f
- microstructures in, 11–12
- phases encountered in, 8
- structure–property linkages for nonmetallic inclusions/steel composite system, study of, 158–165
- structure–property linkages in an inclusion-matrix composite system, study, 120–123
- thermodynamic phases, 39
- Stiffness matrix
- exhibiting cubic crystal symmetry, 137
- exhibiting isotropic properties, 137
- exhibiting orthorhombic symmetry, 136
- Stiffness tensor, 138–139
- Stochastic variables, 24–25
- Strain, 135
- Green's definition of, 135
- Stress
- defined, 131
 - on the surfaces of an infinitesimal cuboidal volume, 131–132
- Stress tensors, 131, 132f
- hydrostatic and deviatoric components, 133
- Stress vectors, 132–133
- Structured data, 21
- Structure–property linkages for nonmetallic inclusions/steel composite system, study of, 158–165
- averaged true stress-strain response to a power hardening law, 161
- cohesive zone model (CZM) parameters, 160
- generating ensemble of microstructures, 159–160
- generating structure–property linkages, 161–162, 163f, 164t
- conventional approach, 161–162
 - data-science approach, 162–165
- macroscale parameters, 162
- macroscale performance parameters, 160–161
- material parameters used, 160t
- modeling of inclusion/steel matrix interface, 160
- Structure–property linkages in an inclusion-matrix composite system, study, 120–123
- autocorrelations, 122–123, 123f
- microstructures considered, 120
- PCA representations, 120–122, 121f
- PCA-approximated autocorrelation, 123f
- spatial correlation plots, 122
- 2-point autocorrelations, 120
- T**
- Taylor model of crystal plasticity computations, 197, 201–202
- Tensors, 33–35, 129–131.
- See also* Stress tensors
- Cauchy stress, 182–184
 - localization, 165–166
 - polarization, 165–166
 - transformation laws for, 45
- Thermodynamic phase identifier, 38–39
- Thermodynamic phases, 8
- Three-dimensional crystal lattice orientations, 10
- 3-D representative volume elements (RVEs), 93, 100–102
- 3-D statistics of the microstructure, 95–97, 98f
- 3-point spatial correlations, 79
- Ti alloys, 1–2
- local states in, 38–39
- Transformation laws for tensors, 45

2-D micromechanical finite element (FE) model, 159–162, 170–171, 175–176
calibration for two delta microstructures, 174
finite element FE meshes, 171–172
periodic boundary conditions, 171–172, 173*f*
predictions of the strain fields, 178*f*

simulations, 171–172
validation microstructures, 174
2-D microstructure, 84–85
2-point autocorrelations, 120
2-point spatial correlations, 77–82, 92, 156

V

Vectors, 130
Velocity, 130

W

Weighted statistical volume elements (WSVEs), 101–102, 103*f*
computational advantages of, 102–103
constraints in, 102
identification of, 102

Z

Zr alloys, 1–2